Delft University of Technology

Determining the structural evolution and strain distribution of a geologically complex area in SE of France by restoring multiphase deformation

By

Cyrille Krijn Jones

In

Reservoir Geology,

Applied Earth Sciences

Supervisors:

Drs. J.C. Blom

Faculty of Civil and Applied Earth Sciences Engineering

TU Delft

August, 2019

Acknowledgment

This project has been carried out during my Master graduation phase. I would like to thank my supervisor Drs. J.C. (Jan Kees) Blom who provided me knowledgeable insight during the course of this project. I'm also grateful to have been part of the 2nd year Bachelor fieldwork in 2018 as a supervisor as well where I learned to guide students during their fieldwork and provide them with geological insight. Finally, I would also like to thank geologist Richard Maillot who has been studying the geology around La Motte-Chalancon for many years and shared his knowledge with me during a day on the field.

Abstract

As natural resources such as oil or gas are concentrated in folded and faulted rock strata in the subsurface of geologically complex areas, understanding the geometry and complexity of such geological structures is crucial. It allows geoscientists and engineers not only to reduce uncertainties and risks but also provides visual representation of the subsurface. This paper provides insight on the impact of a local study on a global (tectonic) scale using a technique involving 3D modelling and restoration of geological structures that have evolved through time under the surface.

The structural evolution, phases and amount of deformation, and the strain distribution of the sedimentary cover of a geologically complex area of 270 km^2 in the French subalpine chains (Southeast of France; in the surroundings of the village La Motte-Chalancon) were deduced from the modelling of two folded and faulted competent layers (Tithonian and Barremian formations) both in 2D and 3D. These models were constructed from collected geological data such as BRGM (Bureau de Recherches Geologiques et Minères) geological maps, previous Bachelor's fieldwork data, new field data and the study of aerial photographs (Google Earth). A grid of 20 vertical 2D cross-sections (10 N-S, and 10 E-W) was generated which was then imported and digitized in the geological modelling software package Move and the 3D model of the competent layers was built, validated and restored to its initial configuration prior to deformation by first removing each fault displacement (Fault Parallel Flow method) and then unfolding each structure (Flexural Slip method) in Move, showing deformation and shortening in two directions: N-S and E-W. The amount of deformation in both directions was estimated from the 3D model. Major deformation took place in the N-S direction with a maximum of 21% shortening for both layers which corresponds to an absolute shortening of 4067m for the Tithonian layer and 4076m for the Barremian layer. Less deformation took place in the E-W direction with a maximum of 9% to 10% for the Tithonian and Barremian horizons respectively which corresponds to an absolute shortening of 1697m and 1976m respectively. This resulted in an area reduction of 16% and 19% of the original area prior to deformation for the Tithonian and Barremian, respectively. These results were determined after reducing the uncertainties related to interpretation errors when constructing the 2D cross-sections and modelling errors. These were estimated during the fault removal and unfolding processes. Misfits of 16-18% were found for both horizons after removing fault displacements. After unfolding the structures, misfits decreased for the Tithonian to 13-14% but increased for the Barremian to 24-27%. Restoration of the 3D model through jigsaw restoration reduced the uncertainties to 7-8% and 10-15% for the Tithonian and Barremian horizons respectively.

Two phases of deformation over geological time were deduced from the orientations of the folds and faults present in the studied area. The presence of NW-SE trending folds and thrust faults (e.g. Mt D'Angele fault, Pommerol fault, or Chalancon fault) along with a conjugate strike-slip system (of one oriented N-S and one NE-SW) reflects the NE-SW compressional stress regime of the first stage of deformation which is related to the Pyrenean phase of the Alpine Orogeny. The second stage, the Alpine phase, which resulted in E-W contractions, is associated with the formation of domal/basinal structures as well as folds with plunging fold axes within the studied area. The northeastern part of the studied area exhibits different fault trends. Two tear faults (L'Aiguille and Ruelles fault), a dextral N-S strike-slip fault (Establet fault), and two E-W trending reverse faults (Peyssias and Hidden fault) resulted from N-S

compression. These are related to the first phase of the Pyrenean stage, and then later partly rotated during the latter phase of the Alpine stage.

The strain maps produced from the 3D model displaying the high-/low-strain zones of the area mainly show E-W and NW-SE trending strain zones which confirm the direction of the main stress regime of the Pyrenean compressional phase oriented NW-SE.

List of tables

List of figures

Table of Contents

1. Introduction

The study of geological structures is of crucial importance in Applied Earth Sciences (AES) since it provides information on the geometry of the rocks found in the subsurface. Natural resources such as petroleum or natural gas commonly accumulate in traps formed by folded and faulted rock strata in the subsurface. Therefore, the location and spatial distribution of these structurally complex areas are key to find these concentrations of economically attractive resources.

Many terrains have undergone multiple phases of deformation over geological time, sometimes creating difficult and unclear structures that aren't easy to unravel. Analyzing the relative timing of these structures, as well as the correlation between the different phases of deformation can be therefore challenging. In order to unravel the complexity and understand better the structural evolution of such terrains, modelling these structures in 3D using geological maps and digitized 2D vertical cross-sections through backward modelling and reverse each deformation phase step by step can provide solutions to these problems.

The designated area for this project is part of a geologically and structurally complex area in the French subalpine chains (Fig.2). The sedimentary cover of this region is part of the Mesozoic Vocontian Basin. This basin's initial sedimentary infill and configuration resulted from an Early Jurassic episode of rifting (Elmi, 1983; Giot et al., 1991) which led to the formation of large-scale tilted horst and graben structures (Bombardiere et al., 2000; Lemoine et al., 1986). Its present structure is due to the Late Cretaceous-Paleogene and Neogene episodes of inversion (Roure et al., 1992) during the Alpine Orogeny. The complexity of the Alpine Chains structures resulted mainly from contraction in two directions, related to two different phases, the Pyrenean- and Alpine stages.

The area of interest has been intensively investigated for many years by AES Bachelor students of TU Delft as it is part of a geological fieldwork. Numerous geological maps, 2D vertical cross-sections and tectonic maps of the area have been produced over the years providing sufficient data for this project. Furthermore, the BRGM (Bureau de Recherches Géologiques et Minières) institution of France has done geological research in the area as well and constructed detailed geological maps (scale of 1:50 000) which were used for this project. Modelling this area's structures in 3D hasn't been done before and is part of a local study (Fig.2) which could be used as a framework to analyze features on bigger scales such as regional and global (tectonic plates) scales.

Previous work on this subject was done on a regional scale by Gratier et al. (1989). They described the strain-displacement fields of the Subalpine Chains caused by the stages of the Alpine Orogeny using a 2D finite element analysis. The total displacement fields derived in their work show that the effect of the Alpine stage (Fig.1; right) was much greater than the Pyrenean stage (Fig.1; left).

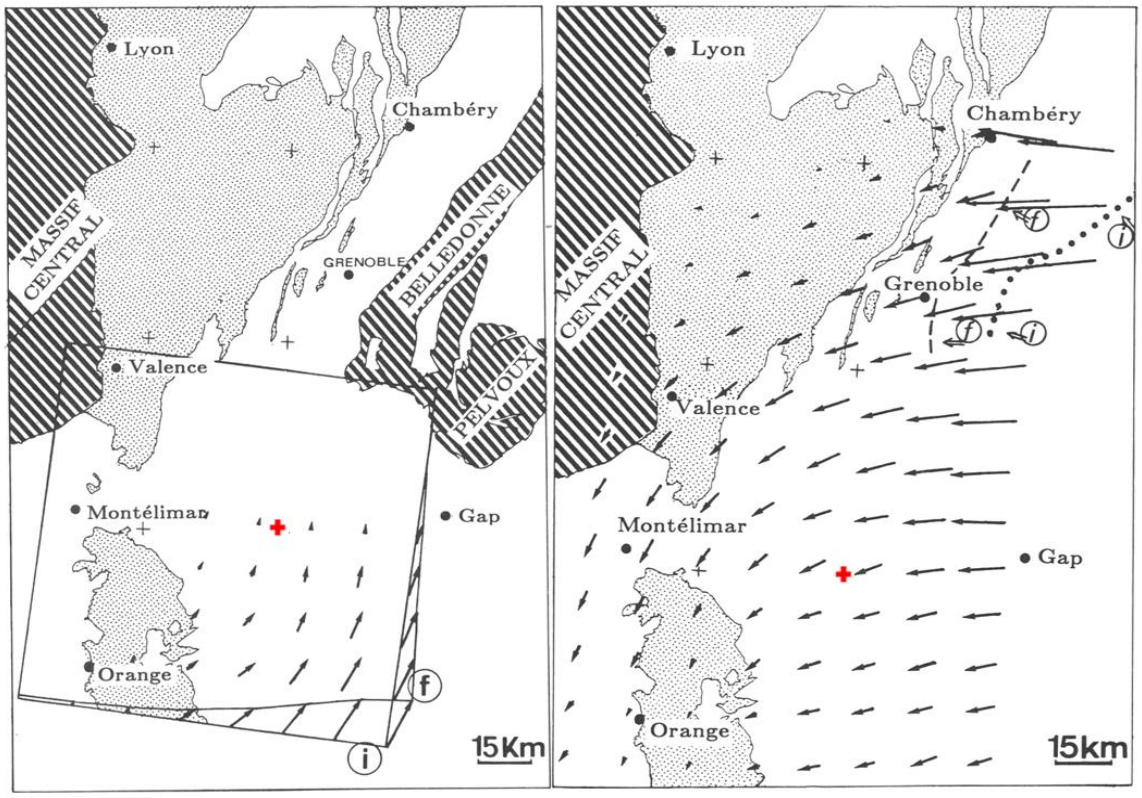

Fig.1: Total displacement fields of the Pyrenean stage (left) and the Alpine stage (right). The location of the studied area is marked by the red cross. (Gratier et al., 1989)

The aim of this project is to build and restore a geologically plausible 3D model of this geologically complex area based on existing geological data such as the BRGM geological maps, Bachelor's field data or aerial photos via Google Earth in order to deduce and analyze its structural evolution, as well as the strain distribution during different phases of deformation first on a local scale and then, relate it to the strain distribution on a regional and global (tectonic) scale.

The studied area is located in the southeast of France, more specifically to the south of the city Die on the eastern side of the Rhône River (Fig.3) and is approximately 270km^2. Complex faults, folds and thrusts structures resulting from compressional regimes are found in this area.

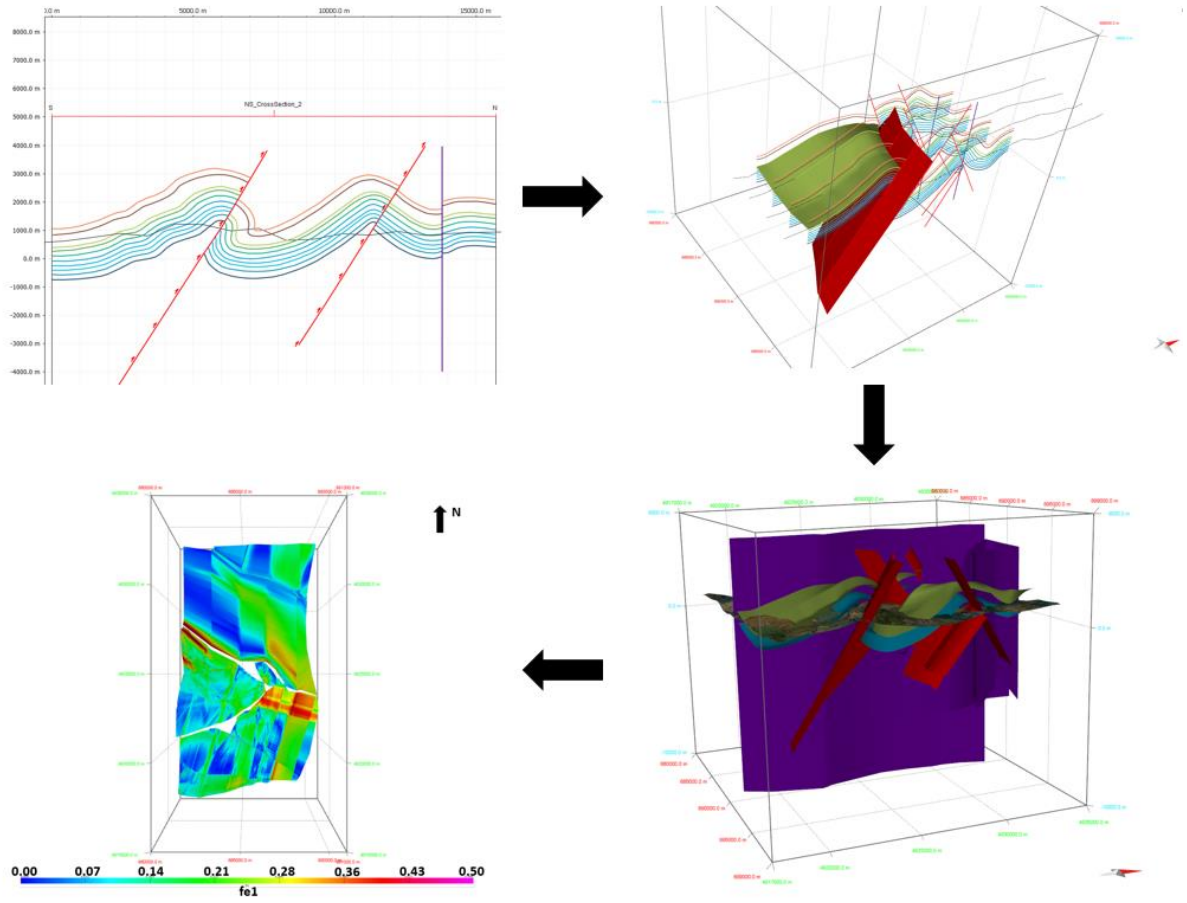

Fig.2: Overview of the methodology used for this project starting with 2D vertical cross-section making (top left), followed by fault/horizon surface generation (top right) resulting in a 3D model (bottom right) and strain maps (bottom left).

Based on geological data such as BRGM geological maps, satellite data (Google Earth), and field observations, a 3D model of the designated area was built using the Move software package provided by Midland Valley (Fig.2). A geological model was first constructed in 2D using the geological data mentioned above, together with geological maps and vertical cross-sections of the area collected during previous Bachelor 2nd year field works. The resulting model was then digitized in Move and surfaces of competent layers (Tithonian and Barremian limestone layers) as well as fault surfaces found in the area were generated (Fig.2). Both the 2D- and 3D model were finally balanced and restored to their initial configuration prior to deformation.

The structural evolution and the amount of shortening were determined based on the restoration. Moreover, correlations between the different phases of deformation of the sedimentary cover of the designated area were deduced. Finally, strain maps of the area were then produced and, as a result, fracture occurrence and densities were predicted.

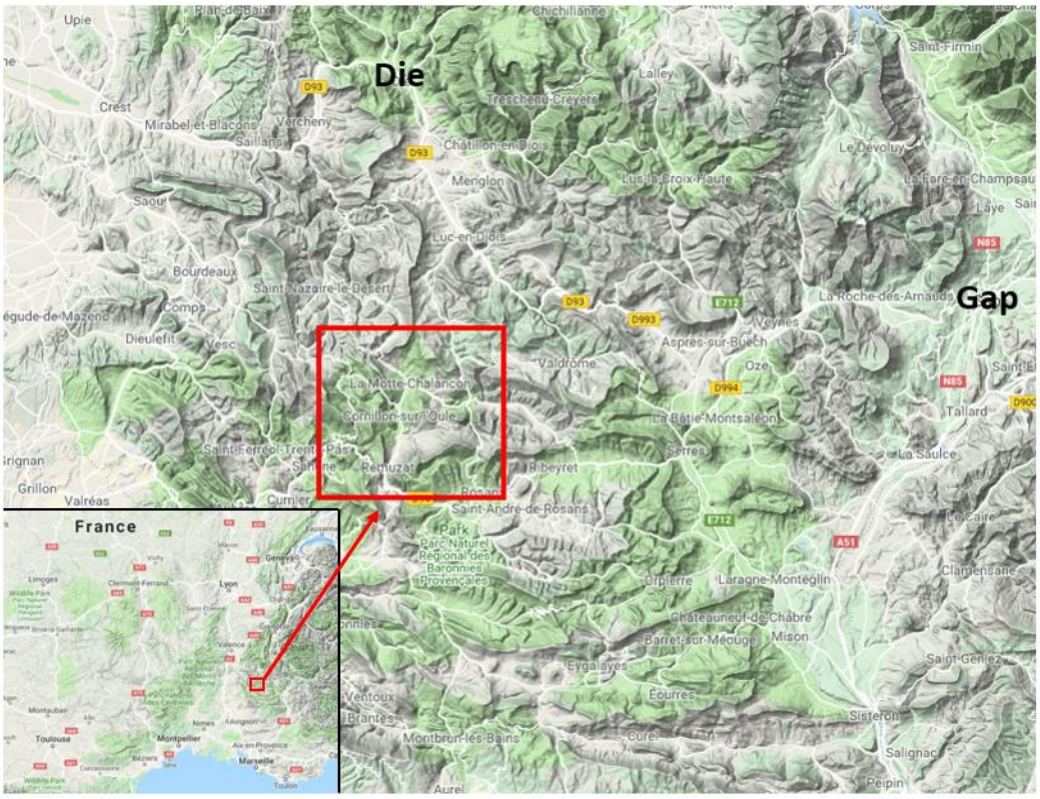

Fig.3: Location of the studied area for this project. (3D Move; Google maps)

2. Geological History

The sedimentary rocks of the area were deposited in the Mesozoic Vocontian Basin. The geological evolution of this basin is described in the section below.

The Vocontian Basin is located on the northwestern margin of the Tethys Ocean in the deeper part of the Dauphinois Basin (Fig. 4); its evolution is essentially related to the opening of the Tethys Ocean (Bombardiere et al., 2000) which was connected to the South Atlantic Ocean (Dardeau et al., 1988). During the Late Jurassic, this area was characterized by synsedimentary extensional tectonics resulting in high rates of subsidence (Graciansky et al., 1999) leading to the formation of horst and graben structures (Bombardiere et al., 2000).

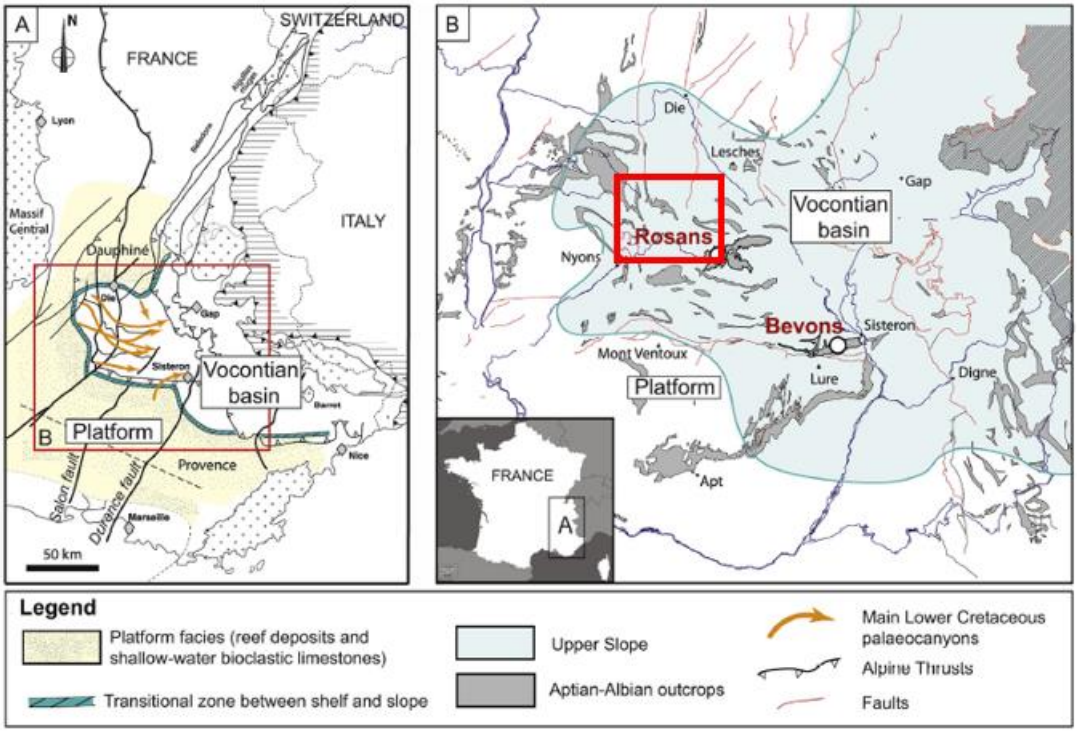

Fig.4: Map indicating the location and palaeogeography of the Vocontian Basin in the south of France during Cretaceous. (Ravier et al., 2015)

This basin consists of three distinct and contrasting sedimentation domains, namely a platform (Fries & Parize, 2003), a long and gentle submarine slope (Graciansky et al., 1999), and a basin. The platform deposits are mainly composed of reef deposits and shallow-water bioclastic limestones (Fries & Parize, 2003), and the slope/basin deposits are mainly represented by pelagic sediments displaying marl/limestone alternations which are disrupted by gravity reworkings (e.g., slumps, debris flows, sandy turbidites) (Ravier et al., 2015).

2.1 Mesozoic evolution of the Tethys Ocean

The Vocontian Basin's sedimentary- and structural configuration is related to the evolution of the Tethys Ocean which consists of four main stages spanning from the Triassic up to the Late Cretaceous.

During the Triassic, a period of pre-rifting with extensional tectonics took place. Mainly marine but shallow-water environments were prevailing leading to deposition of Middle-Upper Triassic platform carbonates and evaporites (Lemoine et al., 1986) in the area which was to become the opposing continental margins of the Tethys Ocean. Rifting then took place during the Early Jurassic to Mid Jurassic leading to the formation of subsiding pelagic-hemipelagic basins (Lemoine et al., 1986), one of them being the Vocontian Basin.

Following this event, during the Late Jurassic to Early Cretaceous, the break-up of the supercontinent Pangea began and resulted in the opening and spreading of the Central Atlantic Ocean as well as the Tethys Ocean. This initiated the eastward movement of Africa with respect to Europe (Lemoine, 1983; Fig. 5). This episode led to a discontinuous deposition of pelagic/hemipelagic sediments in the basin.

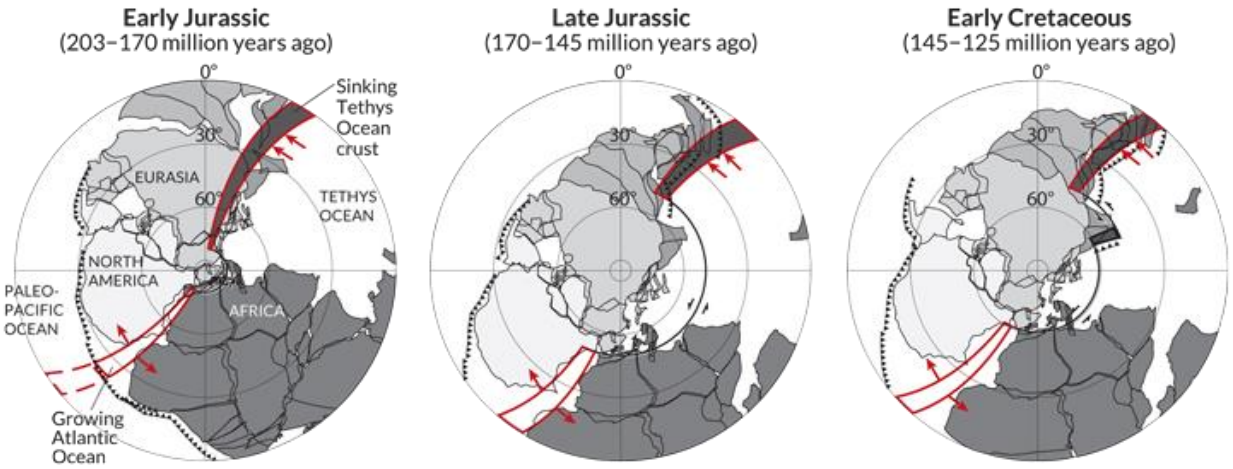

Fig.5: Evolution of the Tethys Ocean from Early Jurassic to Early Cretaceous. (Keppie, 2015)

Finally during the Late Cretaceous, the onward opening of the Atlantic Ocean led to the closure of the Tethys Ocean and the northward movement of Africa towards Europe initiating continental collision. This resulted in the deposition of siliciclastic sediments forming the first flysch basins (Lemoine et al., 1983) which are deep basins forming on the continental side of a mountain building episode.

2.2 Sequence stratigraphy

Sedimentation in the basin was influenced by the tectonic activity, but was also regulated by climate and sea-level changes on the surrounding margins (Graciansky et al., 1999). In Fig.6, a stratigraphic column representing the lithology deposited during the Jurassic-Cretaceous as well as their corresponding sea level changes (red arrows) is shown.

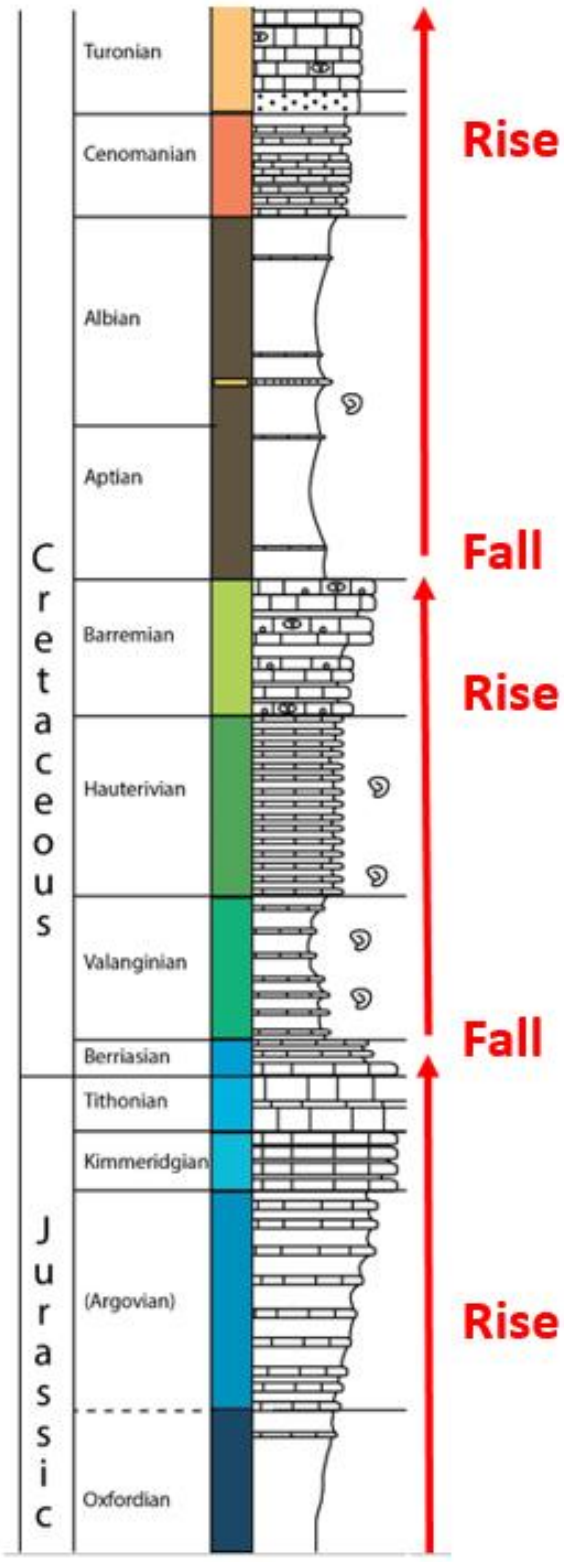

Fig.6: Stratigraphic column of the Jurassic-Cretaceous sequence. Red arrows representing sea-level fluctuations. (Author: Blom, J.C.) For the ages of each formation, refer to Fig. 18.

The deposition of these formations can be subdivided into three cycles, all going from a low-, to a high-sea-level stand (Fig. 6).

Late Jurassic (163.5 – 145 Ma)

During the Early Oxfordian, cold temperatures and low sea-level gave higher erosion rates and low carbonate productivity (Boulila et al., 2010), which in turn led to the deposition of a few hundreds of meters of pelagic marl beds (the so called "Terres Noires") in the basin (Courjault et al., 2011). This was followed by warmer temperatures and sea-level rise in the Late Oxfordian which gave lower erosion rates and high carbonate productivity leading to the cyclic deposition of limestone beds (Boulila et al., 2010) alternating with the marl beds. Furthermore, the Kimmeridgian corresponds to a keep-up transgressive system tract (Colombie & Strasser, 2000) which resulted in the production of more carbonate and thus leading to more limestone beds deposited.

From the Upper Kimmeridgian to the Lower Tithonian, a system of numerous breccias associated with calcarenites were deposited (Ferry et al., 2005). This transition from thin-bedded limestones in the Lower Kimmeridgian to thick-bedded, massive limestones in the Tithonian reflects the basinwards shift of the shelf-derived deposits accompanied by a higher rate of sedimentation (Dromart et al., 1993). The 'Middle' Tithonian to Lower Berriasian is characterized by the deposition of highstand system tract sediments composed of a massive limestone dominant facies (Courjault et al., 2011) which is part of a shelf-margin wedge (Dromart et al., 1993).

Early Cretaceous (145 – 125 Ma)

During the Berriasian, the lithology evolves progressively to a more regular brown-colored argillaceous limestones alternation (Ferry et al., 2005). This alternating sedimentation marks the end of the highstand system tract (Dromart et al., 1993).

The Valanginian is characterized in the Vocontian Basin by the marl/limestone alternations of astroclimatic origin (Huang et al., 1993; Grezelle & Pittet, 2010). The alternations are a result of sea-level fluctuations (Grezelle & Pittet, 2010) which was controlled by short- and long-period orbital cyclicities (Milankovitch cycles) (Boulila et al., 2015).

The Early Valanginian is characterized by asymmetrical sea-level cycles fluctuating from rapid transgressive events to slower regressive events (Grezelle & Pittet, 2010). Moreover, it represents a global change towards a more seasonal and cold climate (Frakes et al., 1992). The Late Valanginian is characterized by a colder and humid climate (Francis & Frakes, 1993) associated with a period of relatively large-scale stable environment (Mattioli et al., 2014) with somewhat more symmetrical sea-level fluctuations. This led to the cyclic deposition of the marl/limestone alternations.

The Hauterivian is characterized by relatively warmer temperatures resulting in more limestone deposition. During this period, a regular alternation of marls and limestones was deposited due to symmetrical sea-level fluctuations. These regular alternations correlate with orbital precession and eccentricity cycles controlling the sea-level fluctuations and deposition of this formation (Grezelle & Pitter, 2010).

The Barremian is characterized by two phases. Tectonic uplift of the Dauphinois Basin starting during the Early Barremian resulted in large, relatively shallow areas creating ideal shallow marine carbonate platform environments on the margin of the basin (Wilpshaar et al., 1997). Tectonic subsidence rapidly increased during the Late Barremian (Wilpshaar et al., 1997) allowing the growth of the carbonate platforms which could keep up with the subsidence and prograde towards the Vocontian Basin (Savary & Ferry, 2004). The basin's relatively narrow width (approximately 150km) with bathyal depth in the center and prograding platforms at its margin creating relatively steep slopes (Wilpshaar et al., 1997) led to the deposition of mass-transported sediments (De Boer, 1983). Grainstones/packstones are deposited as well as huge debris flows and megaslumps (Clavel, 2013) during this phase. While the Vocontian Basin subsided, the Vercors area displayed almost no tectonic subsidence creating an increased tilting with high slope angles between the Vercors and the Vocontian Basin (Whilpsaar et al., 1997; Fig. 6). As a result, the extensive carbonate platform ceased developing due to platform exposure allowing transport of terrigenous sediments into the Vocontian Basin (Cotillon et al., 1984).

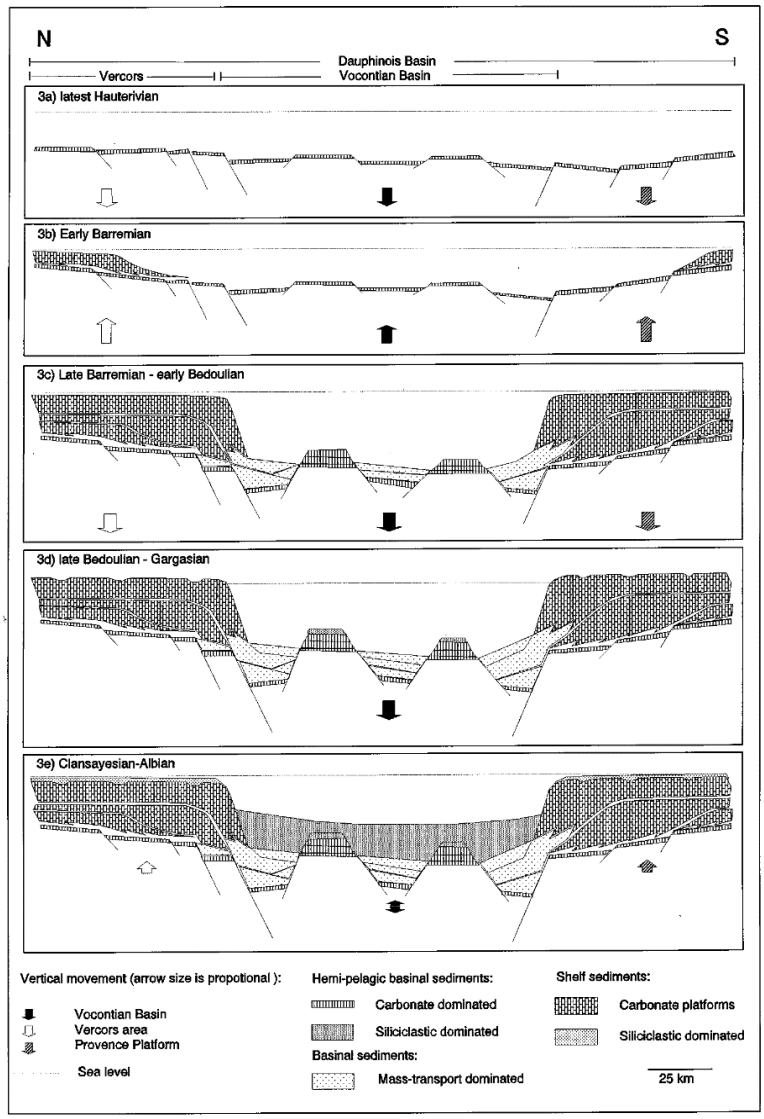

Fig. 6: Evolution of the Vocontian Basin (and the Dauphinois Basin) between the Barremian and the Albian. (Whilpsaar et al., 1997)

Late Cretaceous (125 – 89.8 Ma)

The Aptian and Albian phases are characterized by relatively small rates of subsidence or uplift (Wilpshaar et al., 1997). A thick marly sequence (the so called "Marnes Bleues" formation) accumulated in the basin during this period (Breheret et al., 2000). It consists mainly of soft, dark marls and marly calcareous slope deposits with a range of gravity-driven deposits such as slumps, debris-flow deposits, turbidite packages and massive sandstones (Fries & Parize, 2003). These sandstones are emplaced by high-density turbidity currents or influx of clastic sediments (Ravier et al., 2015) and are the result of an uplift of the basin's margins (Whilpsaar et al., 1997).

During the Cenomanian, a global rise in sea level which reached a maximum in the Early Turonian (Grosheny & Malartre, 2002) led to the deposition of alternating marl/limestone beds. The basinal facies of the Cenomanian is composed of bundles of limestone beds (10-20m thick) separated by equally thick marly intervals (Grosheny et al., 2006). The Upper Cenomanian succession is composed of bedded white limestones and grey marls (Takashima et al., 2009). As well as the Cenomanian, the Turonian is also characterized by a transgressive phase (Goetz et al., 2008) and comprises thick stacked white limestone beds with hummocky cross-stratification indicating an outer platform depositional setting (Grosheny et al., 2006). This carbonate series can have a thickness of 300-400m (Goetz et al., 2008). The Upper Turonian limestones are overlain by chert layers marking the end of the Turonian phase (Goetz et al., 2008).

2.3 Structural setting of the Vocontian Basin

The Vocontian basin's initial configuration and sedimentary infill results mainly from the Tethyan rifting episode during the Early Jurassic (Roure et al., 1994). Its present structure is composed of mainly two sets of compression faults respectively oriented N-S to the south and mainly E-W to the north which correspond to compressional regimes prevailing during the Late Cretaceous and Cenozoic (Huang, 1988; Hibsch et al., 1992).

Fig. 8 shows the plate-tectonic situation at the end of the spreading of the Tethys Ocean before the Iberian plate started to rotate in an eastward motion with respect to Europe. This eastward movement which started in the Aptian (Fig. 9; top) resulted in a sinistral strike-slip fault along the present-day Pyrenean mountain chain (Laubsscher, 1975; Frisch, 1979; Stampfli, 1994) and coincided with the onset of subduction of the eastern part of the Tethys along the Iberian-African plate boundary as Africa also moved eastward but at a slower pace (Handy et al., 2010).

Within the studied area, this Pyrenean phase which spans from the Aptian until the Priabonian (35Ma) approximately resulted in an overall N-S contraction leading to the development of E-W trending folds and faults (Fig. 11) mainly in the south (e.g., The Ventoux-Lure thrust) and some N-S trending dextral strike-slip faults (Gratier et al., 1989; Fig. 11). These strike-slip faults were probably the result of a reactivation of Jurassic synsedimentary normal faults with components of thrust displacements (Gratier et al., 1989) during the Pyrenean deformation stage.

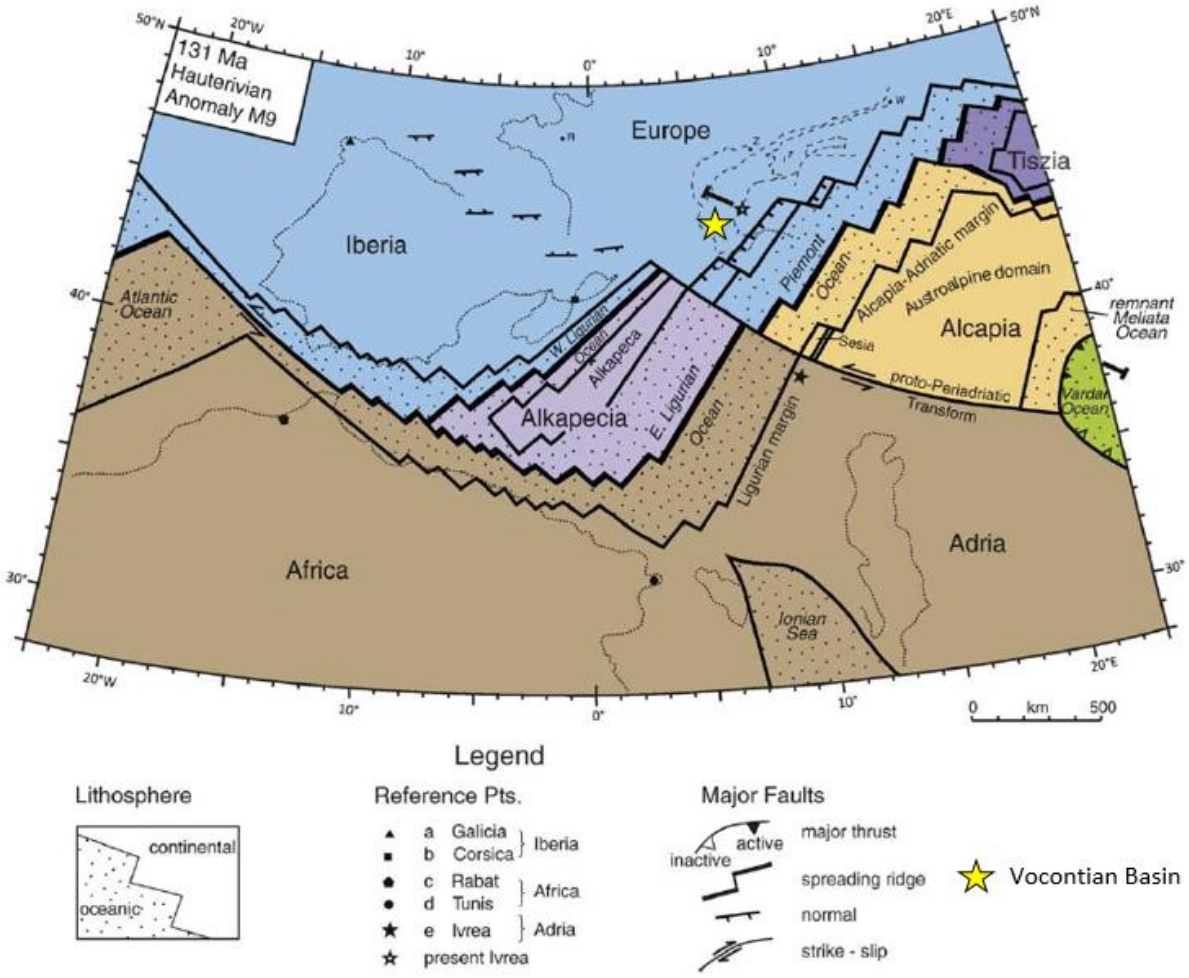

Fig.8: Plate tectonic map of Alpine Tethys in Early Cretaceous time before the eastward motion of the Iberian plate with respect to Europe. (Handy et al., 2010)

Then, between the Aptian and Cenomanian times (Fig. 9), the Adriatic plate rotated in a counter-clockwise motion and started to move away from Africa. These continental plates were later reunited between the Cenomanian (Fig. 9; bottom) and the Santonian (Fig. 10a).

This was then followed by a change in motion of this combined Adriatic-African plate in an oblique propagating motion towards the NNW with respect to the European-Iberian plate. This motion was maintained throughout the Late Cretaceous until collision (Fig. 10b) during the Aquitanian (Handy et al., 2010) and led to the counter-clockwise movement of the Adriatic plate with respect to Europe. Finally, the NW-directed thrusting of the Adriatic-African continental plate onto the European continental plate (Fig. 10b) gave rise to the formation of the Alps today (Handy et al., 2010).

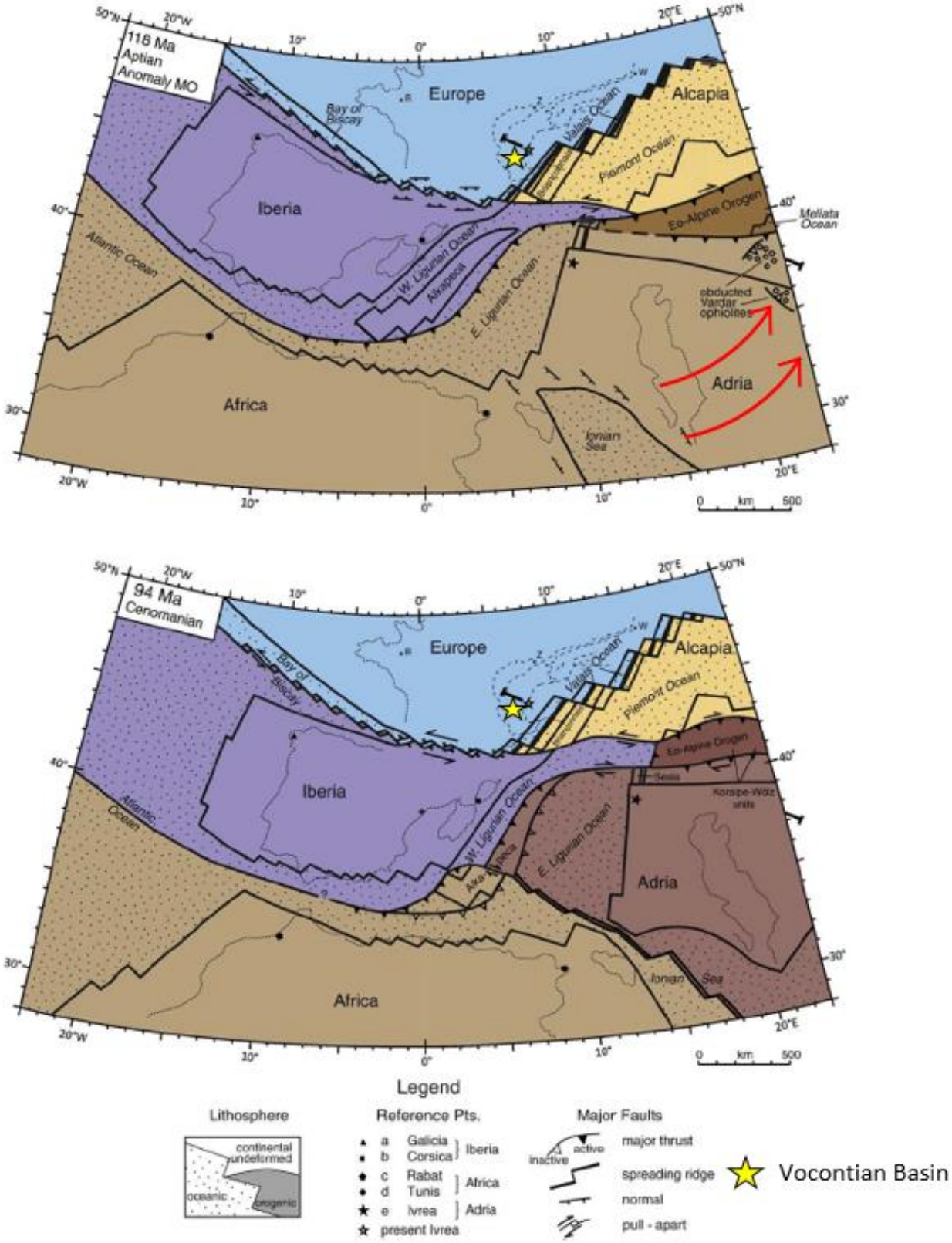

Fig.9: Plate tectonic maps of Alpine Tethys and adjacent continental margins during Late Cretaceous time showing the anti-clockwise motion of the Adriatic plate (top) moving away from Africa and later reuniting (bottom). (Handy et al., 2010)

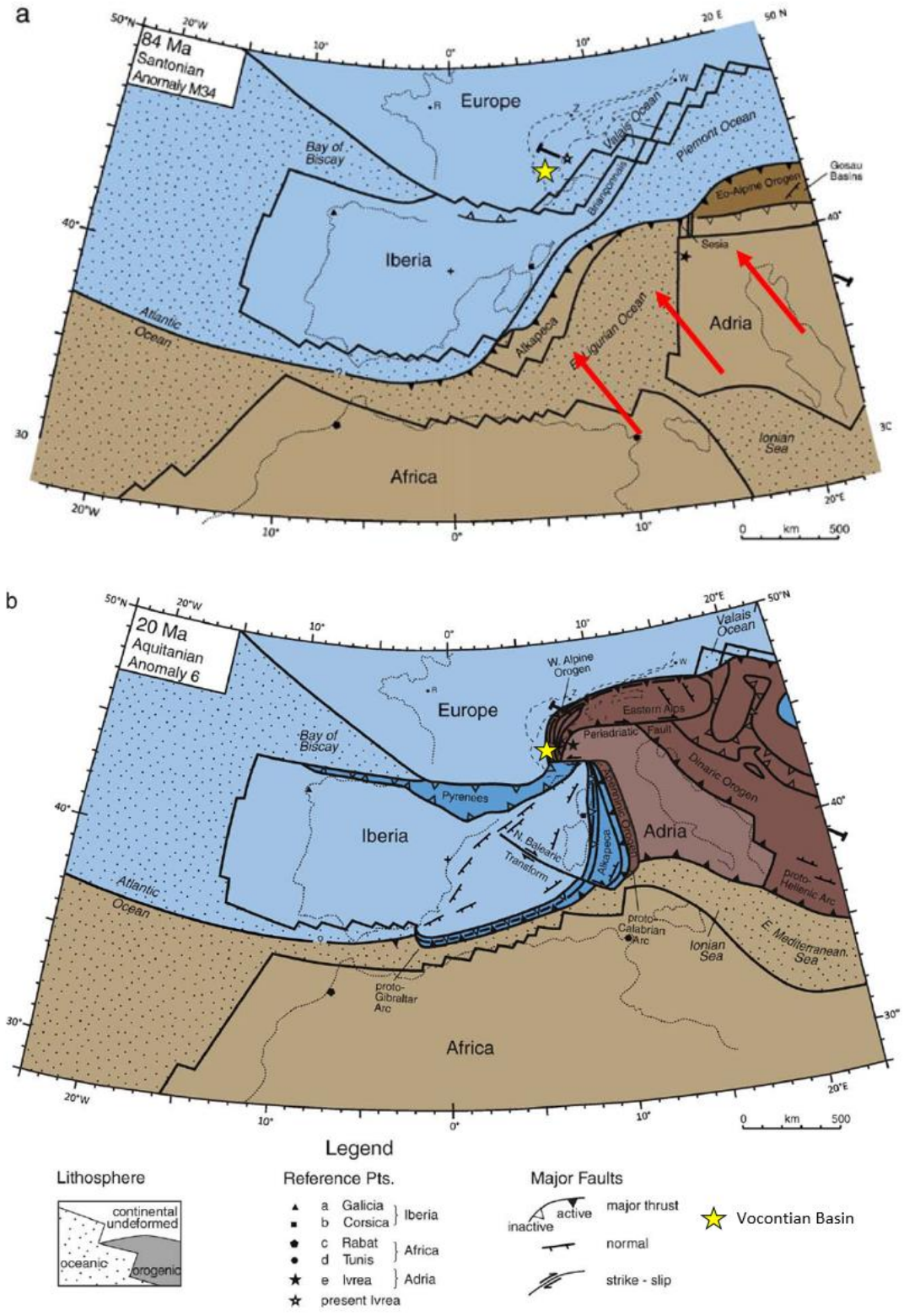

Fig.10: Plate tectonic maps of Alpine Tethys and surrounding continental margins: (a) during NW motion of Africa towards Europe (84Ma); (b) during collision of combined Adriatic-African plate with Europe (20Ma) leading to the formation of the Alps and the Pyrenees. (Handy et al., 2010)

As a result of this Alpine stage, major E-W contraction within the studied area's surroundings led to the formation of N-S to NE-SW trending faults mainly in the northeast (Belledonne and Pelvoux Massif), and an amplification of the already existing E-W folds of the Pyrenean phase (Goguel, 1963).

The studied area (Fig. 11, red box) is bounded to the north by N-S to NE-SW trending folds and thrusts of the Vercors Mountains (Roure et al., 1994) and to the west and south by the NW-SE trending La Lance and the E-W trending Ventoux-Lure thrust folds respectively (Villeger & Andrieux, 1987; Ford 1995).

Between these boundaries, the area is thus affected by E-W trending folds and faults mainly to the south, N-S trending faults more to the north, and some N-S to NE-SW strike-slip faults with some internal NW-SE faults in between.

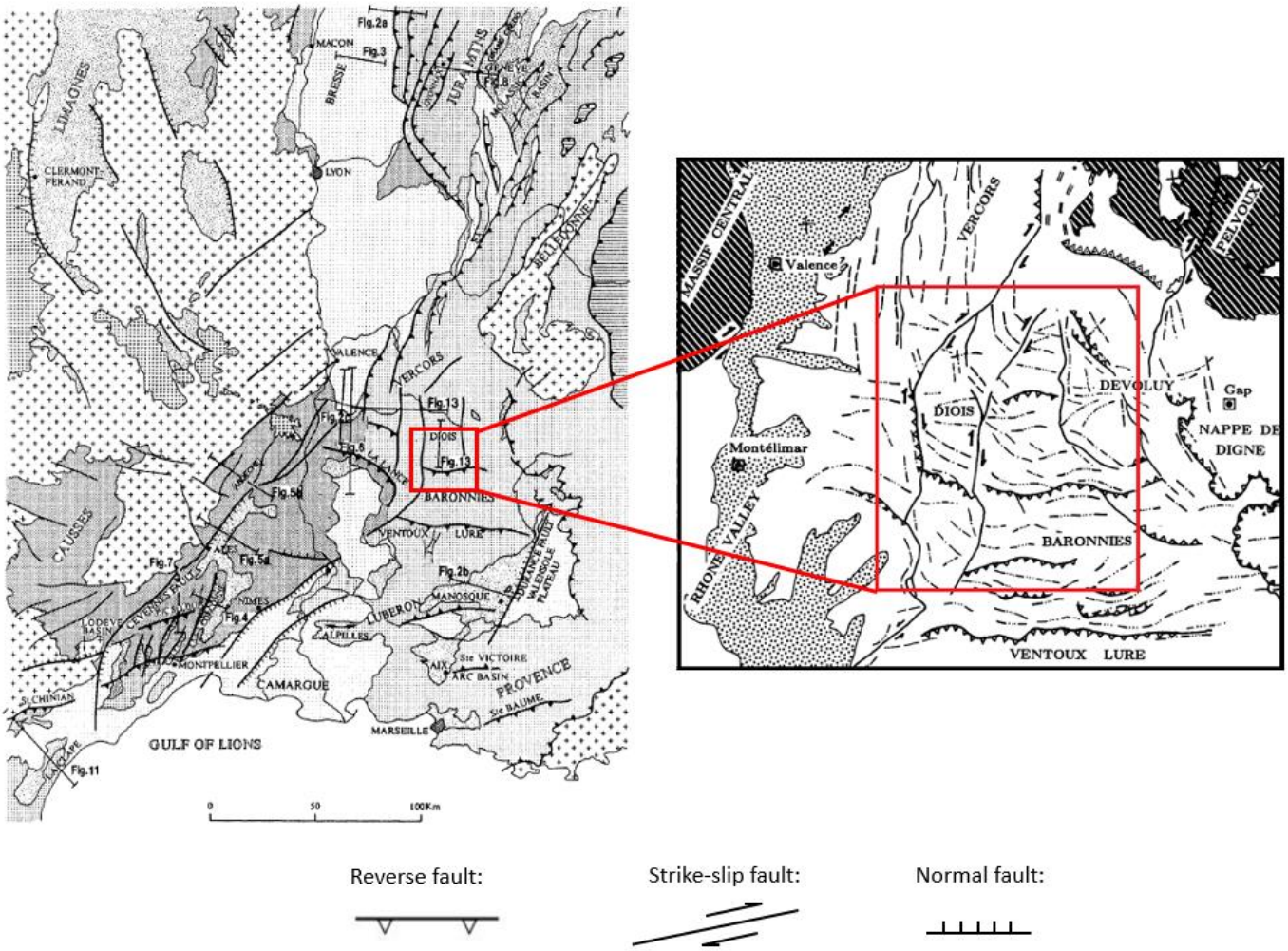

Fig.11: Structural map of the Alpine foreland basin in southeastern France (left: Roure et al., 1994) and the studied area (right: Gratier et al., 1989).

3. Data Acquisition

The geological interpretation of the area is made based on the following geological data:

- Geological maps, tectonic maps, and cross-sections of 2nd year Bachelor fieldwork of Applied Earth Sciences (TU Delft)
- A DEM (Digital Elevation Model) provided by TU Delft (resolution: 26x29m)
- BRGM (Bureau de Recherches Géologiques et Minères, France) geological maps (source: brgm.fr)
- Satellite data (Google Earth)
- Fieldwork observations

2nd year Bachelor fieldwork data

The designated area has been intensively studied for many years. It is part of the fieldwork organized by TU Delft for 2nd year Bachelor students in Applied Earth Sciences. The data of the Bachelor research projects (i.e., tectonic maps, geological maps, and cross-sections; Fig. 12) have been gathered from 16 reports over the last 12 years (Table 1) to better understand and interpret the geological structuration of the studied area.

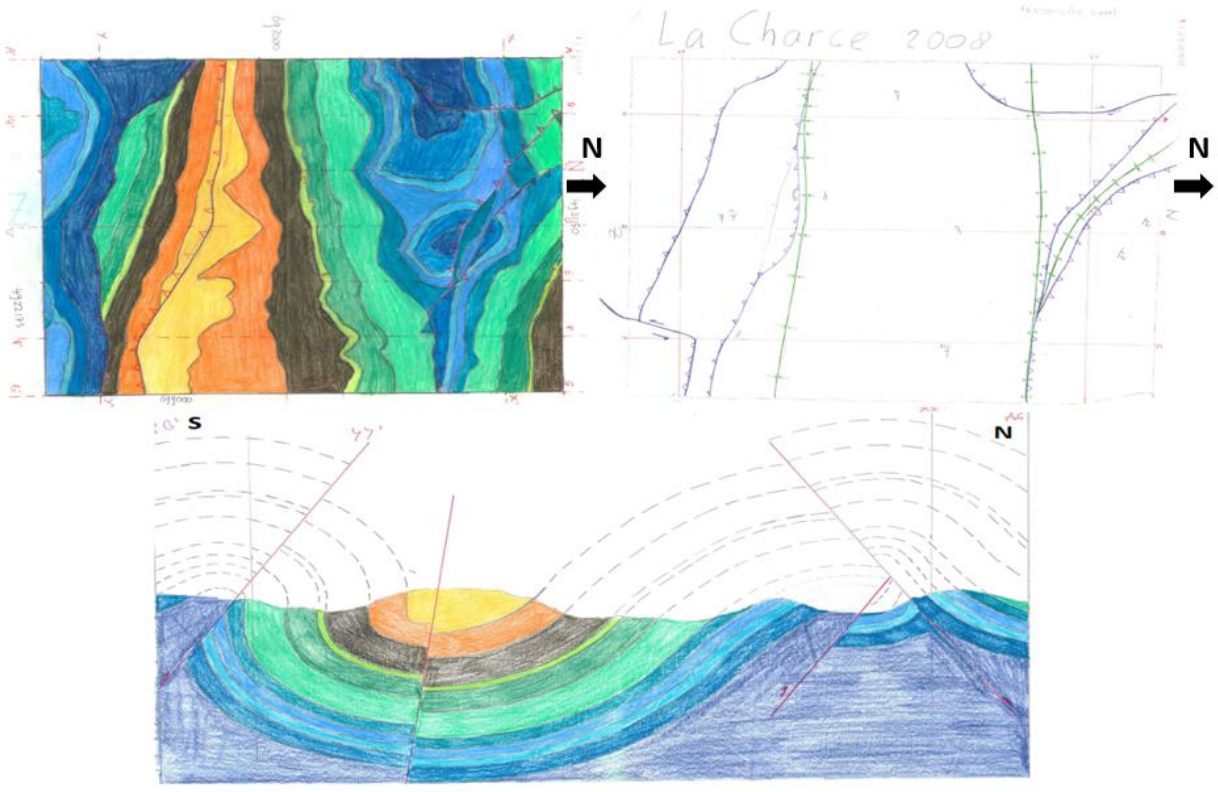

Fig.12: Anonymized example of Bachelor fieldwork data around the village of La Charce. Top left: Geological map of La Charce area; Top right: Tectonic map; Bottom: N-S cross-section (refer to Fig. 5 for the color legend). (La Charce Fieldwork, 2008)

Table 1: List of Bachelor fieldwork data collected for this project for which the name, the year, number of cross-sections, the geological map and tectonic map (V if present; - when missing) are showed for each fieldwork project. For a more detailed description of each project, refer to Appendix A.

Name	Year	Geological Map	Tectonic map	Number of cross-sections
Pommerol	2006	V	-	5
	2014	V	V	3
	2017	V	-	3
La Charce	2008	V	V	10
Villeperdrix	2009	V	V	3
La Motte	2014	V	V	3
	2015	V	V	6
	2017	V	-	5
Rottier	2015	V	-	5
Remuzat	2015	V	V	10
	2016	V	-	6
St Dizier	2017	V	V	5
St May	2017	V	V	8
Arnayon	2017	V	V	0
Cornillon	2017	V	V	5
Aiguebelle	2017	V	V	6

The geological maps matching the designated area, or having overlapping parts, were overlaid on top of each other and compared. These were then used to construct a geological map of the designated area. This was also done with the vertical cross-sections of each area. From these comparisons, 8 of the 16 reports appeared to fit best the geological structures for the studied area. These are highlighted in Table 1 and were used to help build the model. A detailed description of these reports regarding their coverage (boundary coordinates and area) as well as cross-sections and geological maps is given in Appendix A.

DEM (Digital Elevation Model)

In order to construct 2D cross-sections, the topography of the area is needed. Therefore, a digital elevation data grid provided by TU Delft is used to produce a relief map where topography is displayed (Fig. 13). The parameters of the DEM is given in the table below.

Table 2: Grid parameters of DEM (i: horizontal axis; j: vertical axis).

	Grid	
	i	**j**
Size [m]	26	29
Number of intervals [m]	989	983.9
Map area [km^2]	**733**	

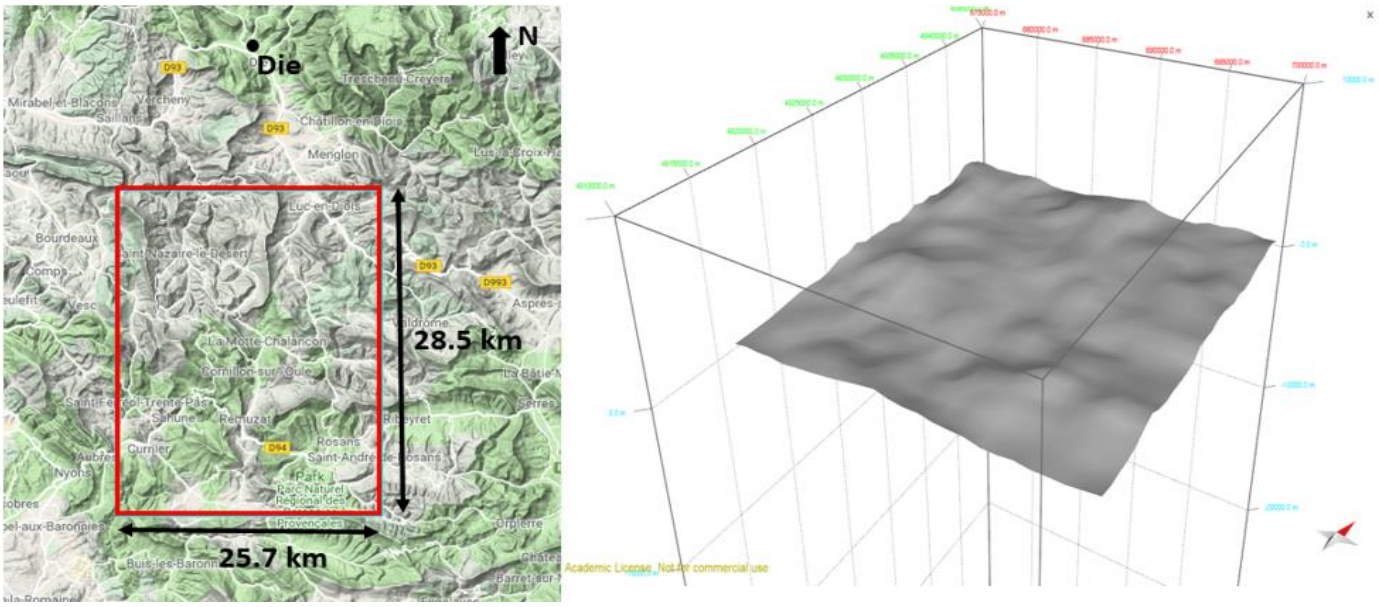

Fig. 13: Dimensions and location of the DEM (left) and a 3D view of it (right) in Move.

BRGM (Bureau de Recherches Géologiques et Minières) geological maps

The BRGM is the French Geological Survey institution for Earth Science applications. After more than two centuries of geological research, numerous geologists have been employed to construct geological maps of France (scale of 1:50 000). Four of these maps (See table 3) have been combined together (Fig. 14) and used in this project to identify boundaries between formations outcropping at the surface. The coordinates and dimensions of the bounding box of the studied area are listed in the tables below (Table 4 & 5). Furthermore, informations about geological structures such as folds and faults are also found in these maps and interpreted in combination with other data in order to construct a plausible geological map for the area of interest.

Table 3: BRGM geological map coordinates.

	Bounding Box Coordinates XY [m]			
	Dieulefit	**Luc-en-Diois**	**Nyons**	**Serres**
Code	XXXI-38	XXXII-38	XXXI-39	XXXII-39
Top	4933636	4933636	4925771.2	4925771
Bottom	4925771.2	4925771.2	4917907.8	4917908
Left	680909	690683.4	680909	690683.4
Right	690683.4	698180.7	690683.4	698180.7

Table 4: Coordinates of the edges of the studied area.

Bounding Box Studied Area			
Coordinates XY [m]		**Coordinates XY [m]**	
Top	4933636	**Left**	680909
Bottom	4917907.8	**Right**	698180.7

Table 5: Dimensions of the studied area.

Dimensions Bounding Box		
X distance [km]	**Y distance [km]**	**Area [km2]**
17.27	15.73	271.65

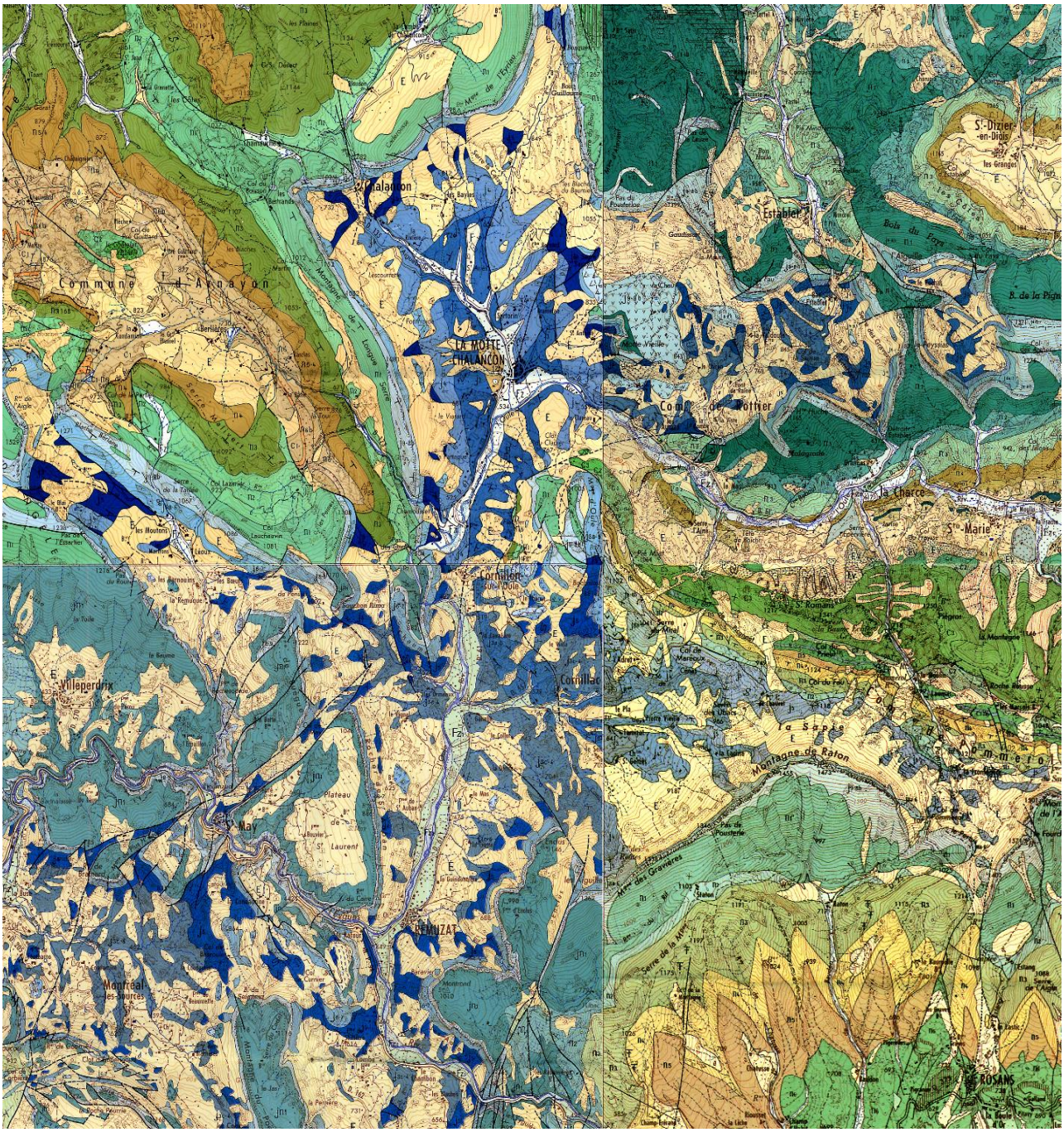

Fig. 14: Geological map of the studied area containing the lithology and geometry of the different formations of different ages during which different color schemes were used (Blue representing the Jurassic and green and brown the Cretaceous). This map is the product of combined BRGM geological maps.

Satellite data (Google Earth)

When the rest of the data is not sufficient to interpret some more complex structures, satellite data was used. Google Earth is a useful tool to look at structures in a somewhat more three dimensional way. The geometry of some structures can best be observed at a larger scale. An example of a large-scale syncline with Turonian limestone in its core is highlighted using Google Earth in Fig.15.

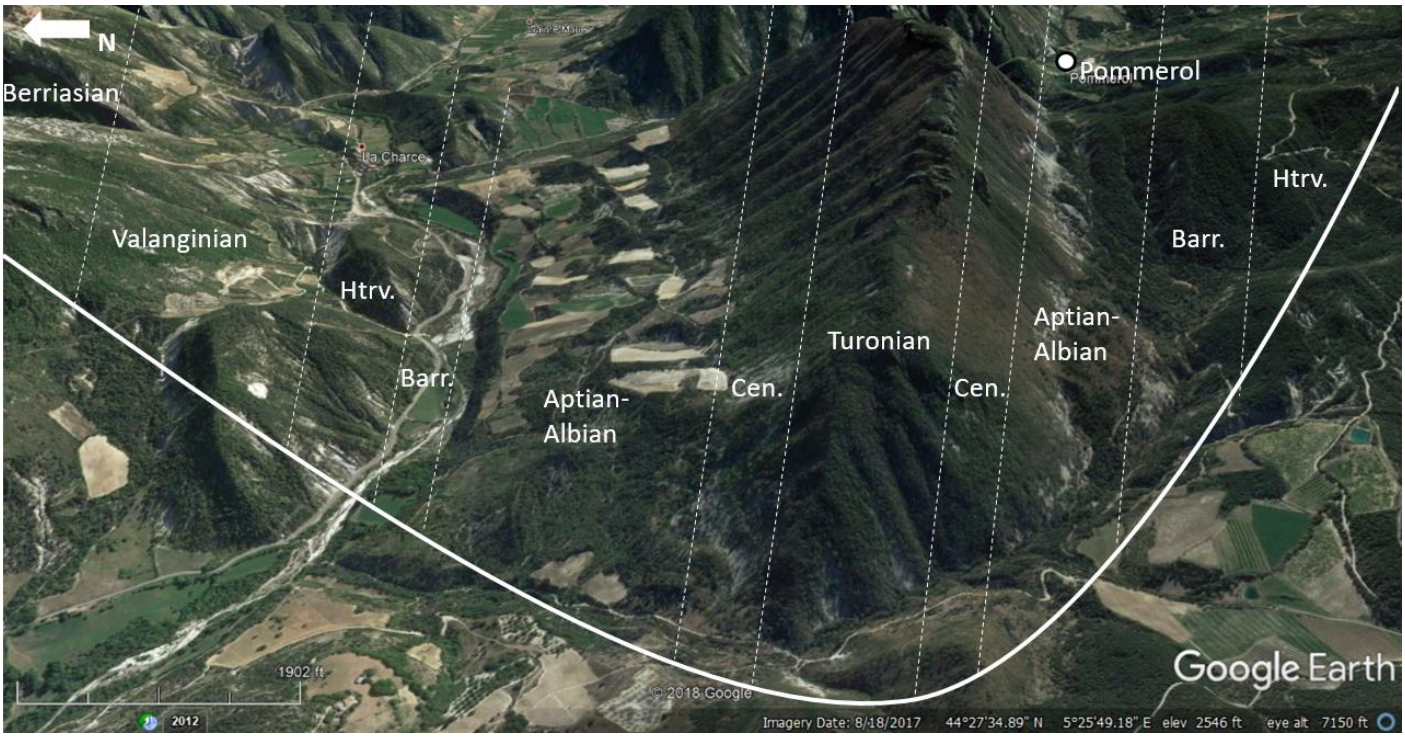

Fig. 15: Bird's eye view to the East of Google Earth showing DEM and draped satellite image of a syncline close to the village Pommerol highlighted by the solid white line. Dotted lines represent the boundaries between formations. Cen.: Cenomanian; Barr. Barremian; Htrv.: Hauterivian. (Google Earth)

To identify most of the structures, a reference layer was used which is, on average, consistent over the whole area and mostly easy to follow. The massive limestone layer of the Tithonian (Fig. 16) was therefore chosen as it is a competent layer that is outcropping extensively in the area. Because of the thickness and hardness of this formation, it mostly forms the ridge of a hill or mountain and is easier to identify using aerial data (Google Earth).

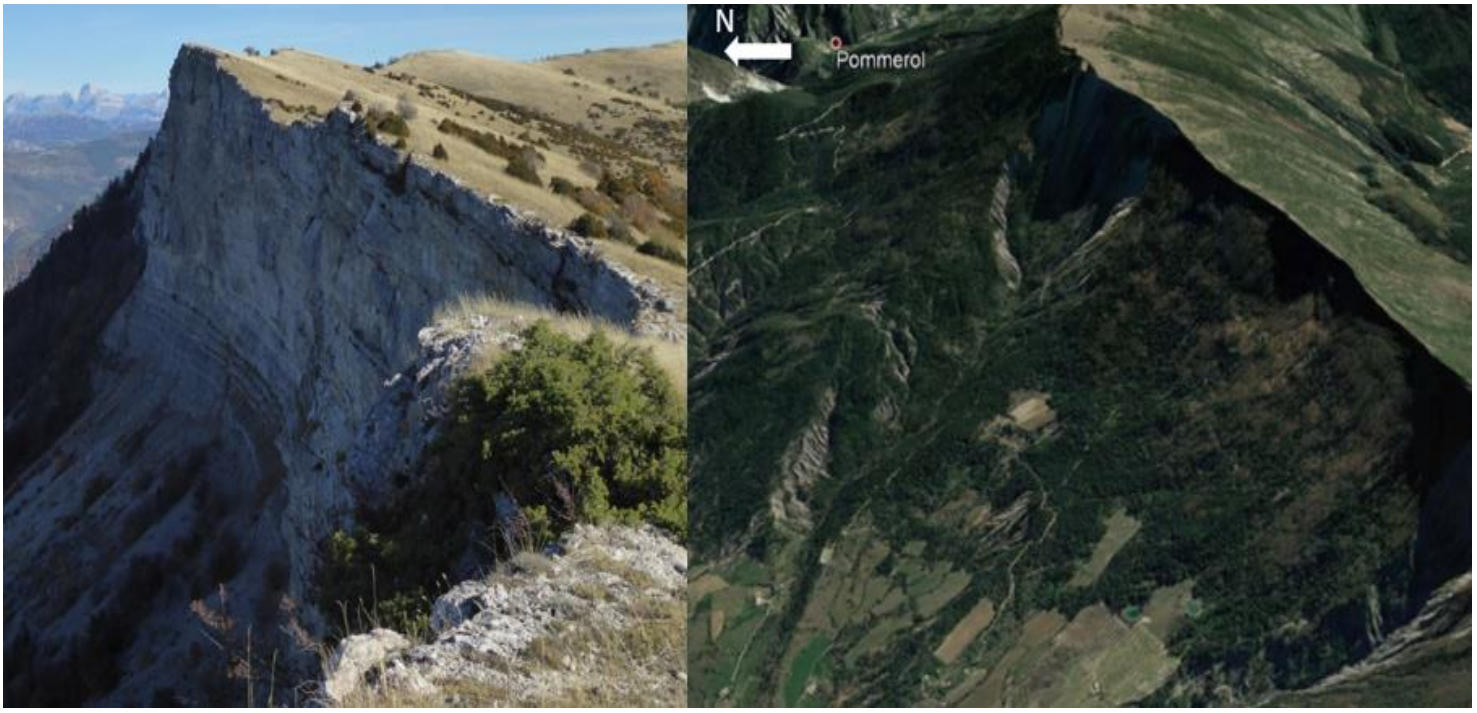

Fig. 16: Left: the Tithonian limestone ridge of the Montagne de Raton near La Motte-Chalancon, France (source: rando-sud-est.com). Right: Montagne de Raton viewed from aerial image in Google Earth.

Fieldwork

During the supervising of the yearly Bachelor fieldwork that took place between May 20th and June 8th 2018, new field data of the designated area was gathered. Parts of the area such as the northeastern part or the southwestern part which were still unclear before the fieldwork were investigated during the fieldwork. Data such as bedding orientations, formation boundaries or possible folds or faults orientations were collected and interpreted providing useful informations on the overall geological structures present. These data were then used to improve already made 2D vertical cross-sections and construct a series of new cross-sections of the studied area, together with the geological map.

The data acquisition has been done using a digital mapping application (the FieldMove Clino). Layers orientations, dips or formation lithologies at specific locations (Fig.17) have been interpreted on the field and inputted in this application. The collected data could then be imported and visualized in Move (Fig.18).

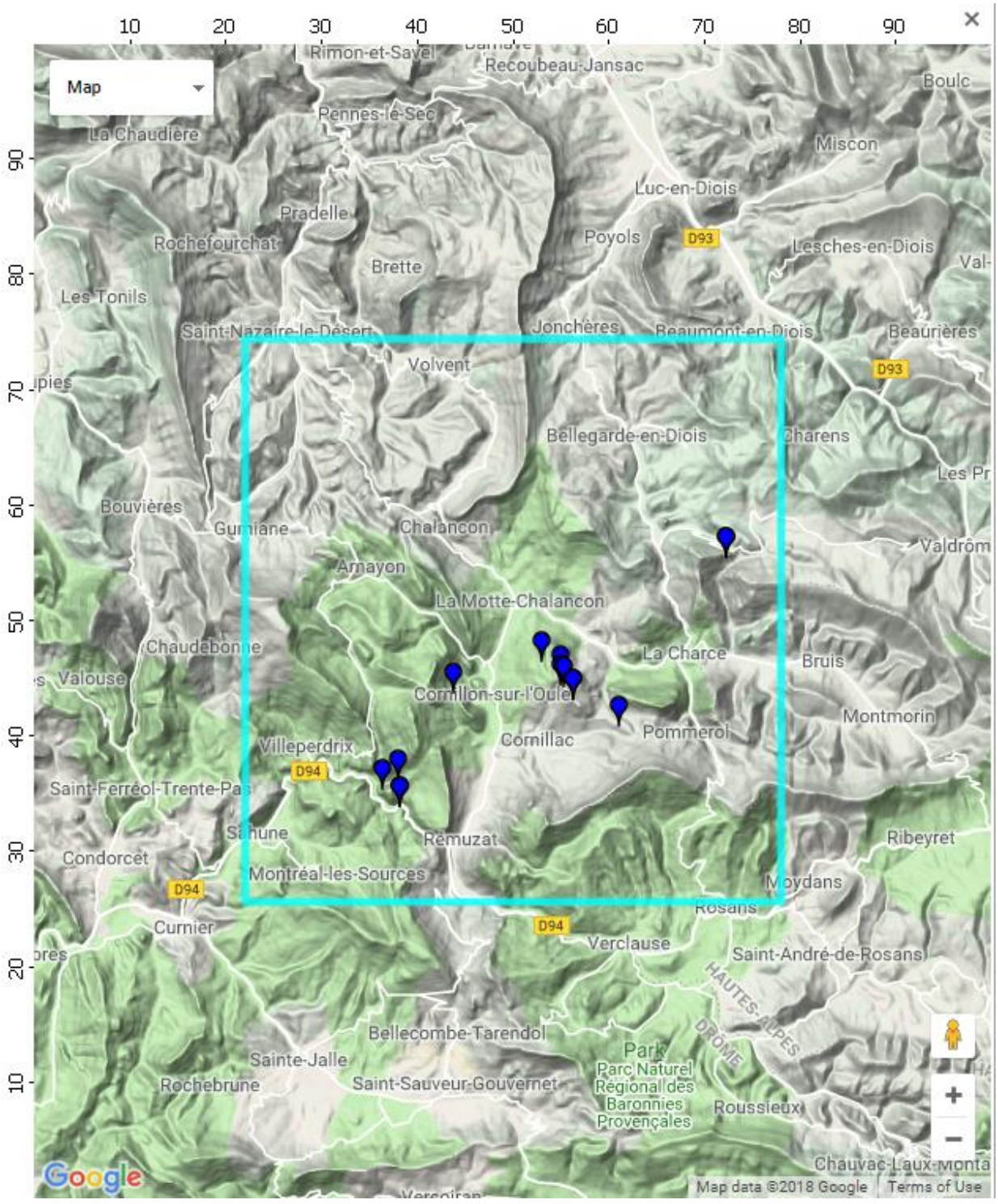

Fig.17: Location of field observation points displayed in FieldMove Clino application.

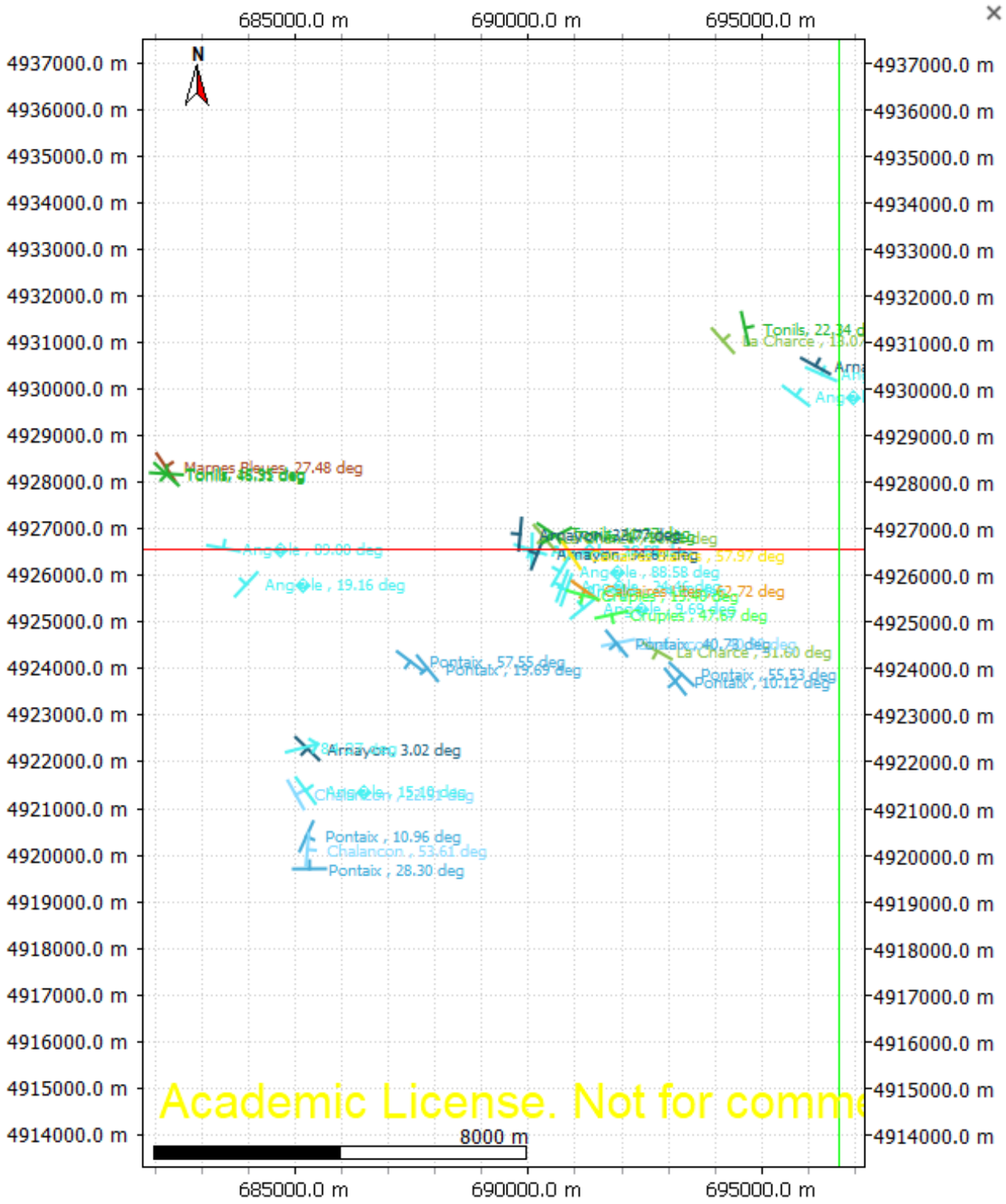

Fig.18: Map view of the field observations (orientations and dips) imported in Move.

4. Methods & Results: Data Processing

The data acquired such as the Bachelor's geological maps and 2D vertical cross-sections was then imported in Move using their XY coordinates and compared to the BRGM maps, together with the new field data gathered and Google Earth in order to construct the following in Move:

- Generation of a stratigraphic column
- To draw a plausible geological map of the different structures and faults in the designated area
- To produce 2D cross-sections of specific/strategic locations

Stratigraphic column

First of all, a stratigraphic overview needs to be defined in Move in order to construct the geological map. A specific color was defined for each of the different formations as shown in Fig. 19. For the Tithonian, Barremian, and Turonian formations, a brick-shaped pattern is assigned representing the formations containing massive limestone layers. This stratigraphic column will be used as a reference throughout the project to define the specific formations and build the 3D model accordingly.

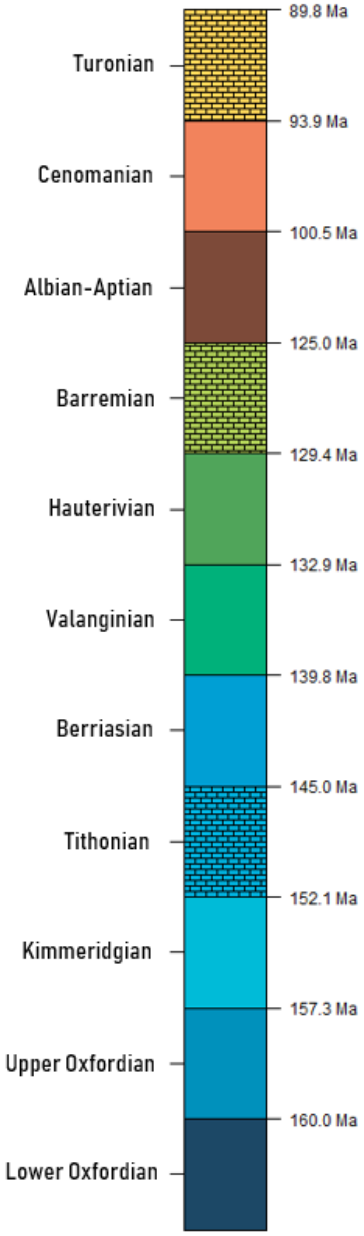

Fig.19: Stratigraphic column made in Move representing the different formation's color attribute and age plotted with equal thickness for every formation, meaning the column is not on relative depth or scale.

Geological map

An interpretation of the different geological structures found in the studied area was made based on the data imported in Move. This way, a self-interpreted 2D map view was constructed (Fig. 20) using Move representing the different faults occurring in the area. The same was done for the folds present in the designated area (Fig. 21). The different formation boundaries found at the surface are also displayed according to its stratigraphic order.

This geological map is only a top view of the 3D structures present in the area. Therefore, hand-made 2D vertical sections were also drawn in order to define and predict the structures' geometries in the subsurface as well as high above the surface where parts of these structures are not visible. By balancing these cross-sections using the collected data, the final geological map (Fig. 20) was constructed.

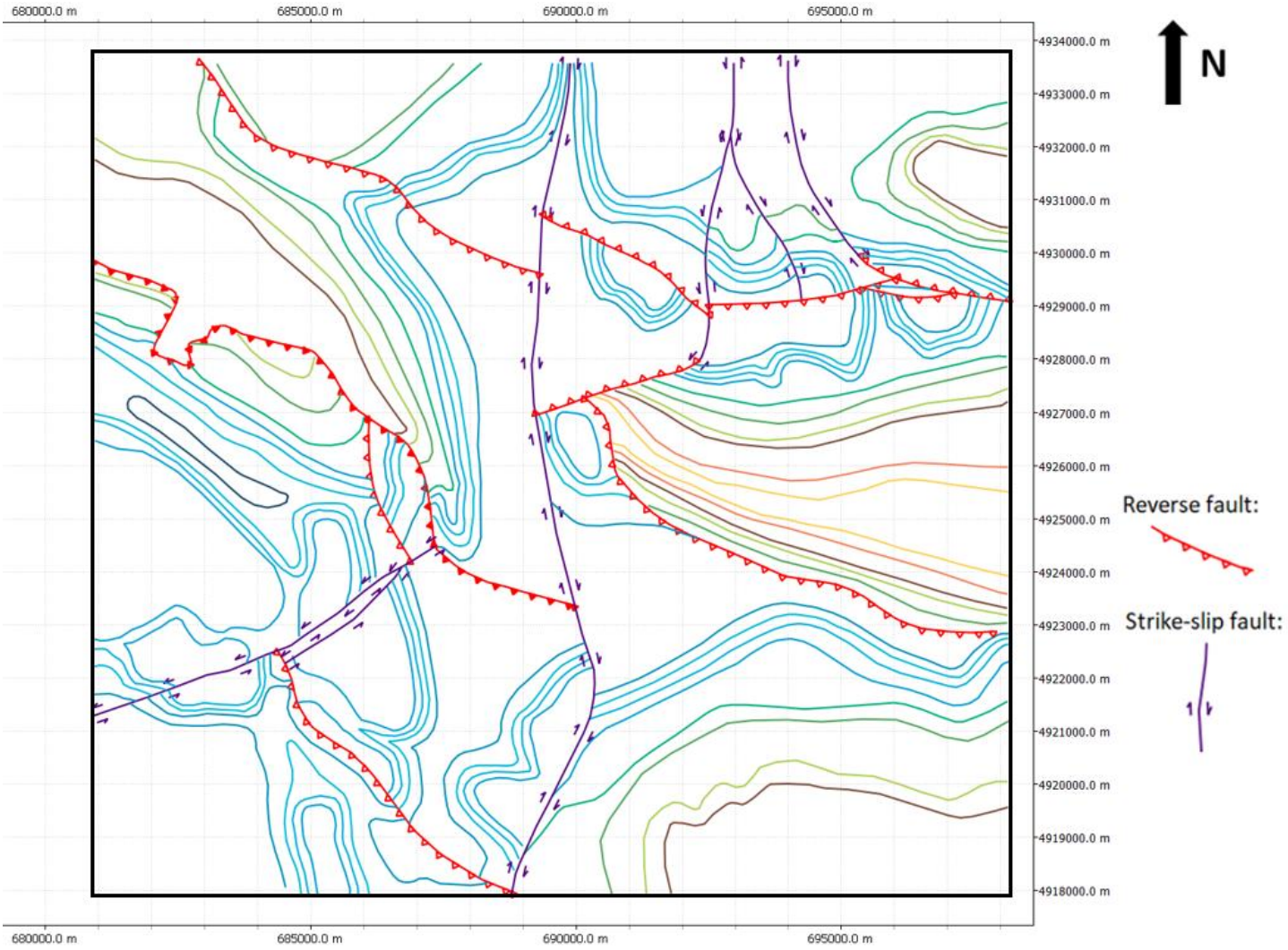

Fig.20: Geological map of the studied area displaying the bottom of each formation boundary and faults lines. Refer to Fig. 18 for the legend.

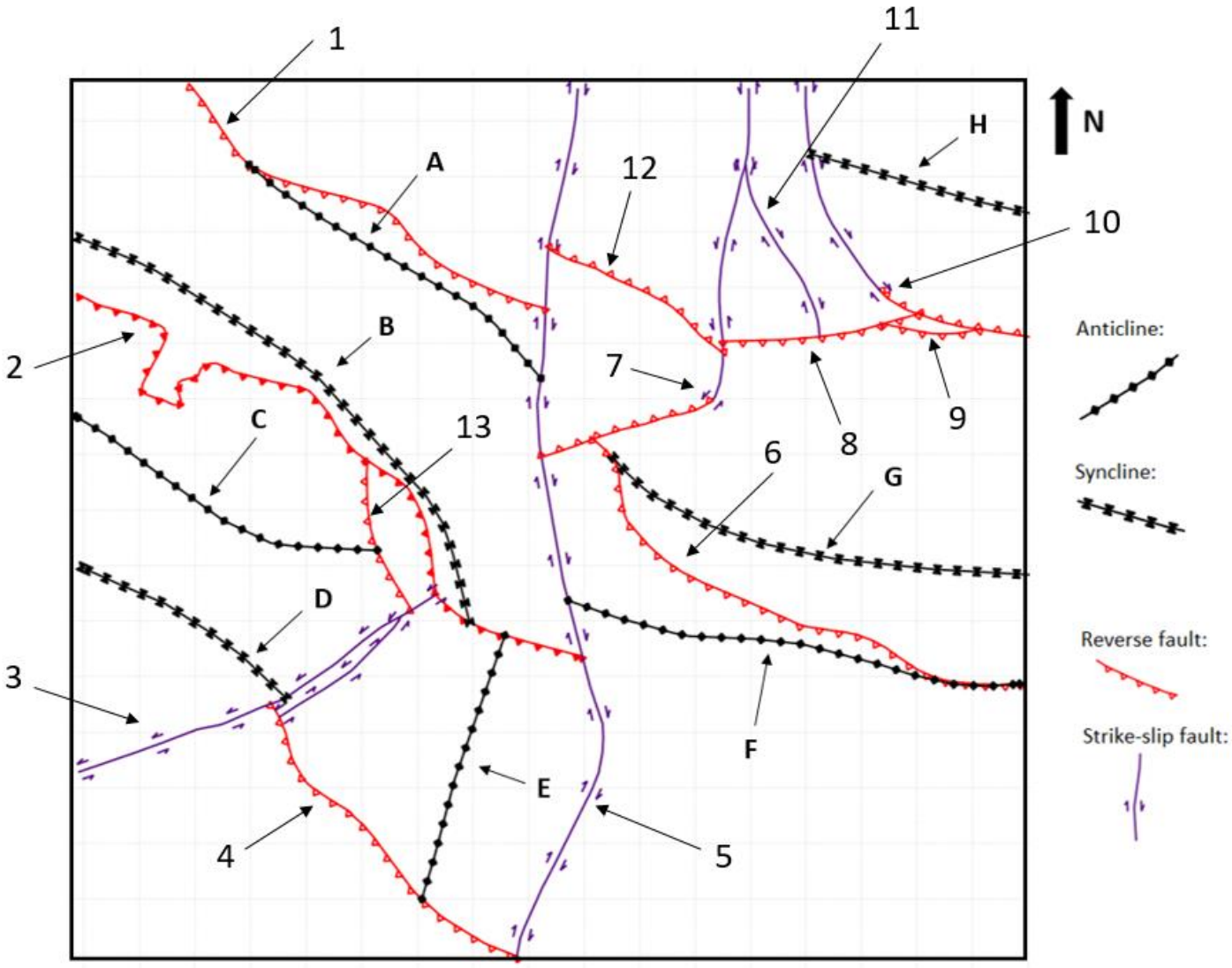

Fig.21: Tectonic map of the area displaying the labeled folds and faults present.

In table 6 and 7 respectively, the type and fold axis of each labeled fold as well as the name, type and strike of each labeled fault displayed in Fig. 21 are listed. The name of these faults will be used throughout the course of this report.

Table 6: Type and fold axis of folds present in the tectonic map.

	Type of fold	Fold axis
A	Anticline	NW-SE
B	Syncline	NW-SE to N-S
C	Anticline	NW-SE
D	Syncline	NW-SE
E	Anticline	NNE-SSW
F	Anticline	E-W
G	Syncline	E-W to N-S
H	Syncline	NW-SE

Table 7: Name, type and strike of faults present in the tectonic map.

	Name	Type of fault	Strike
1	Chalancon	Reverse	108
2	Mt d'Angele	Thrust	106
3	St May	Strike-slip	236
4	La Condamine	Reverse	130
5	Jonchère	Strike-slip	000
6	Pommerol	Reverse	114
7	Ruelles	Tear fault	250
8	Peyssias	Reverse	81
9	Hidden	Reverse	93
10	L'Aiguille	Tear fault	287
11	Establet	Strike-slip	000
12	Altiport	Reverse	299
13	Souchon Rima	Reverse	168

2D cross-sections

Hand-made 2D cross-sections displaying the structures' geometries vertically were constructed and balanced. First, the area was divided into 20 cross-sections (10 N-S, and 10 W-E cross-sections) forming a grid covering the whole area (Fig. 22). This way, a 3D model can be built accurately based on the correlation between the different cross-sections. For example, the layers' positions should be matching at the intersection of two cross-sections. This is discussed below.

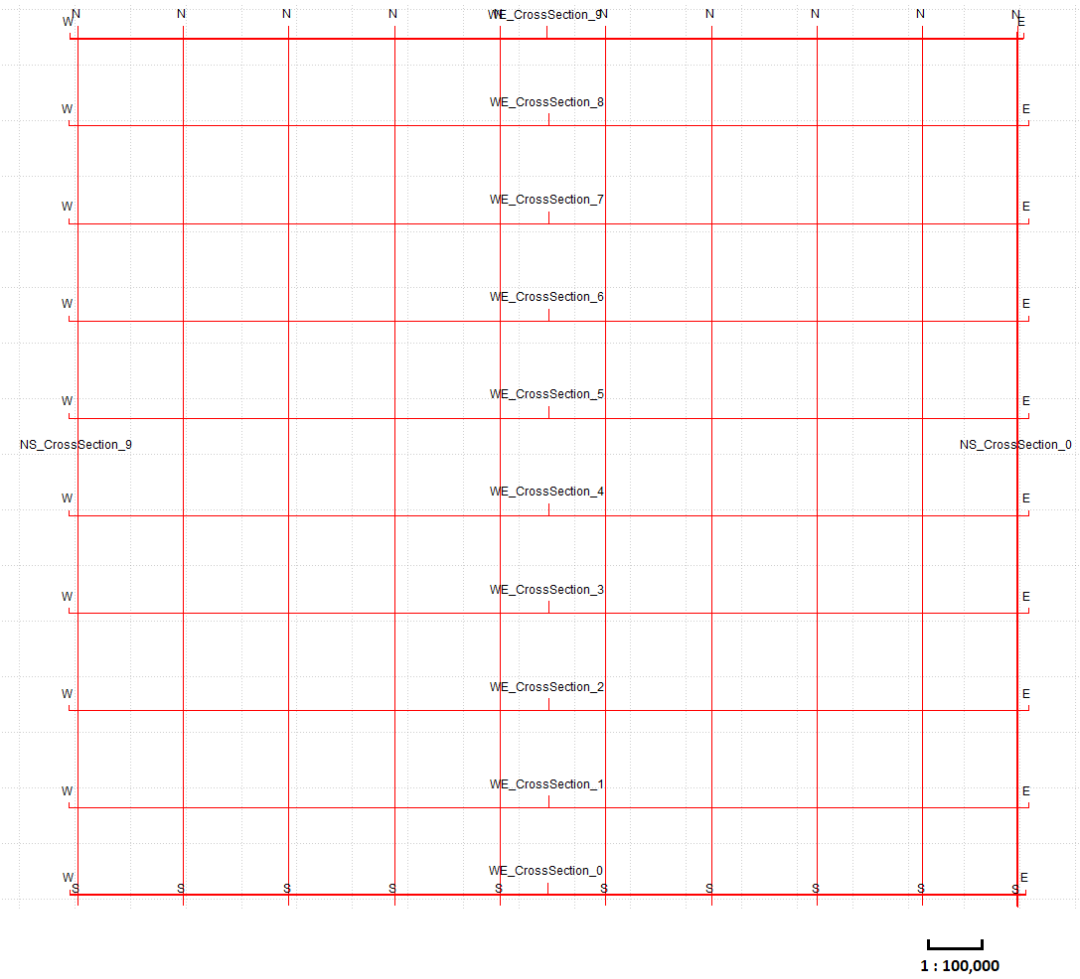

Fig.22: Grid made in Move showing the N-S and W-E cross-sections in the designated area.

In order to construct 2D cross-sections, the DEM is used in Move to display the topography for each of the cross-sections. The intersection points of the different horizons and faults with the surface (Fig. 23) were determined using the data collected from the previous Bachelor fieldworks and using the BRGM's geological maps. The different formation layers were then drawn consistently (Fig. 24).

Doing this for each cross-section, the layers drawn were then compared with adjacent cross-sections at their intersection points. If the layers weren't matching, they were then re-interpreted and redrawn accordingly.

Once all the cross-sections were drawn and matching others at their intersections, they were imported in Move to be further digitized (Fig. 25) in order to first generate a 2D geological model containing all the cross-sections constructed of the designated area. The digitized cross-sections are displayed in Appendix B.

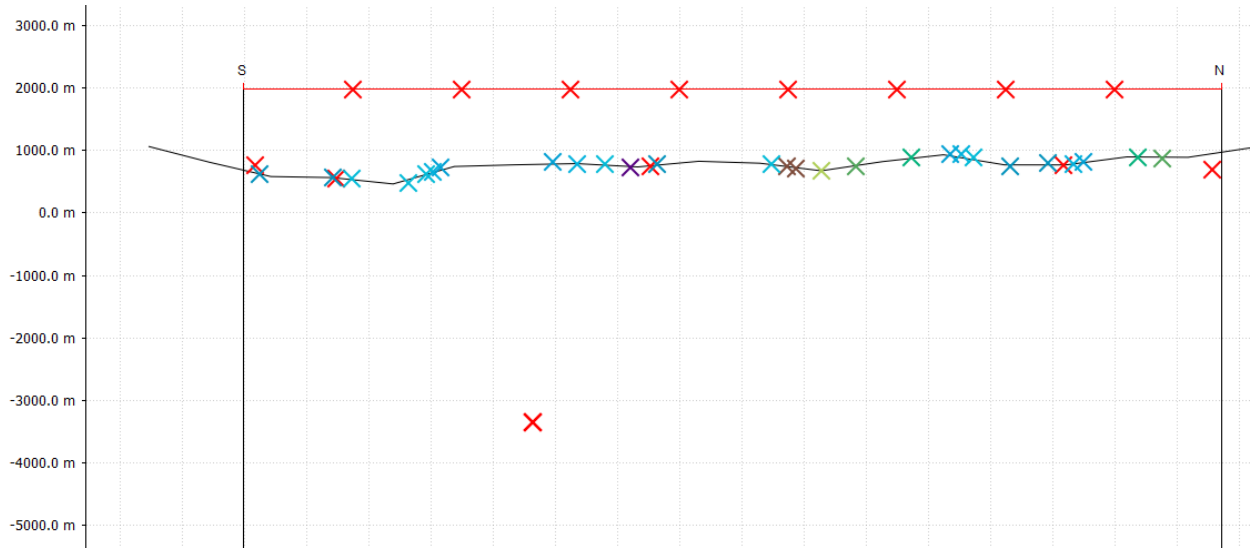

Fig.23: N-S cross-section 6 is shown here with its topography and surface intersections (scale: 1:100 000).

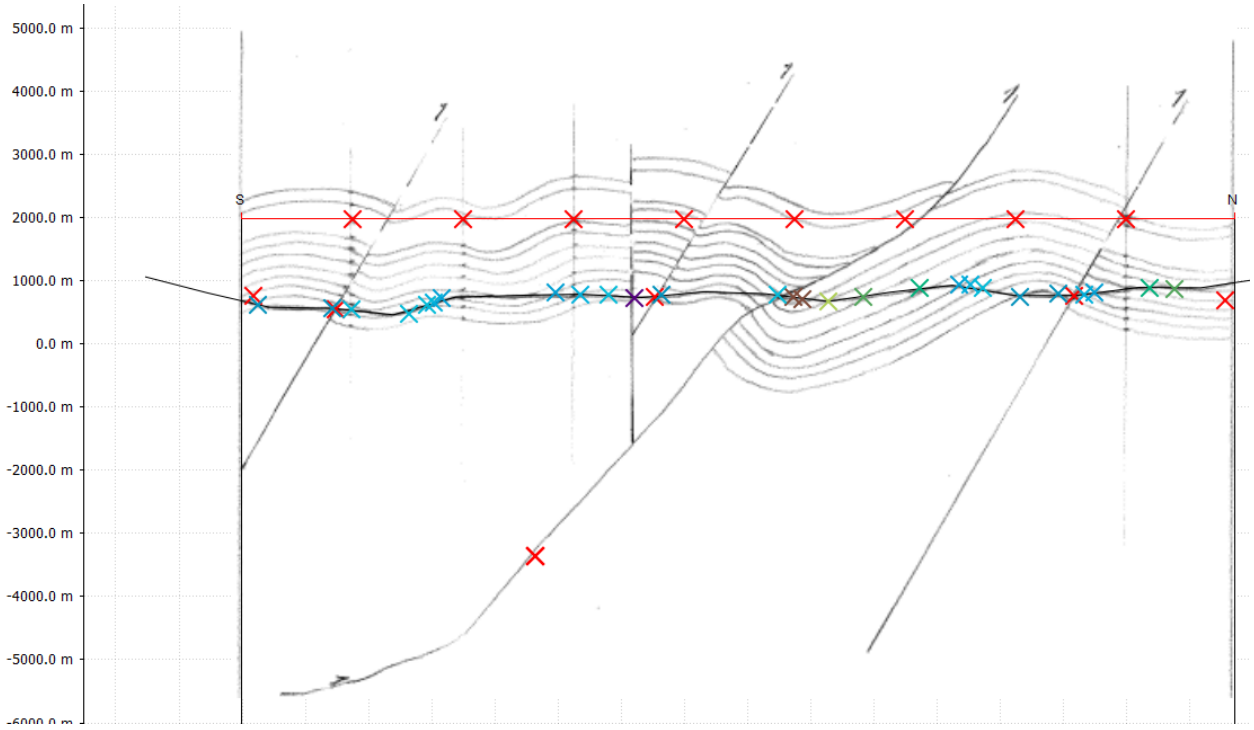

Fig.24: Resulting cross-section (N-S cross-section 6) displaying the vertical geometry of the different structures.

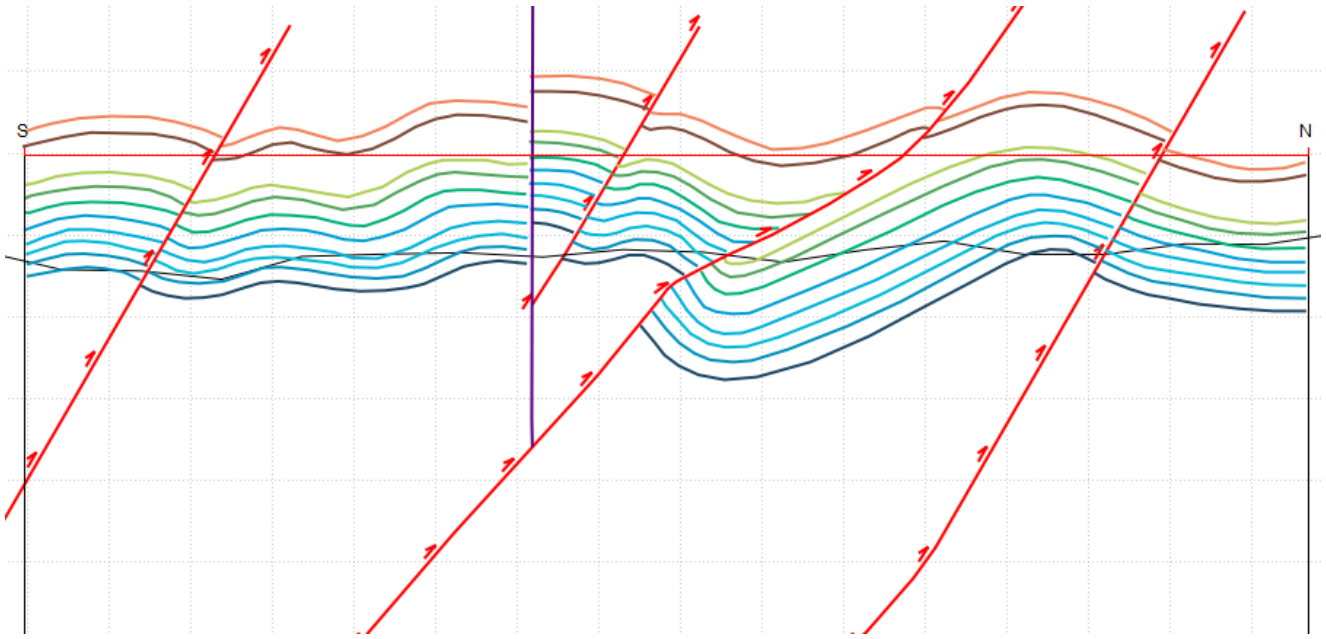

Fig. 25: N-S cross-section 6 digitized in Move (scale: 1:100,000).

Each cross-section, once constructed, was then balanced and restored in 2D. First, each fault displacement was removed (Fig.26) using the Fault Parallel Flow method (see following chapter Geo-modelling). For some cases, this could result in horizon mismatches where some horizons, on each side of a fault, would display an offset (Fig.26) and therefore wouldn't connect properly. These offsets were then corrected manually in Move (Fig.27) after the fault displacement was removed. Once the mismatches were corrected, the horizons were then unfolded (Fig.28) using the Flexural Slip method (also see following chapter Geo-modelling). Some horizons would still show some folding at some places after unfolding. These were then flattened out manually in Move (Fig.29) and the line length and thickness of each horizon after restoration could then be determined (Fig.29; top).

Finally, a 2D model of the structures of both before and after restoration (Fig.30) was constructed. Therefore, the amount of shortening in the N-S direction as well as in the E-W direction can be quantified and later compared with the resulting 3D model.

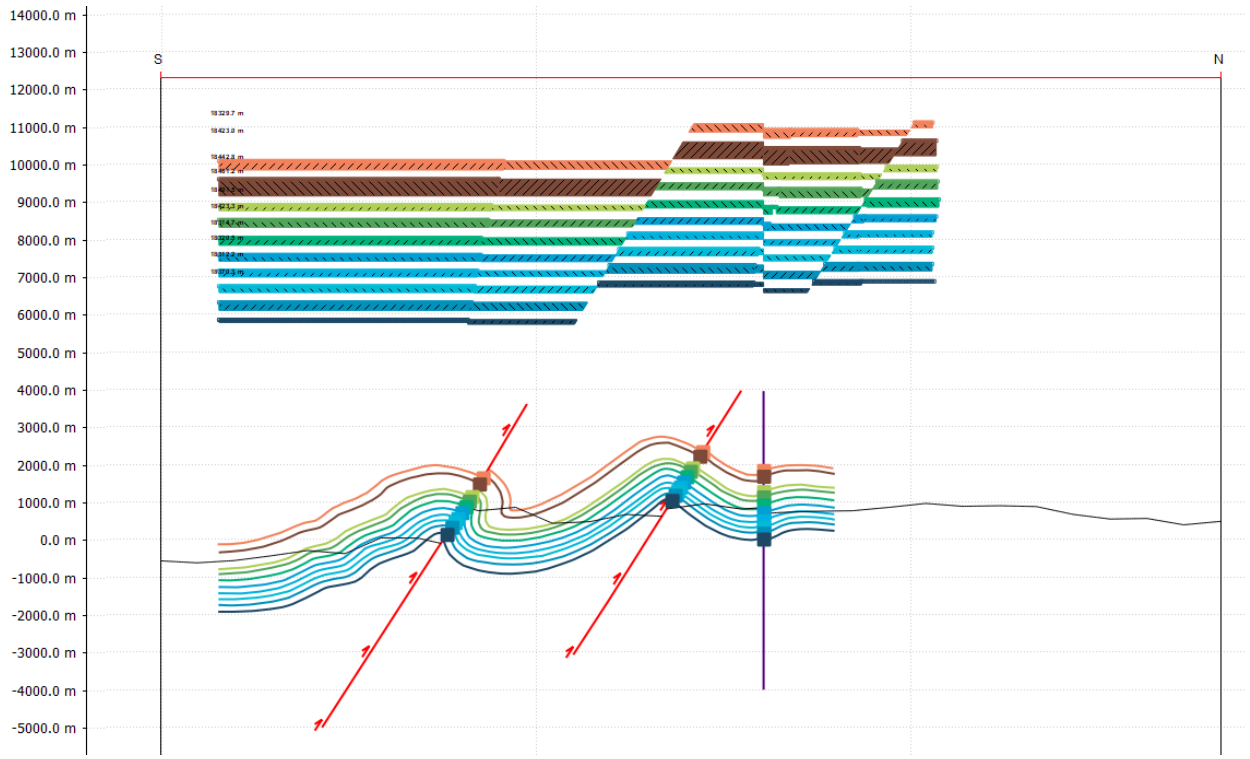

Fig.26: Step 1 - Removing the displacement of each fault using the Fault Parallel Flow method in Move.

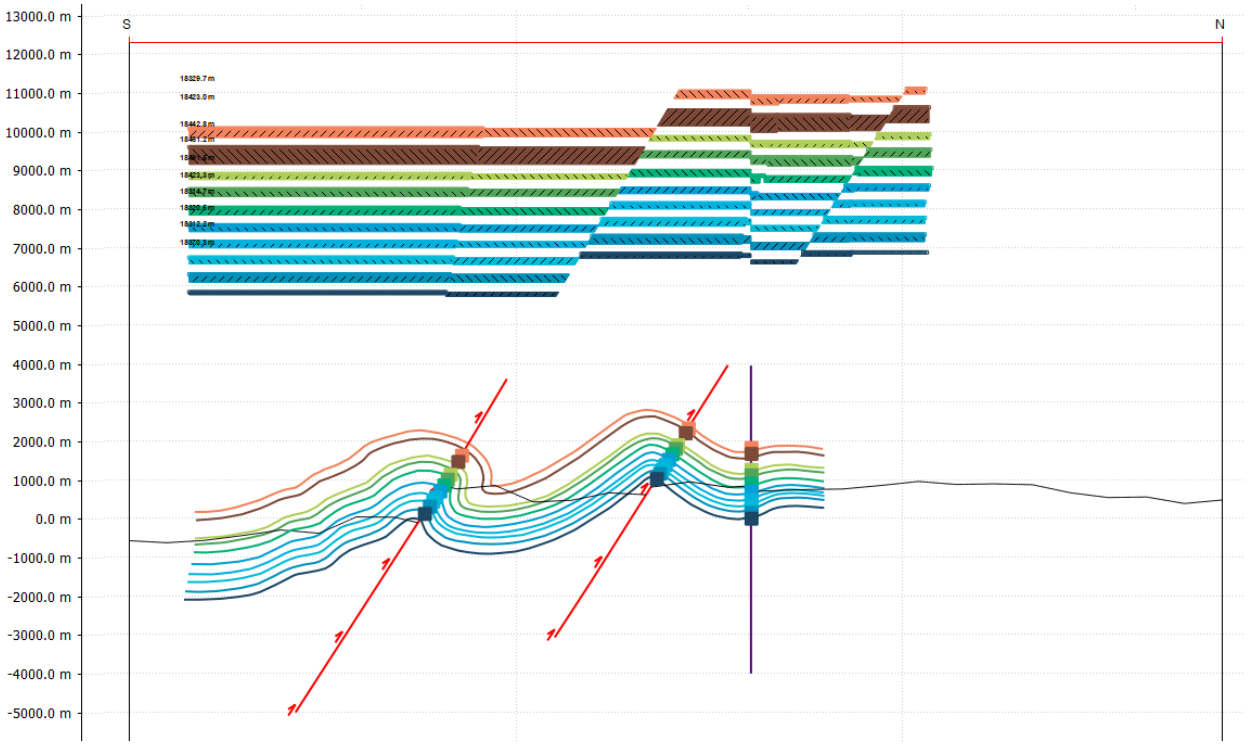

Fig.27: Step 2 - Correcting for the horizon mismatches after fault removal.

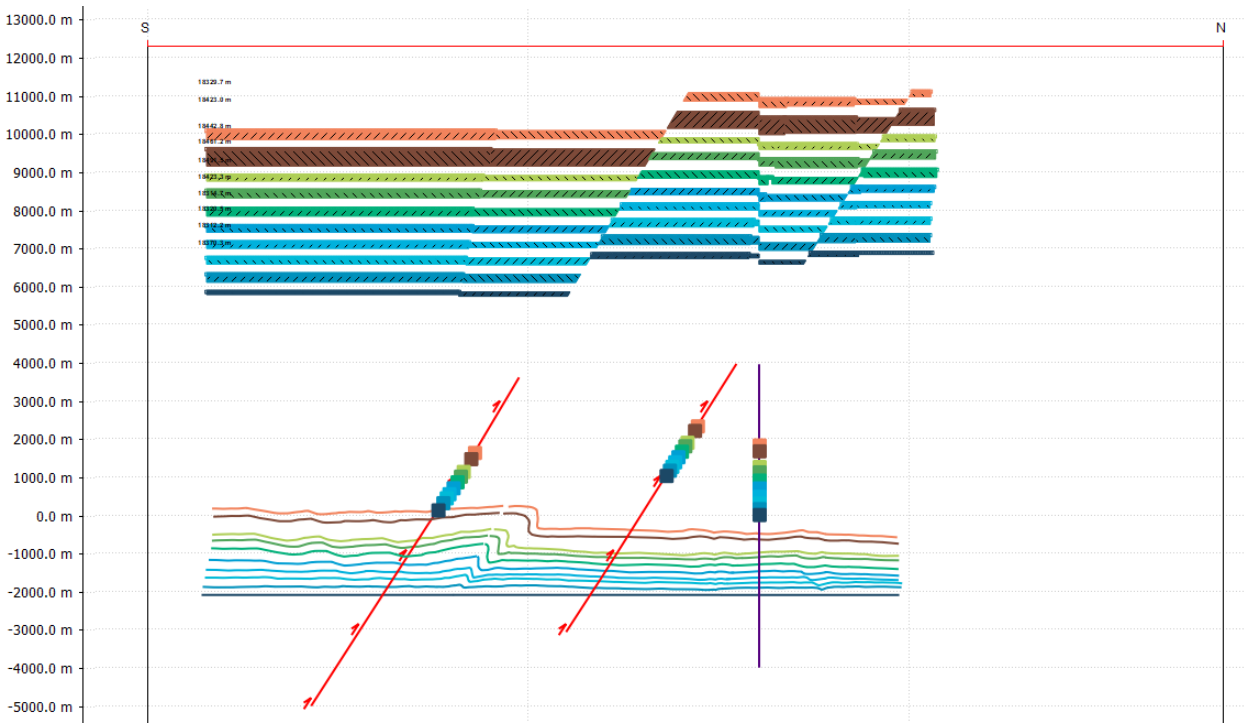

Fig.28: Step 3 - Unfolding the structures based on a template bed ("Terres Noires").

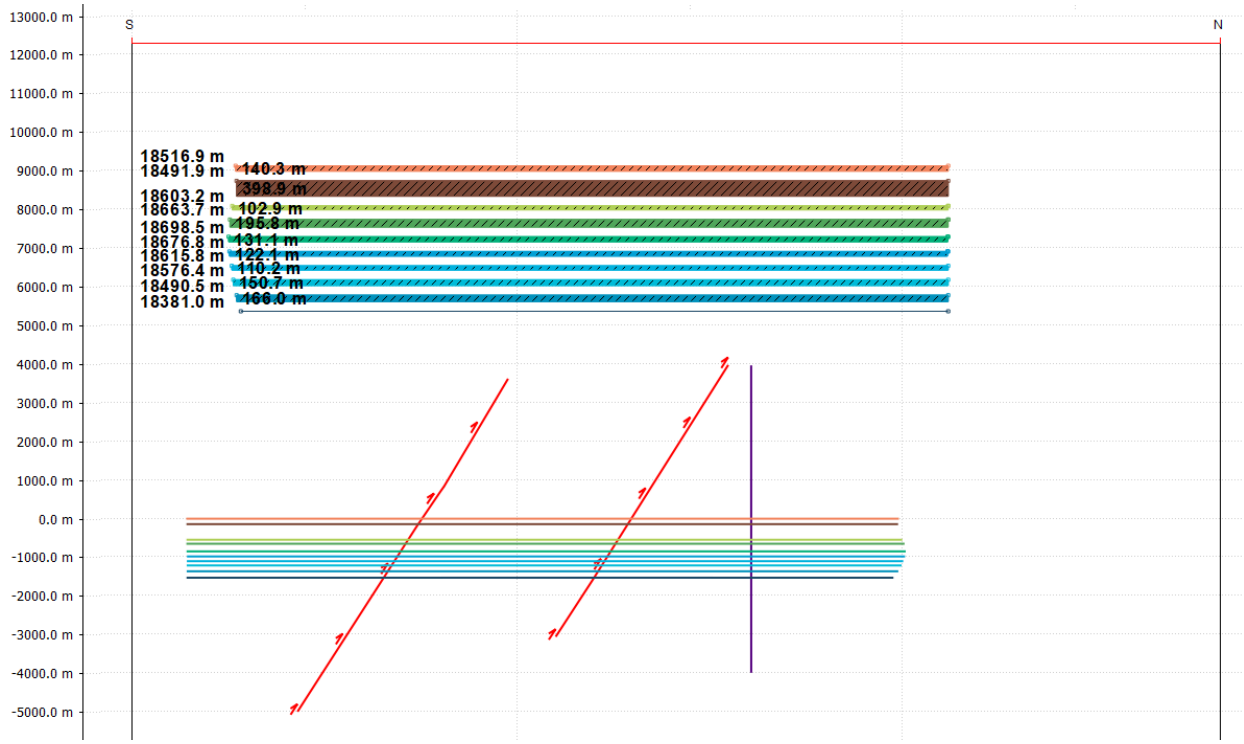

Fig.29: Step 4 - Correcting for the horizon mismatches after unfolding. Length and thicknesses of each horizon is given above the section.

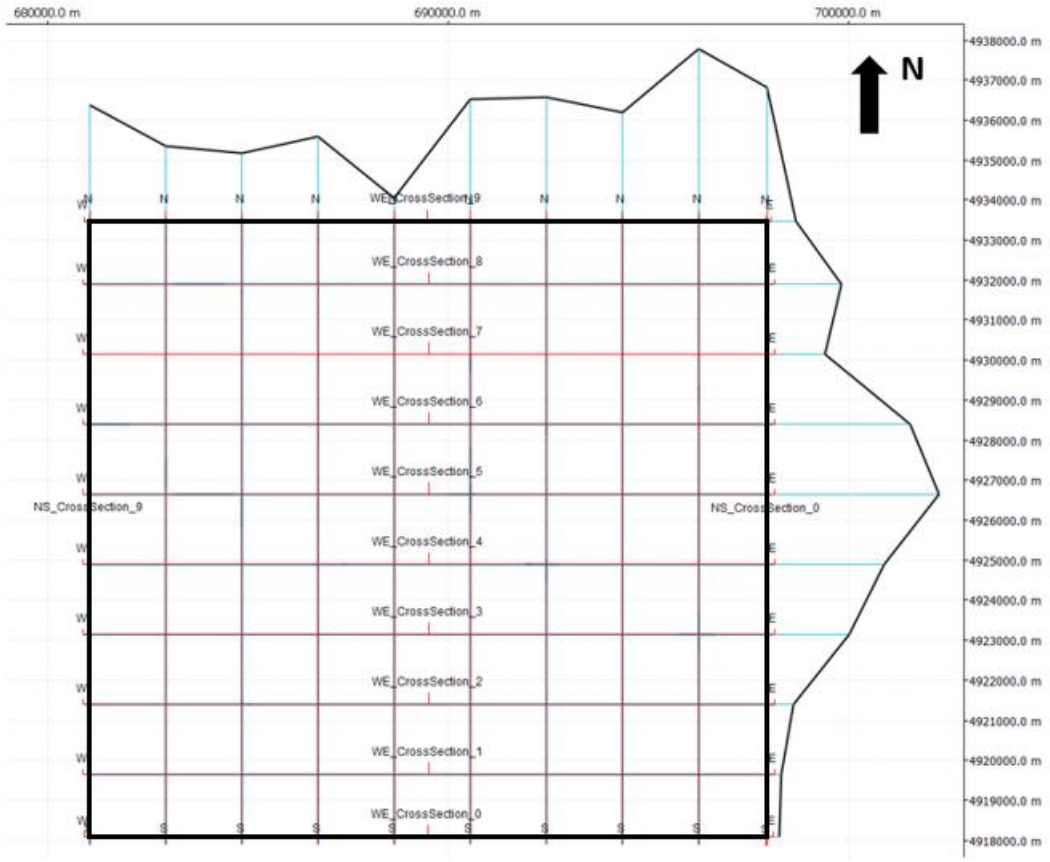

Fig.30: 2D model displaying the amount of shortening of the Tithonian horizon in both the N-S and E-W direction.

From the digitized vertical cross-sections of the 2D model, a 3D geological model containing all the horizon surfaces and fault planes present in the studied area was then generated, balanced, and restored.

5. Methods & Results: Geo-Modelling

Once the structural geometries in each cross-section have been digitized in 2D using the Fault and Horizon tools in Move, fault and horizon surfaces were constructed. A 3D model was then built from these surfaces. Finally, each 3D structure was restored (3D jigsaw restoration) to its initial configuration prior to deformation. This was done by first removing the displacement of each fault present in the area, then unfolding each structure. As a result, gaps and overlaps were found and quantified using the 3D Area Misfit tool after each process.

5.1 Fault surfaces

Each fault surface was created from the polylines digitized in the corresponding cross-sections. The surfaces were created using Linear Method. This method joins neighboring control points with straight lines and produces a grid of triangles between control points. Using this method, a number of control points are inserted between the initial polylines selected and the surface's smoothness is then controlled by its sample density. In this case, the sample density is low (of about 5) for faster computational processing. An example of the creation of one of the fault surfaces present in the area is shown in Fig.31.

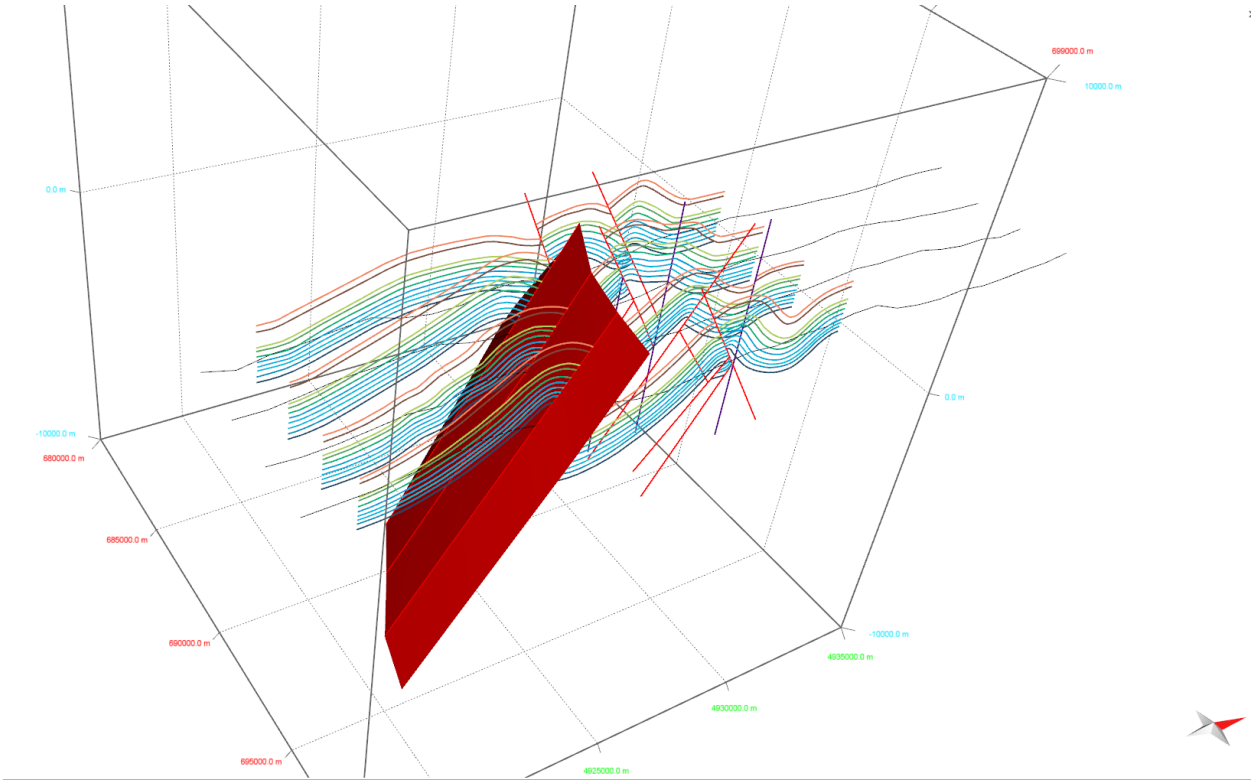

Fig.31: Example of the creation of a fault surface using Linear Method in Move. This fault is a reverse fault located nearby Pommerol village.

5.2 Horizon surfaces

Modelling the horizon surfaces was done using a Spline Curve Method. This method is a mathematical approach where the shape of complex curves is controlled using a set of control points. Using the digitized polylines of a specific horizon in the corresponding cross-sections, the Spline Curve Method creates a curve which closely honors the control points in order to create a surface. An example of the modelling of the Barremian limestone horizon surface is shown in Fig.32.

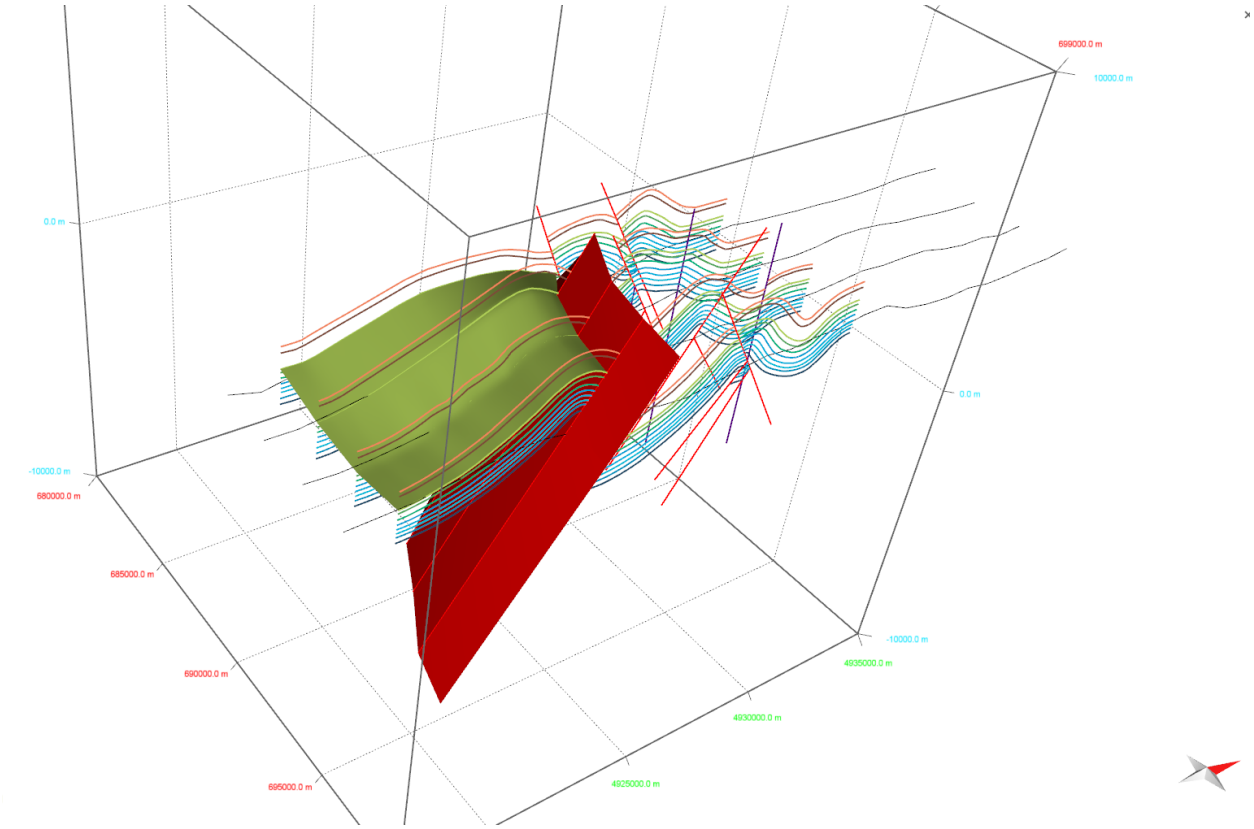

Fig. 32: Example of the modelling of a horizon surface using digitized polylines of different cross-sections in Move.

For this project, only two horizons were modelled in 3D, these are the hard limestones of the Tithonian and Barremian respectively. These formations are hard, brittle layers that are easily distinguishable from the other formations. Their hardness determines most of the deformation and show almost no ductile deformation apart from “large-scale” folding. Therefore, the Tithonian horizon was used as the reference layer and the Barremian horizon as a secondary layer.

Finally, a 3D model of the geological structures present in the designated area was built from these fault and horizon surfaces. In Fig.33 and Fig.34, a generated 3D model containing all faults and all of the Tithonian and Barremian horizons of the west- and east-side of the area respectively is shown.

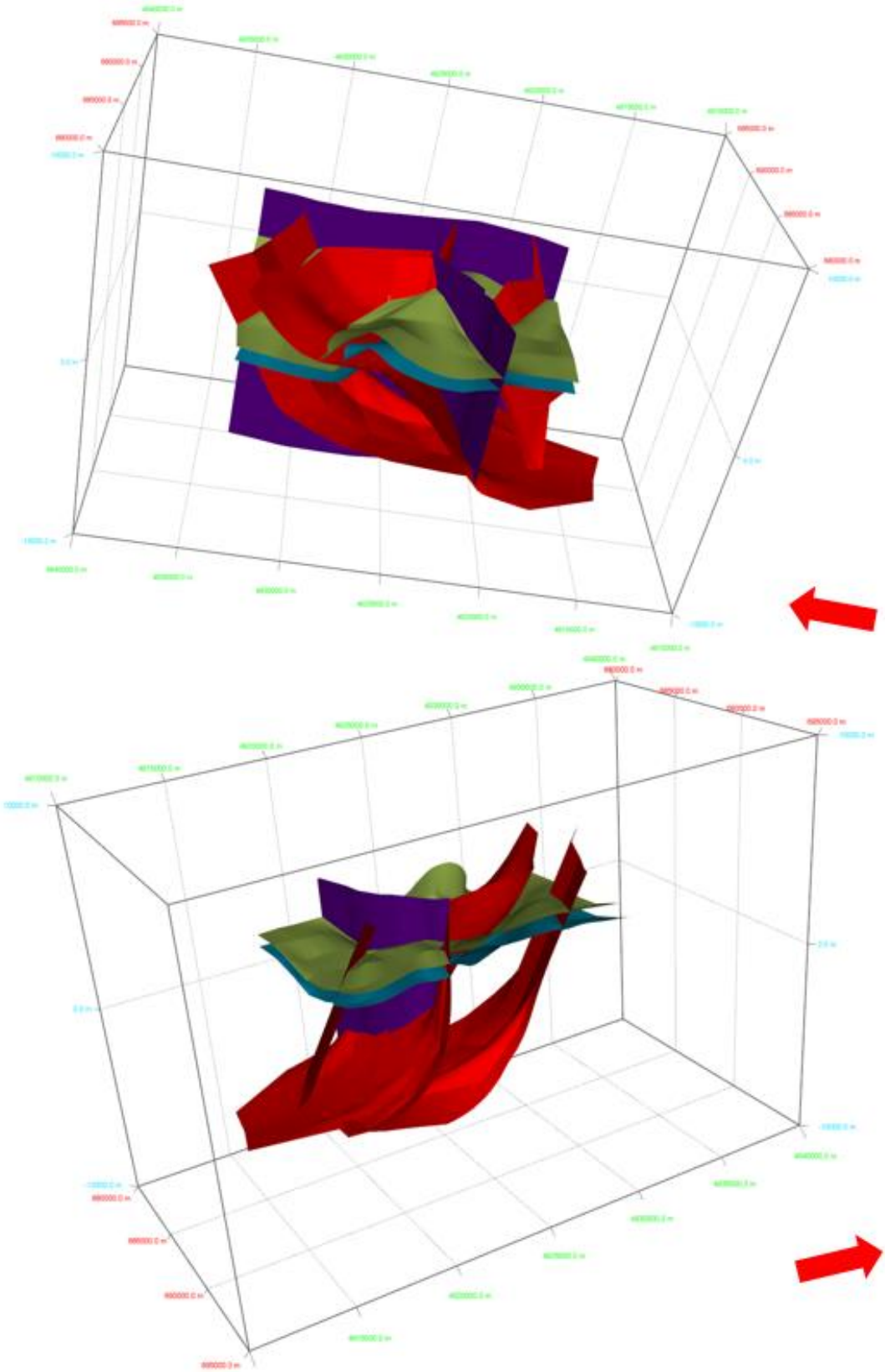

Fig.33: 3D model of the structures of the western part of the studied area. Red surfaces are thrust faults; purple surfaces are strike-slip faults. The Tithonian horizon is represented in blue and the Barremian in green. (Red arrow indicates north)

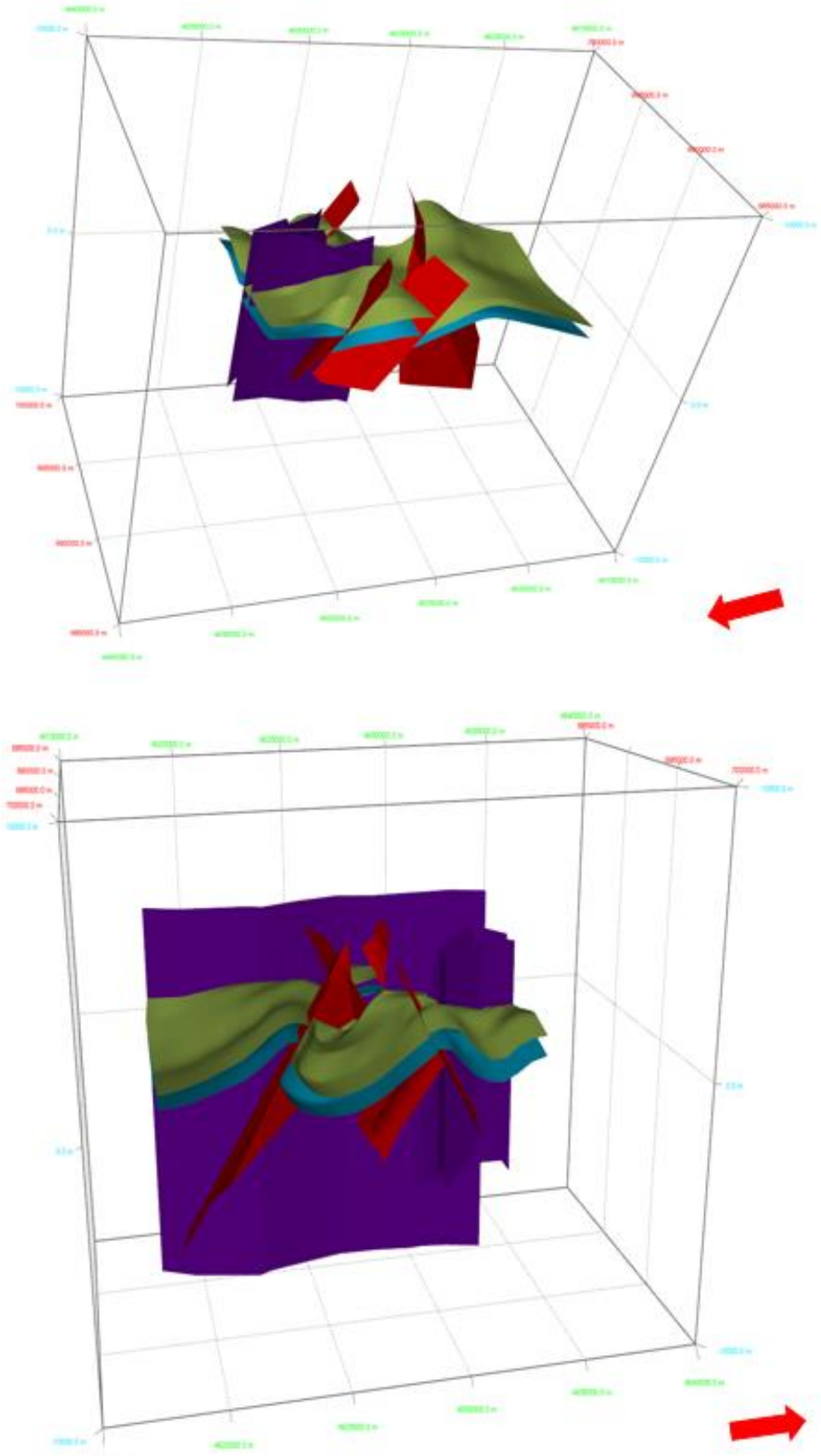

Fig.34: 3D model of the structures of the eastern part of the studied area. Red surfaces are thrust faults; purple surfaces are strike-slip faults. The Tithonian horizon is represented in blue and the Barremian in green. (Red arrow indicates north)

In order to determine the structural evolution of the area and the amount of shortening that occurred after deformation, each structure had to be restored first. This was done using the methods described below.

5.3 Removing fault displacement (3D Move-On-Fault)

Each fault present was first removed using The Fault Parallel Flow method. This algorithm models hanging wall folds through an analogue of laminar particulate flow over a fault surface. Since no axial surfaces have to be calculated, more complex fault geometries can be modelled. This algorithm maintains the volume of the hanging wall beds.

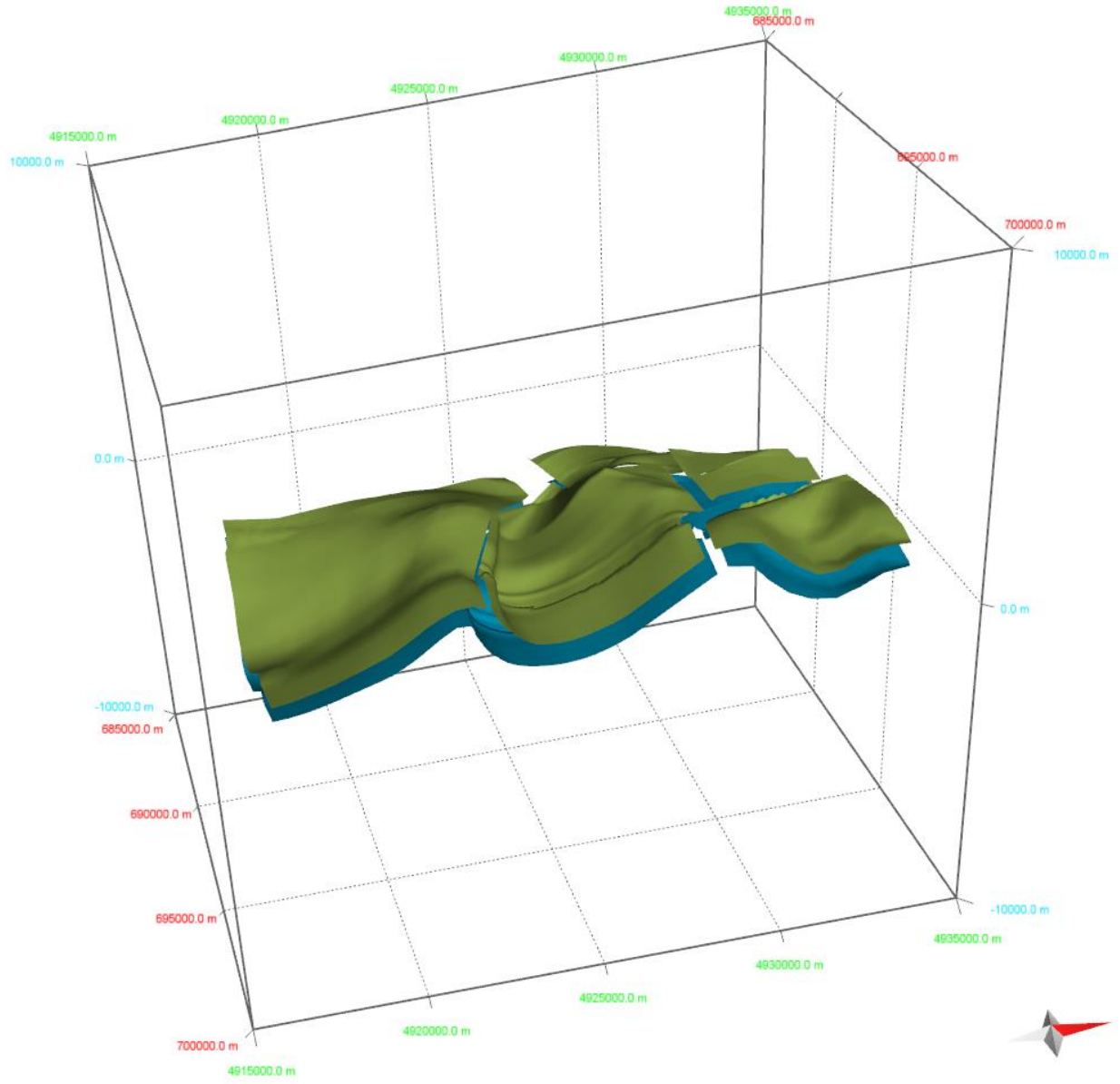

Fig.35: 3D model of the structures of the eastern part after each fault displacement was removed.

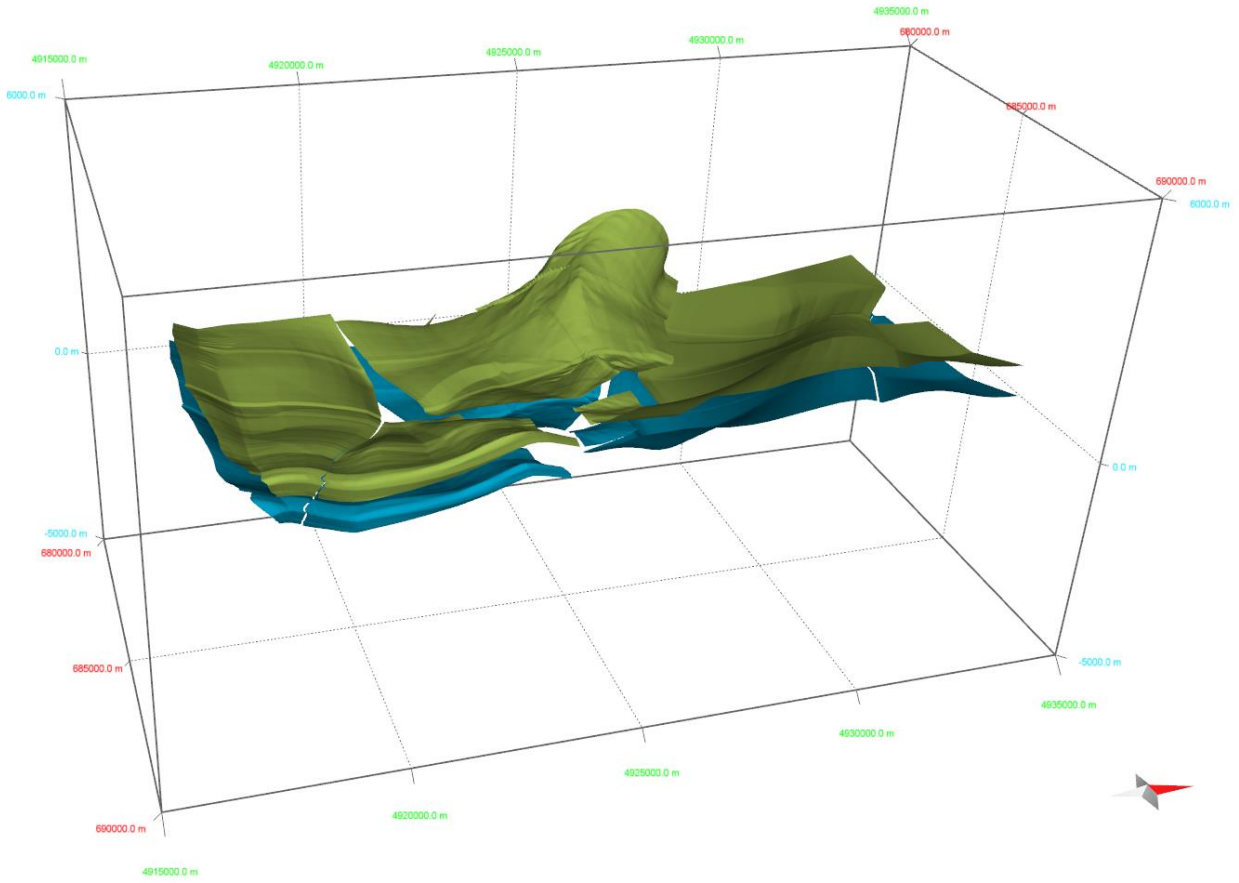

Fig.36: 3D model of the structures of the western part after each fault displacement was removed.

5.4 Unfolding

The tectonic map of Fig.21 displays the main folds present in the area. The folds type, shape, and fold axis orientations are displayed in table 6.

Each structure was then unfolded according to The Flexural Slip method. This algorithm allows unfolding while preserving the thickness between surfaces, bed thickness variations, and line-length of the template bed in the unfolding direction. This algorithm is a two-part process. Surfaces are rotated to horizontal or a target surface as the flexural slip component of the fold is removed. When unfolding a structure, two planes were used. A grey plane representing the unfolding plane is oriented perpendicular to the fold axis and a red plane representing the pin plane fits through the hinge of the fold (Fig. 37).

In the tables 8 and 9, the dip and dip direction of the unfolding plane of each fault block of the western and eastern parts of the area (Fig. 38) are given.

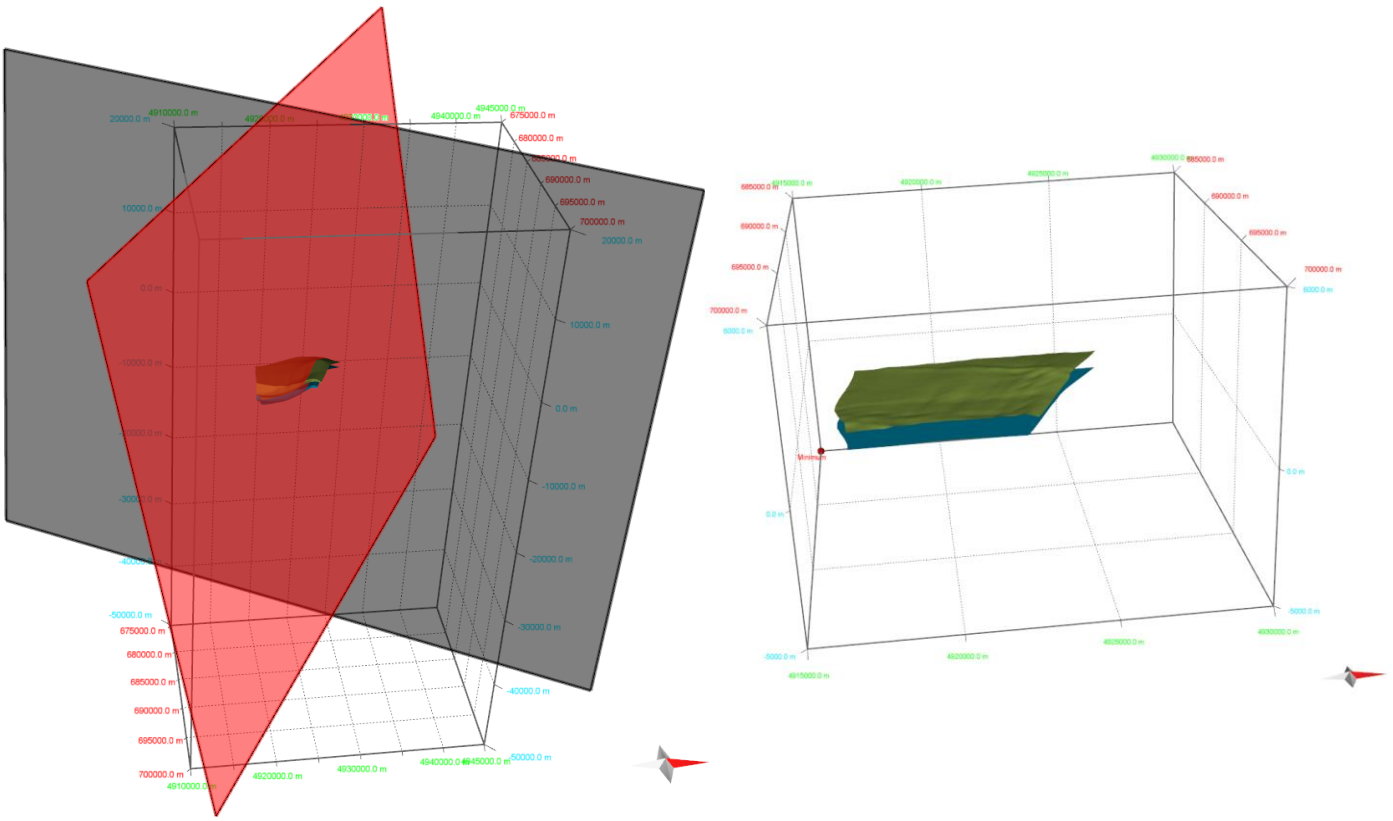

Fig.37: Unfolding an anticline present in the area using the Flexural Slip method (left) using a unfolding plane in grey and a pin plane in red resulting in an unfolded structure (right).

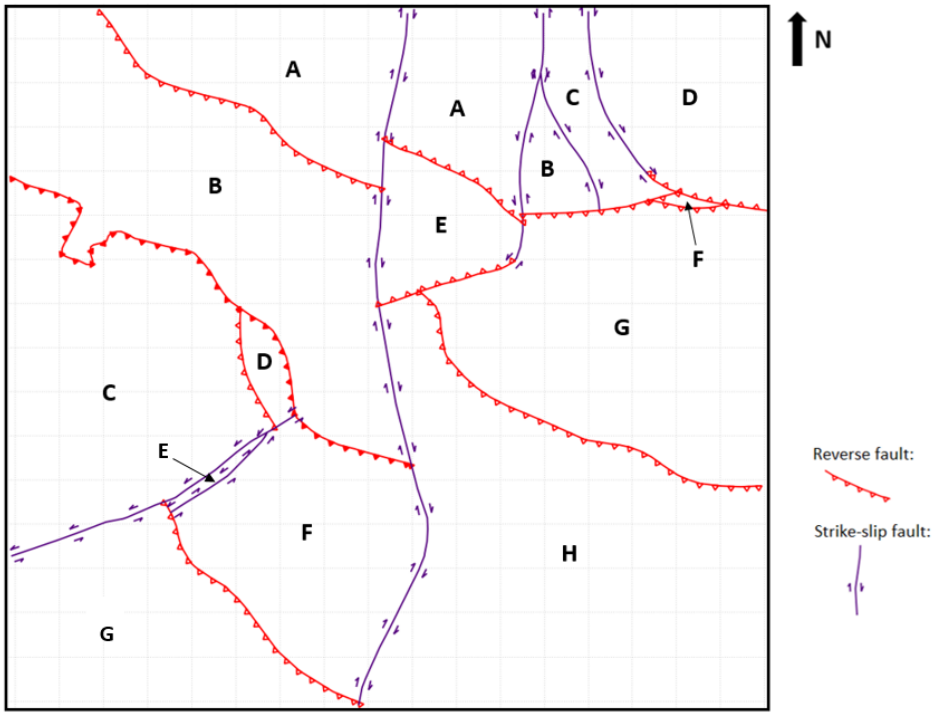

Fig.38: Location of each fault block labeled on each side of the main strike-slip fault.

Table 8: Unfolding planes of the western fault blocks.

Fault Block	Unfolding Planes West	
	Dip	Dip direction
A	79	108
B	84	117
C	77	308
D	73	154
E	68	56
F	85	16
G	79	276

Table 9: Unfolding planes of the eastern fault blocks.

Fault Block	Unfolding Planes East	
	Dip	Dip direction
A	70	146
B	83	119
C	78	191
D	89	284
E	67	124
F	81	92
G	89	288
H	83	116

The resulting structural models of the eastern- and western part (Fig. 39) were then analyzed and validated using an Area Misfit tool in Move. The different fault blocks were reassembled and any space problems in the interpretation of the structures present in the area were identified. The amount of gaps/overlaps between each block was then quantified.

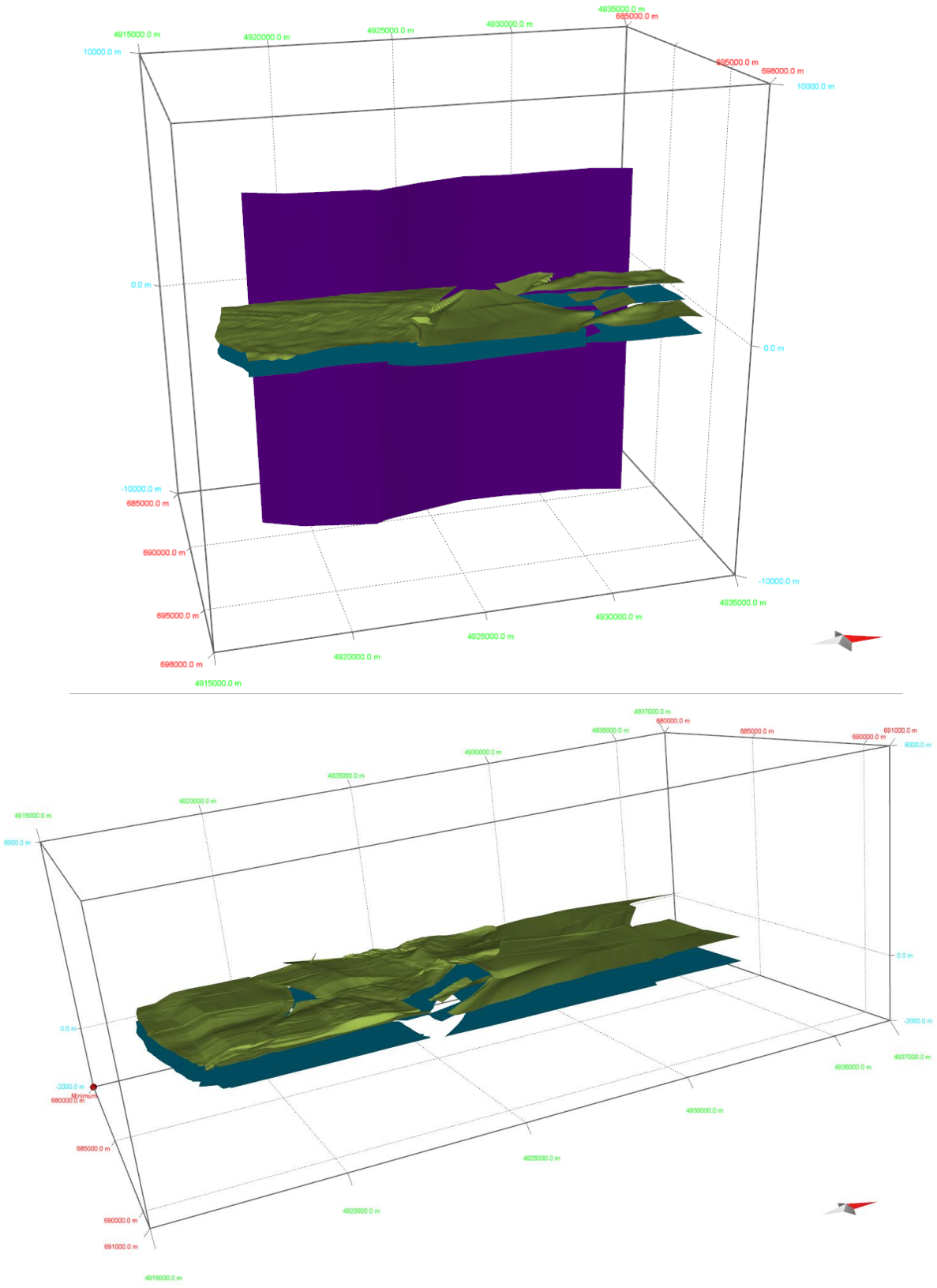

Fig. 39: 3D model of the structures of the eastern part (top) and western part (bottom) after unfolding.

5.5 Area misfit

After removing the displacement of each fault and unfolding each structure, some gaps and overlaps were found for both the Tithonian and Barremian horizons. These features indicate a geological or non-geological solution. The latter could be due to either an incorrect interpretation of the structures present in the area or an incorrect application in the software (e.g. wrong Move-On-Fault- or Unfolding-algorithm). These errors were quantified for both horizons by calculating their area after each process and determining their misfit. The results are listed in the tables below.

Areas after removing fault displacement

The Tithonian horizon was taken as the template bed when removing each fault displacement and the Barremian horizon as the passive bed. The Tithonian hanging wall and footwall of each fault were joined in 3D using the Fault Parallel Flow method in Move and the Barremian layers, acting as passive beds, moved accordingly. The resulting shapes of the Tithonian and Barremian horizons after removing all fault displacements are shown in Fig.40 and Fig.41 respectively.

In these figures, gaps (red areas) were formed when joining the beds on each side of the faults. For example, a significant gap was formed in the northeastern part while the beds seem to fit well at first glance. There, an error made when joining the beds using the fault removal method might have caused this gap to form. This gap was later removed when restoring the fault blocks after unfolding them.

A large overlap of the Barremian horizon is found in Fig.41 in the western part which is not found in the Tithonian model. Since the Barremian layers were joined passively based on the template beds of the Tithonian, the large overlap created there might be due to an incorrect interpretation of the Barremian horizon when constructing the 2D vertical cross-sections. The length of the Barremian horizon close to the fault should probably be smaller than interpreted in the cross-sections in order to remove this large overlap.

Table 10: Area of the Tithonian after removing all fault displacements.

	Area [km^2]	
Tithonian	**West**	**East**
Horizon	136.98	140.85
Overlap	0.65	2.08
Gap	21.54	16.24
Misfit	22.19	18.32
Misfit %	16.20	13.01
Total	**157.87**	**155.00**

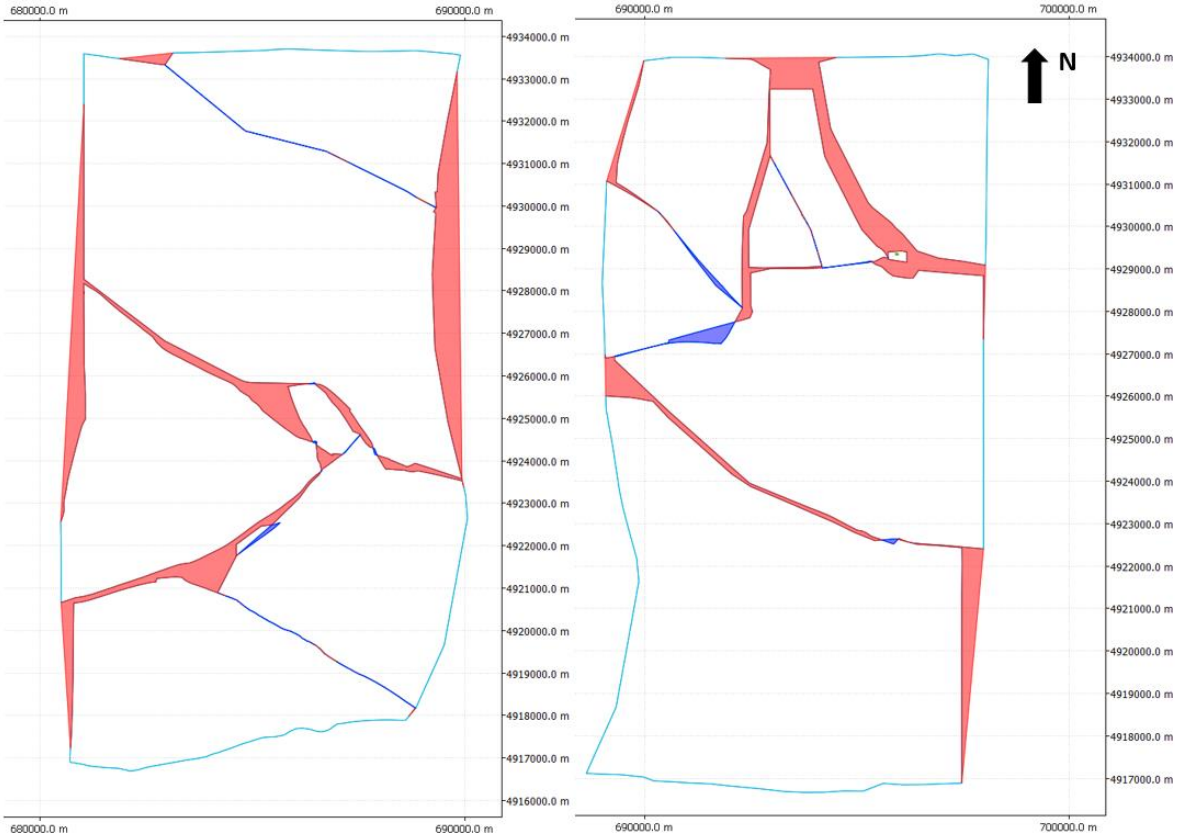

Fig.40: Map view of the Tithonian of the west part (left) and east part (right) after removing faults. Overlaps (blue) and gaps (red) are also displayed.

Table 11: Area of Barremian after removing all fault displacements.

	Area [km2]	
Barremian	**West**	**East**
Horizon	145.86	139.99
Overlap	11.54	2.71
Gap	14.07	14.28
Misfit	25.61	16.99
Misfit %	17.56	12.14
Total	**148.38**	**151.57**

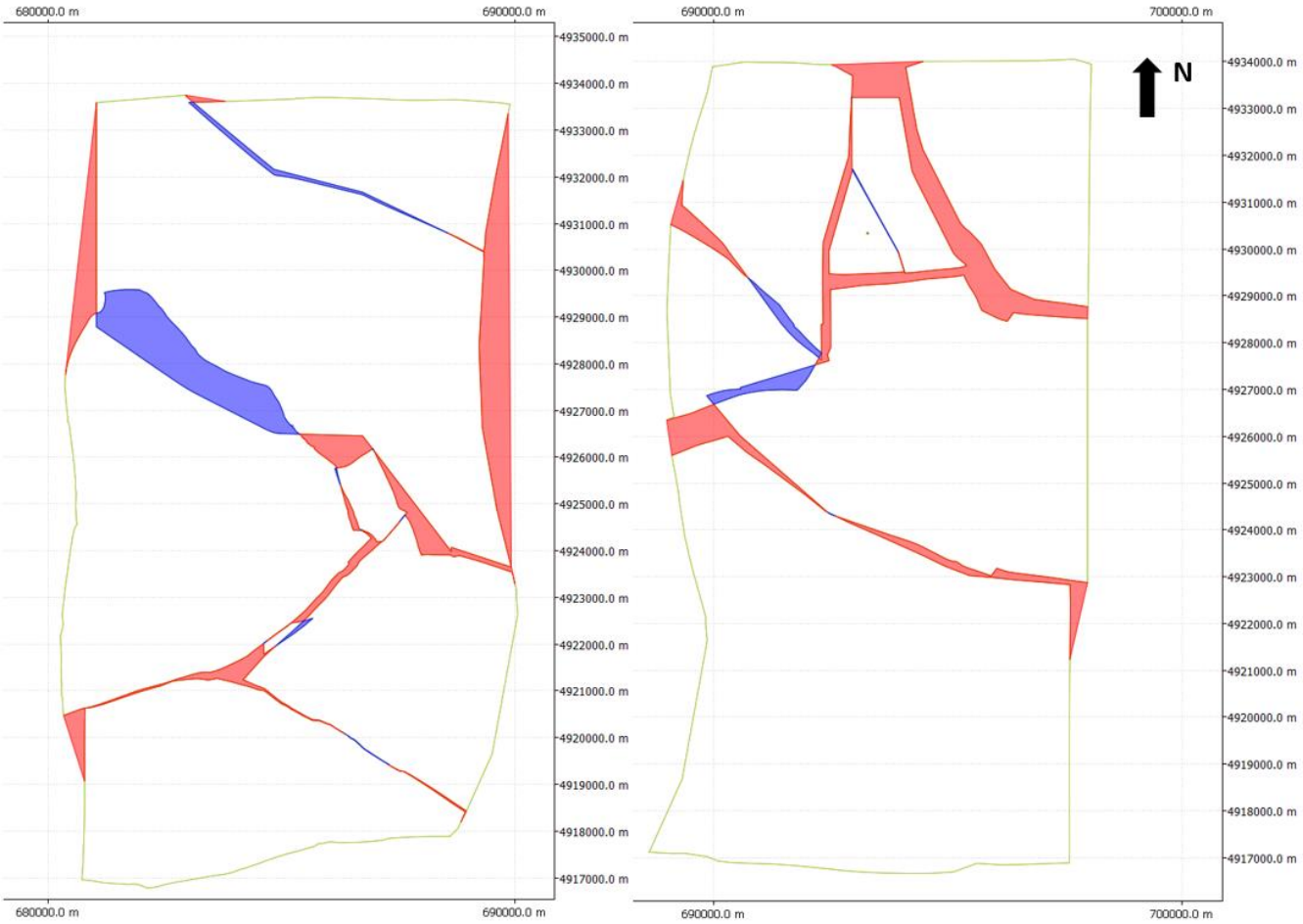

Fig.41: Map view of the Barremian of the west part (left) and east part (right) after removing faults. Overlaps (blue) and gaps (red) are also displayed.

Areas after unfolding all structures

Once each fault was removed, each structure was then unfolded independently in 3D using the Flexural Slip method in Move. There again, the Tithonian horizon was taken as the template bed and the Barremian horizon as the passive bed. Unfolding the structures resulted in a large amount of overlaps (Fig.42 and Fig.43; blue areas). Since each fault block was kept in place when unfolding, overlaps were formed resulting in a larger misfit (Table 12 and 13) compared to the previous models. These overlaps were then removed in the next section when restoring the area to its initial configuration prior to deformation.

Table 12: Area of Tithonian after unfolding all structures.

	Area [km2]	
Tithonian	**West**	**East**
Horizon	146.80	152.69
Overlap	8.98	17.53
Gap	9.66	3.31
Misfit	18.65	20.85
Misfit %	12.70	13.65
Total	**147.48**	**138.47**

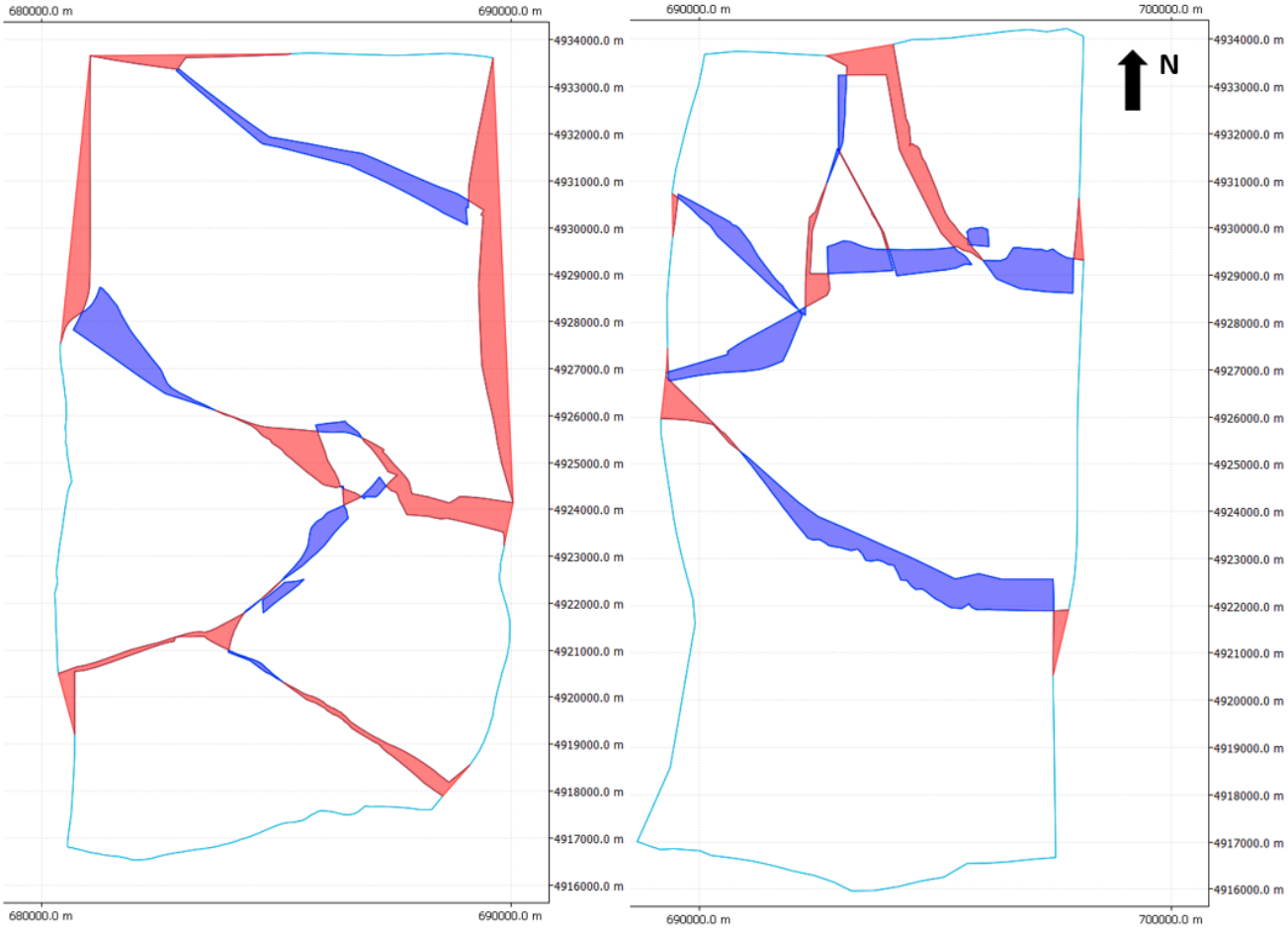

Fig.42: Map view of the Tithonian of the west part (left) and east part (right) after unfolding all structures. Overlaps (blue) and gaps (red) are also displayed.

Table 13: Area of Barremian after unfolding all structures.

	Area [km2]	
Barremian	**West**	**East**
Horizon	149.95	152.99
Overlap	30.86	23.32
Gap	11.06	13.54
Misfit	41.92	36.85
Misfit %	27.96	24.09
Total	**130.15**	**143.21**

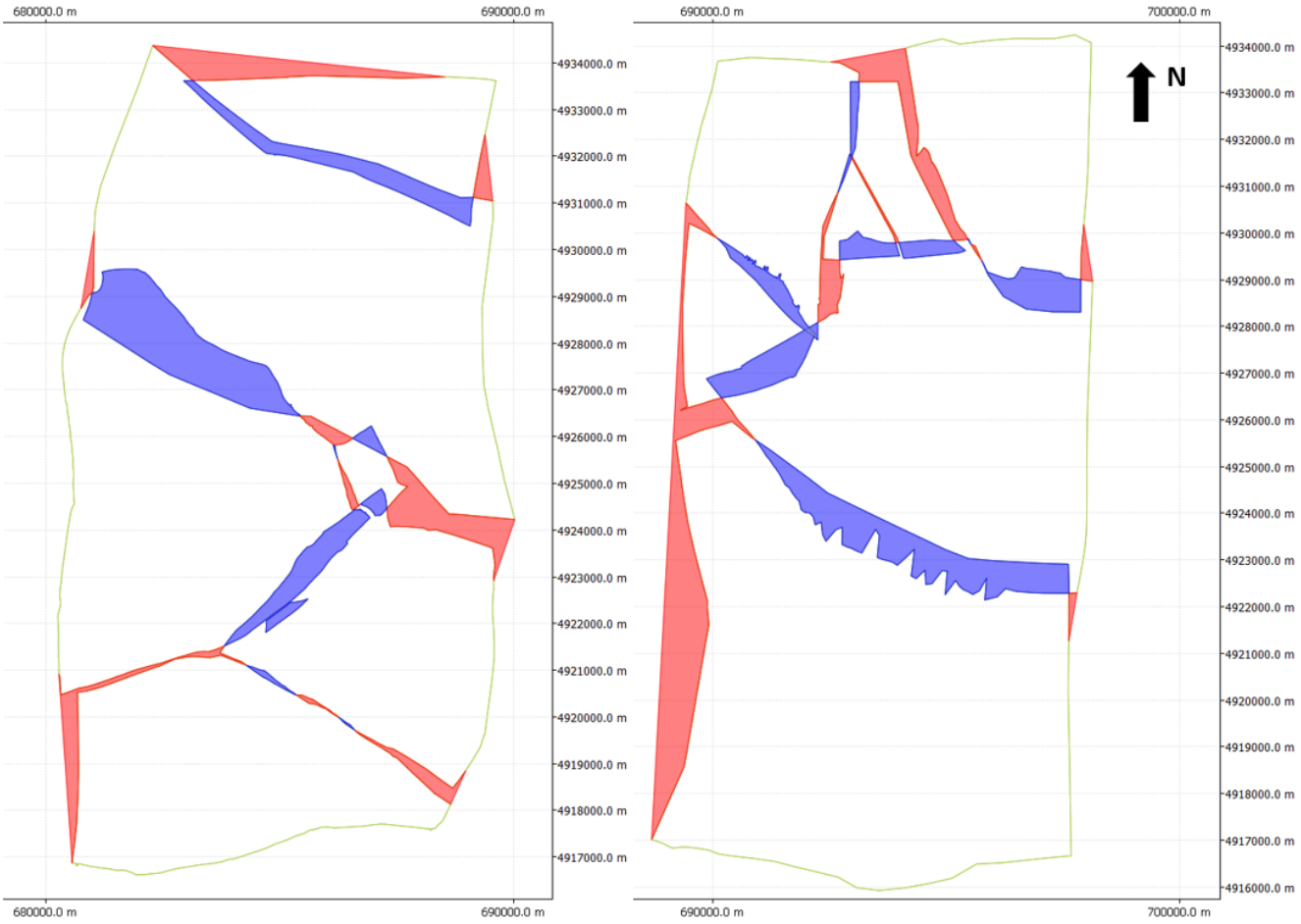

Fig.43: Map view of the Barremian of the west part (left) and east part (right) after unfolding all structures. Overlaps (blue) and gaps (red) are also displayed.

5.6 3D jigsaw restoration

Once all the faults were removed and all structures were unfolded, each fault block of the Tithonian and the Barremian was then translated and/or rotated back together in order to remove the potential errors (gaps/overlaps) caused during the building of the 3D model. This way, the area can be restored to its initial configuration before deformation. As a result, the amount of shortening could then be quantified and compared to the 2D model.

Table 14: Area of Tithonian after jigsaw restoration.

	Area [km2]	
Tithonian	**West**	**East**
Horizon	146.80	152.69
Overlap	0.06	0.07
Gap	11.94	11.38
Misfit	12.01	11.45
Misfit %	8.18	7.50
Total	**158.67**	**164.00**

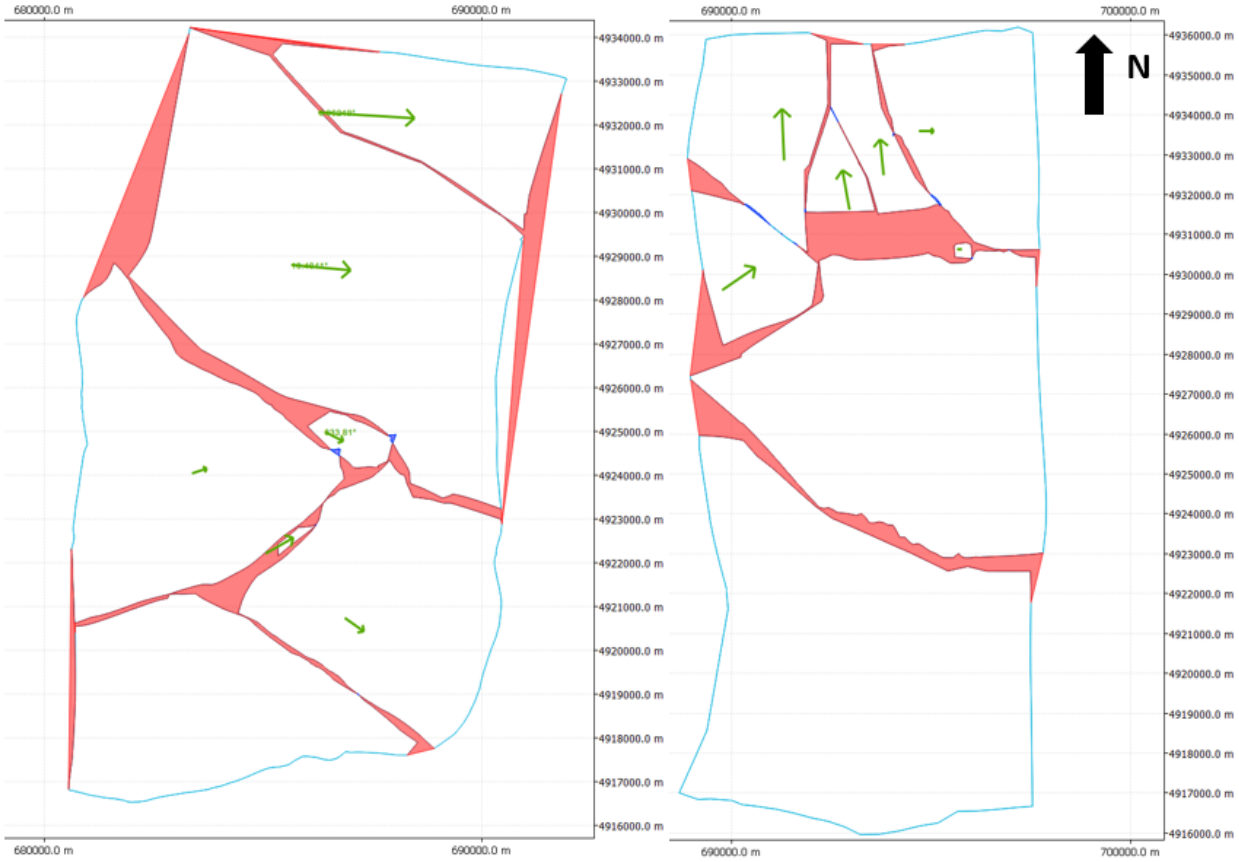

Fig.44: Map view of the Tithonian of the west part (left) and east part (right) after restoration. Remaining gaps (red) are also displayed.

Table 15: Area of Barremian after jigsaw restoration.

	Area [km2]	
Barremian	**West**	**East**
Horizon	149.95	152.99
Overlap	1.80	3.54
Gap	21.37	13.07
Misfit	23.17	16.61
Misfit %	15.45	10.86
Total	**169.51**	**162.51**

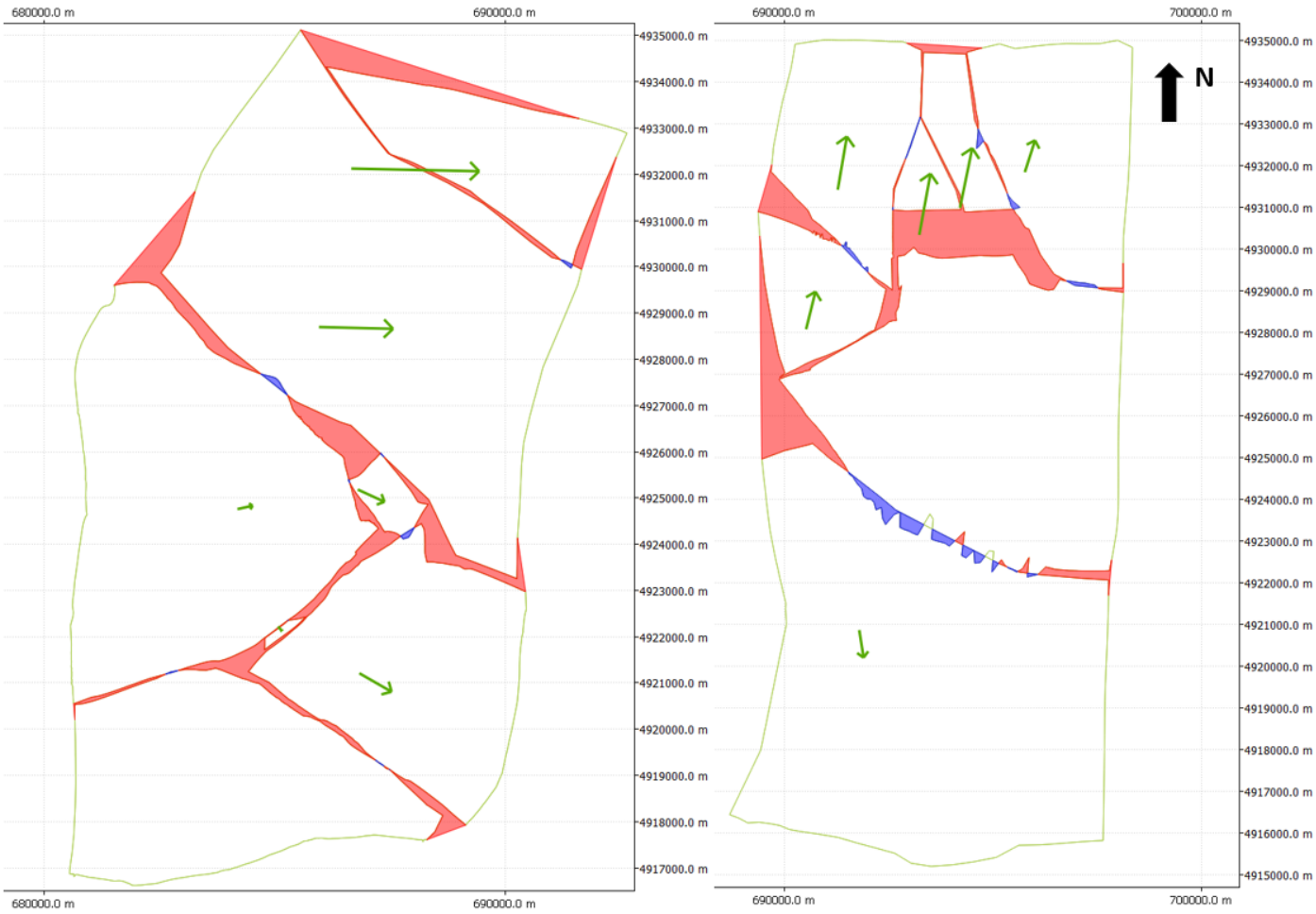

Fig.45: Map view of the Barremian of the west part (left) and east part (right) after restoration. Remaining gaps (red) are also displayed.

The resulting 2D and 3D models, once built and restored, were analyzed in terms of structural evolution and amount of shortening. Furthermore, the type and location of the faults present in the studied area were identified based on the geological and tectonic maps. Strain maps were produced for the Tithonian horizon based on the resulting 3D model. Based on these results, the distribution of the principal stress regimes could be deduced.

5.7 Tectonics

Folds

Most of the folds are oriented NW-SE to the exceptions of fold E, F, and G (Table 6) which have a fold axis oriented NNE-SSW, E-W and E-W to N-S respectively. Fold A (Fig.21) is part of a domal structure which indicates that both N-S and E-W contractions took place. The same holds for Fold H (Fig.21) and the fold just outside the southeastern part of the area, which are both part of a basin structure (Fig.21). The anticlines of C and F, as well as the synclines of B and G are all much more heavily folded compared with the other folds present in the area with a maximum amount of shortening of 1500m and 560m for C and F respectively, and a maximum amount of shortening of 550m and 1400m for B and G respectively. This would indicate that the direction of the main compressional phase that caused these structures to fold was oriented NE-SW.

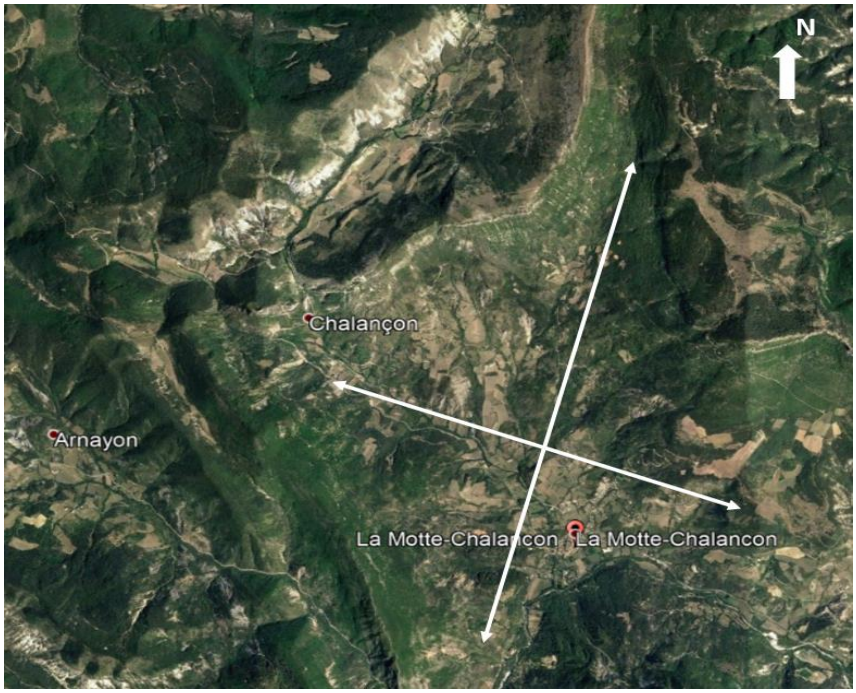

Fig.46: Top view of the domal structure near Chalancon (Fold A) in Google Earth.

Fig.47: Top view of the basinal structures of Fold H (top) and close to Rosans in the southeast of the area (bottom) in Google Earth.

The shape of the anticlines C and F as well as the synclines B and H on each side of faults 2 and 6 also show some E-W deformation due to their plunging fold axis. The anticline C becomes narrower towards the west and wider towards the east. The opposite is true for the syncline B on the other side of fault 2. In the east, the syncline H becomes narrower towards the west and wider towards the east.

Furthermore, the synclines B and G (Fig.21) show an interesting pattern. Both their fold axis vary laterally. They are oriented NW-SE and E-W respectively at the outskirts of the studied area and change to N-S close to the main strike-slip fault in the middle of the system (fault 5: Jonchère fault, Fig. 21). This gives a clear indication on the sense of movement of the major strike-slip fault, as well as its time of occurrence. The fact that these synclinal structures are bending from NW-SE or E-W to N-S towards the major strike-slip fault in a clockwise manner suggests that the Jonchère fault had a right-lateral (dextral) sense of movement and that folds B and G were formed before the activity along the Jonchère fault.

The folds' orientations give a clear indication on the direction of the principal stresses acting on the system. Folds having a fold axis oriented NW-SE result in a maximum principal stress (σ_1) that would be oriented NE-SW and a minimum principal stress (σ_3) that would be parallel to that fold axis, so NW-SE.

The trend of these folds clearly shows different phases of compression: a major NE-SW compressional phase for the folds of A, B, C, D, and H which are oriented NW-SE; a N-S compression (fold F and G) and an E-W compressional phase due to the domal/basinal structures and the plunging fold axis of the anticlines and synclines found on each side of fault 2 and 6.

Faults

The tectonic map of Fig.21 shows a system of reverse-, thrusts-, strike-slip-, and tear-faults. These faults carry different strikes (Table 7). Regarding the reverse and thrust faults, two strike components are distinguished. Faults 1, 2, 4, 6, and 12 have a strike oriented approximately NW-SE. Faults 8 and 9 have a strike orientated mainly E-W, and fault 13 which has a N-S strike approximately.

The strike-slip faults also show different strike components. Fault 5 which was defined as a dextral strike-slip fault has a N-S strike. Fault 3 which is a sinistral strike-slip has a NE-SW strike, and fault 11 which is a dextral strike-slip has a NNW-SSE strike.

Further, two tear faults are also present in the northeastern part of the area, namely faults 7 and 10. Fault 7 has a sinistral strike-slip component with a N-S strike and a thrust component with a WSW-ENE strike. Fault 10, on the other hand, has a dextral strike-slip component with a NNW-SSE strike and a thrust component with a WNW-ESE strike which could be an indication of E-W shortening due to its sense of movement.

Faults 3 and 5 seem to form a clear conjugate set, as well as fault 7 and 11. From a conjugate set of strike-slip faults, the maximum compressive stress direction can be predicted. It lies at an angle of approximately 30 degrees from the fault on the smaller angle of the X-shaped conjugate fault pattern. In the case of fault 3 and 5, the maximum principal stress would be oriented NNE-SSW to NE-SW. Then, the minimum horizontal principal stress would be oriented perpendicular to it, so WNW-ESE to NW-SE respectively. However, fault 7 and 11 show a slightly different maximum compressive stress direction. The maximum principal stress deduced for this set of faults would be oriented N-S with a minimum horizontal principal stress oriented E-W with a difference of around 15˚ compared to the stress direction of the first conjugate set.

Furthermore, an anti-clockwise rotation of approximately 15˚ of the hanging wall of the major thrust fault 2 to the west of fault 3 (Fig.21) was observed when restoring the fault blocks. This rotation probably resulted from the activity of the St May strike-slip fault (fault 3; Fig.21).

As a result of this rotation, the activity of the conjugate set of the St May fault and the Jonchère fault (fault 5; Fig.21) probably caused the formation of the Souchon Rima fault (fault 13; Fig.21) and the Condamine fault (fault 4; Fig.21).

Regarding the northeastern part of the studied area, the trend of the faults present there suggests that these were formed approximately under an identical stress regime, namely a N-S contraction. Fault 12, which is enclosed between fault 5 and 7 (Fig.21), probably resulted from the activity of the tear fault of Ruelles (fault 7; Fig.21) due to its sinistral strike-slip component during a N-S compressional stage.

Finally, combining the stress directions of both the folds and faults present in the tectonic map of Fig.21, the distribution of the principal stress regimes could be deduced. Indeed, a dominant NE-SW compressive stress regime, a N-S, although less dominant and only in the northeastern part of the area, and a minor E-W compressive stress regime were found. The NE-SW contraction resulted in the formation of folds A, B, C, D, F, and I and the formation of faults 1, 2, 3, 4, 5, and 6 (Fig.21). Then the N-S contraction, on the other hand, resulted in the formation of folds H and G and the formation of faults 7, 8, 9, 10, 11, and 12. Finally, the E-W contraction resulted in the domal structure of fold A (Fig. 46) and the basinal structure of fold H and the one in the southeastern corner (Fig. 47).

The first regime, the Pyrenean phase, which led roughly to the formation of E-W trending structures in the South East of France could have caused the formation of all the NW-SE trending folds and probably the formation of faults 1, 2, and 6 within the studied area, although this regime had a general maximum compressive stress oriented N-S.

The tectonic map shows less evidences of the activity of the second compressional regime, the Alpine phase which led to N-S trending structures expect for the folds which do show E-W compression (Fig.46 & 47). Furthermore, the 2D and 3D model constructed also show a clear shortening both in the N-S, and the E-W direction. Indeed, both the length of 2D model and the 3D model increased in the E-W direction when restoring them back to their original shape prior to deformation. This indicates that somehow, an E-W component was involved which could be related to the Alpine deformation phase. This component may have not formed the present faults, but it did cause some folding (dome/basin structures).

5.8 Structure analysis

2D Model

The resulting shape of the studied area for the Tithonian and the Barremian after removing each fault displacement and unfolding all structures is shown in Fig.48 and Fig.49 respectively. A trend is visible in both the N-S and E-W direction. The same trend is found for both horizons. The amount of N-S shortening varies from a large shortening in the western corner, followed by a small decrease towards the east and then increases to a maximum shortening in the most eastern corner. On the eastern part, the amount of E-W shortening shows a maximum peak shortening in the center and decreases gradually to almost no shortening towards the edges of the model.

Regarding the Tithonian, the N-S shortening varies from 403m to 4134m with more contraction in the eastern part than in the western part and its E-W shortening varies from 259m to 4254m with a high peak contraction at the level of WE_CrossSection_5 (Fig.48). The width of the original area prior to restoration is 17km and its length is 16km. Therefore, the N-S shortening of the 2D model varies from 3% to 21% and the E-W shortening varies from 2% to 20%.

Regarding the Barremian, the N-S shortening varies from 395m to 3774m with slightly more contraction in the east than in the west and its E-W shortening varies from 274m to 5799m with a high peak contraction at the same level as for the Tithonian. The width of the original area prior to restoration is 17km and its length is 16km. Therefore, the average N-S shortening of the 2D model varies from 2% to 19% and the average E-W shortening varies from 2% to 25%.

The area outside the original bounding box was calculated for both formations using a script written in Python. This way, the area of reduction could be determined. The resulting total area for the Tithonian after restoration was of 338km^2 and the original total area of 270km^2. The area reduction for this formation was of 68km^2 which corresponds to a reduction of 20% of the original area prior to deformation.

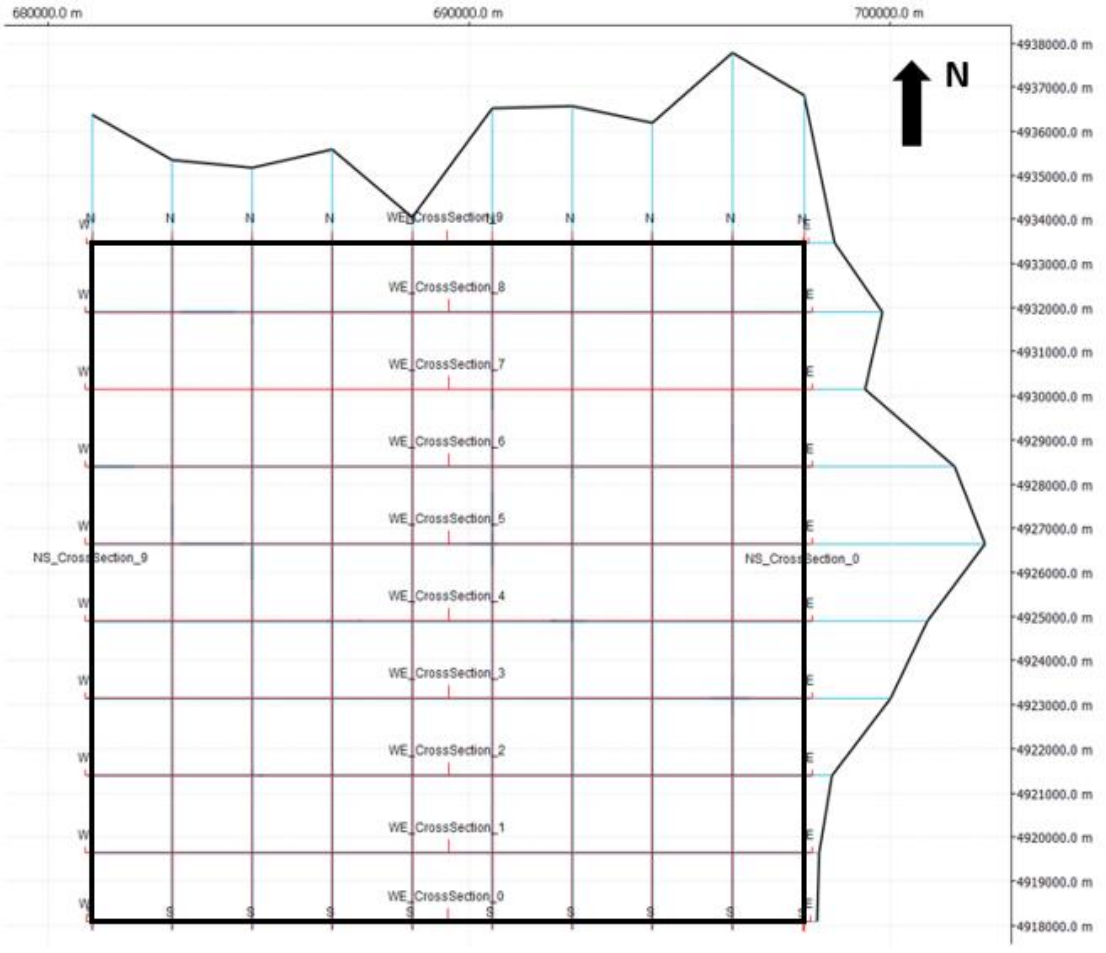

Fig.48: Map view of the 2D model showing the distribution of the amount of shortening for the Tithonian due to deformation.

The resulting total area for the Barremian after restoration was of 345km^2 and the original total area of 270km^2. The area reduction for this formation was of 75km^2 which corresponds to a reduction of 22% of the original area prior to deformation.

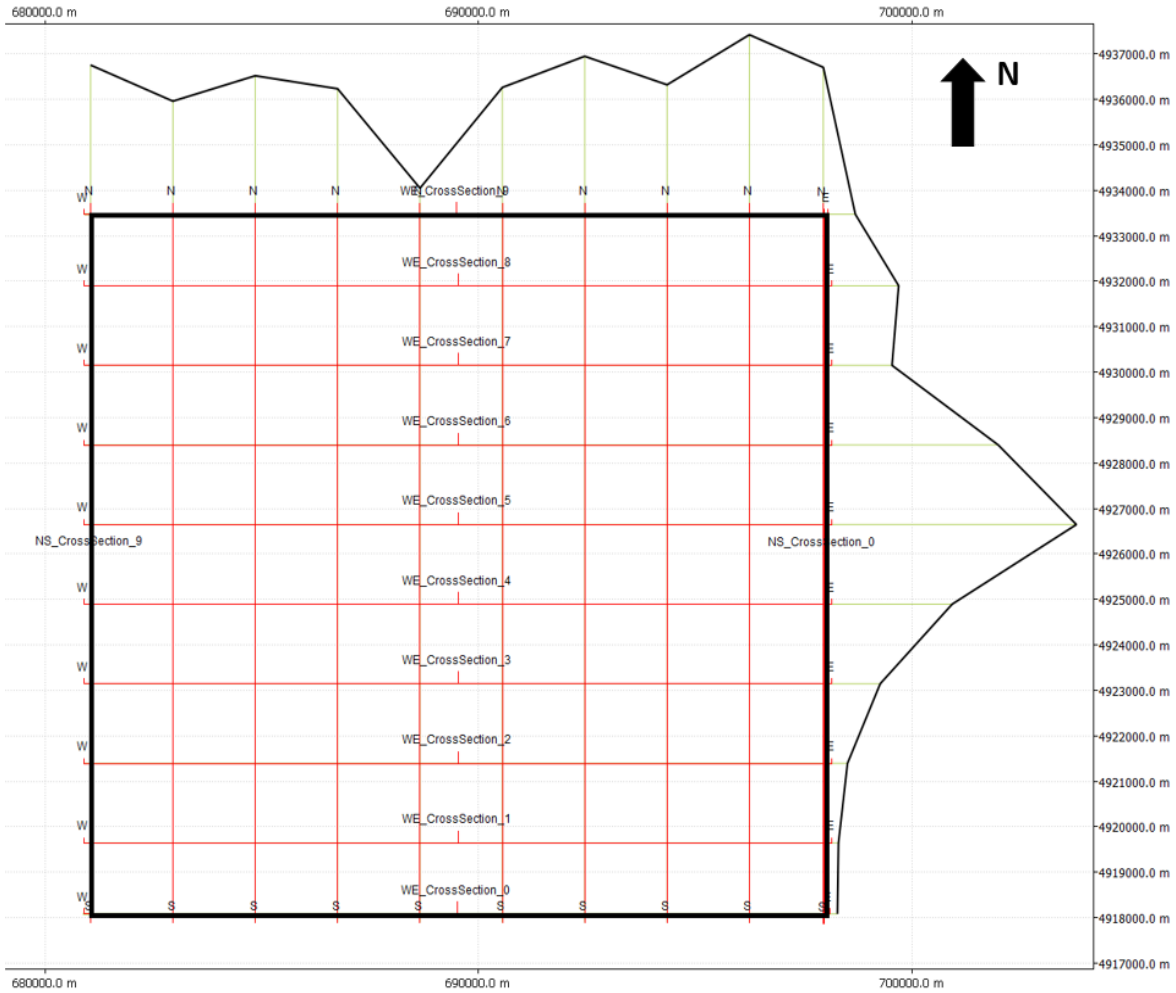

Fig.49: Map view of the 2D model of the Barremian and its amount of shortening caused due to deformation.

3D Model

A map view of the western- and eastern part of the Tithonian and the Barremian after restoration is shown in Fig. 50 and 52, respectively. Fig. 51 and 53 shows the deformed model of the Tithonian and Barremian respectively compared to their original area prior to deformation. Here as well, the distribution of the amount of shortening shows a similar trend as in the 2D models for both horizons. A significant amount of N-S shortening and a smaller amount of E-W shortening can be observed. The trends of the faults and

folds, as well as the shortening found in the 3D model imply that most of the deformation resulted from a N-S to NE-SW compression with a minor E-W component.

From these maps, the validity of the model was analyzed. After restoration, some gaps were formed such as small gaps found along the fault surfaces or between fault blocks. A major gap can be seen in the northern part of the area where the Tithonian horizon seems to be missing. Possible causes for these gaps are discussed in the section below.

Then, the amount of shortening of the 3D model was determined for the Tithonian and Barremian formations, for both in the N-S and E-W directions. The N-S shortening of the Tithonian varies from 179m to 4067m and its E-W shortening varies from 135m to 1697m. The width of the original area prior to restoration is 17km and its length is 16km. Therefore, the N-S shortening for the 3D model varies from 1% to 20% and the E-W shortening varies from 1% to 9%.

The N-S shortening of the Barremian varies from 236m to 4076m and its E-W shortening varies from no shortening to 1976m. The width of the original area prior to restoration is 17km and its length is 16km. Therefore, the N-S shortening for the 3D model varies from 2% to 21% and the E-W shortening is varies from 0% to 10%.

The total area of the Tithonian after restoration was of 323km^2 and its original total area of 270km^2. The area of reduction was then of 53km^2 which corresponds to a reduction of 16% of the original area prior to deformation.

Finally, the total area of the Barremian after restoration was of 332km^2 and its original total area of 270km^2. The area of reduction was then of 62km^2 which corresponds to a reduction of 19% of the original area prior to deformation.

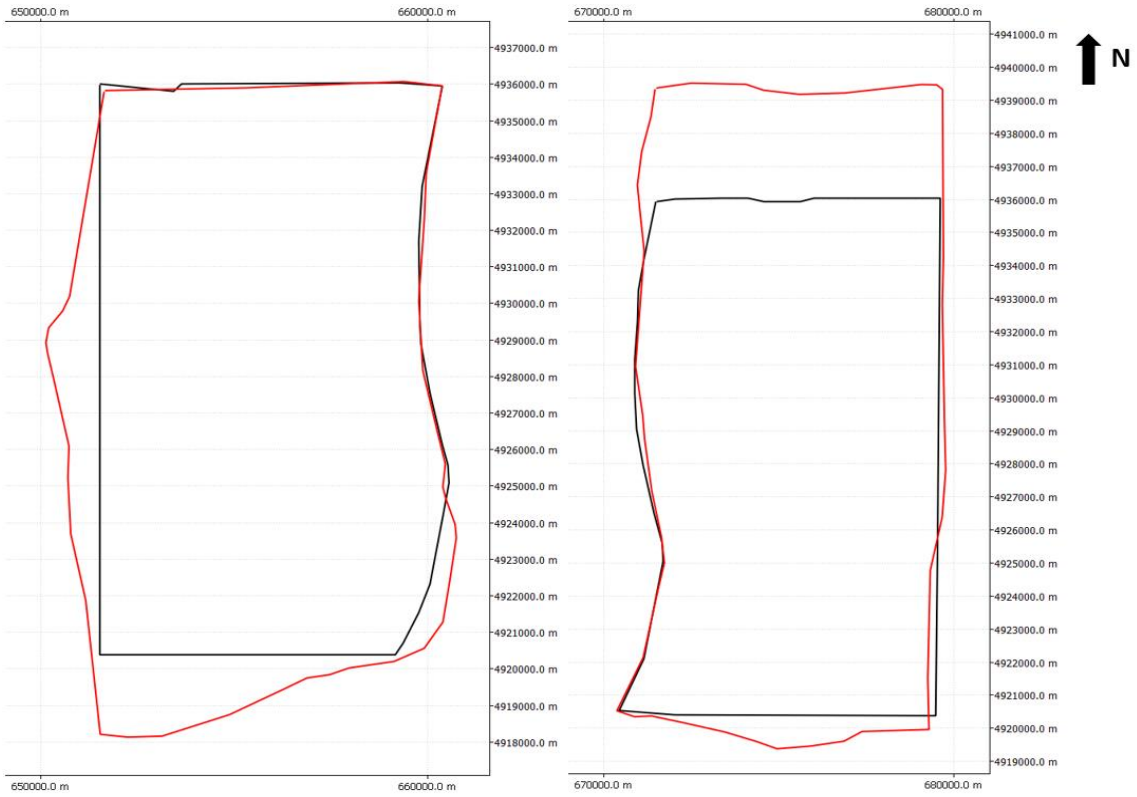

Fig.50: Map view of the western (left) and eastern (right) part of the Tithonian horizon before (black) and after (red) restoration.

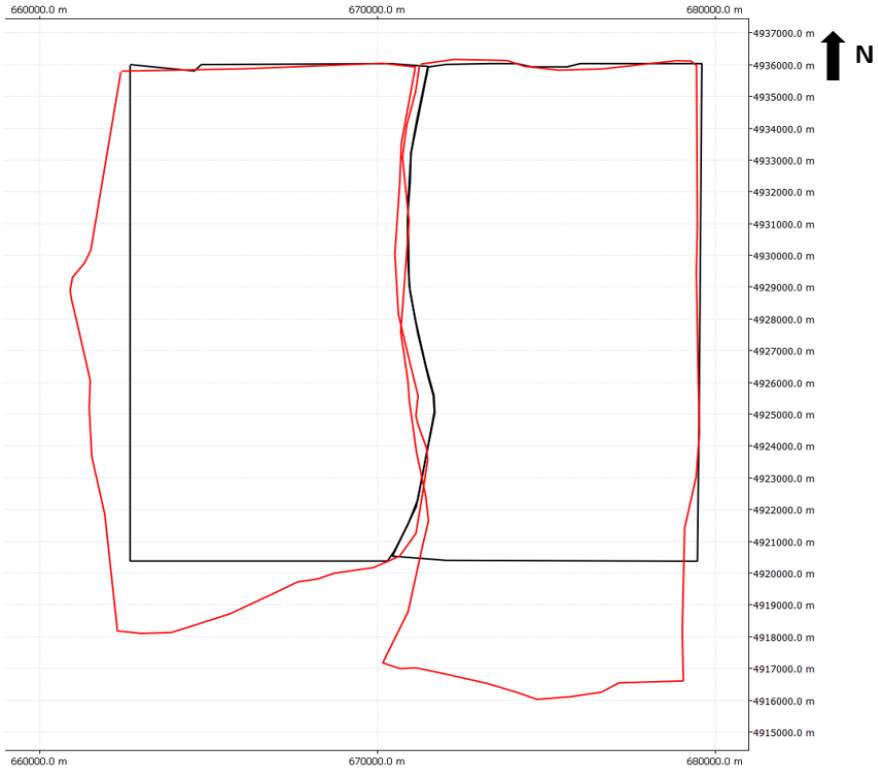

Fig.51: Map view of the studied area before (black) and after (red) restoration.

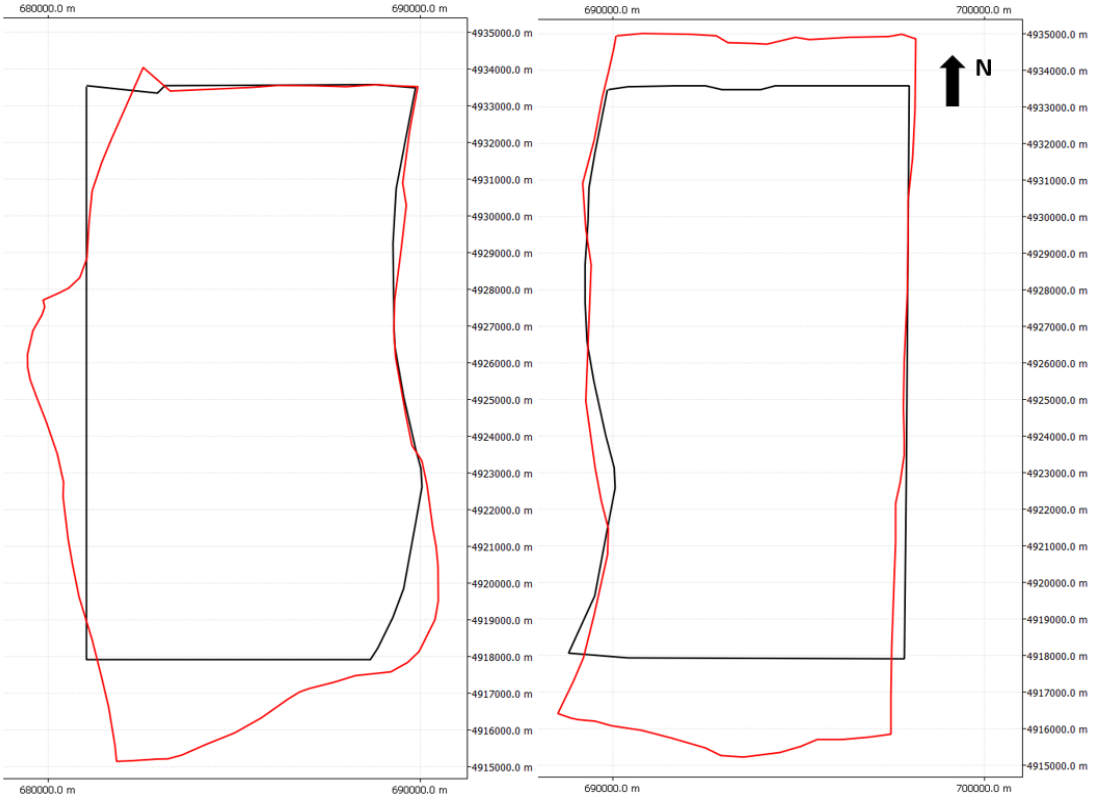

Fig. 52: Map view of the western (left) and eastern (right) part of the Barremian horizon before (black) and after (red) restoration.

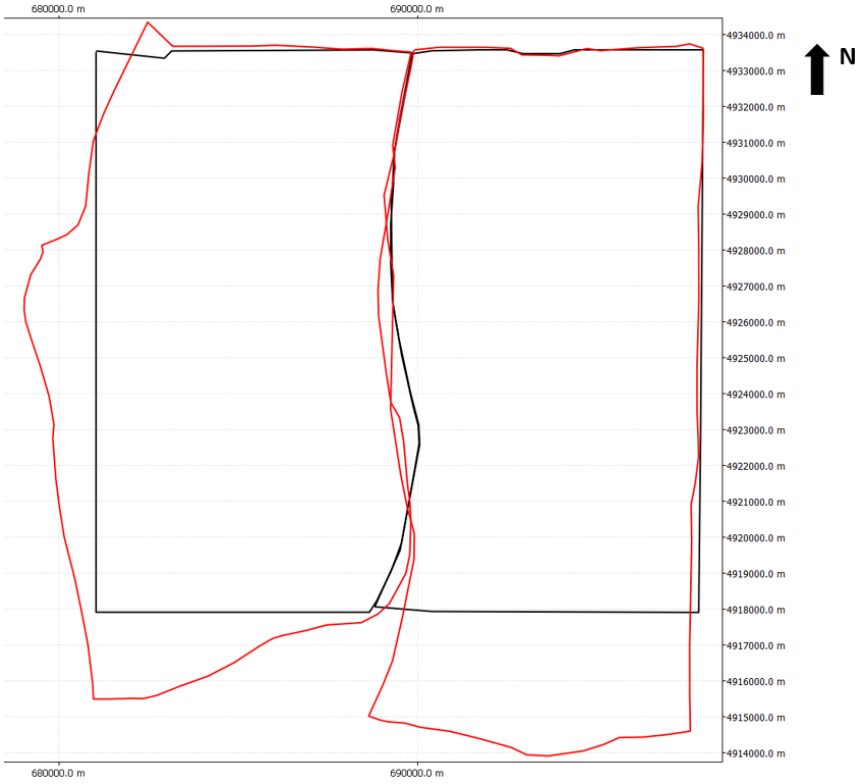

Fig. 53: Map view of the Barremian before (black) and after (red) restoration.

5.9 Strain maps

From the 3D model, strain maps of the western part (Fig.54) and eastern part (Fig.55) of the area were produced. These maps display the location of high- and low-strain zones. The high-strain zones are located mainly close to the fault zones where most of the deformation occurred and where the layers underwent heavy folding. Low-strain zones, on the other hand, are located away from these fault- and folding zones where almost no deformation was found. The high-strain zones are mainly oriented E-W or NW-SE which confirms the direction of the principal strain regimes being mainly N-S and NE-SW.

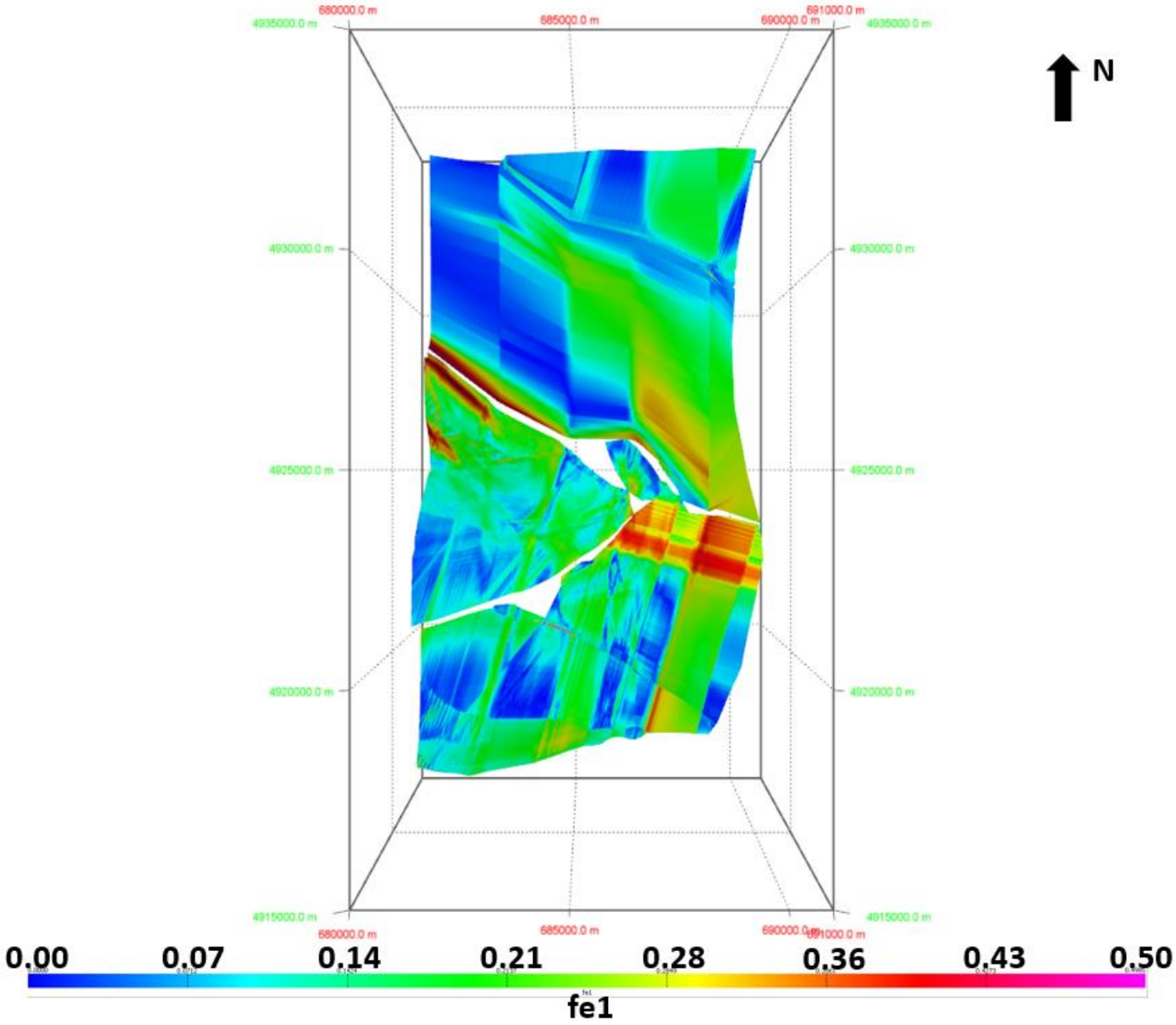

Fig.54: Strain map of the western part of the Tithonian horizon.

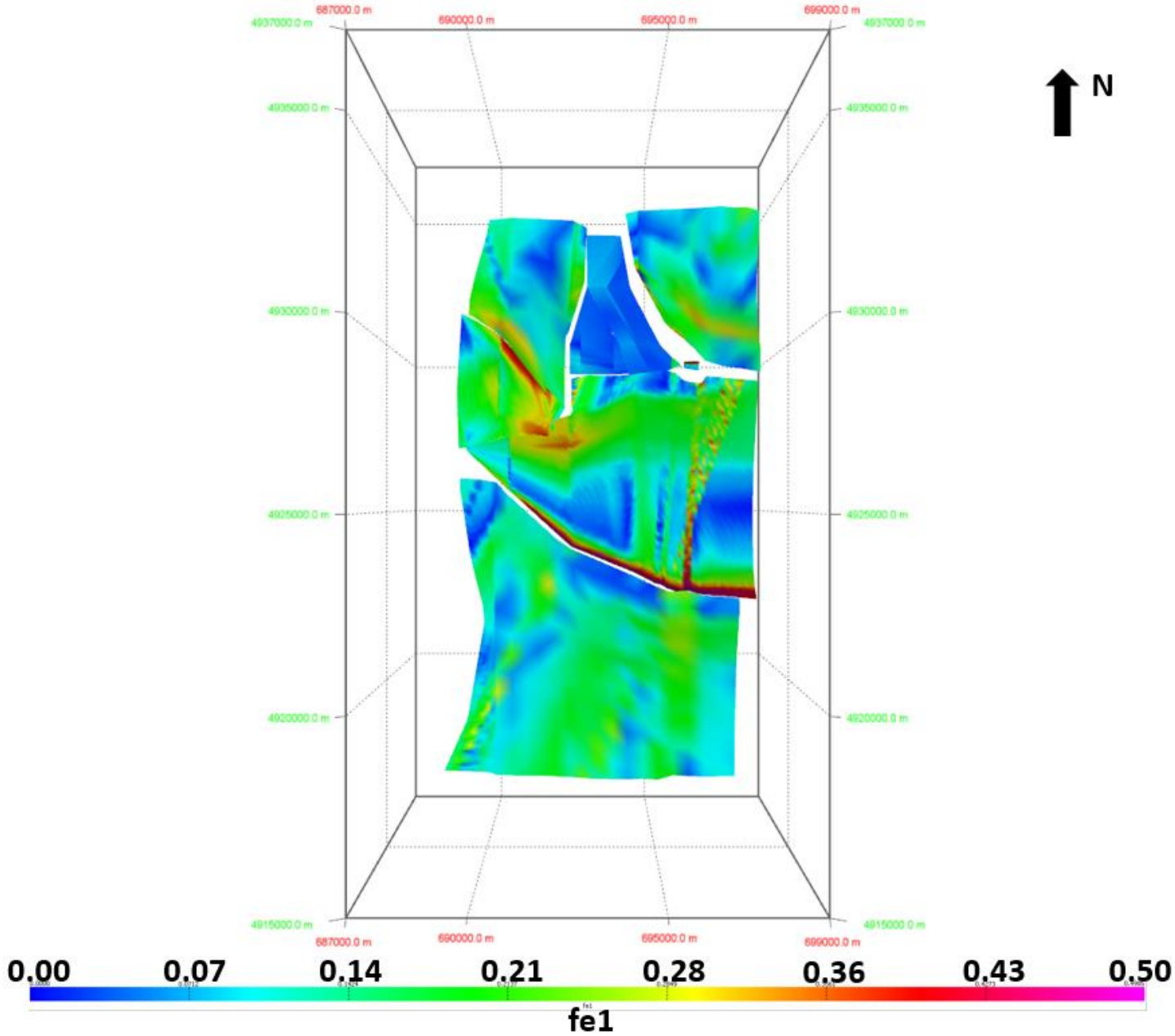

Fig.55: Strain map of the eastern part of the Tithonian horizon.

6. Discussion

Structure analysis

Cross-sections and geological map

Since constructing the 2D vertical cross-sections and the geological map was first done by hand, some uncertainties arose. Regarding the vertical thickness, each formation was assumed to have a constant thickness. This turned out not to be the case everywhere and was encountered during the unfolding process (Fig.28). Keeping the thicknesses constant in the parts of a cross-section found between the intersection of a N-S and E-W cross-section was difficult because of the lack of available data at these locations. This led to gaps and overlaps during the fault removal and unfolding processes (Fig.40 to 43). Therefore, some formations have varying thicknesses and the unfolding process wasn't always a success. In order to cope with that, some formations had to be moved up and down and redrawn to fit the same intersecting formation of another cross-section. The geological map was modified accordingly as well. A way to solve the thickness variations would have been to construct more cross-sections and therefore increase the resolution in order to reduce the uncertainties in between the intersected cross-sections. Due to time constraints, this couldn't be done but would be useful in future research in order to increase the accuracy of the model.

Since the geological map was modified along with the cross-sections, some location on the map didn't match the BRGM geological map anymore. Some boundaries between formations were slightly shifted compared to the BRGM map. There, the position of the modeled layers intersecting the surface will result in uncertainties and can derive from reality.

2D Model

Some anomalies are found in the 2D model (Fig.48 and 49) for both the Tithonian and Barremian horizons. An abrupt decrease in shortening is found at the level of NS_CrossSection_5 and WE_CrossSection_7. At the intersection of these two cross-sections, an anticline is found. This fold could have been wrongly interpreted. Only "Terres Noires" formation can be seen at that location. However, the BRGM map divides the "Terres Noires" further in older and younger "Terres Noires".

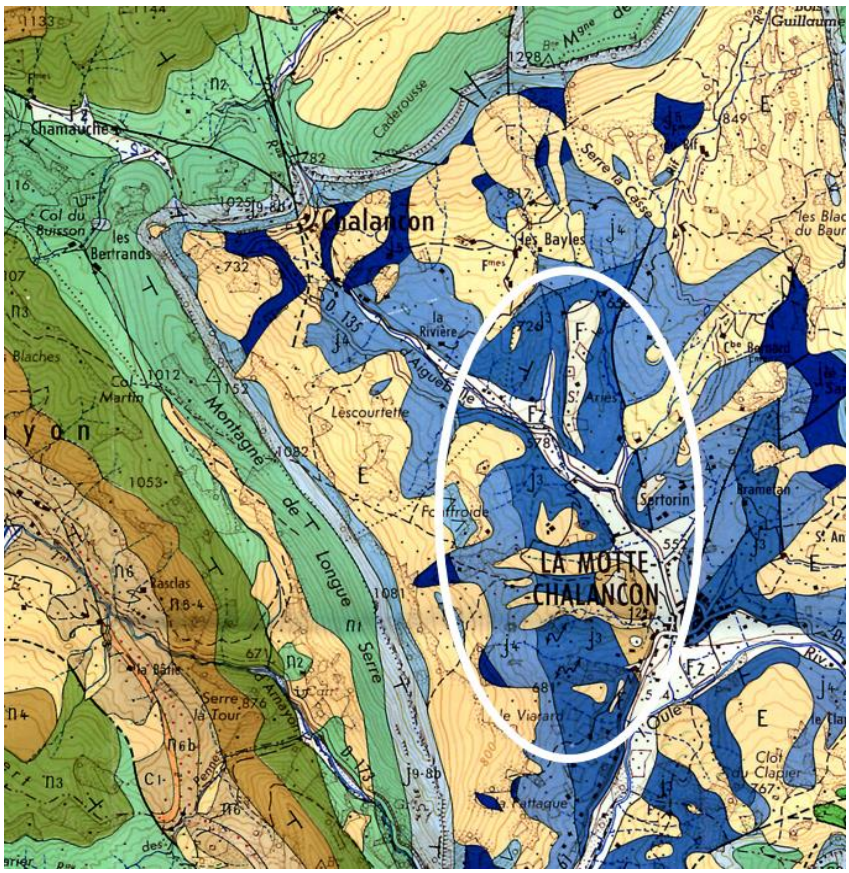

Fig.56: Geological map of the BRGM showing the older Terres Noires encircled in white.

At the intersection of the cross-sections, the BRGM map does show older "Terres Noires" (Fig.56) which indicates that the anticline should indeed be higher than modelled. Increasing the height of this anticline (Fig.57) did solve the problem for the shortening amount in the E-W direction and reduced the gap in the N-S direction (Fig.58). Yet, a gap remains in the N-S direction which means that there should be a mismatch somewhere else.

At the intersection between NS_CrossSection_5 and WE_CrossSection_2, the amount of shortening suddenly decreases as well in the E-W direction. This could be due to the Souchon Rima fault (fault 13; Fig.21) that could possibly extend more to the east towards the Jonchère fault (fault 5; Fig.21) instead of ending on the St May strike-slip fault (fault 3; Fig.21).

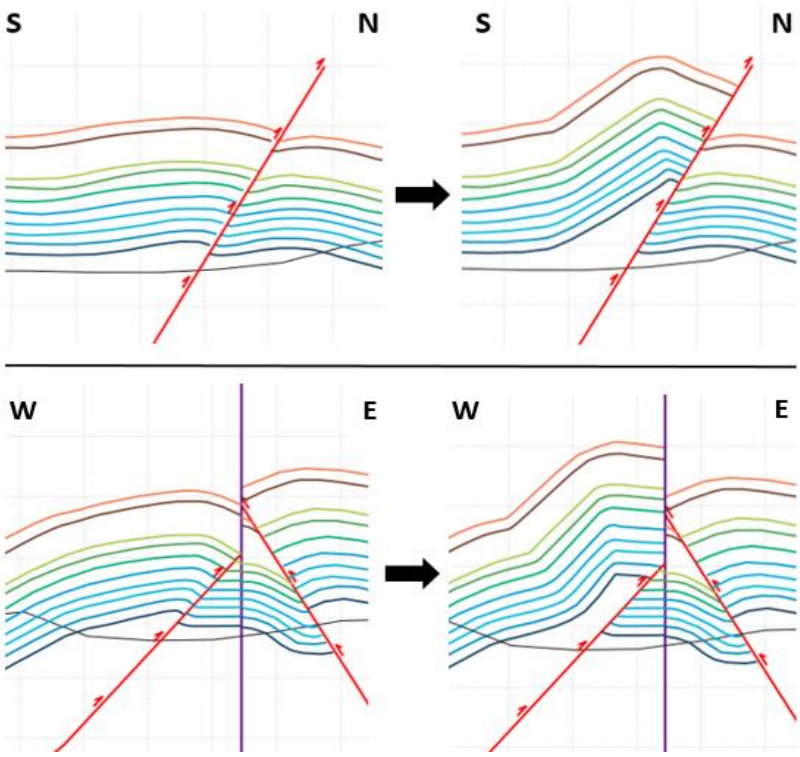

Fig.57: Anticline of NS_CrossSection_5 (top) and WE_CrossSection_7 (bottom) modified.

Fig.58: Map view of area with amount of shortening after modifying anticline.

This would lead to more displacement and more shortening in the N-S direction at the level of NS_CrossSection_5. Unfortunately, no clear indications were found on the field or derived from the BRGM maps since the only formation present at that location was the “Terres Noires”. However, to the north of that intersection and to the south of the village Cornillon Sur l’Oule (Fig.59), the BRGM map does show an age difference in the “Terres Noires”. Moreover, different orientations are found there within this older “Terres Noires”. To the south, it dips toward the southwest and to the north it is dipping toward the northeast displaying the shape of an anticline structure. Increasing the height of the anticline in NS_CrossSection_5 (Fig.60) solved the problem for the lack of shortening in the N-S direction along this cross-section (Fig.61).

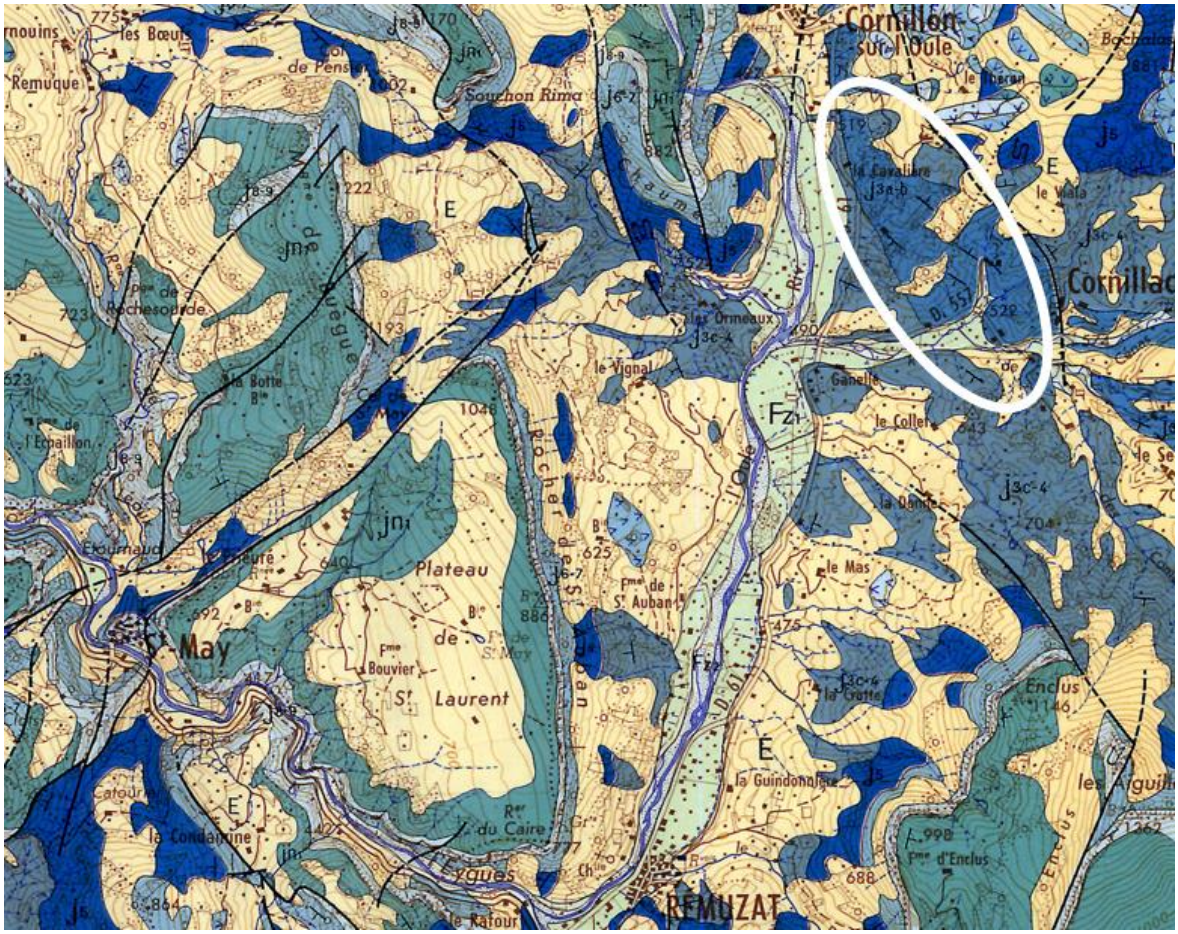

Fig.59: Geological map of the BRGM showing the older formation (encircled in white) of the Terres Noires compared to the surrounding Terres Noires formation.

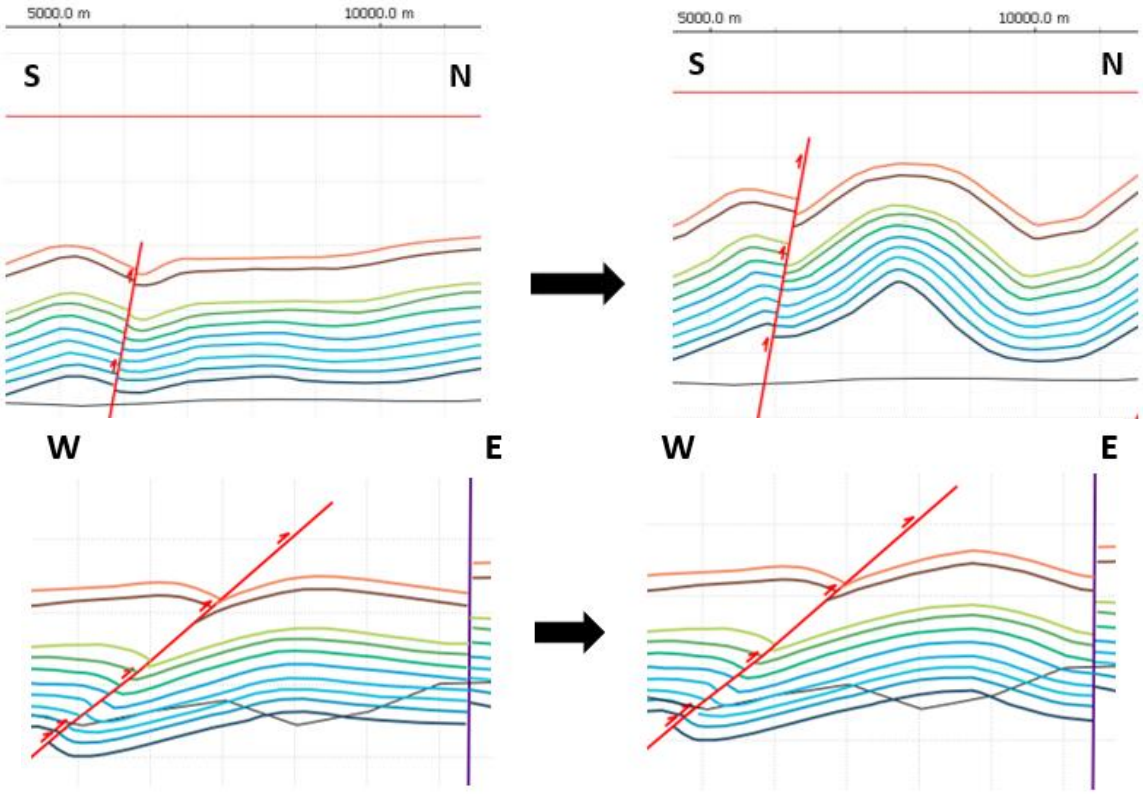

Fig.60: Anticline to the north of the Mt D'Angele fault in NS_CrossSection_5 (top) and WE_CrossSection_2 (bottom) modified.

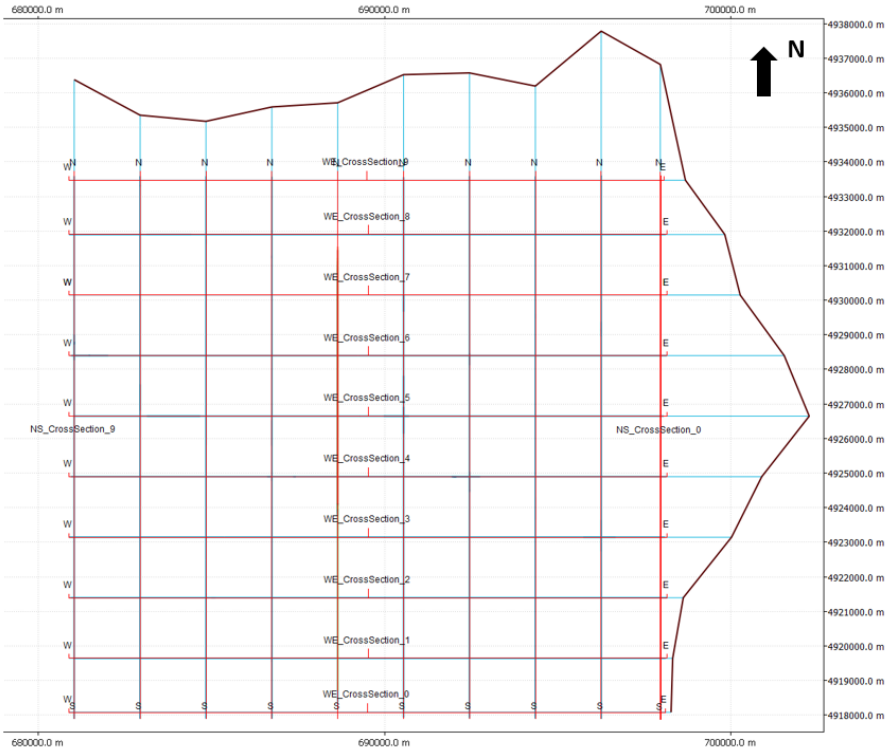

Fig.61: Map view of Tithonian in the 2D model after correcting for the anticline in NS_CrossSection_5.

3D Model

Once the 3D model was restored for both horizons, the same issue as for the one in the 2D model occurred regarding the amount of shortening. A gap was formed on the western part of the model where the part of the horizon is missing (Fig.62). This was probably due to the misinterpretation of the height of the folds along NS_CrossSection_5 which caused the horizon to be shorter than its surroundings. This should be improved by increasing the height of the anticlines in this cross-section before modelling these structures in 3D.

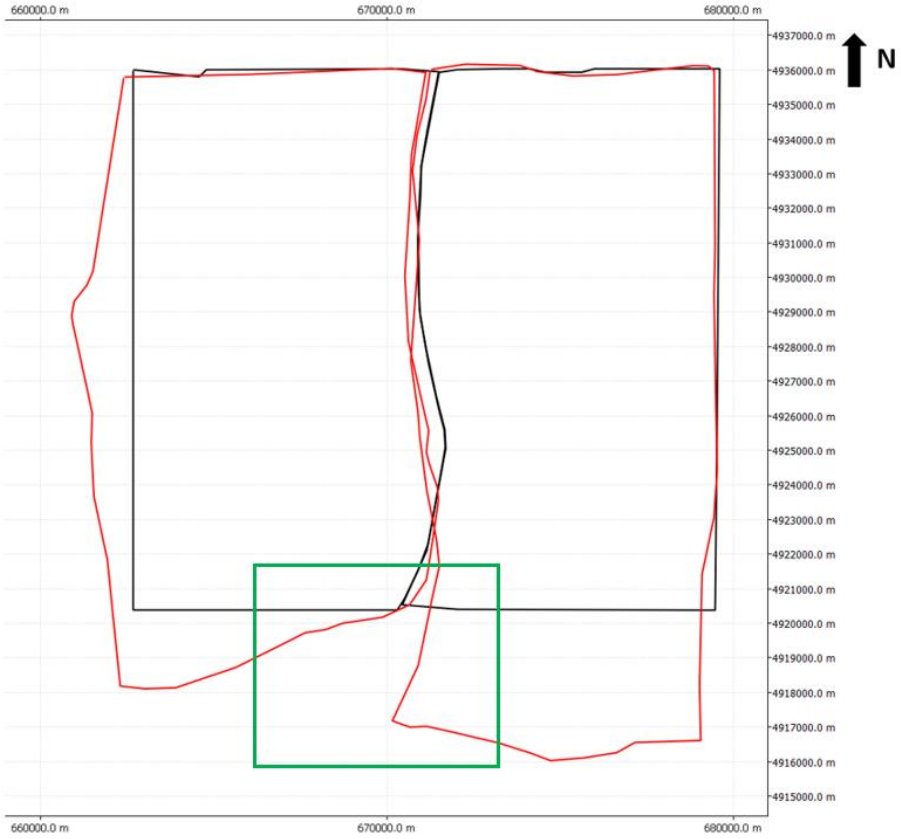

Fig.62: Gap (green rectangle) caused by geological misinterpretation of some folds.

Furthermore, the presence of gaps within the model can be observed (Fig.63) and could indicate a non-geological solution. These may be due to errors made during modelling. For example, some horizons couldn't be correctly extended to a fault surface when modelled resulting in small missing parts (Fig.63).

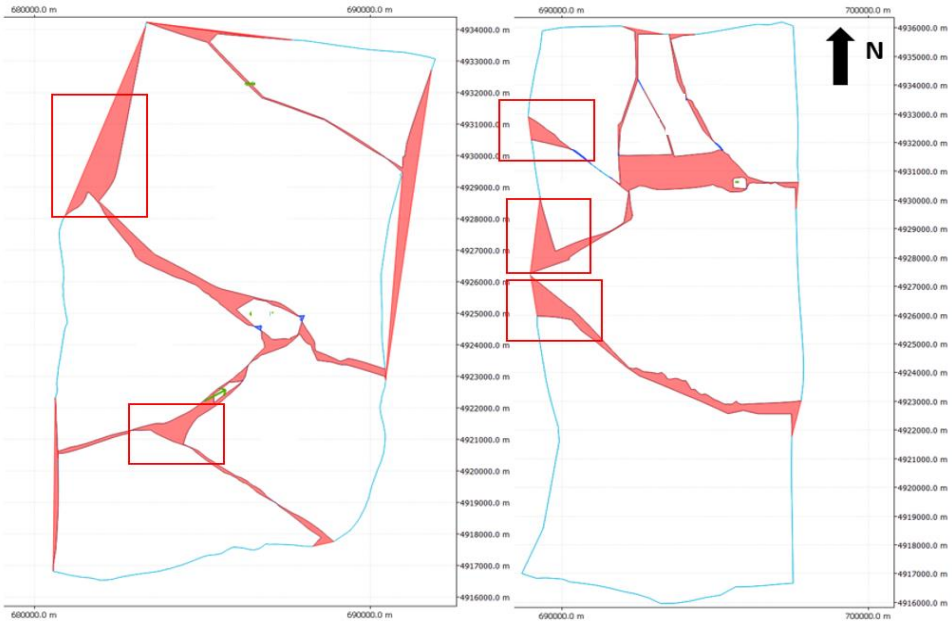

Fig.63: Gaps caused by modelling errors (red rectangles).

Then, in the northeastern part of the studied area (Fig.64), a major gap was formed due to the way the fault blocks were restored during jigsaw restoration. There was insufficient data available around this location in order to predict the extent of the Tithonian or the Barremian horizon. During the fieldwork, a splinter of the Tithonian horizon oriented vertically was observed at the location specified in Fig.64.

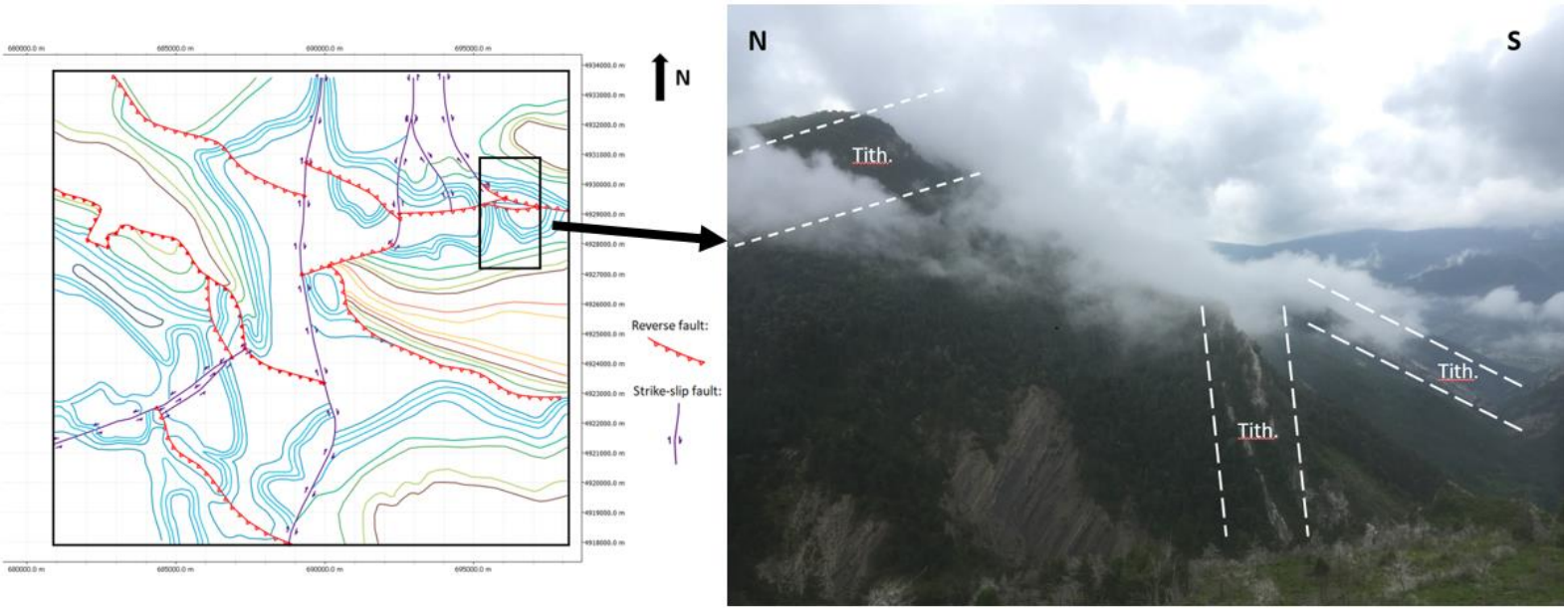

Fig.64: Photo taken during fieldwork showing the deformation of the Tithonian in the northeastern part of the area (rectangle).

However, the layer didn't seem to extend laterally to the west or to the east or at least not at the surface. The presence of this splinter led to the interpretation of the Hidden fault (fault 9; Fig.21), which would have caused the Tithonian layer to deform in such a way. The formation of this gap when restoring the model suggests that the layer could actually extend laterally to the west. This would imply that the Hidden fault should be longer than estimated on the map. However, more research should be conducted around this area in order to unravel the spatial complexity of the structures found there and fill-in the present gap caused by the lack of information and insight at this location.

Comparison 2D – 3D Model

The amount of shortening for both the Tithonian and Barremian horizons in 2D and 3D is listed in the table below.

Table 16: Amount of N-S and E-W shortening for the 2D and 3D model of both horizons.

	Tithonian				Barremian			
	2D		3D		2D		3D	
	Min	**Max**	**Min**	**Max**	**Min**	**Max**	**Min**	**Max**
NS shortening [m]	403	4134	179	4067	395	3774	236	4076
EW shortening [m]	259	4254	135	1697	274	5799	0	1976
NS shortening [%]	3	21	1	21	2	19	2	21
EW shortening [%]	2	20	1	9	2	25	0	10

The amount of N-S shortening between the Tithonian and the Barremian, both in 2D and 3D show little differences. These differences probably have a non-geological cause and could be related to misinterpretation errors when drawing the Barremian horizon in the 2D vertical cross-sections before being modelled.

However, the amount of E-W shortening between the 2D and the 3D model for both horizons varies significantly. Regarding the Tithonian, the maximum amount of E-W shortening is of 20% for the 2D model and only 9% for the 3D model. Concerning the Barremian, the maximum amount of shortening is of 25% for the 2D model and only 10% for the 3D model.

These large variations in the amount of E-W shortening between the 2D and 3D model are probably due to the way the layers were unfolded during the modelling process. In 3D, the structures were unfolded as surfaces based on the orientation of the unfolding planes. These were chosen based on the main orientation of the fold axis of each structure which in this case was mainly NE-SW. In 2D, the horizons were unfolded as lines based on their length in one specific direction, either N-S or E-W. Since most of the folds and faults are orientated NW-SE to E-W, the main direction of stress is oriented NE-SW to N-S and the deformation should be much greater in that direction. The amount of E-W shortening of the 2D model in table 16 seems to be as much or even larger than the amount of N-S shortening which doesn't quite match the expected stress distribution. The 3D model, on the other hand, seems to match the expected stress distribution better. Table 16 shows a maximum amount of shortening of 21% in the N-S direction and 9% to 10% in the E-W direction for the Tithonian and Barremian respectively.

Strain maps

The strain maps produced for this project give an approximation on the location of high/low strain zones based on the geological interpretation of the 3D model. These results could be used to predict the type and amount of fractures found at these high- or low-strain zones and this can be validated on the field.

Some artifacts can be observed, especially in the western part (Fig.65). These could have been caused during the fault removal step. After applying the Fault Parallel Flow algorithm, some of the Tithonian surfaces lost their smoothness creating some small scale height differences on those layers. This resulted in these peak strain lines when capturing strains after unfolding these layers. These strain lines seem to be all parallel to each other and perpendicular to the trend of the folds and faults present in this part which suggests that they do not fit the overall trend of the NE-SW to N-S principal strain regime.

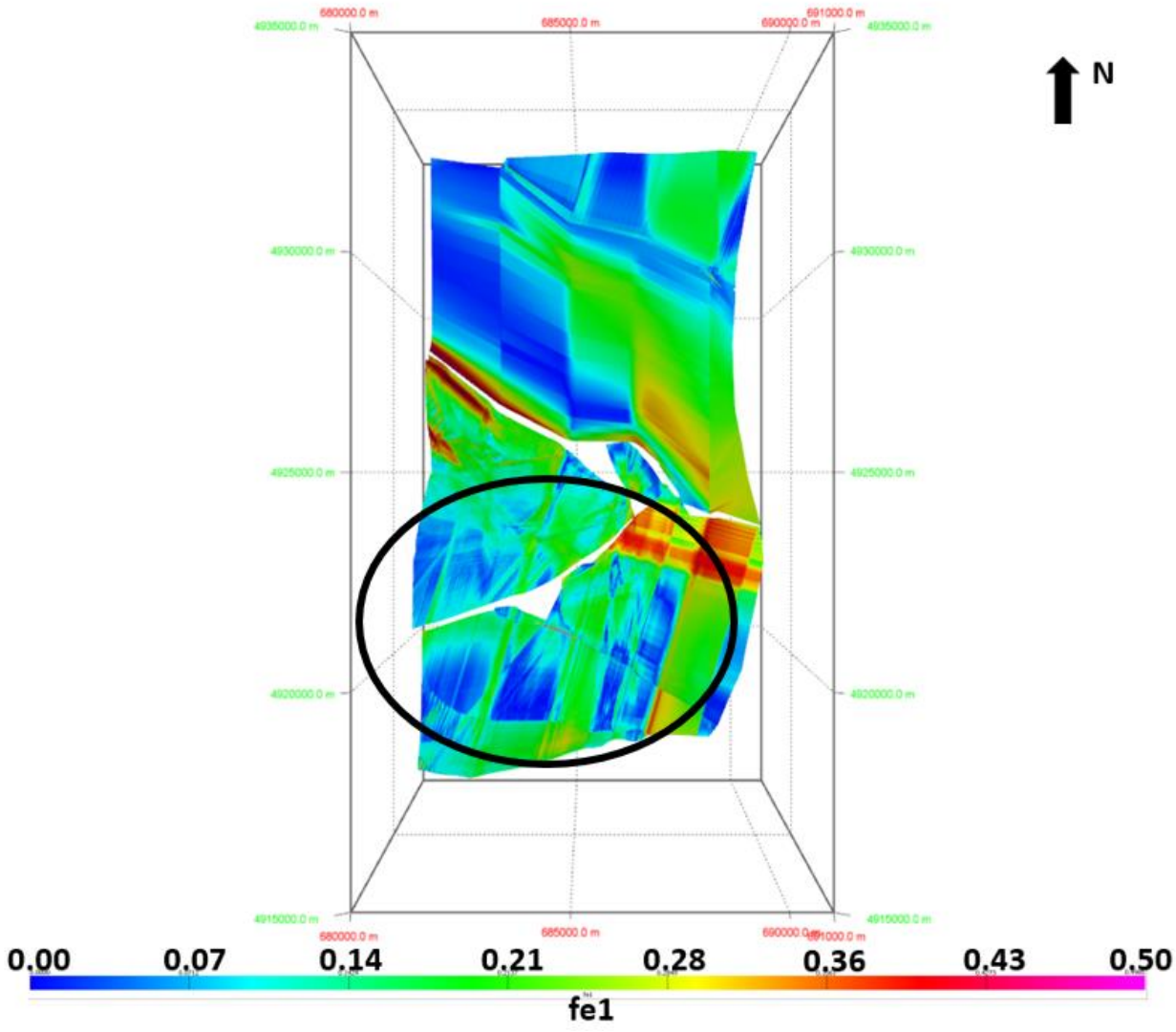

Fig.65: Artifacts encircled in black on the strain map of the western part of the studied area.

Tectonics

According to Gratier et al., the displacement pattern during the Pyrenean stage didn't just result from a N-S contraction. Instead, it evolved from NE-SW contractions to a more NNE-SSW to N-S contractions when moving towards the north (Fig.2; left). The amount of displacement decreases from east to west and from south to north up to an undeformed domain north of the line Montélimar-Gap.

The second stage, the Alpine deformation, shows a different displacement pattern. It started with an E-W displacement in the Chartreuse-Vercors around Grenoble and in the surroundings of Gap (Fig.2; right) and was carried towards the southwest with a more NE-SW displacement domain towards the Ventoux resulting in a general counter-clockwise rotation of the subalpine chains. The amount of displacement decreases from east to west and from north to south (Fig.2; right).

From the restoration of the 2D and the 3D model, the designated area was clearly subjected to two different compressional phases. Its present configuration resulted from a N-S compression and an E-W compression.

According to the tectonic map of the studied area, most of the folds are oriented NW-SE to the exception of fold E (Fig.21) which is oriented NNE-SSW. Fold A and H, as mentioned earlier, are part of a domal- and basinal structure respectively which resulted from NW-SE compression as well as E-W compression. Then, due to further compression in the NE-SW direction, the folded layers underwent even higher amount of stress and started to break resulting in the development of NW-SE trending faults such as faults 1, 2, 4, and 6 (Fig.21).

Furthermore, the orientation of the conjugate sets of strike-slip faults (Fig.21: 7 & 11; 3 & 5) show two slightly different stress regimes: a NE-SW and a N-S compression regime, respectively. Although the conjugate set of 7 and 11 is not as clear, it is probable that these strike-slip faults formed at the same time together with the faults found in the northeastern part of the area during a roughly N-S compressional phase.

When trying to link the two major events described by Gratier et al. (1989) with the resulting structures of the tectonic map generated for this project, some of these structures can be related to these events but others still remain unclear.

According to Gratier et al. (1989), the formation of the folds would have occurred during the Pyrenean stage. The layers within the studied area first folded before breaking during a first shortening event. This means that the NE-SW contraction that lead to the formation of the NW-SE trending folds present in the area must have occurred first. The fact that fold A, E, and H show some E-W contraction and that they are part of a domal/basinal structure can be explained by the fact that a second compressional regime, although less pronounced than the first regime, led to some folding in the E-W direction. These NW-SE trending folds could indeed correspond to the Pyrenean stage as Gratier et al. (1989) suggest in their work since the displacement orientation in Fig.2 (left) shows a NE-SW contraction at the location of the studied area (red cross). The second component responsible for the folding of some structures in the E-W direction could then correspond to the Alpine stage as shown in Fig.2 (right) where an ENE-WSW compressional regime took place.

Due to further compression during the first event, the layers started to break and faults started to form. Within the studied area, faults 2 and 6 (Fig.21) probably occurred earlier than the others. Faults 1, 4 and

13 probably occurred later as a result of the activity of the conjugate set of faults 3 and 5 which caused folds B and G, as well as faults 2 and 6 to bend N-S close to fault 5 (Fig.21) during the same NE-SW compressional regime (the Pyrenean phase) that led to the formation of the NW-SE trending folds.

Gratier et al. (1989) argue that the N-S to NE-SW trending strike-slip faults were old synsedimentary normal faults that were reactivated during the Alpine stage. However, the orientation of these faults is perpendicular to the direction of the second compressional phase and is therefore unlikely to have been reactivated during this stage. A way to find out whether or not these faults were normal faults would be to look at thickness variations of the Tithonian horizon across the fault. Only if the Tithonian was much thicker on one side would indicate that it is indeed part of a synsedimentary fault.

Regarding the northeastern part, the strike-slip faults 7 and 11 form an unclear conjugate set with a maximum principal stress oriented N-S and faults 8 and 9 have an E-W strike that also resulted from the NE-SW compression. So faults 7 to 12 might have occurred approximately at the same time during this compressional phase. The faults in the northeastern part seem to result from a N-S compression whereas the first stress regime was oriented NE-SW. Possibly, they could have formed during the NE-SW contraction of the Pyrenean phase, and then later during the ENE-WSW contraction of the second phase of the Alpine stage, partly rotated or folded resulting in their present configuration.

7. Conclusion

For this project, a geologically plausible 3D model of a complex geological area in the Subalpine Chains in the southeast of France was constructed and restored to its initial configuration prior to deformation. The data collected such as geological maps, previous Bachelor's fieldwork reports, new field data or aerial photos via Google Earth have been used to produce a grid of 20 different 2D vertical cross-sections and a geological map of the studied area. These were then imported and digitized using the geological modelling Move software package by Midland Valley in order to generate fault- and horizon surfaces.

First, a 2D model of two competent layers, the Tithonian and Barremian horizons, was built from the digitized cross-sections. This 2D model was then balanced and restored in order to determine the amount of shortening prior to deformation.

Then, a 3D model of both horizons was built in Move from the fault- and horizon surfaces. This model was restored by first removing each fault displacement using the Fault Parallel Flow algorithm from the 3D Move-On-Fault tool and then unfolding each structure using the Flexural Slip algorithm from the 3D Unfolding tool. Strain maps of the Tithonian horizon were finally produced from the balanced and restored 3D model and the distribution of high- and low-strain zones of the studied area were deduced.

The structural evolution and the phases of deformation of the area were then interpreted based on these models. The different trends of the folds and faults found on the tectonic map (Fig. 21) give clear indications on the direction of the principal stress regimes that took place over geological time. The structures present which first folded before faulting mainly have NW-SE fold axes with minor E-W trends resulting from a NE-SW trending maximum compressive stress regime which could be related to the first stage of the Pyrenean phase. Once these structures started faulting, thrusts faults with a NW-SE trend started forming especially in the western part and in the south of the eastern part of the studied area (faults 1, 2, and 6; Fig.21). The main dextral strike-slip fault (fault 5; Fig.21) forms a conjugate set with the strike-slip fault of St. May (fault 3; Fig.21). The activity of this conjugate set also resulted from the same NE-SW compressive stress regime and lead to the formation of the reverse faults 4 and 13 (Fig.21). However, the faults present in the northeastern part show a different trend. The strike-slip faults 7 and 11 (Fig.21) which also form a conjugate set together with the E-W trending faults 8 and 9 (Fig.21) all resulted from a N-S compressive stress regime. It is very likely that these faults resulted from the first phase which later, partially rotated due to local disturbances during the second phase. According to Gratier et al. (1989), the second deformation stage of the Alpine phase resulted in ENE-WSW compression within the studied area. According to this research, this compression phase didn't have as much impact as the first phase. It only resulted in the formation of some folds but no faults. Indeed, the domal/basinal structures, as well as the plunging fold axis of the major folds present in the area were the result of compression both in the N-S and the E-W direction. The latter being related to this second stage, the Alpine phase. These folds were thus first folded during the NE-SW compression which resulted in major faulting as well, and then later folded in the E-W direction during the Alpine phase. The larger impact of the second phase as described by Gratier et al. (1989) was not observed in this area.

The amount of shortening deduced from the 2D and 3D models for both the Tithonian and Barremian horizons also show deformation from two different phases. Major deformation took place in the N-S direction with a maximum amount of shortening of 21% for both the 2D and 3D model of the Tithonian,

and a maximum of 19%, and 21% for the 2D and 3D model of the Barremian respectively. In the E-W direction, deformation differs significantly between the 2D and 3D model. A maximum of 20% of shortening for the 2D model compared to a maximum of 9% of shortening for the 3D model regarding the Tithonian horizon and a maximum of 25% for the 2D model compared to a maximum of 10% for the 3D model regarding the Barremian horizon.

Finally, the strain maps produced from the 3D model for the Tithonian horizon for both the western- and the eastern part confirm the effect of the major principal stress regime that was derived from the tectonic map and the 3D models, namely a NE-SW to N-S compressive stress regime which corresponds to the first stage of the Pyrenean phase.

Based on the methodology used in this project, the strain distribution resulting from this local study could provide useful insight on the regional and global (tectonic) scale. Despite the errors found in the cross-sections and the geological map due to misinterpretation and lack of data, a plausible 2D and 3D geological model of the area could be built. However, uncertainties during the fault removal and unfolding processes resulted in an overall 10-20% misfit. This was due to gaps and overlaps created during the modelling process which was caused by the lack of information in some areas. Therefore, more research should be conducted on the field at these, still unraveled, locations such as the northeastern part of the studied area. This study and methodology is only a first attempt to take into account all geological data available and provide as much knowledge as possible on the subsurface of such a structurally complex area as the one investigated in this project.

8. Recommendations

The knowledge gained through the collected geological data made it possible to build a geologically plausible 3D model of the subsurface. Some areas such as the northeastern part or the area along NS_CrossSection_5 which still remain unclear, although partly unraveled thanks to the 3D model, require further research. The structures along NS_CrossSEction_5 which were misinterpreted in the first place when building the model should be looked at more carefully in order to improve the validity of the 3D model. The BRGM maps defines different ages of the "Terres Noires" there which were first interpreted as one formation. Therefore, more research should be conducted on the field as to where these formation boundaries are found in order to improve the geometry of the structures found along this cross-section.

Furthermore, research can be conducted on the fault continuity in the subsurface. For example, the distance from the Lower Oxfordian "Terres Noires" to the basement and detachment layer close to the fault could be determined by looking at the area of "Terres Noires" accumulated under structures such as anticlines. Since this formation deforms as a ductile rock and based on the amount of shortening of these structures, the depth to the basement layer can be deduced. Seismic data, if available, can also be used to predict the thickness of the "Terres Noires" formation and the depth of the faults deeper in the subsurface.

Modelling neighboring areas can also be useful in order to determine the behavior of some faults such as the Jonchère fault or the Hidden fault outside the boundaries of the studied area. This way, the 3D model built for this project can be compared/validated based on the geological interpretation of the structures found in the surrounding areas. Moreover, the direction of the principal stress regimes found for the studied area can be compared to the principal stresses found in neighboring areas and it can therefore be correlated on a larger scale.

Gratier et al. (1989) argue that the large strike-slip faults found in the area and surroundings are a part of Jurassic synsedimentary normal faults that have been reactivated as strike-slip faults at a later stage. This could be proven by taking a look at the thickness of the Tithonian formation on both sides of the main strike-slip fault (Jonchère fault) at several locations. If the thickness is identical on each side, this would contradict their argument. If the thickness does vary, the opposite would be true and this fault could be part of a synsedimentary normal fault.

Finally, the strain maps produced for this model can be used further to gain knowledge and predict the type, density, and location of fractures present in the area depending on the geological structure and the phase of deformation that took place.

9. References

BOER DE, P. L. (1983). ASPECTS OF MIDDLE CRETACEOUS PELAGIC SEDIMENTATION IN SOUTHERN EUROPE: PRODUCTION AND STORAGE OF ORGANIC MATTER, STABLE ISOTOPES, AND ASTRONOMICAL INFLUENCES (DOCTORAL DISSERTATION, UTRECHT UNIVERSITY).

BOMBARDIERE, L., & GORIN, G. E. (2000). STRATIGRAPHICAL AND LATERAL DISTRIBUTION OF SEDIMENTARY ORGANIC MATTER IN UPPER JURASSIC CARBONATES OF SE FRANCE. SEDIMENTARY GEOLOGY, 132(3-4), 177-203.

BOULILA, S., GALBRUN, B., HINNOV, L. A., COLLIN, P. Y., OGG, J. G., FORTWENGLER, D., & MARCHAND, D. (2010). MILANKOVITCH AND SUB-MILANKOVITCH FORCING OF THE OXFORDIAN (LATE JURASSIC) TERRES NOIRES FORMATION (SE FRANCE) AND GLOBAL IMPLICATIONS. BASIN RESEARCH, 22(5), 717-732.

BRÉHÉRET, J. G., & BRUMSACK, H. J. (2000). BARITE CONCRETIONS AS EVIDENCE OF PAUSES IN SEDIMENTATION IN THE MARNES BLEUES FORMATION OF THE VOCONTIAN BASIN (SE FRANCE). SEDIMENTARY GEOLOGY, 130(3-4), 205-228.

COLOMBIÉ, C., STRASSER, A., 2000. A KEEP-UP TRANSGRESSIVE SYSTEMS TRACT ON THE LOWER KIMMERIDGIAN PLATFORM IN THE SWISS JURA. 8TH MEETING OF SWISS SEDIMENTOLOGISTS, FRIBOURG, SWITZERLAND, 13.

COURJAULT, T., GROSHENY, D., FERRY, S., & SAUSSE, J. (2011). DETAILED ANATOMY OF A DEEP-WATER CARBONATE BRECCIA LOBE (UPPER JURASSIC, FRENCH SUBALPINE BASIN). SEDIMENTARY GEOLOGY, 238(1-2), 156-171.

COTILLON, P., ARNAUD-VANNEAU, A., ARNAUD, H., BOISSEAU, T., BUSNARDO, R., CHAROLLAIS, J., & DEMAY, J. L. (1984). CRÉTACÉ INFÉRIEUR. SYNTHESE GÉOLOGIQUE DU SUD-EST DE LA FRANCE, 1, 287-338.

DARDEAU, G. É. R. A. R. D., ATROPS, F. R. A. N. Ç. O. I. S., FORTWENGLER, D., DE GRACIANSKY, P. C., & MARCHAND, D. I. D. I. E. R. (1988). JEUX DE BLOCS ET TECTONIQUE DISTENSIVE AU CALLOVIEN ET A L'OXFORDIEN DANS LE BASSIN DU SUD-EST DE LA FRANCE. BULLETIN DE LA SOCIÉTÉ GÉOLOGIQUE DE FRANCE, 4(5), 771-777.

DROMART, G., FERRY, S., ATROPS, F., POSAMENTIER, H. W., SUMMERHAYES, C. P., HAQ, B. U., & ALLEN, G. P. (1993). ALLOCHTHONOUS DEEP-WATER CARBONATES AND RELATIVE SEA-LEVEL CHANGES: THE UPPER JURASSIC-LOWERMOST CRETACEOUS OF SOUTHEAST FRANCE. IN SEQUENCE STRATIGRAPHY AND FACIES ASSOCIATIONS (VOL. 18, PP. 295-305).

ELMI, S. (1983). LA STRUCTURE DU SUD-EST DE LA FRANCE: UNE APPROCHE À PARTIR DE LA BORDURE VIVARO-CÉVENOLE DU MASSIF CENTRAL. CR ACAD. SCI. PARIS, 296(2), 1615-1620.

FERRY, S., ATROPS, F., BACKERT, N., LOZANO-GARCIA, F., & SAVARY, B. (2005). SYSTÈMES TURBIDITIQUES CALCAIRES DU TITHONIEN ET DU BARRÉMO-BÉDOULIEN SUBALPINS (SE DE LA FRANCE) (1-3 SEPTEMBRE 2005). EXCURSION DU GROUPE FRANÇAIS DU CRÉTACÉ, 44-P.

FORD, M., & STAHEL, U. (1995). THE GEOMETRY OF A DEFORMED CARBONATE SLOPE-BASIN TRANSITION: THE VENTOUX-LURE FAULT ZONE, SE FRANCE. TECTONICS, 14(6), 1393-1410.

FRANCIS, J. E., & FRAKES, L. A. (1993). CRETACEOUS CLIMATES. SEDIMENTOLOGY REVIEW/1, 17-30.

FRIES, G., & PARIZE, O. (2003). ANATOMY OF ANCIENT PASSIVE MARGIN SLOPE SYSTEMS: APTIAN GRAVITY-DRIVEN DEPOSITION ON THE VOCONTIAN PALAEOMARGIN, WESTERN ALPS, SOUTH-EAST FRANCE. SEDIMENTOLOGY, 50(6), 1231-1270.

FRISCH, W. (1979). TECTONIC PROGRADATION AND PLATE TECTONIC EVOLUTION OF THE ALPS. TECTONOPHYSICS, 60(3-4), 121-139.

LAWRENCE A.. FRAKES, & JANE E.. FRANCIS. (1992). CLIMATE MODES OF THE PHANEROZOIC: THE HISTORY OF THE EARTH'S CLIMATE OVER THE PAST 600 MILLION YEARS. CAMBRIDGE UNIVERSITY PRESS.

GIOT, D., ROURE, F., ELMI, S., LAJAT, D., & STEINBERG, M. (1991 A). GÉOMÉTRIE ET DYNAMIQUE D'UNE MARGE CONTINENTALE MÉSOZOÏQUE, ARDÈCHE, FRANCE. CR ACAD SCI PARIS, 312, 747-754.

GIOT, D., ROURE, F., DROMART, G., ELMI, S., NAVILLE, C., PERRIN, J., & DROMART, G. (1991 B). DYNAMIQUE D'UNE MARGE PASSIVE JURASSIQUE: LES PRINCIPALES ÉTAPES DE REJEU DE LA FAILLE D'UZER RÉVÉLÉES PAR LE FORAGE DE BALAZUC N° 1 (ARDÈCHE, FRANCE). PROGRAMME GÉOLOGIE PROFONDE DE LA FRANCE. COMPTES RENDUS DE L'ACADÉMIE DES SCIENCES. SÉRIE 2, MÉCANIQUE, PHYSIQUE, CHIMIE, SCIENCES DE L'UNIVERS, SCIENCES DE LA TERRE, 313(12), 1463-1469.

GOGUEL, J. (1963). L'INTERPRETATION DE L'ARC DES ALPES OCCIDENTALES. BULLETIN DE LA SOCIÉTÉ GÉOLOGIQUE DE FRANCE, 7(1), 20-33.RN ALPS. GEOLOGICAL SOCIETY, LONDON, SPECIAL PUBLICATIONS, 45(1), 65-81.

GÖTZ, A. E., FEIST-BURKHARDT, S., & RUCKWIED, K. (2008). PALYNOFACIES AND SEA-LEVEL CHANGES IN THE UPPER CRETACEOUS OF THE VOCONTIAN BASIN, SOUTHEAST FRANCE. CRETACEOUS RESEARCH, 29(5-6), 1047-1057.

GRÉSELLE, B., & PITTET, B. (2010). SEA-LEVEL RECONSTRUCTIONS FROM THE PERI-VOCONTIAN ZONE (SOUTH-EAST FRANCE) POINT TO VALANGINIAN GLACIO-EUSTASY. SEDIMENTOLOGY, 57(7), 1640-1684.

GRACIANSKY, P. C. D., DARDEAU, G., BODEUR, Y., ELMI, S., FORTWENGLER, D., JACQUIN, T., & THIERRY, J. (1999). LES TERRES NOIRES DU SUD-EST DE LA FRANCE (JURASSIQUE MOYEN ET SUPÉRIEUR): INTERPRÉTATION EN TERMES DE STRATIGRAPHIE SÉQUENTIELLE. BULLETIN DU CENTRE DE RECHERCHES ELF EXPLORATION–PRODUCTION, 22, 35-66.

GRATIER, J. P., MÉNARD, G., & ARPIN, R. (1989). STRAIN-DISPLACEMENT COMPATIBILITY AND RESTORATION OF THE CHAÎNES SUBALPINES OF THE WESTE

GROSHENY, D., & MALARTRE, F. (2003). RECONSTRUCTION OF OUTER SHELF PALEOENVIRONMENTS IN THE TURONIAN–CONIACIAN OF SOUTHEAST FRANCE (MICROPALEONTOLOGY–SEDIMENTOLOGY: LOCAL AND GLOBAL CONTROLLING FACTORS. MARINE MICROPALEONTOLOGY, 47(1-2), 117-141.

GROSHENY, D., BEAUDOIN, B., MOREL, L., & DESMARES, D. (2006). HIGH-RESOLUTION BIOTRATIGRAPHY AND CHEMOSTRATIGRAPHY OF THE CENOMANIAN/TURONIAN BOUNDARY EVENT IN THE VOCONTIAN BASIN, SOUTHEAST FRANCE. CRETACEOUS RESEARCH, 27(5), 629-640.

HANDY, M. R., SCHMID, S. M., BOUSQUET, R., KISSLING, E., & BERNOULLI, D. (2010). RECONCILING PLATE-TECTONIC RECONSTRUCTIONS OF ALPINE TETHYS WITH THE GEOLOGICAL–GEOPHYSICAL RECORD OF SPREADING AND SUBDUCTION IN THE ALPS. EARTH-SCIENCE REVIEWS, 102(3-4), 121-158.

HIBSCH, C. H. R. I. S. T. I. A. N., KANDEL, D. E. N. I. S., MONTENAT, C. H. R. I. S. T. I. A. N., & OTT D'ESTEVOU, P. (1992). EVENEMENTS TECTONIQUES CRETACES DANS LA PARTIE MERIDIONALE DU BASSIN SUBALPIN (MASSIF VENTOUX-LURE ET PARTIE ORIENTALE DE L'ARC DE CASTELLANE, SE FRANCE); IMPLICATIONS GEODYNAMIQUES. BULLETIN DE LA SOCIÉTÉ GÉOLOGIQUE DE FRANCE, 163(2), 147-158.

HUANG, Q. (1988). GEOMETRY AND TECTONIC SIGNIFICANCE OF ALBIAN SEDIMENTARY DYKES IN THE SISTERON AREA, SE FRANCE. JOURNAL OF STRUCTURAL GEOLOGY, 10(5), 453-462.

HUANG, Z., OGG, J. G., & GRADSTEIN, F. M. (1993). A QUANTITATIVE STUDY OF LOWER CRETACEOUS CYCLIC SEQUENCES FROM THE ATLANTIC OCEAN AND THE VOCONTIAN BASIN (SE FRANCE). PALEOCEANOGRAPHY, 8(2), 275-291.

KEPPIE, D. F. (2015). HOW THE CLOSURE OF PALEO-TETHYS AND TETHYS OCEANS CONTROLLED THE EARLY BREAKUP OF PANGAEA. GEOLOGY, 43(4), 335-338.

LAUBSCHER, H. P. (1975). PLATE BOUNDARIES AND MICROPLATES IN ALPINE HISTORY. AMERICAN JOURNAL OF SCIENCE, 275(8), 865-876.

LEMOINE, M. (1983). RIFTING AND EARLY DRIFTING-MESOZOIC CENTRAL ATLANTIC AND LIGURIAN TETHYS. INITIAL REPORTS OF THE DEEP SEA DRILLING PROJECT, 76(NOV), 885-895.

LEMOINE, M., BAS, T., ARNAUD-VANNEAU, A., ARNAUD, H., DUMONT, T., GIDON, M., & TRICART, P. (1986). THE CONTINENTAL MARGIN OF THE MESOZOIC TETHYS IN THE WESTERN ALPS. MARINE AND PETROLEUM GEOLOGY, 3(3), 179-199.

MATTIOLI, E., PITTET, B., RIQUIER, L., & GROSSI, V. (2014). THE MID-VALANGINIAN WEISSERT EVENT AS RECORDED BY CALCAREOUS NANNOPLANKTON IN THE VOCONTIAN BASIN. PALAEOGEOGRAPHY, PALAEOCLIMATOLOGY, PALAEOECOLOGY, 414, 472-485.

RAVIER, E., GUIRAUD, M., GUILLIEN, A., VENNIN, E., BUONCRISTIANI, J. F., & PORTIER, E. (2015). MICRO-TO MACRO-SCALE INTERNAL STRUCTURES, DIAGENESIS AND PETROPHYSICAL EVOLUTION OF INJECTITE NETWORKS IN THE VOCONTIAN BASIN (FRANCE): IMPLICATIONS FOR FLUID FLOW. MARINE AND PETROLEUM GEOLOGY, 64, 125-151.

ROURE, F., BRUN, J. P., COLLETTA, B., & VAN DEN DRIESSCHE, J. (1992). GEOMETRY AND KINEMATICS OF EXTENSIONAL STRUCTURES IN THE ALPINE FORELAND BASIN OF SOUTHEASTERN FRANCE. JOURNAL OF STRUCTURAL GEOLOGY, 14(5), 503-519.

ROURE, F., BRUN, J. P., COLLETTA, B., & VIALLY, R. (1994). MULTIPHASE EXTENSIONAL STRUCTURES, FAULT REACTIVATION, AND PETROLEUM PLAYS IN THE ALPINE FORELAND BASIN OF SOUTHEASTERN FRANCE. IN HYDROCARBON AND PETROLEUM GEOLOGY OF FRANCE (PP. 245-268). SPRINGER, BERLIN, HEIDELBERG.

SAVARY, B., & FERRY, S. (2004). GEOMETRY AND PETROPHYSICAL PARAMETERS OF A CALCARENITIC TURBIDITE LOBE (BARREMIAN-APTIAN, PAS-DE-LA-CLUSE, FRANCE). SEDIMENTARY GEOLOGY, 168(3-4), 281-304. CLAVEL, B., CONRAD, M. A., BUSNARDO, R., CHAROLLAIS, J., & GRANIER, B. (2013). MAPPING THE RISE AND DEMISE OF URGONIAN PLATFORMS (LATE HAUTERIVIAN-EARLY APTIAN) IN SOUTHEASTERN FRANCE AND THE SWISS JURA. CRETACEOUS RESEARCH, 39, 29-46.

STAMPFLI, G. M. (1994). EXOTIC TERRAINS IN THE ALPS-A SOLUTION FOR A SINGLE JURASSIC OCEAN. SCHWEIZERISCHE MINERALOGISCHE UND PETROGRAPHISCHE MITTEILUNGEN, 74, 449-452.

TAKASHIMA, R., NISHI, H., HAYASHI, K., OKADA, H., KAWAHATA, H., YAMANAKA, T., & MAMPUKU, M. (2009). LITHO-, BIO-AND CHEMOSTRATIGRAPHY ACROSS THE CENOMANIAN/TURONIAN BOUNDARY (OAE 2) IN THE VOCONTIAN BASIN OF SOUTHEASTERN FRANCE. PALAEOGEOGRAPHY, PALAEOCLIMATOLOGY, PALAEOECOLOGY, 273(1-2), 61-74.

VILLEGER, M. A. R. C., & ANDRIEUX, J. E. A. N. (1987). PHASES TECTONIQUES POST-EOCÈNES ET STRUCTURATION POLYPHASÉE DU PANNEAU DE COUVERTURE NORD PROVENÇAL (ALPES EXTERNES MÉRIDIONALES). BULLETIN DE LA SOCIÉTÉ GÉOLOGIQUE DE FRANCE, 3(1), 147-156.

WILPSHAAR, M., LEEREVELD, H., & VISSCHER, H. (1997). EARLY CRETACEOUS SEDIMENTARY AND TECTONIC DEVELOPMENT OF THE DAUPHINOIS BASIN (SE FRANCE). CRETACEOUS RESEARCH, 18(3), 457-468.

Appendix A: Bachelor's fieldwork data

Pommerol 2014

	Coordinates (XY in m)					
Image	Top	Bottom	Left	Right	Distance N-S [m]	Distance W-E [m]
Geological Map	4927000	4921000	690000	698000	-	-
Cross Section 1	4927000	4921000	695376.7	695376.7	6000	0
Cross Section 2	4927000	4921000	692000	692000	6000	0
Cross Section 3	4927000	4925585	690000	692557.6	1414.6	2557.6

Geological map

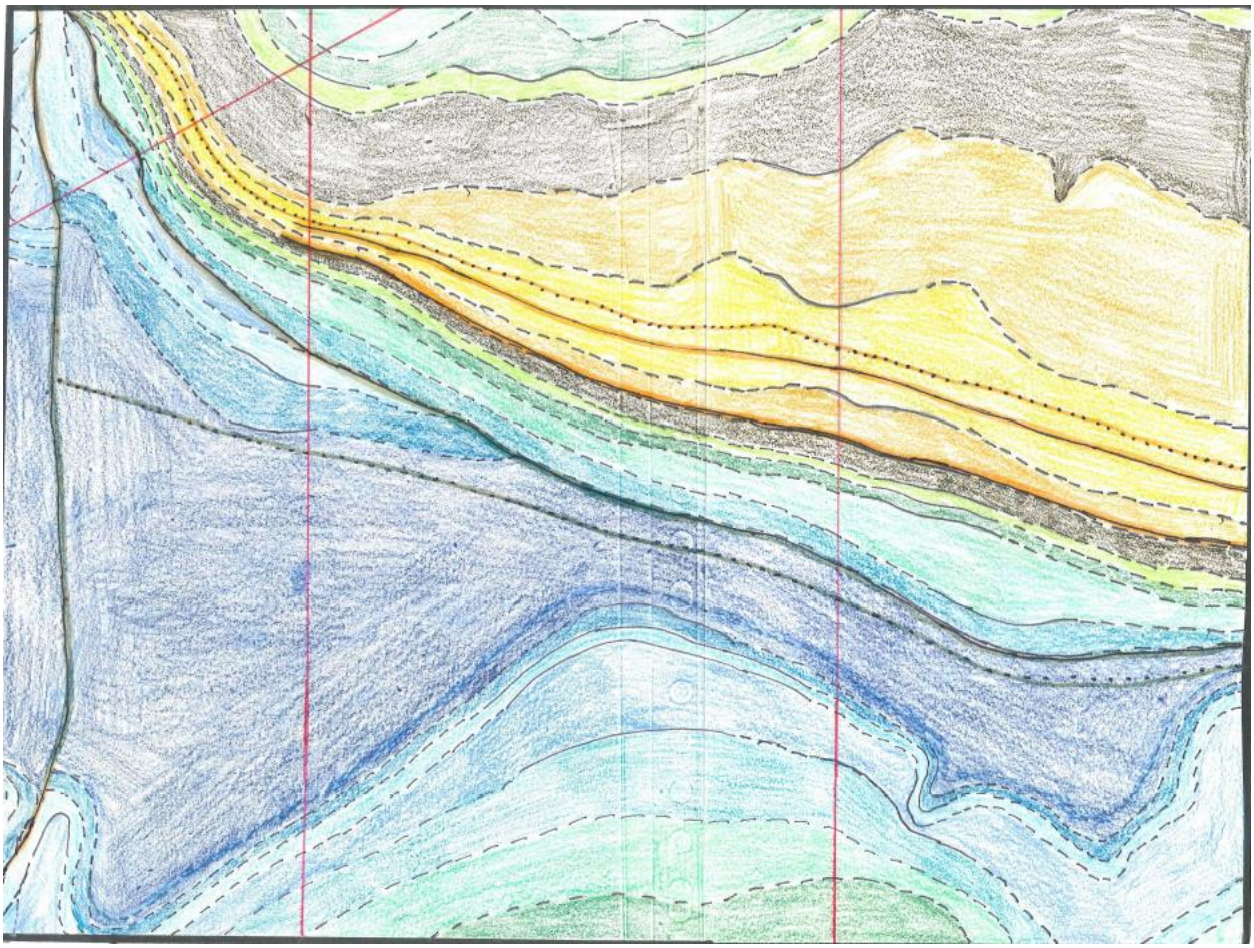

Tectonic map

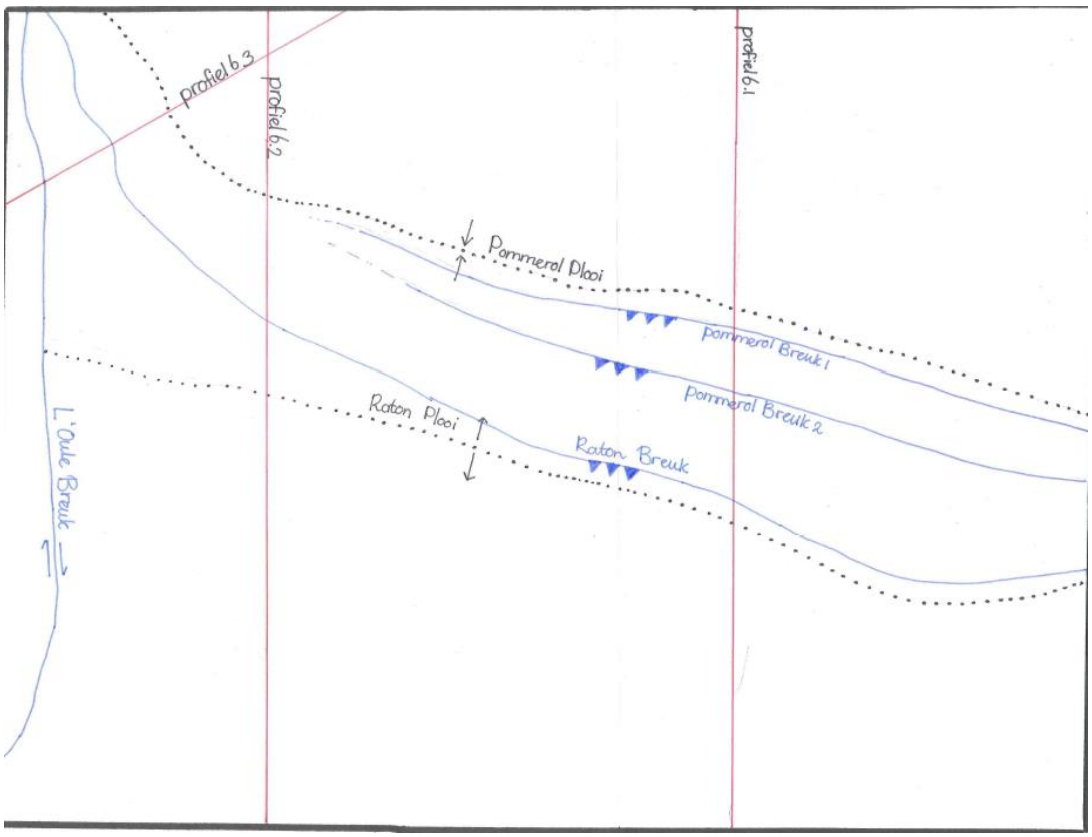

Cross-section 1

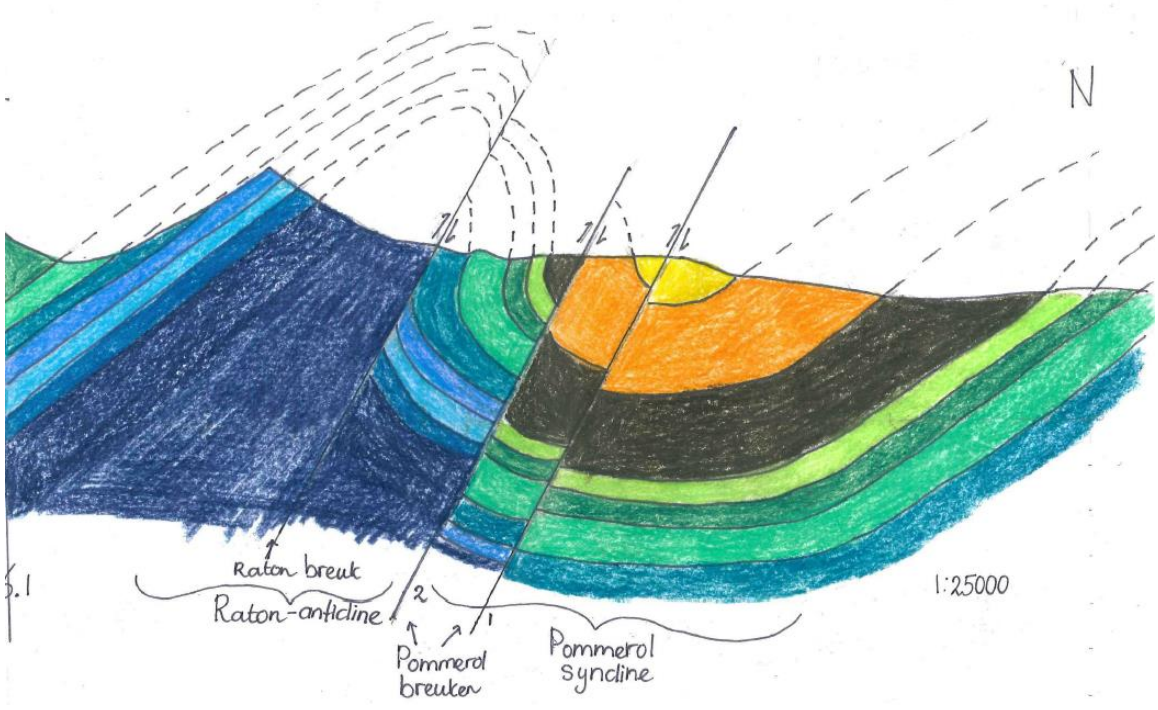

Cross-section 2

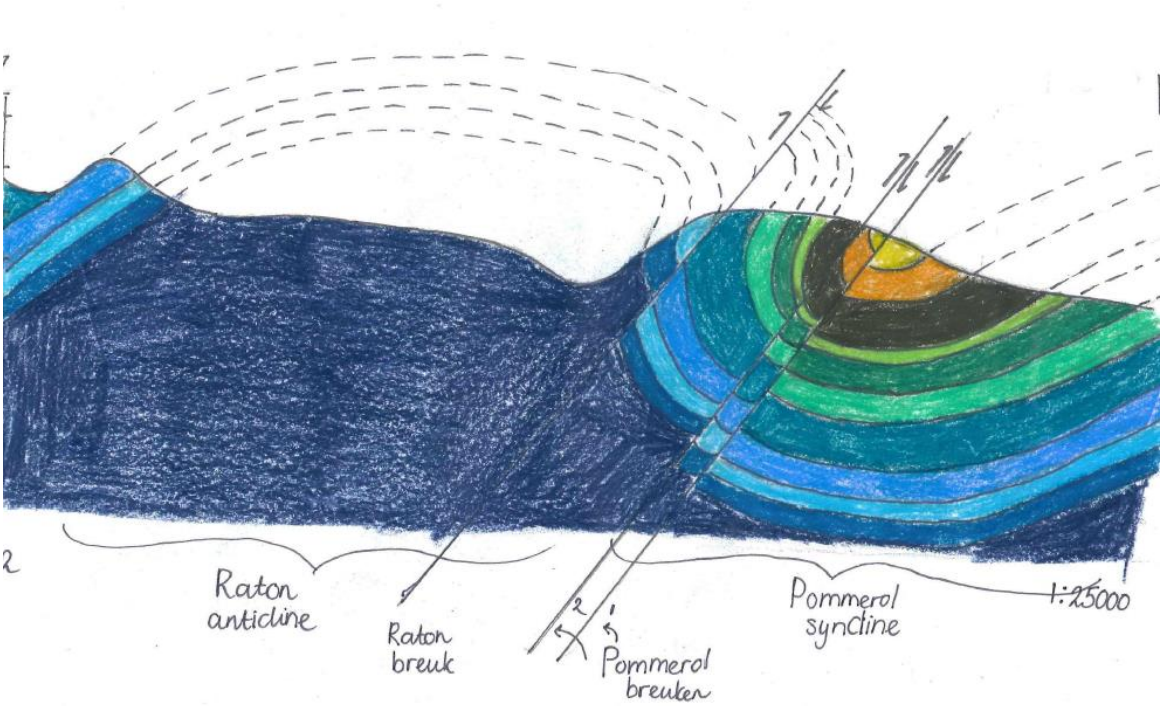

Cross-section 3

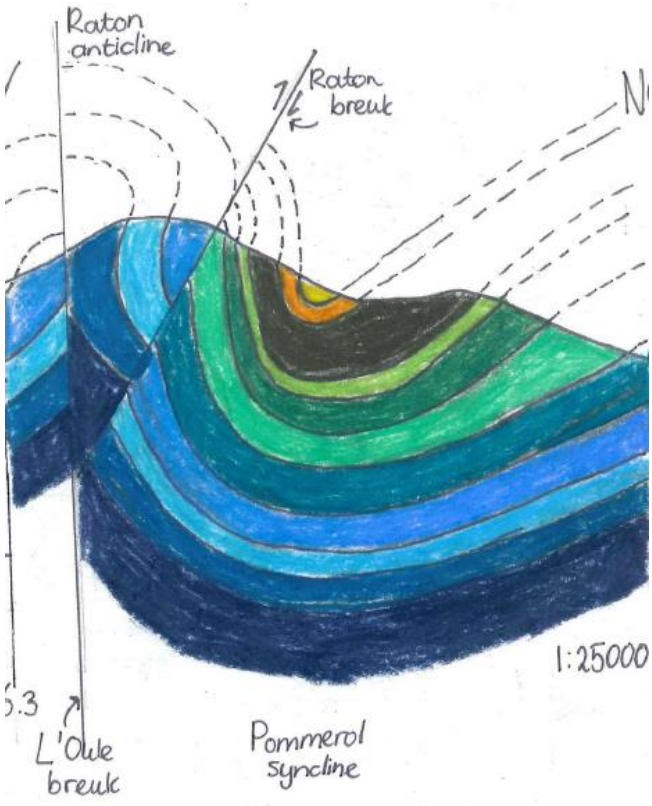

La Charce 2008

	Coordinates (XY in m)					
Image	**Top**	**Bottom**	**Left**	**Right**	**Distance N-S [m]**	**Distance W-E [m]**
Geological Map	4931150	4922175	693000	699000	-	-
Cross Section AA'	4931150	4922175	693000	693000	8975	0
Cross Section BB'	4931150	4922175	693979.8	693979.8	8975	0
Cross Section CC'	4931150	4926575	695000	695000	4575	0
Cross Section DD'	4931150	4922175	695987.5	695987.5	8975	0
Cross Section EE'	4931150	4926575	697000	697000	4575	0
Cross Section FF'	4931150	4922175	698000	698000	8975	0
Cross Section AG	4931150	4931150	693000	699000	0	6000
Cross Section A'G'	4922175	4922175	693000	699000	0	6000
Cross Section YY'	4923166.9	4923166.9	693000	699000	0	6000
Cross Section XX'	4930163.4	4930163.4	693000	699000	0	6000

Geological map

Cross-section AA'

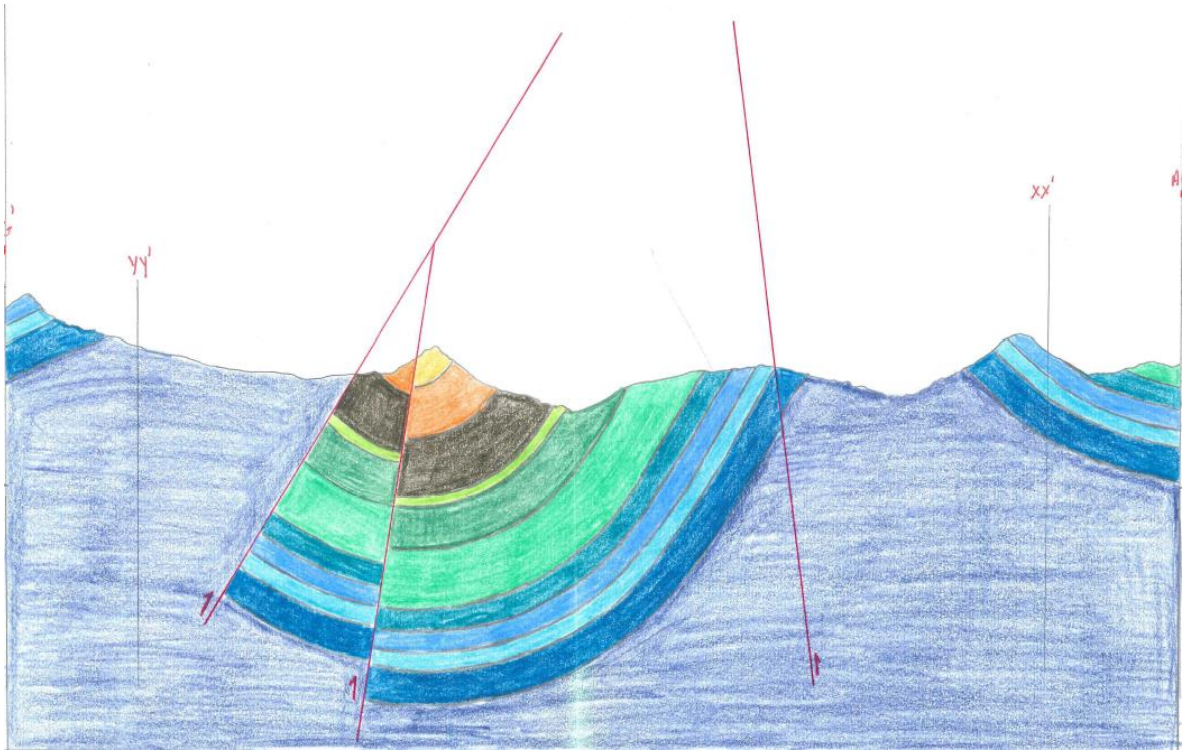

Cross-section BB'

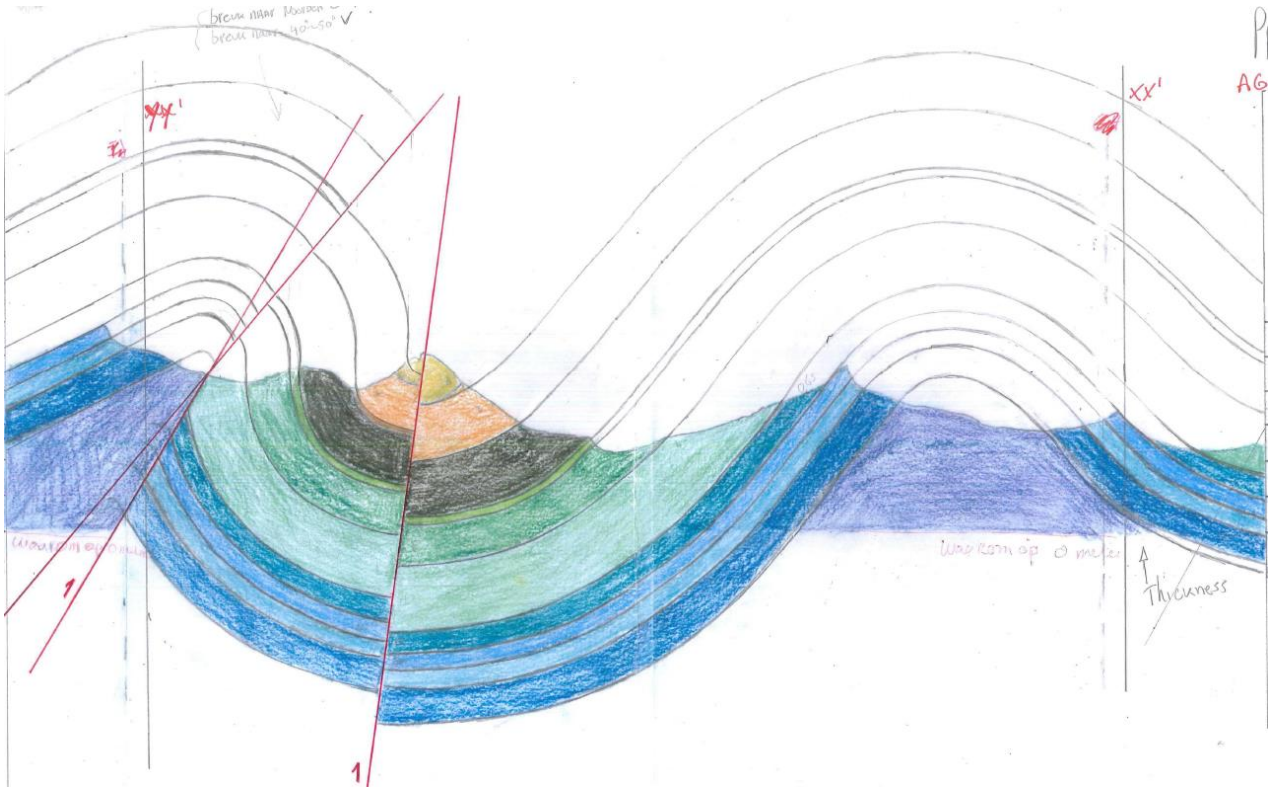

Cross-section CC'

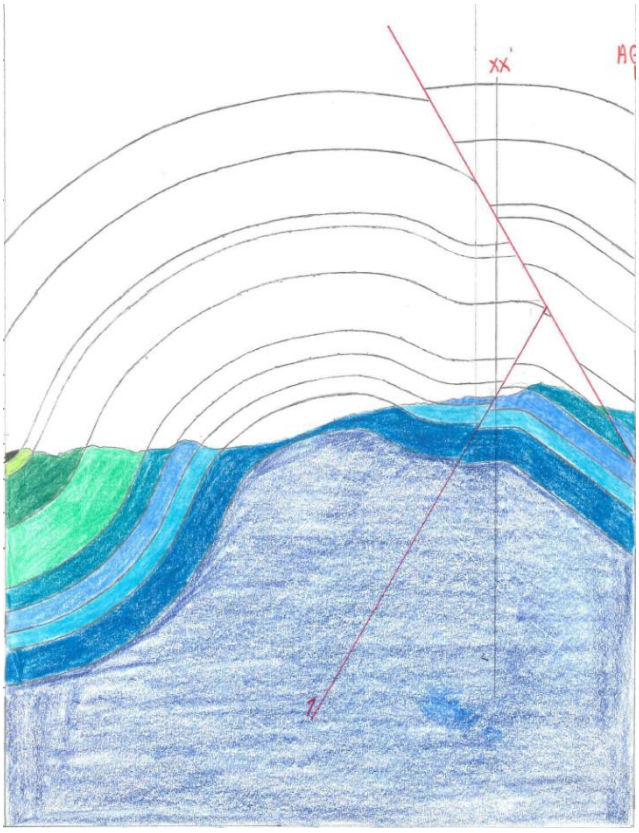

Cross-section DD'

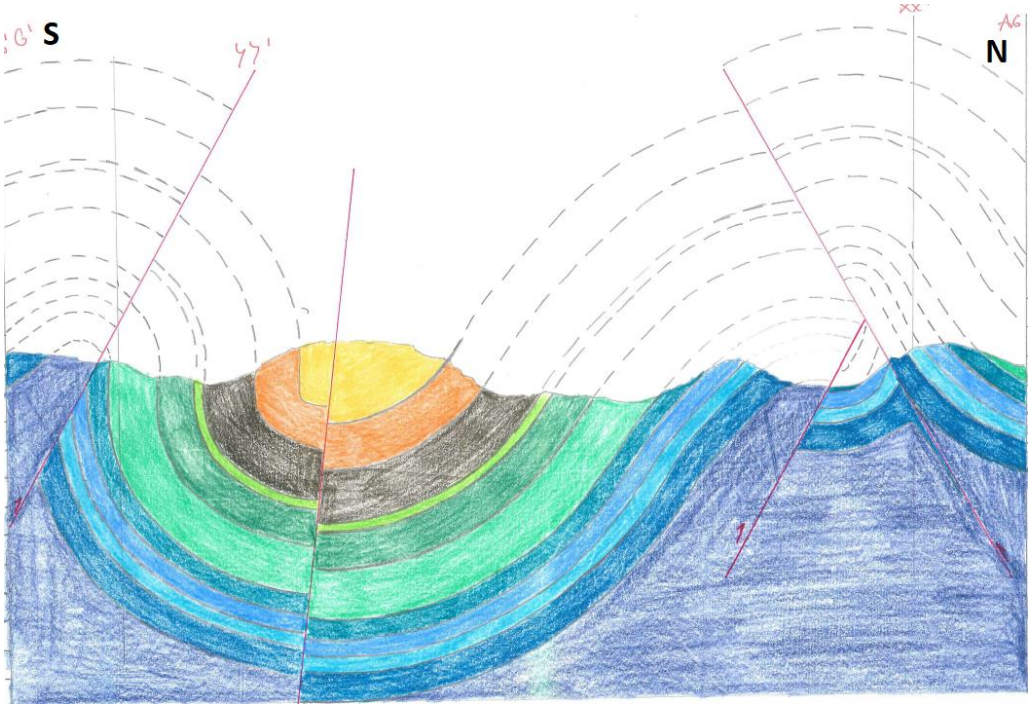

Cross-section EE'

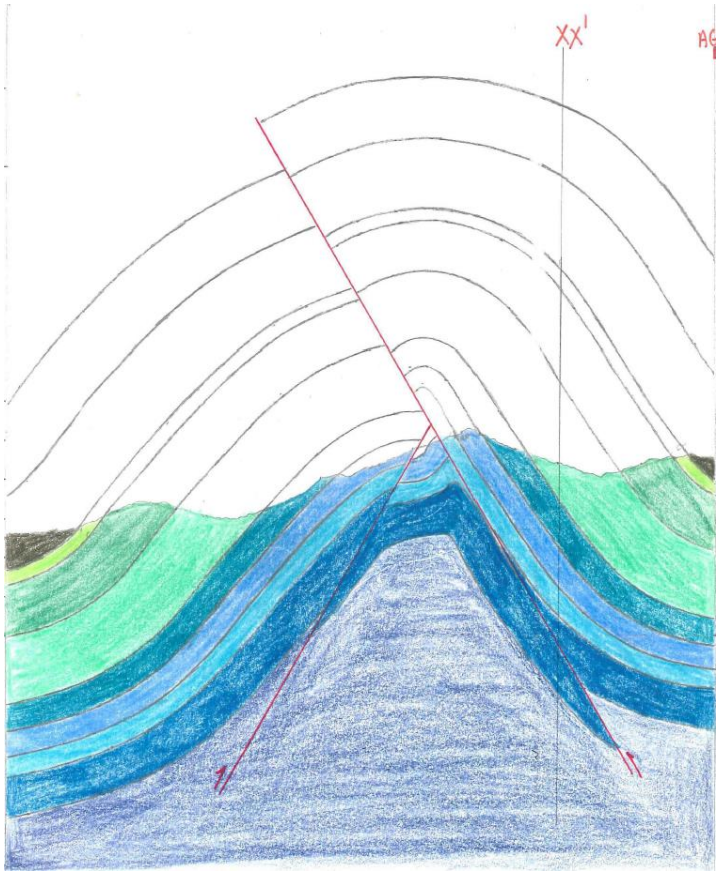

Cross-section FF'

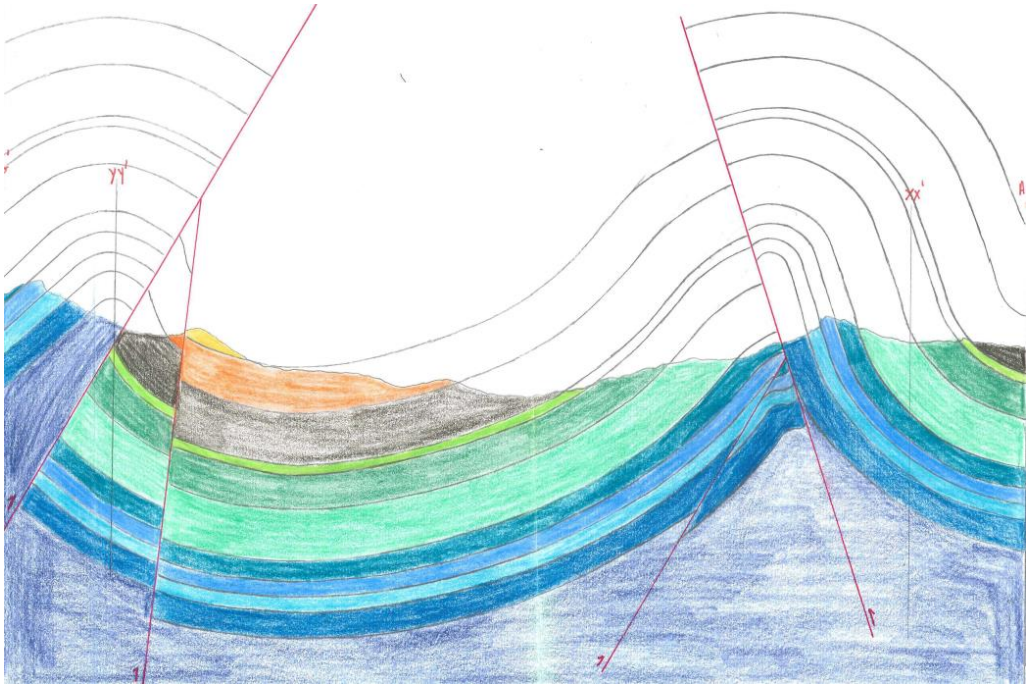

Cross-section AG

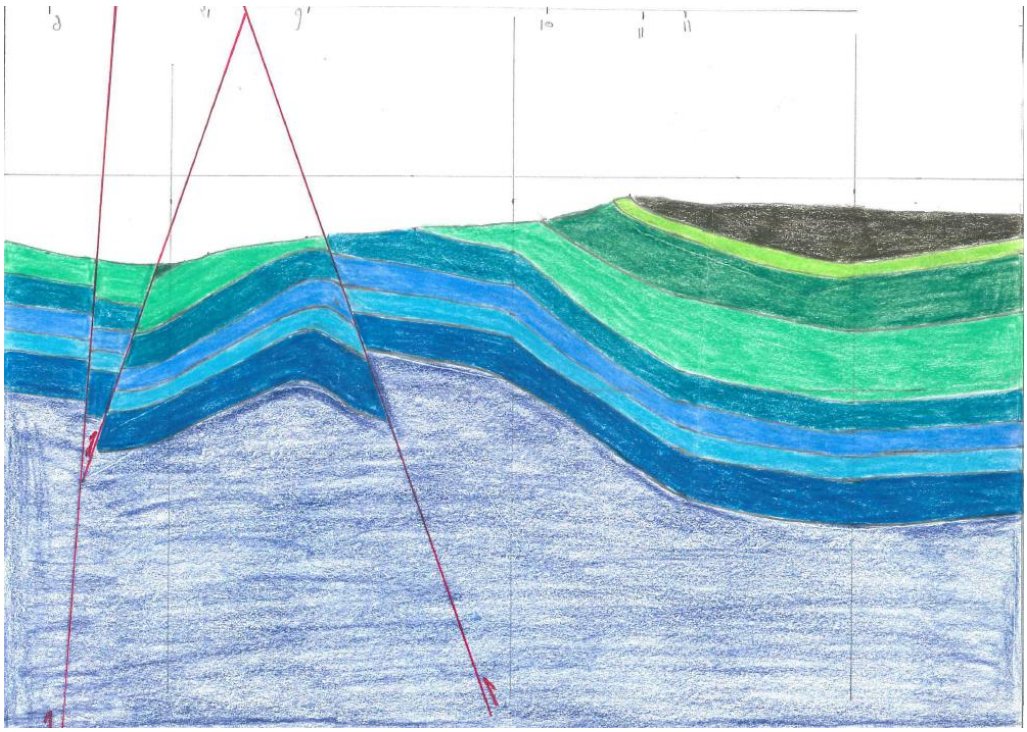

Cross-section A'G'

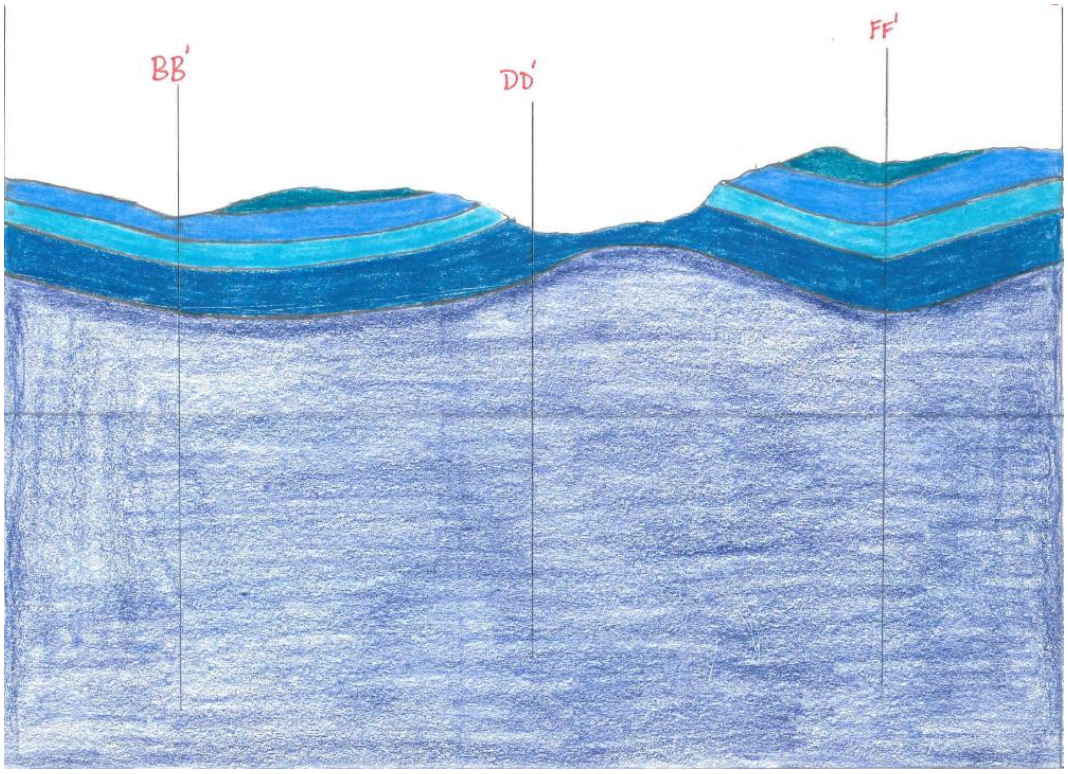

Cross-section YY'

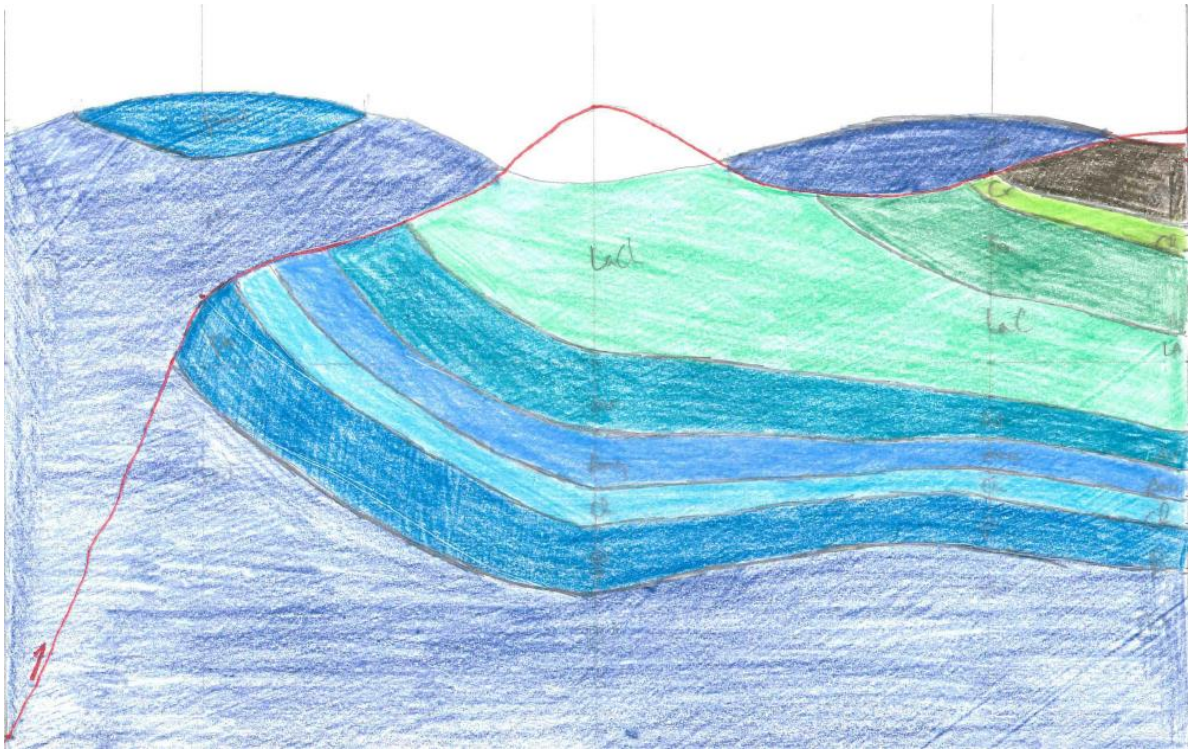

Cross-section XX'

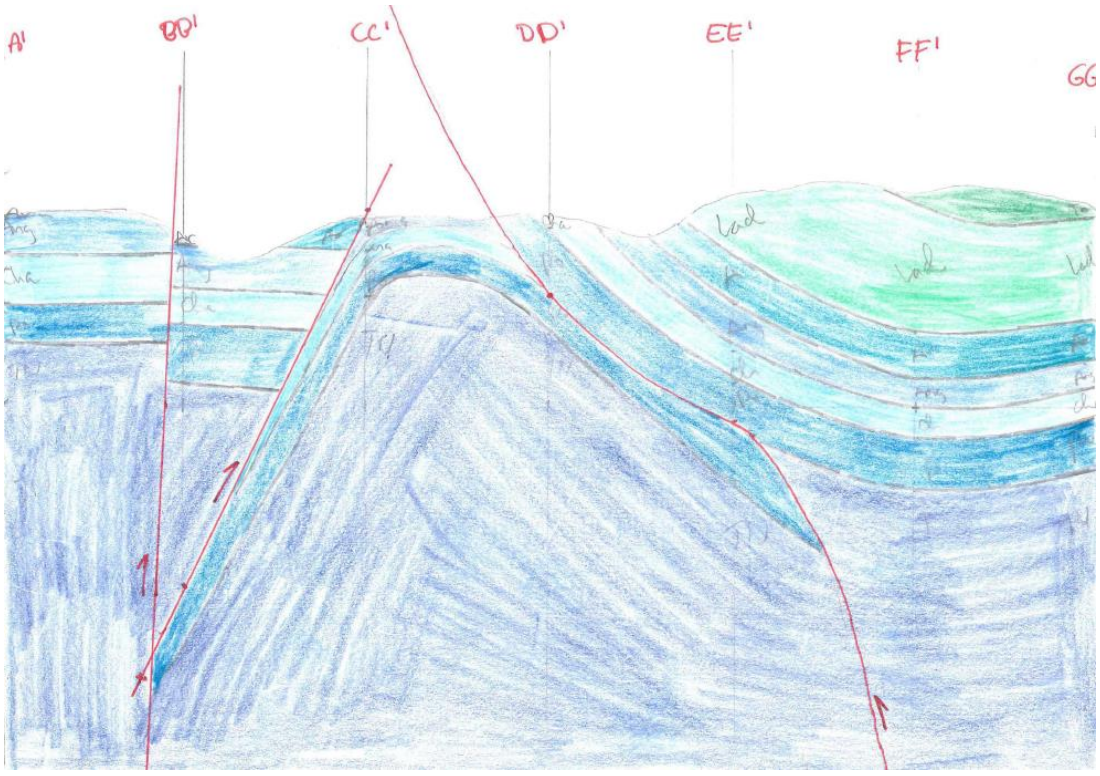

Villeperdrix 2009

	Coordinates (XY in m)					
Image	**Top**	**Bottom**	**Left**	**Right**	**Distance N-S [m]**	**Distance W-E [m]**
Geological Map	4930000	4921000	681000	687000	-	-
Cross Section 2	4930000	4921000	682000	682000	9000	0
Cross Section 3	4930000	4921000	684000	684000	9000	0
Cross Section 4	4930000	4921000	686000	686000	9000	0

Geological map

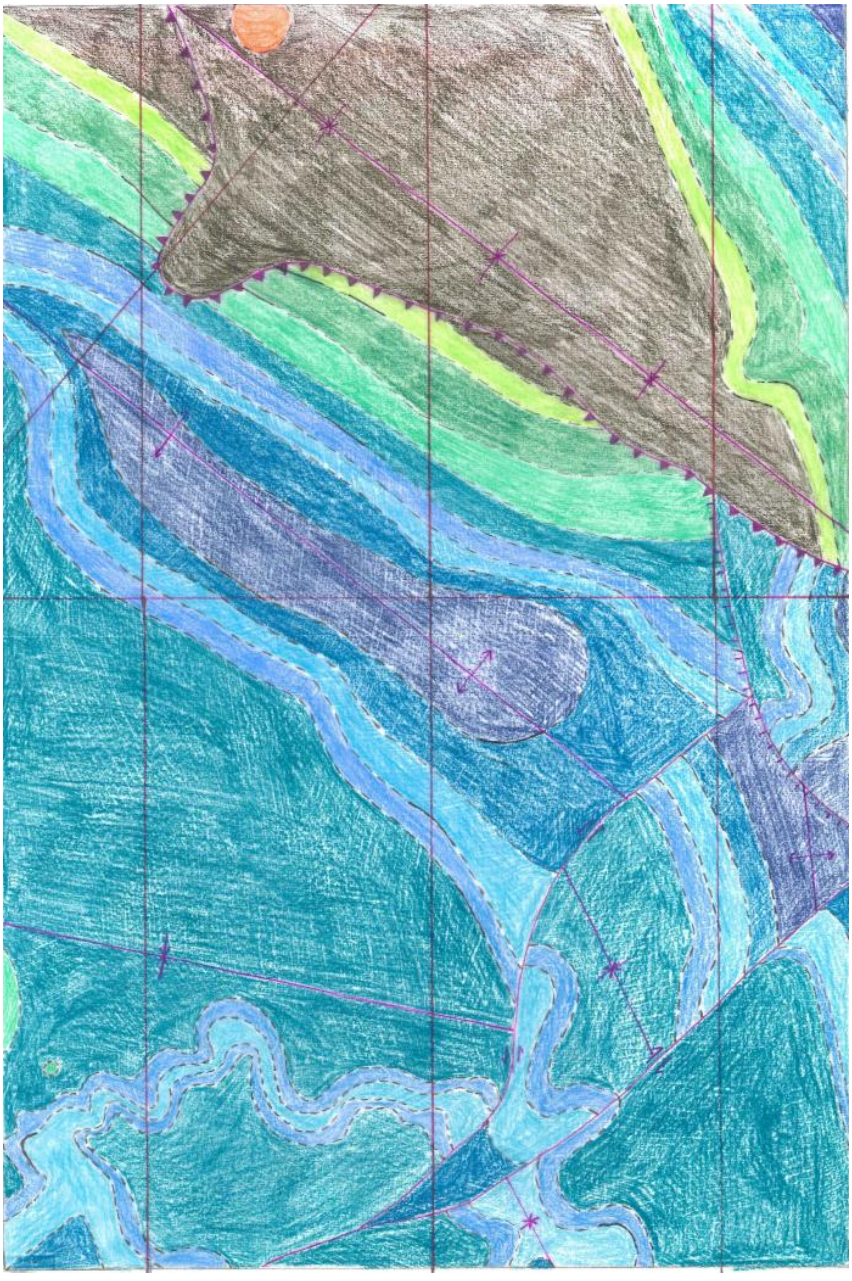

Tectonic map

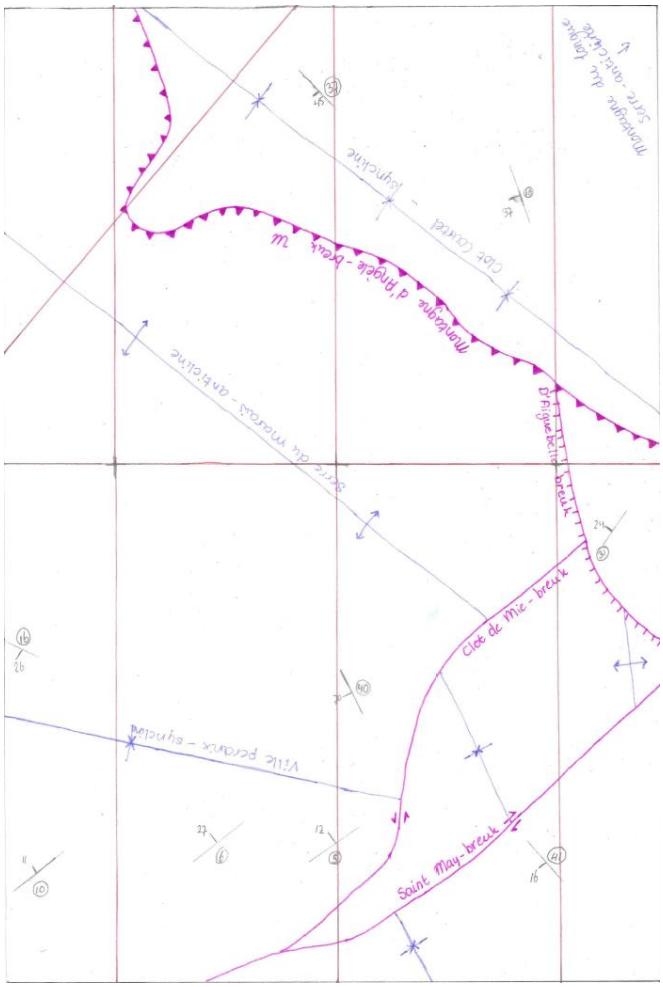

Cross-section 2

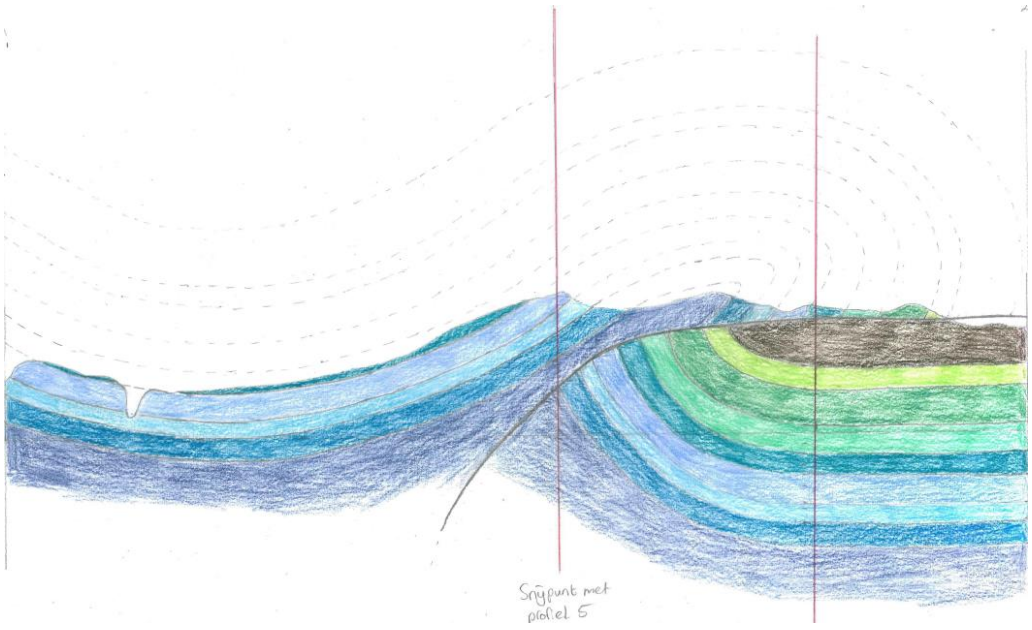

Cross-section 3

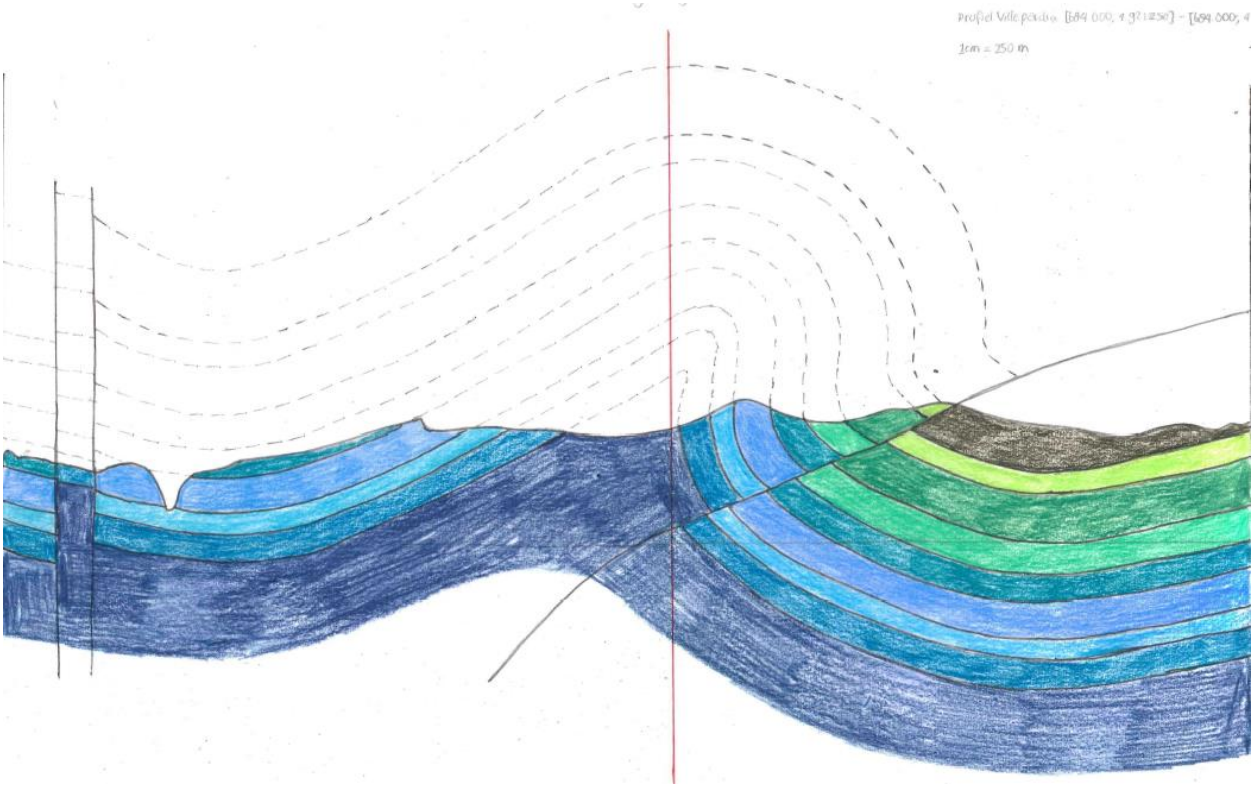

Cross-section 4

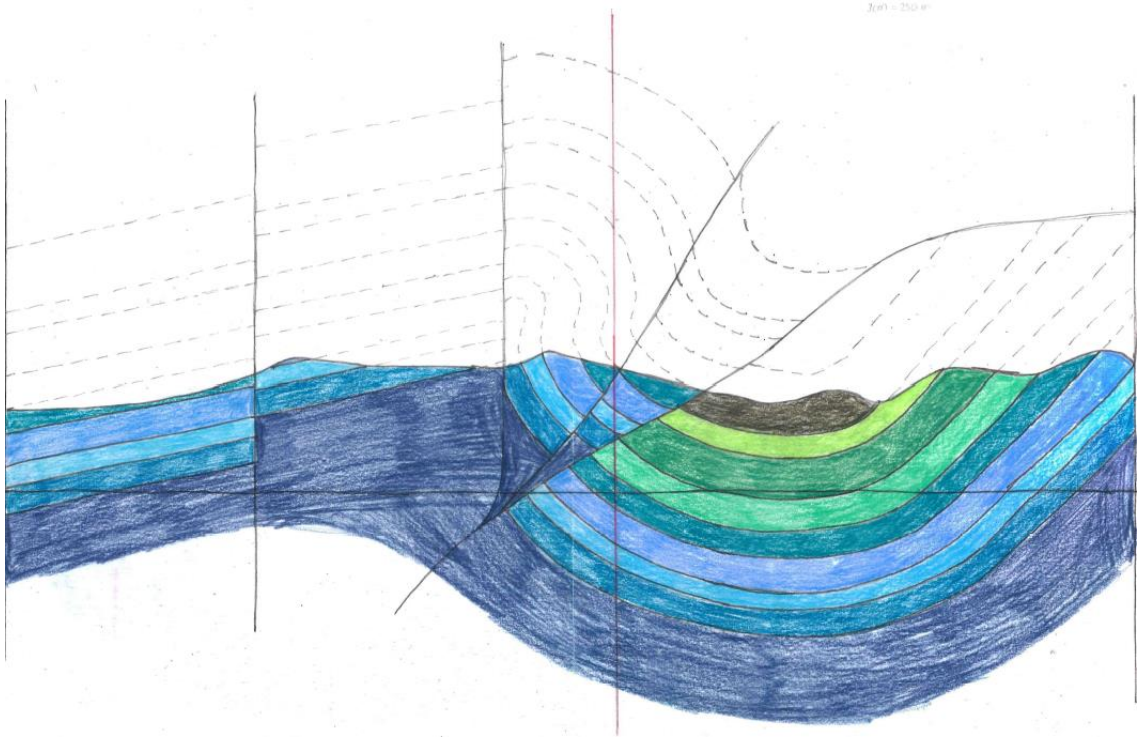

La Motte 2014

	Coordinates (XY in m)					
Image	**Top**	**Bottom**	**Left**	**Right**	**Distance N-S [m]**	**Distance W-E [m]**
Geological Map	4931000	4925000	685000	693000	6000	8000
Cross Section 1	4931000	4927049	685000	692270	3951	7270
Cross Section 2	4925858	4925595	685000	693000	263	8000
Cross Section 3	4931000	4925000	691000	691000	6000	0

Geological map

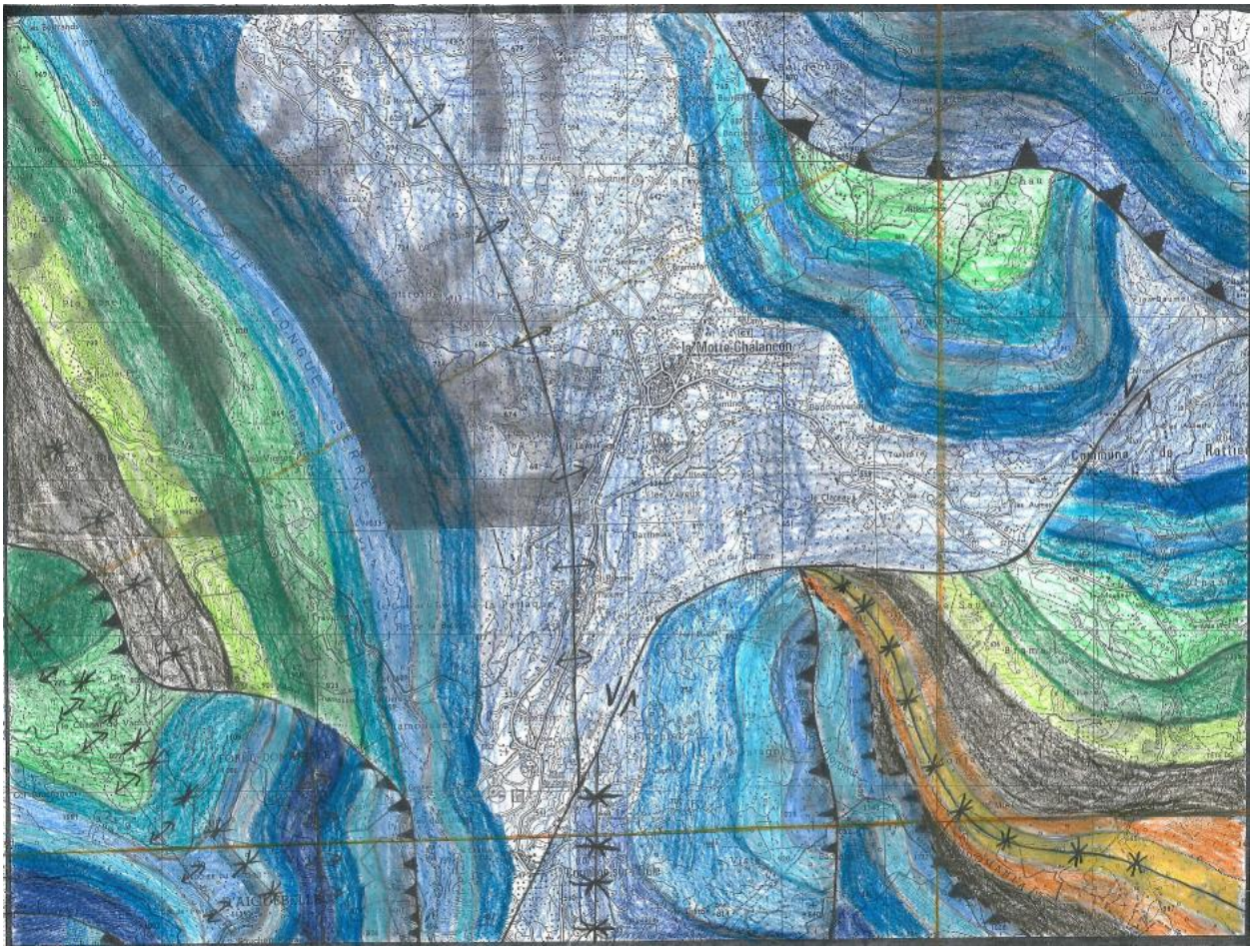

Cross-section 1

Cross-section 2

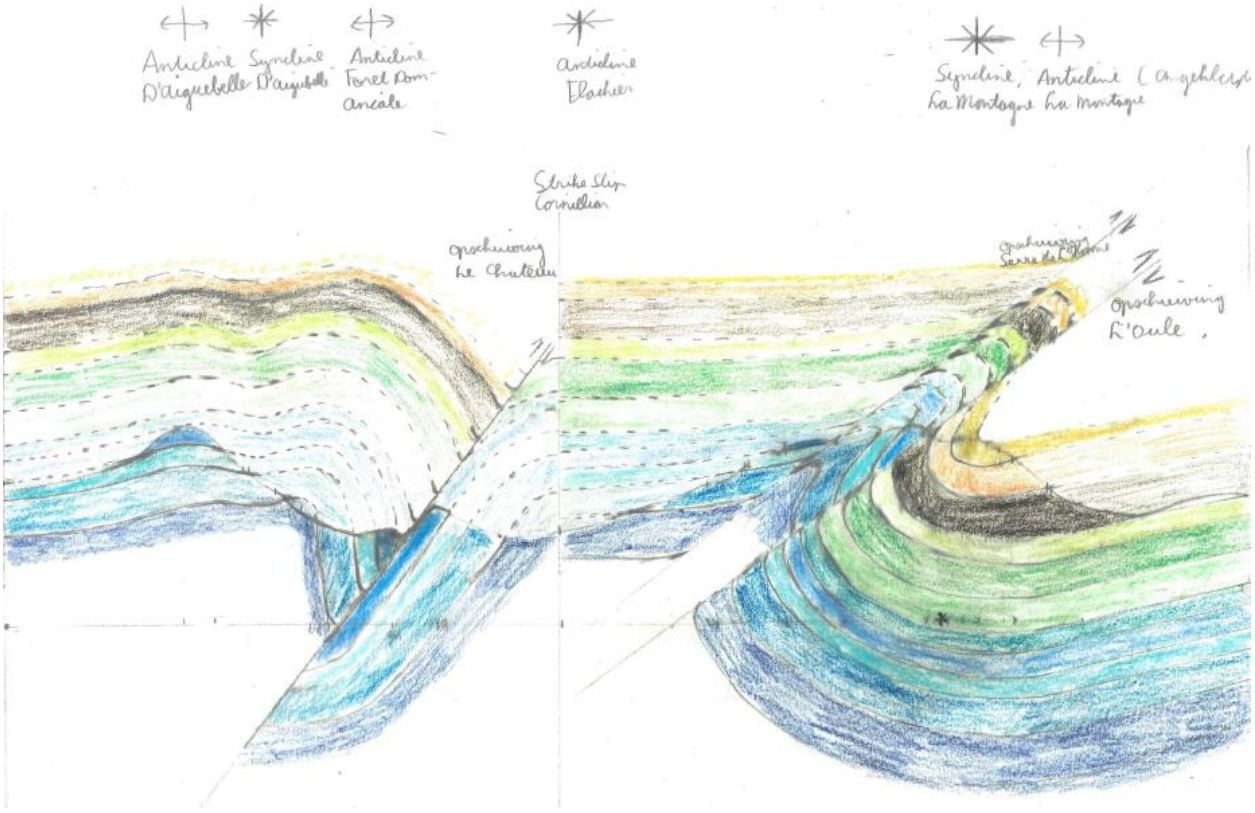

Cross-section 3

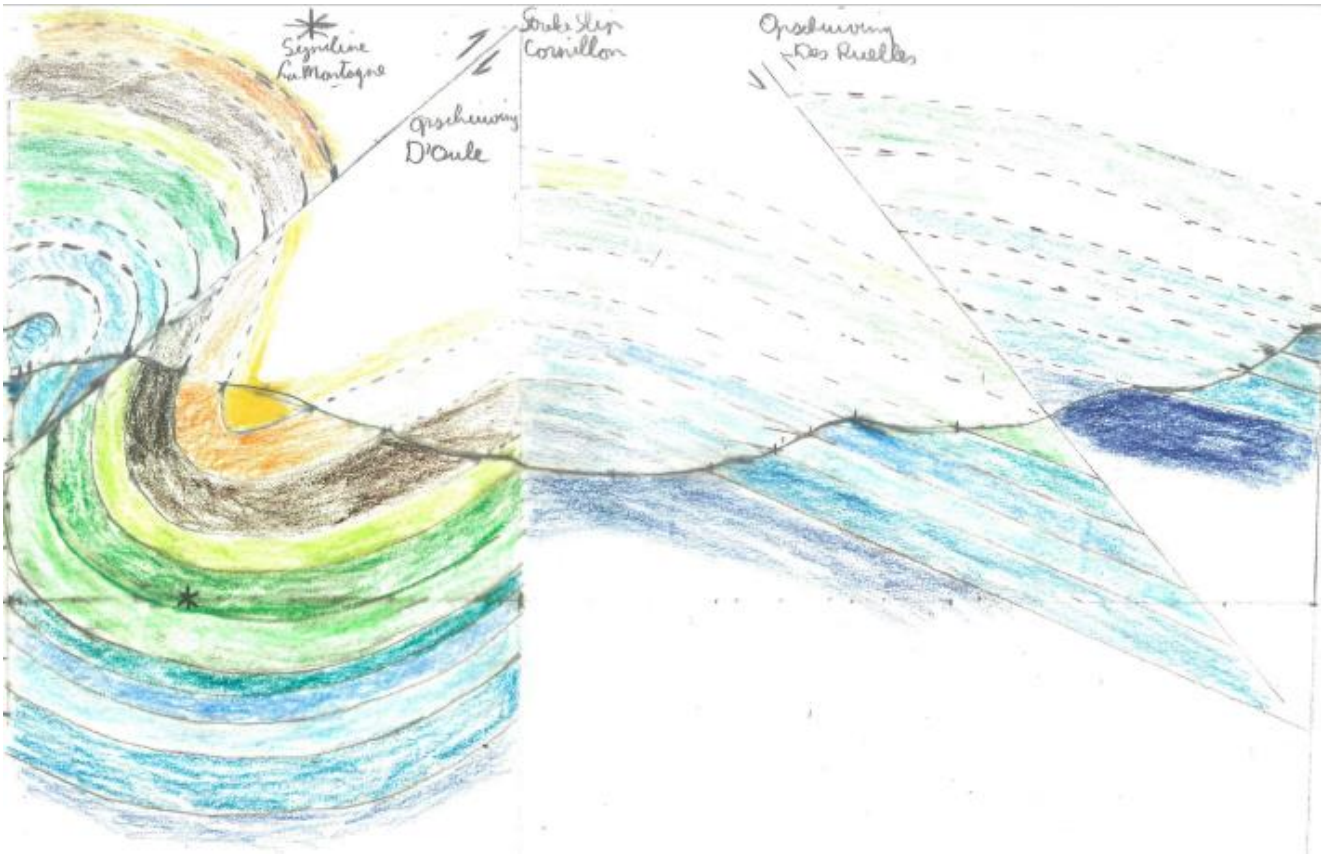

St Dizier 2017

	Coordinates (XY in m)					
Image	**Top**	**Bottom**	**Left**	**Right**	**Distance N-S [m]**	**Distance W-E [m]**
Geological Map	4935000	4927000	693000	699000	-	-
Cross Section AB	4935000	4927000	693000	693000	8000	0
Cross Section GH	4935000	4927000	694000	694000	8000	0
Cross Section IJ	4935000	4927000	696000	696000	8000	0
Cross Section EF	4935000	4927000	698000	698000	8000	0
Cross Section KL	4930000	4930000	693000	699000	0	6000

Geological map

Cross-section AB

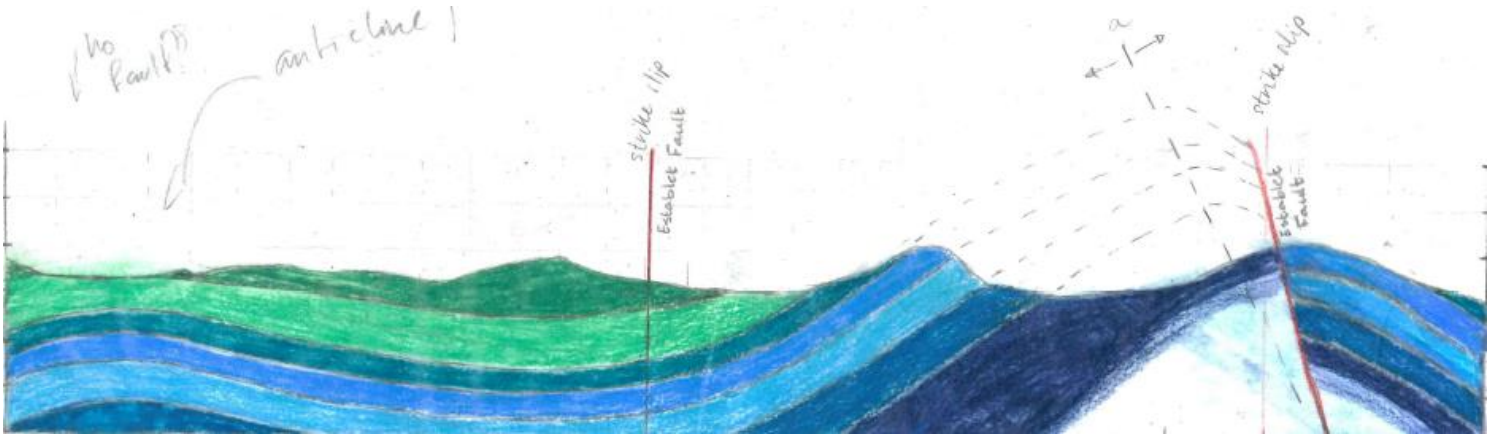

Cross-section GH

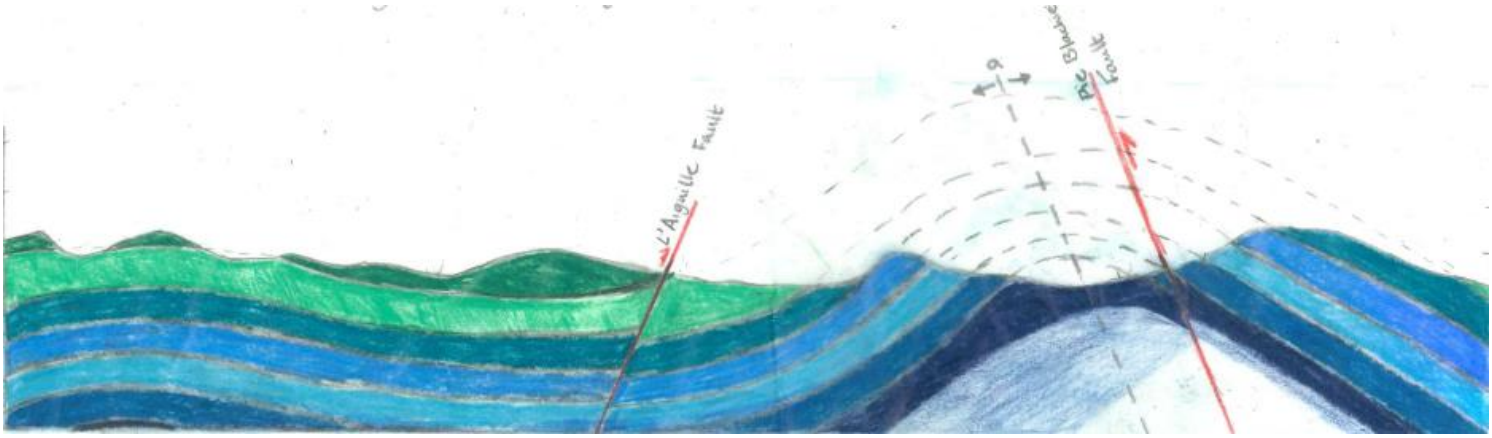

Cross-section IJ

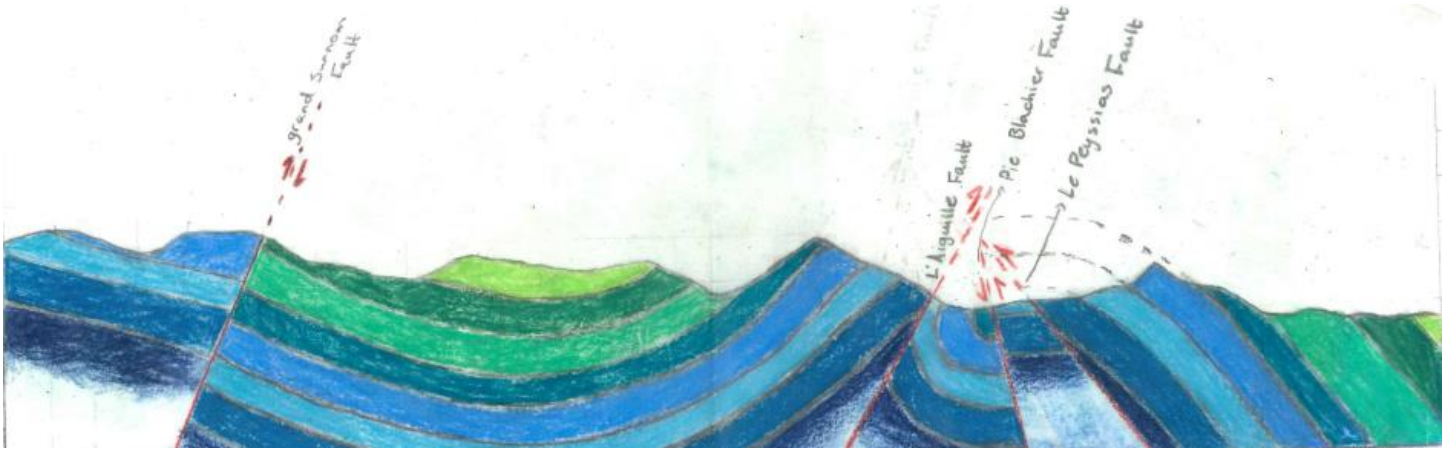

Cross-section EF

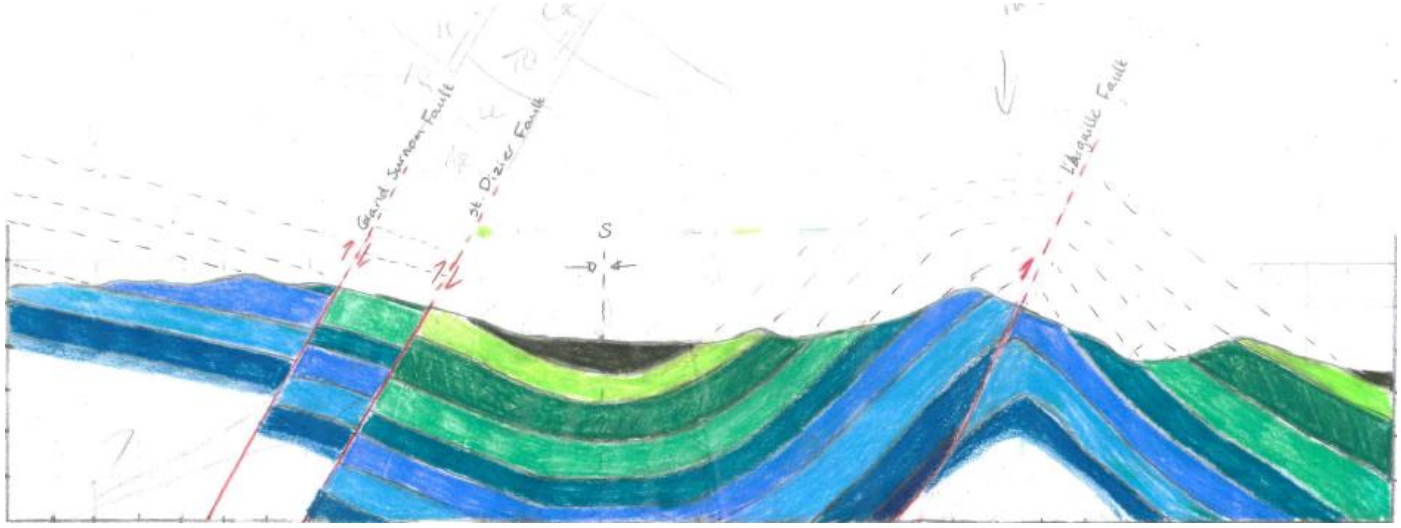

Cross-section KL

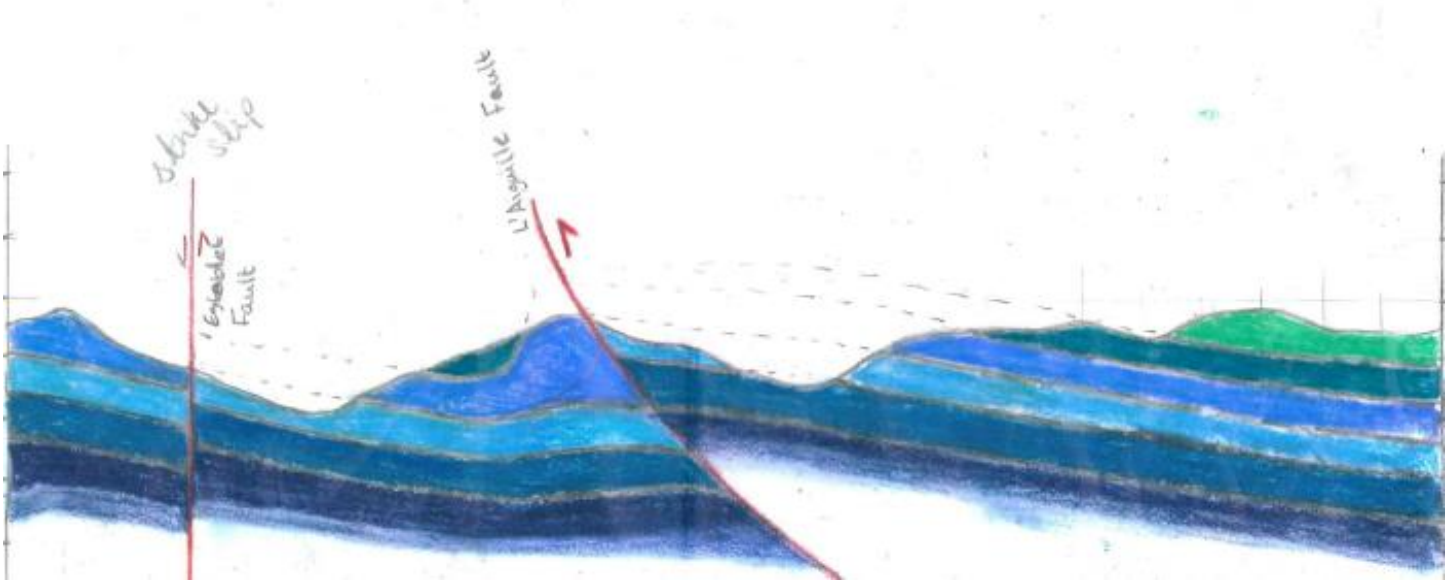

St May 2017

	Coordinates (XY in m)					
Image	**Top**	**Bottom**	**Left**	**Right**	**Distance N-S [m]**	**Distance W-E [m]**
Geological Map	4923000	4917000	682000	690000	-	-
Cross Section 1	4922000	4922000	682000	690000	0	8000
Cross Section 2	4920000	4920000	682000	690000	0	8000
Cross Section 3	4918000	4918000	682000	690000	0	8000
Cross Section 4	4917259	4917259	682000	690000	0	8000
Cross Section 5	4923000	4917000	689230	689230	6000	0
Cross Section 6	4921855	4917000	686500	690000	4855	3500
Cross Section 7	4923000	4917000	686000	686000	6000	0
Cross Section 8	4923000	4917000	683000	683000	6000	0

Geological map

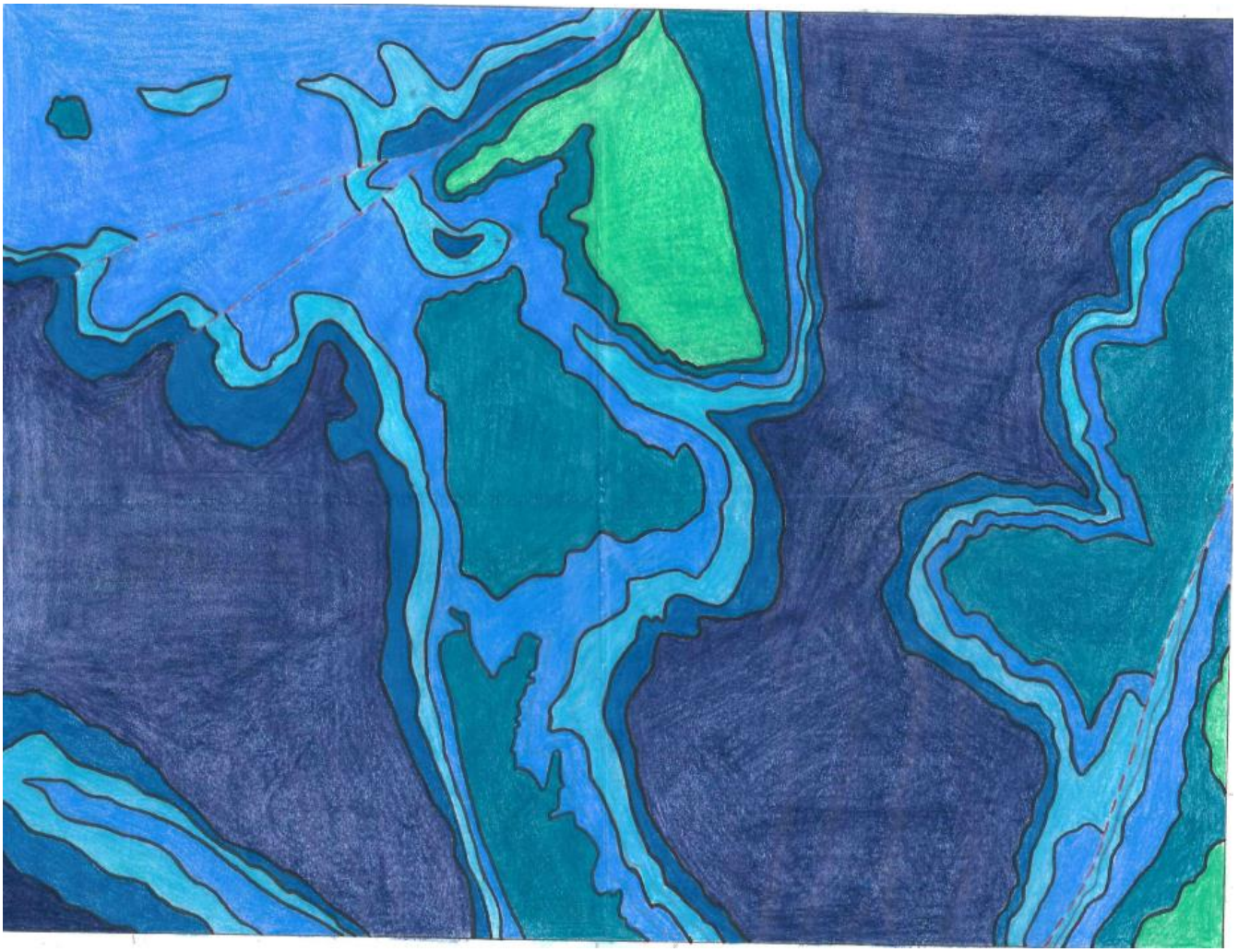

Tectonic map

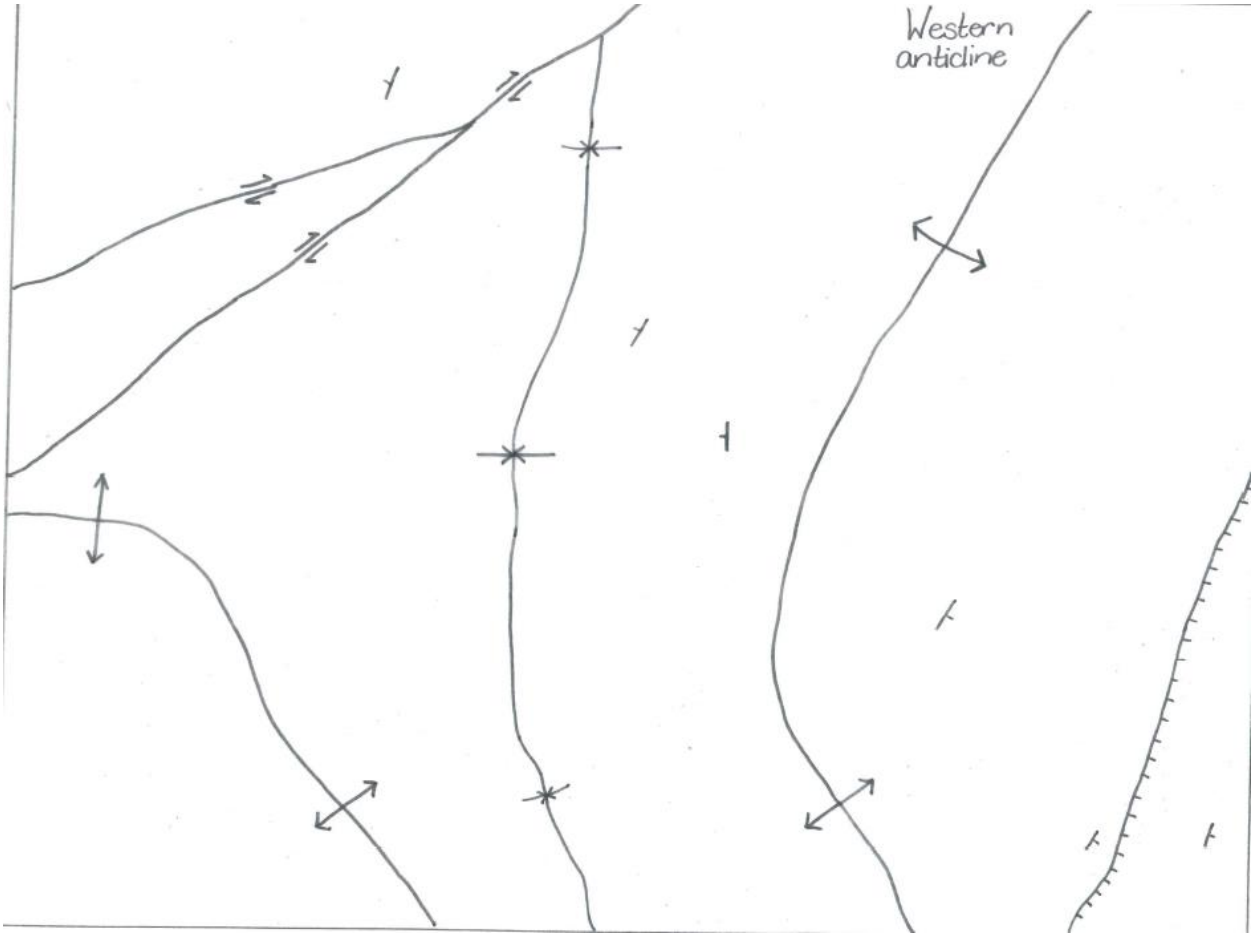

Cross-section 1

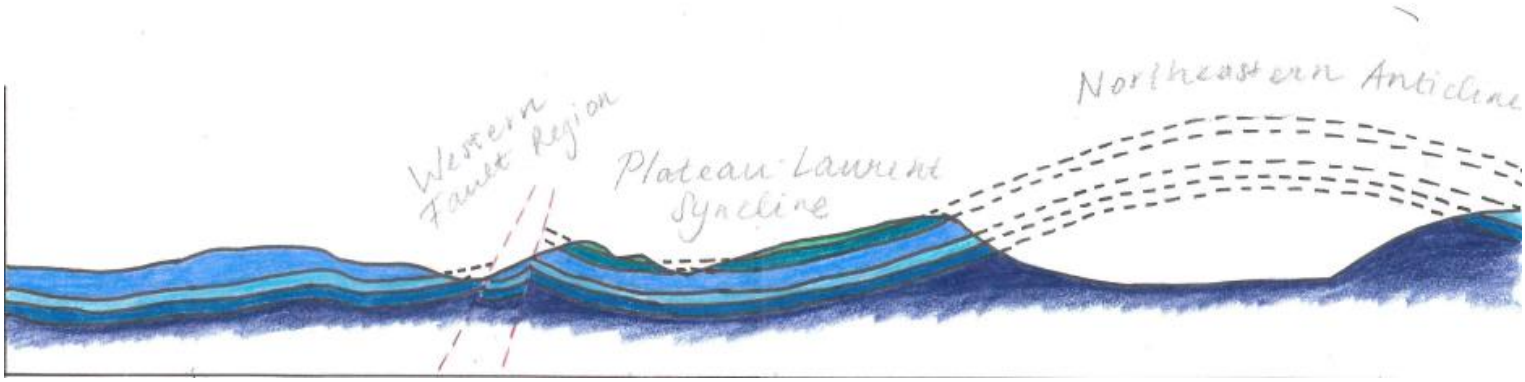

Cross-section 2

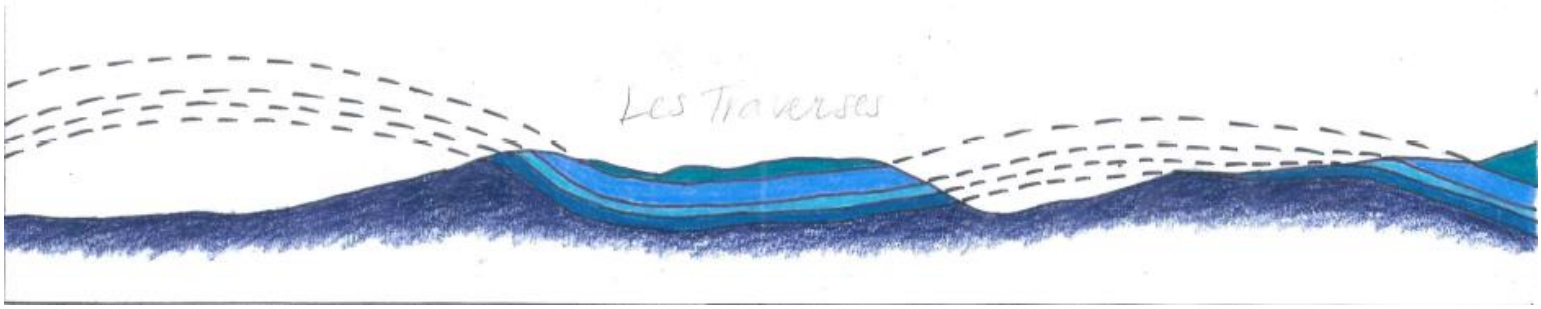

Cross-section 3

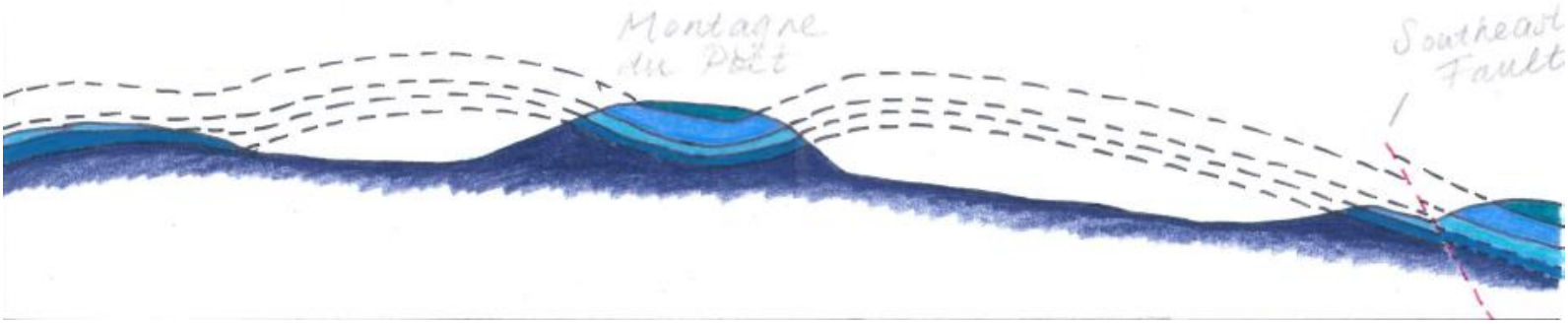

Cross-section 4

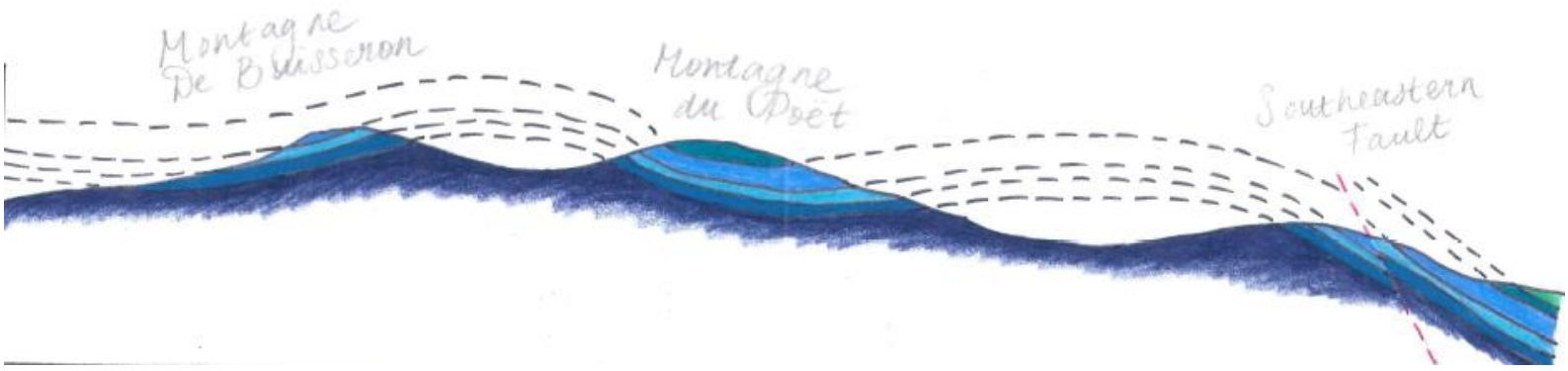

Cross-section 5

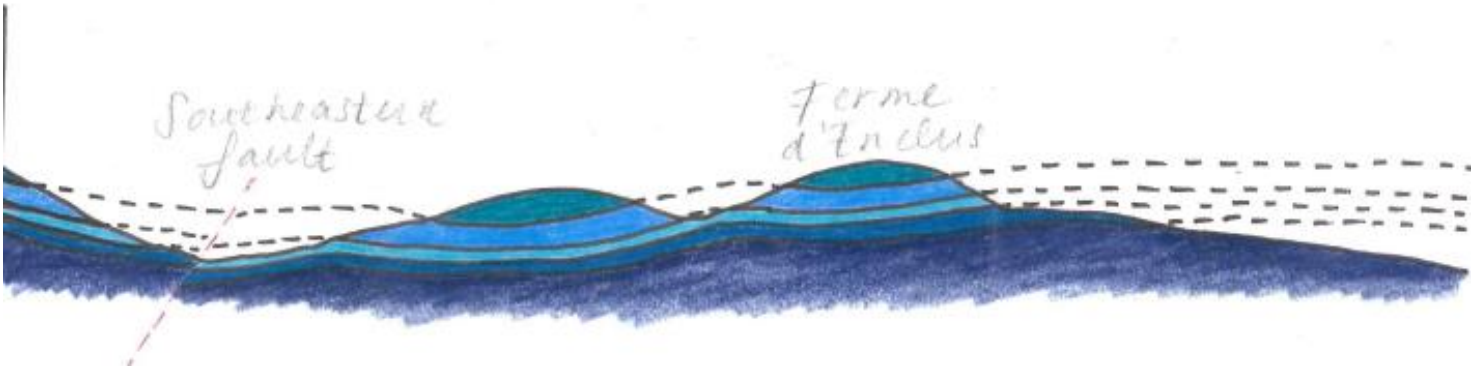

Cross-section 6

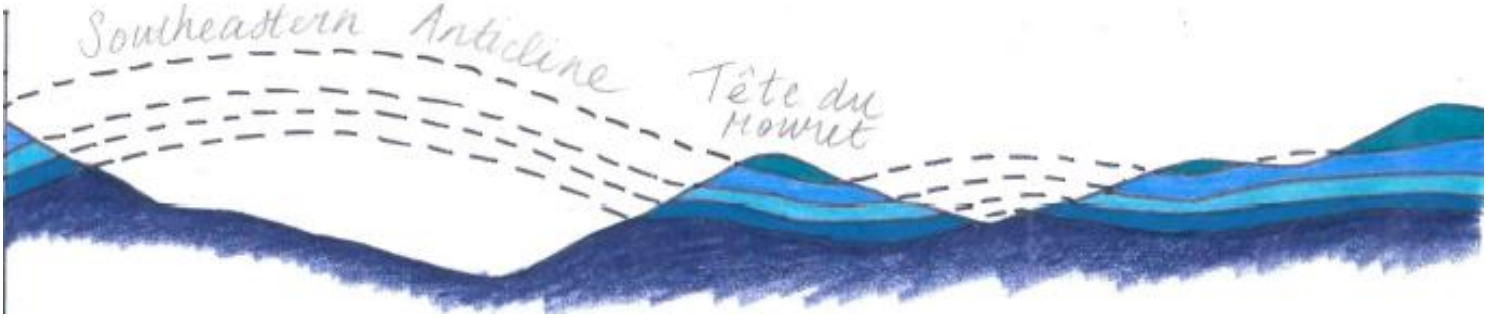

Cross-section 7

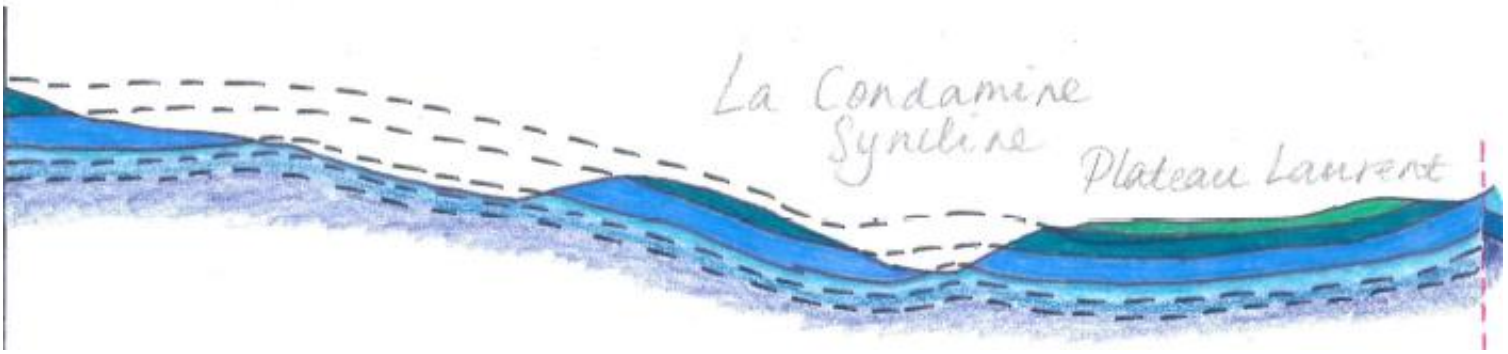

Cross-section 8

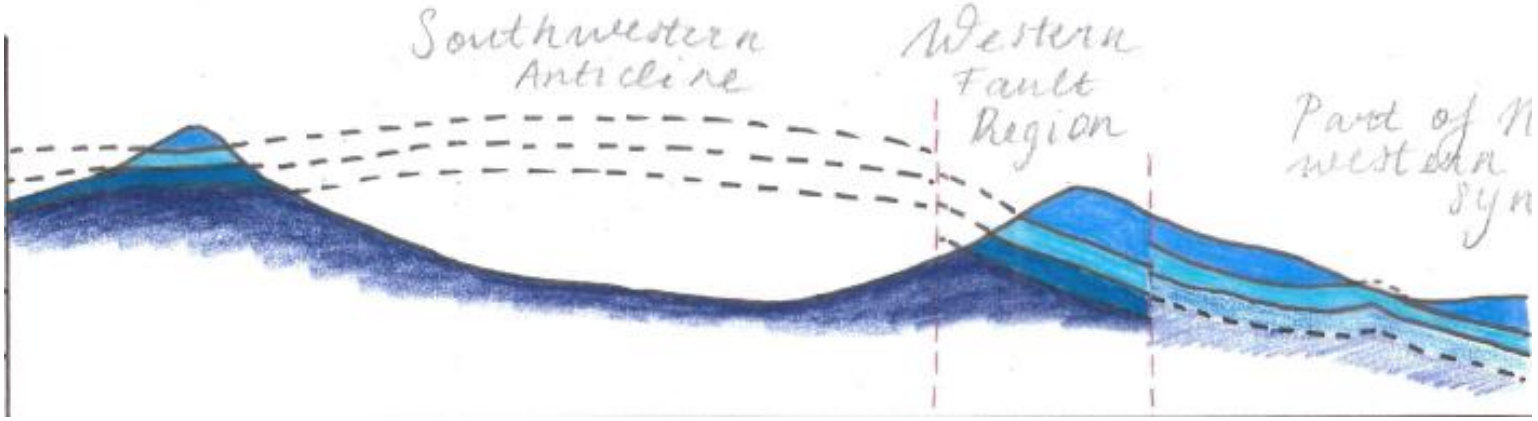

Arnayon 2017

	Coordinates (XY in m)			
Image	**Top**	**Bottom**	**Left**	**Right**
Geological Map	4934000	4928000	680000	688000

Geological map

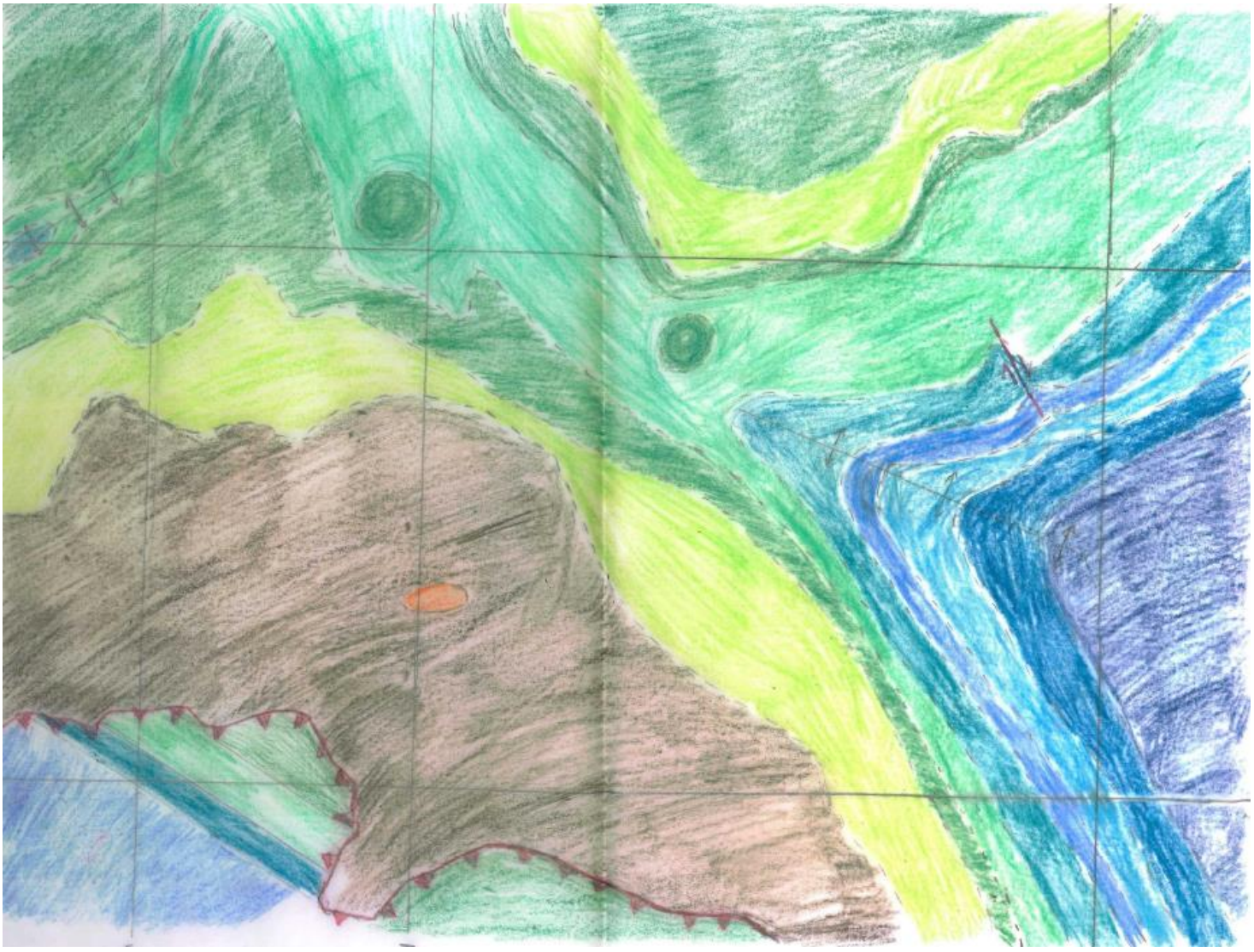

Cornillon 2017

	Coordinates (XY in m)					
Image	**Top**	**Bottom**	**Left**	**Right**	**Distance N-S [m]**	**Distance W-E [m]**
Geological Map	4929000	4923000	686000	695000	-	-
Cross Section 1	4928202	4928202	686000	690952	0	4952
Cross Section 2	4927423	4926000	686000	690952	1423	4952
Cross Section 3	4925568	4925568	686000	689045	0	3045
Cross Section 4	4923492	4923492	686000	689045	0	3045
Cross Section 5	4929000	4924867	690887	692717	4133	1830

Geological map

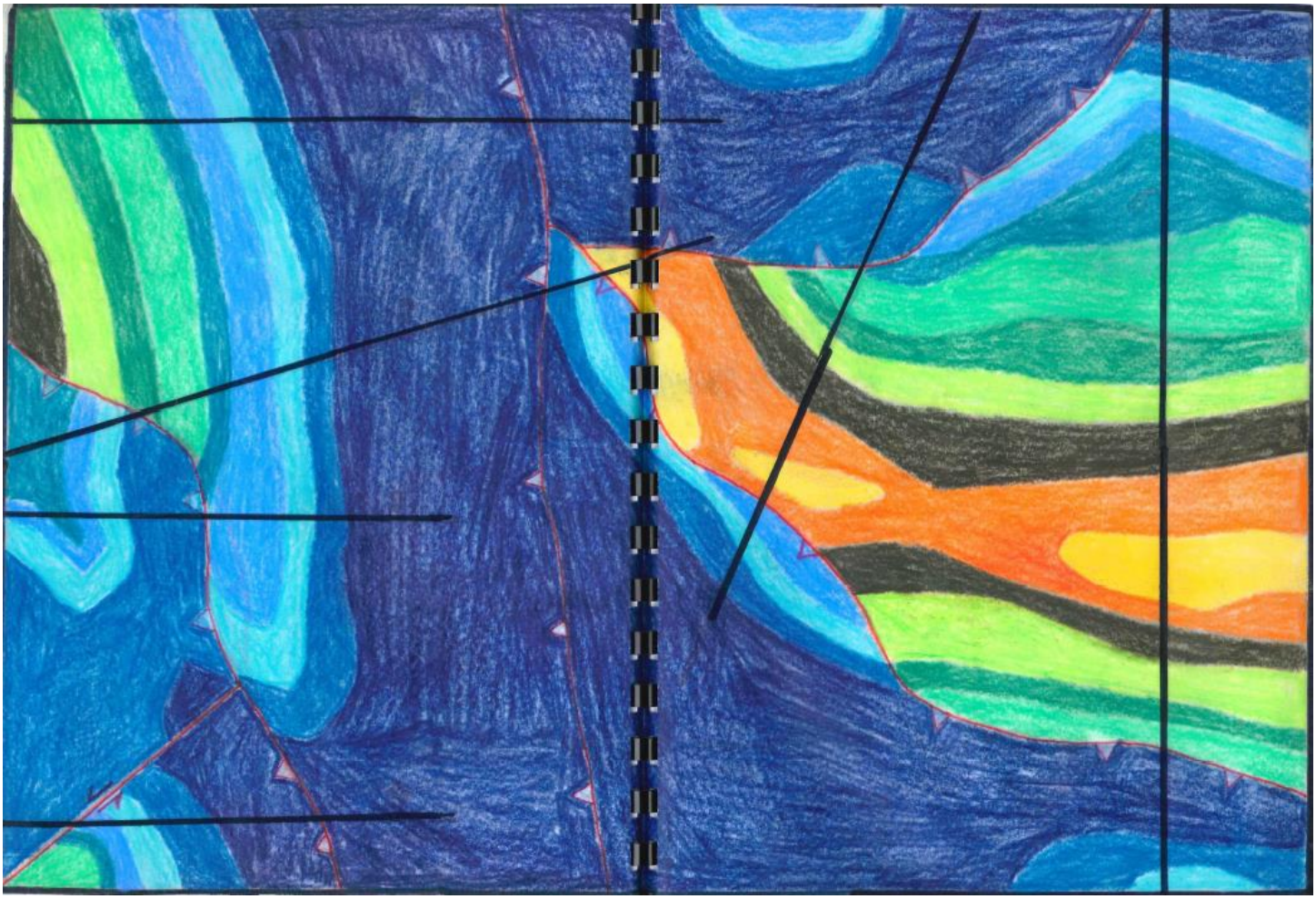

Cross-section 1

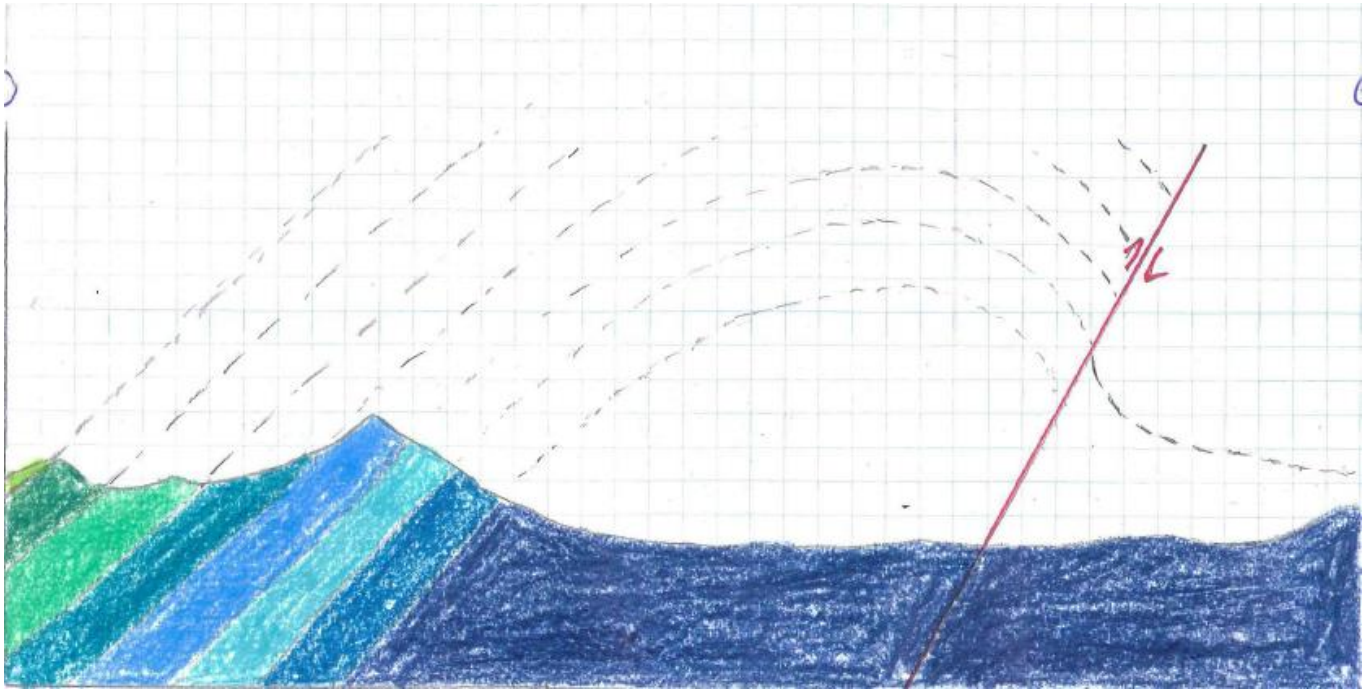

Cross-section 2

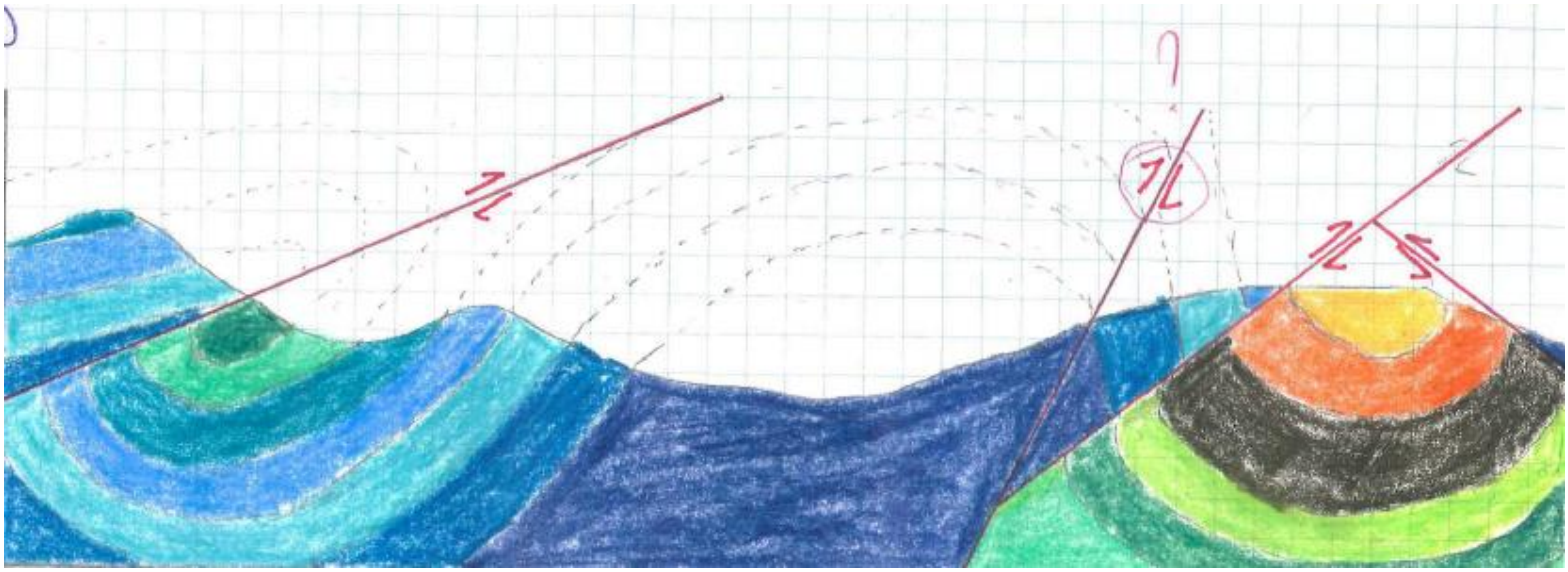

Cross-section 3

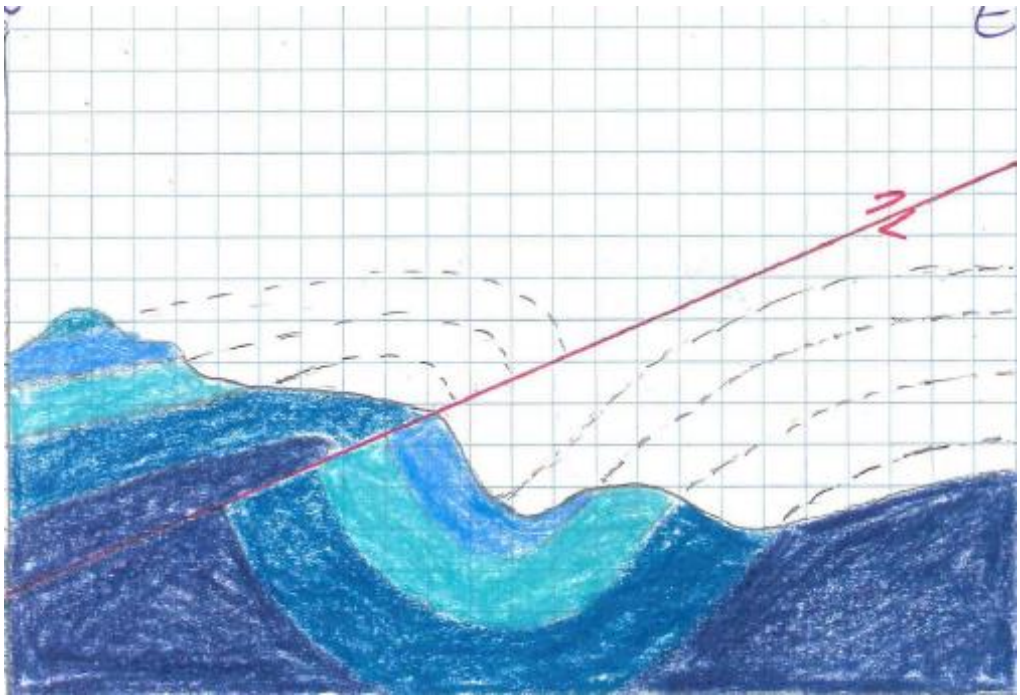

Cross-section 4

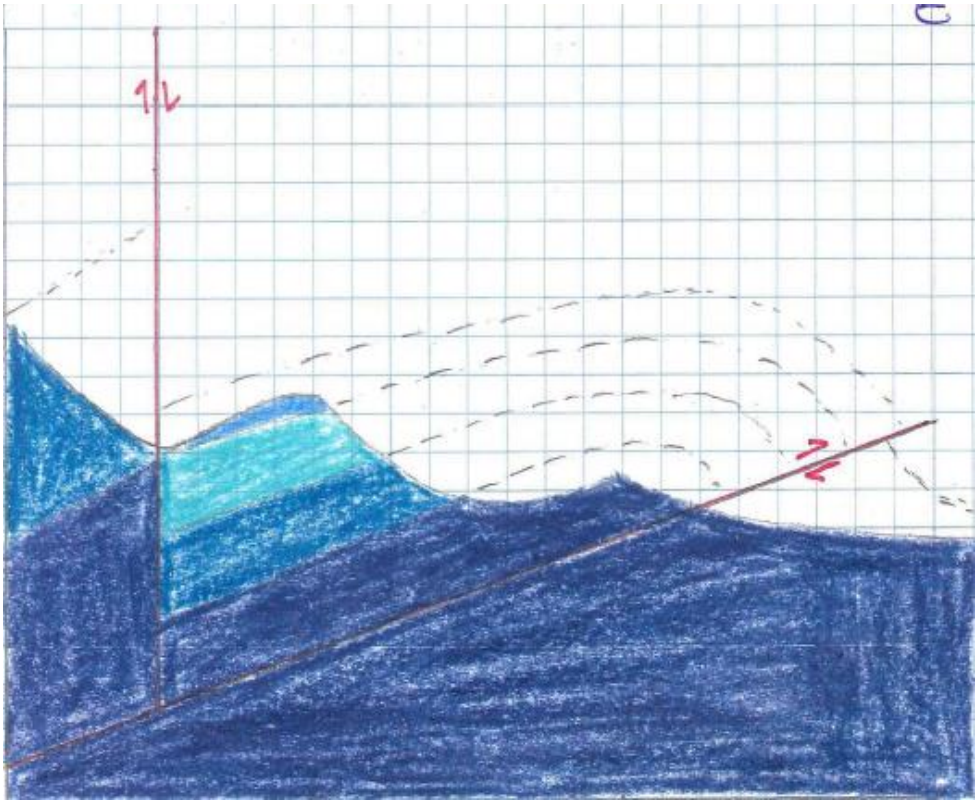

Cross-section 5

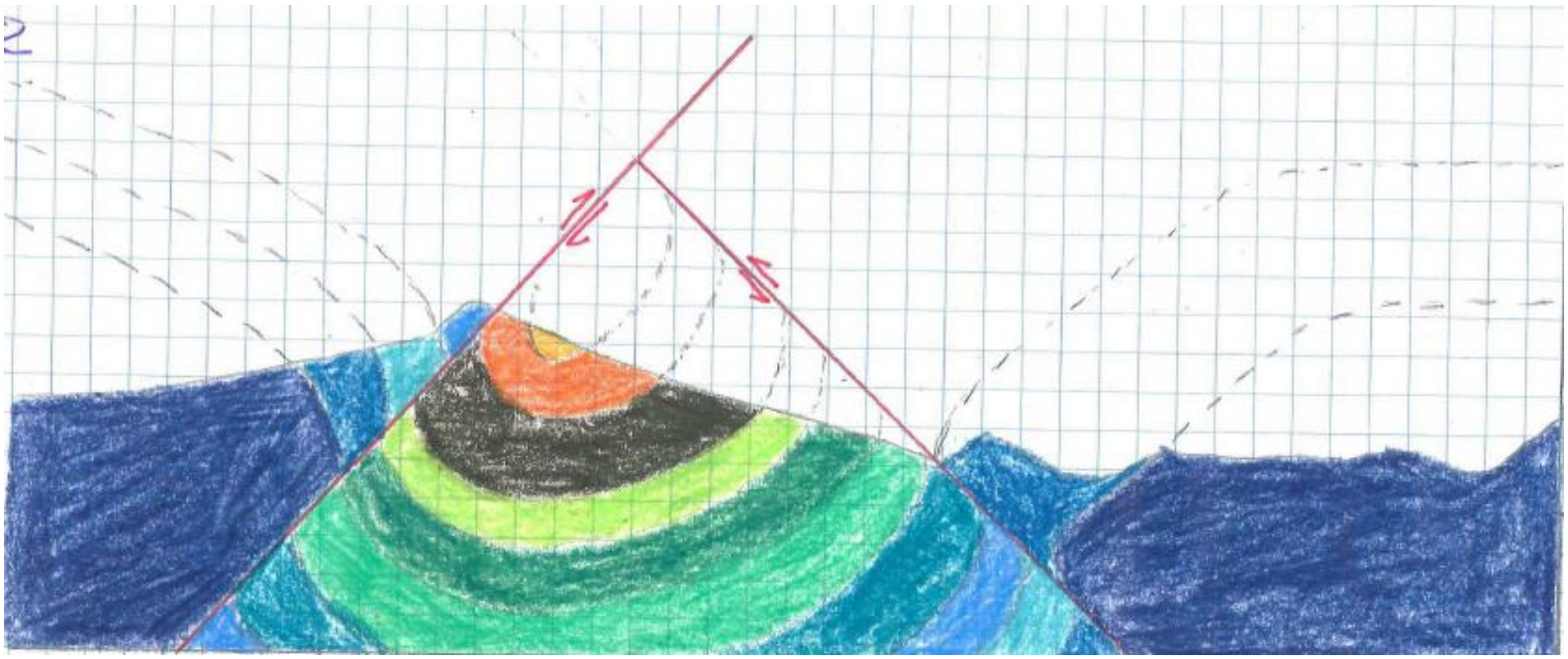

Appendix B: 2D digitized vertical cross-sections

N-S cross-section 0

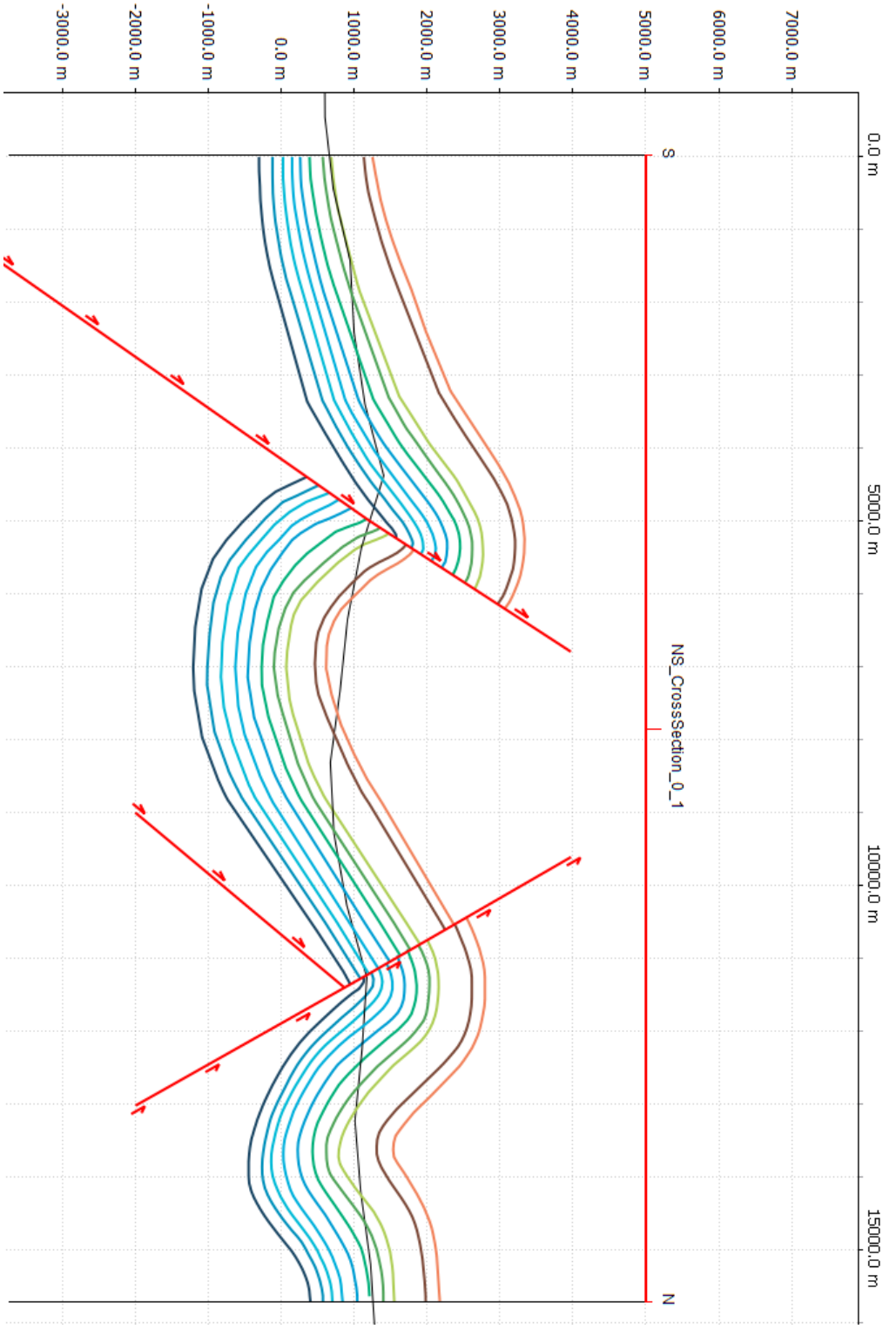

N-S cross-section 1

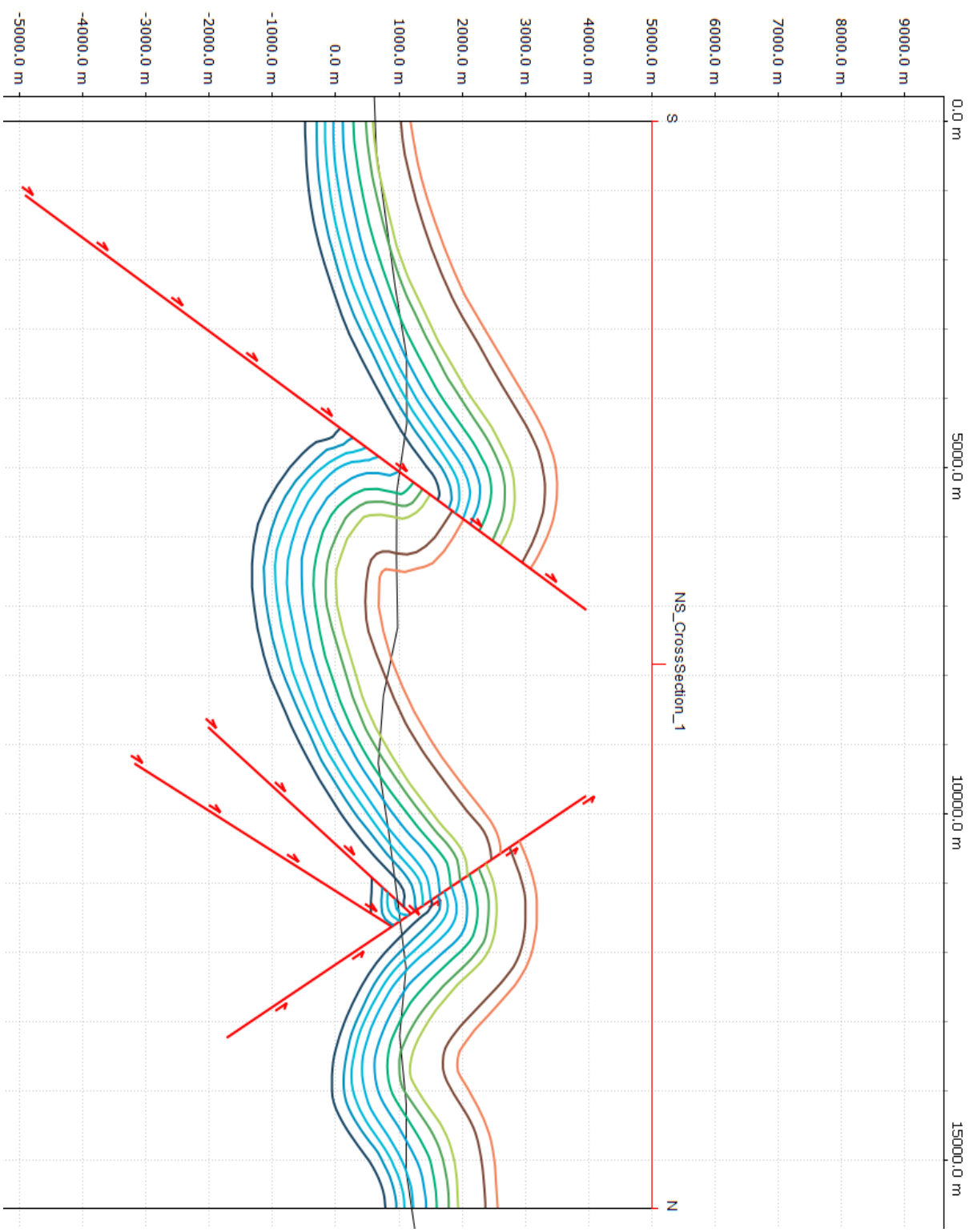

N-S cross-section 2

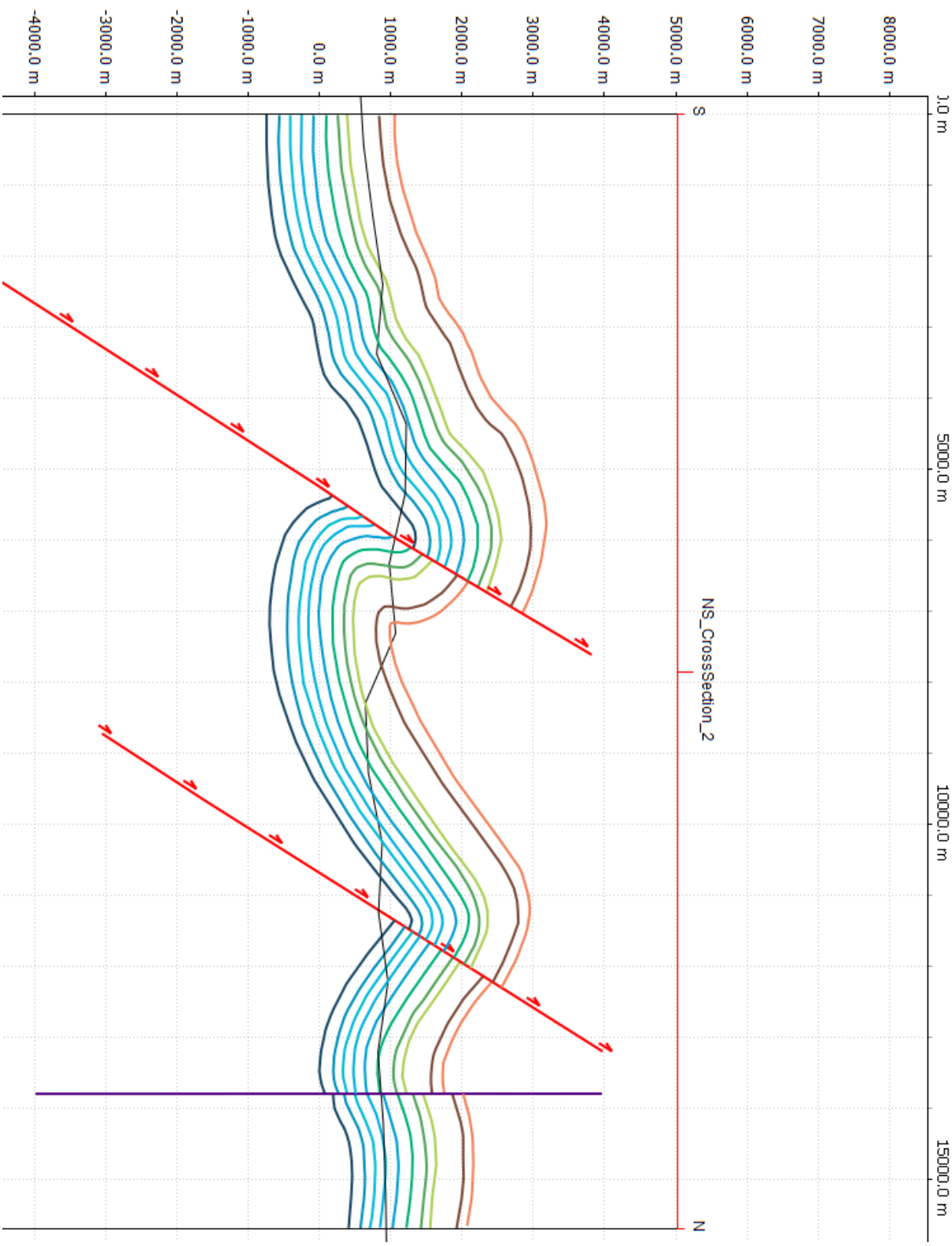

N-S cross-section 3

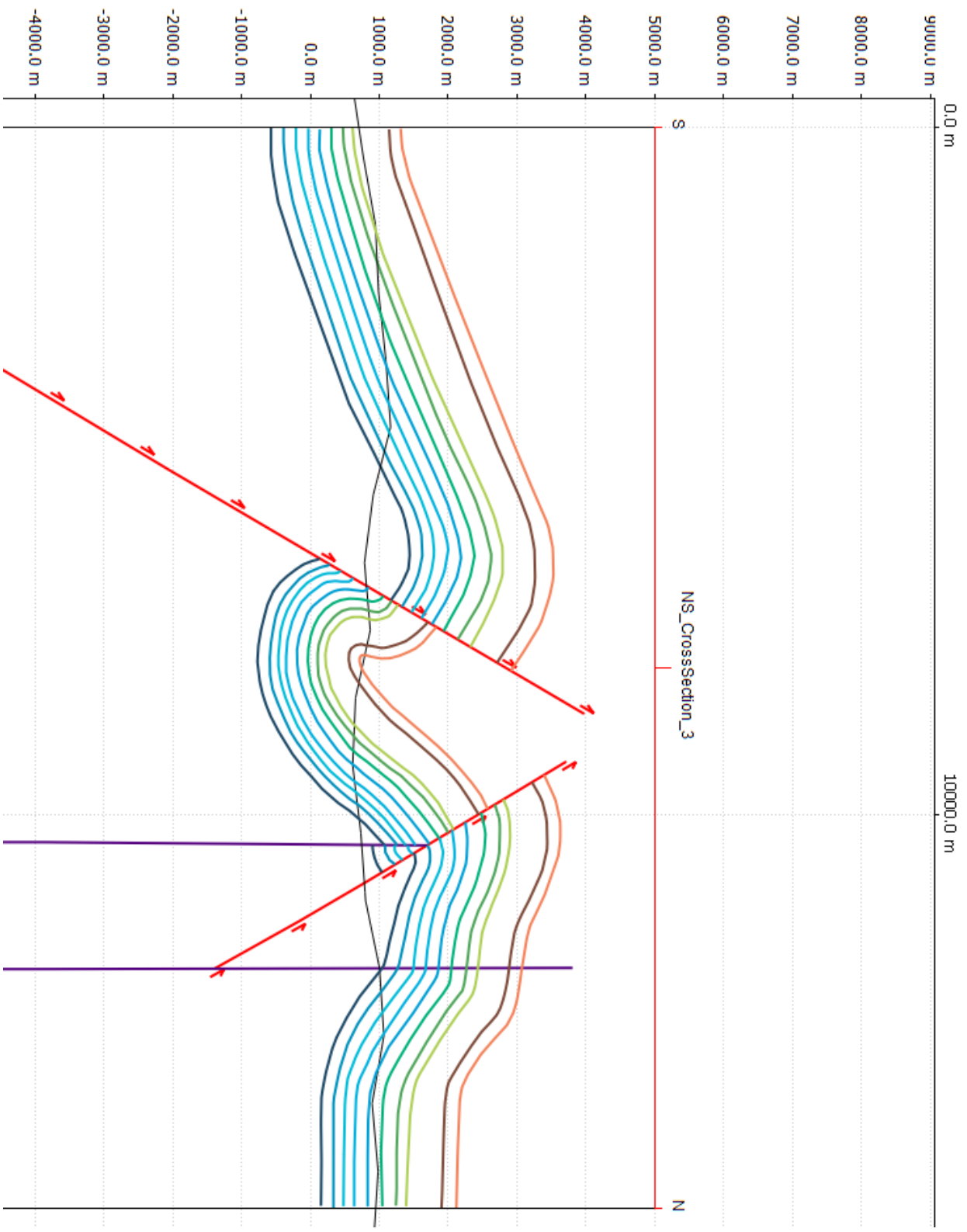

N-S cross-section 4

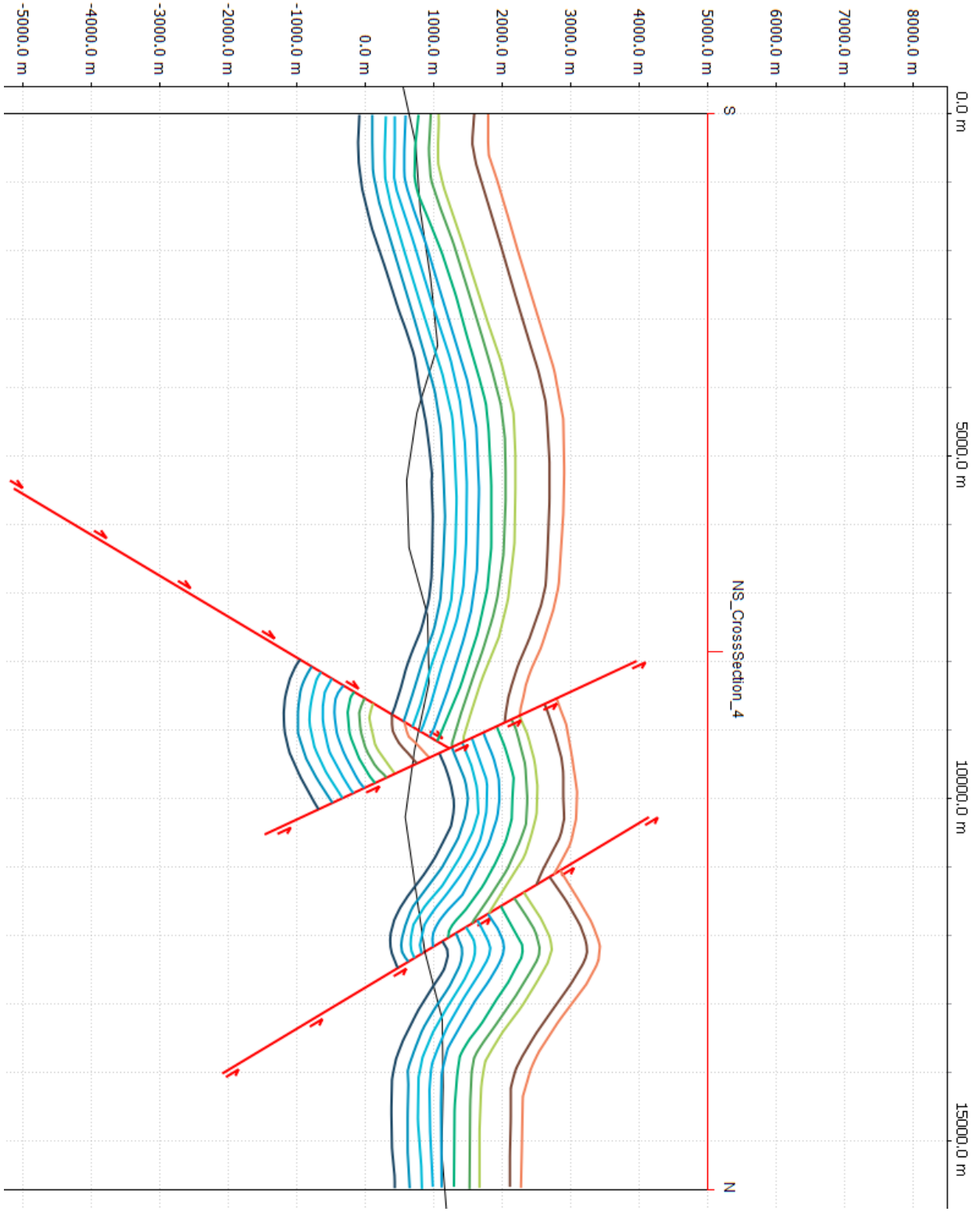

N-S cross-section 5

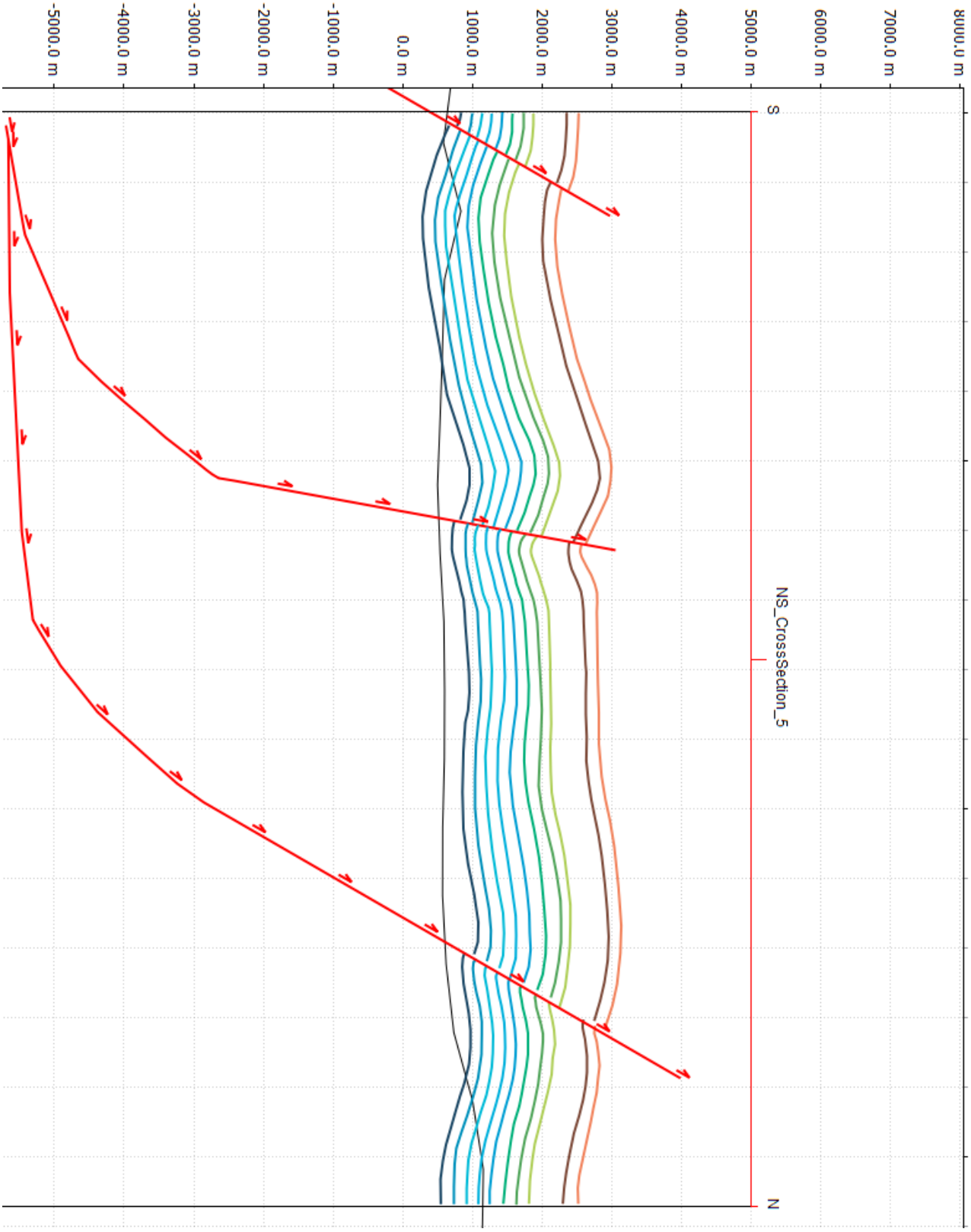

N-S cross-section 6

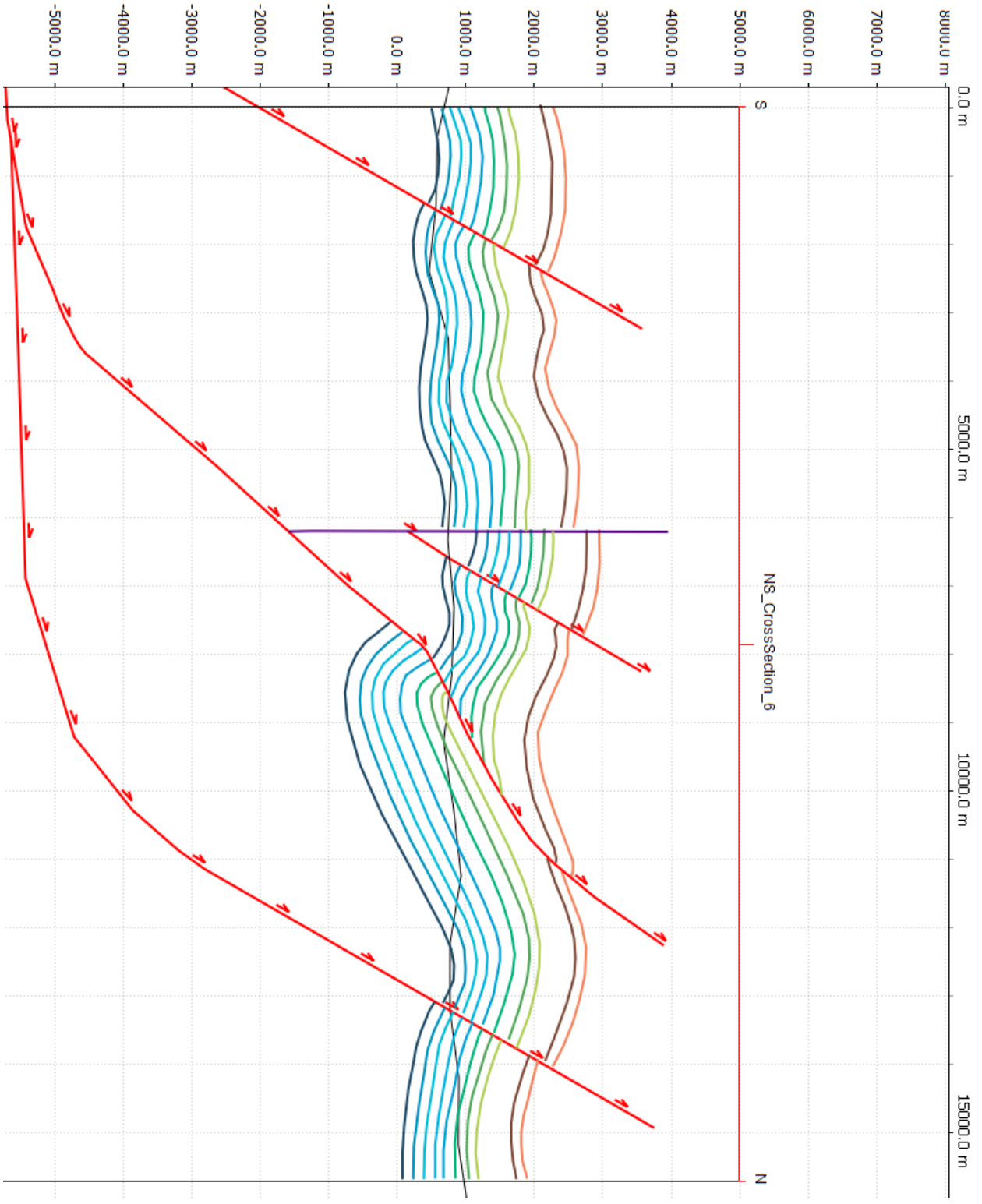

N-S cross-section 7

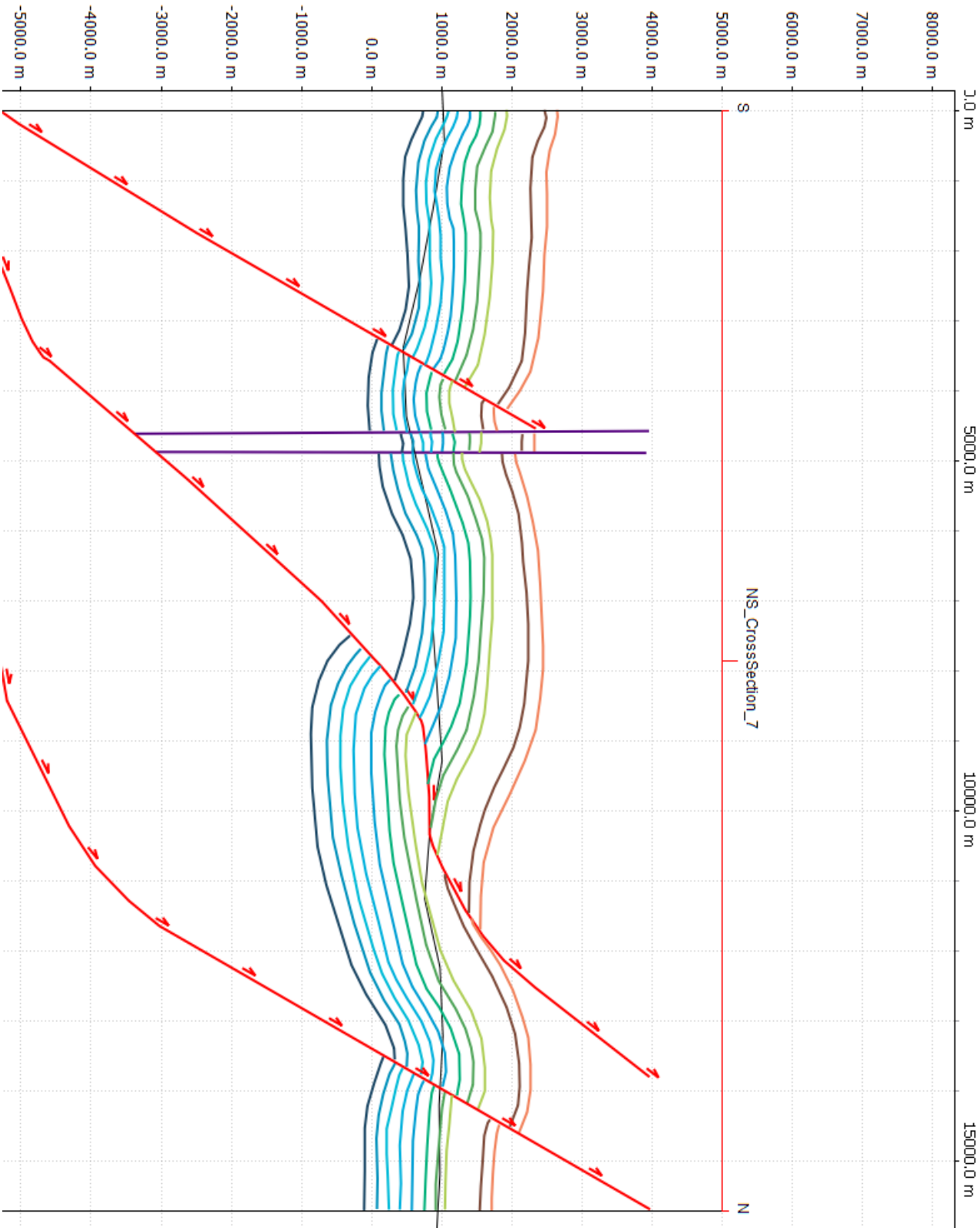

N-S cross-section 8

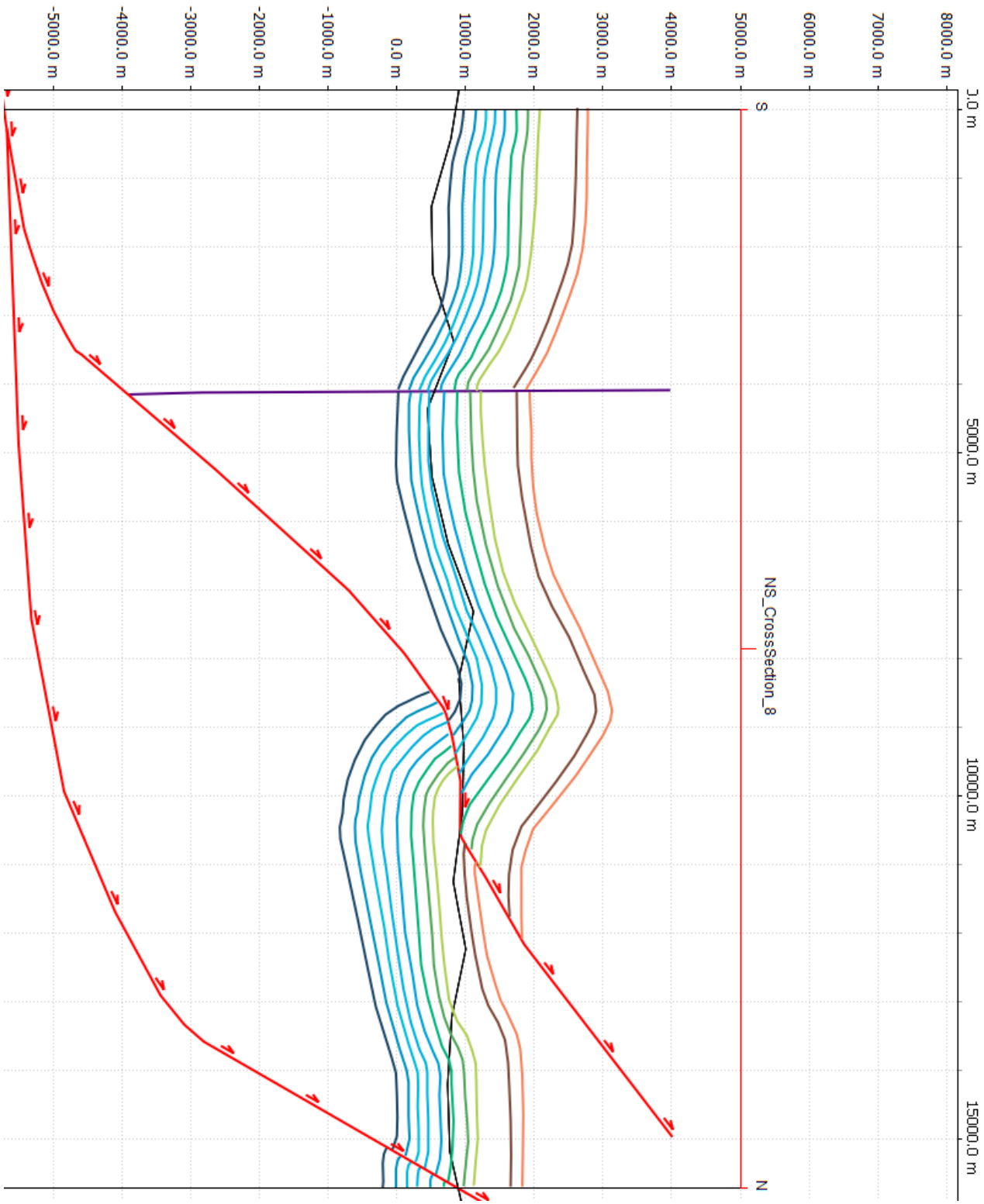

N-S cross-section 9

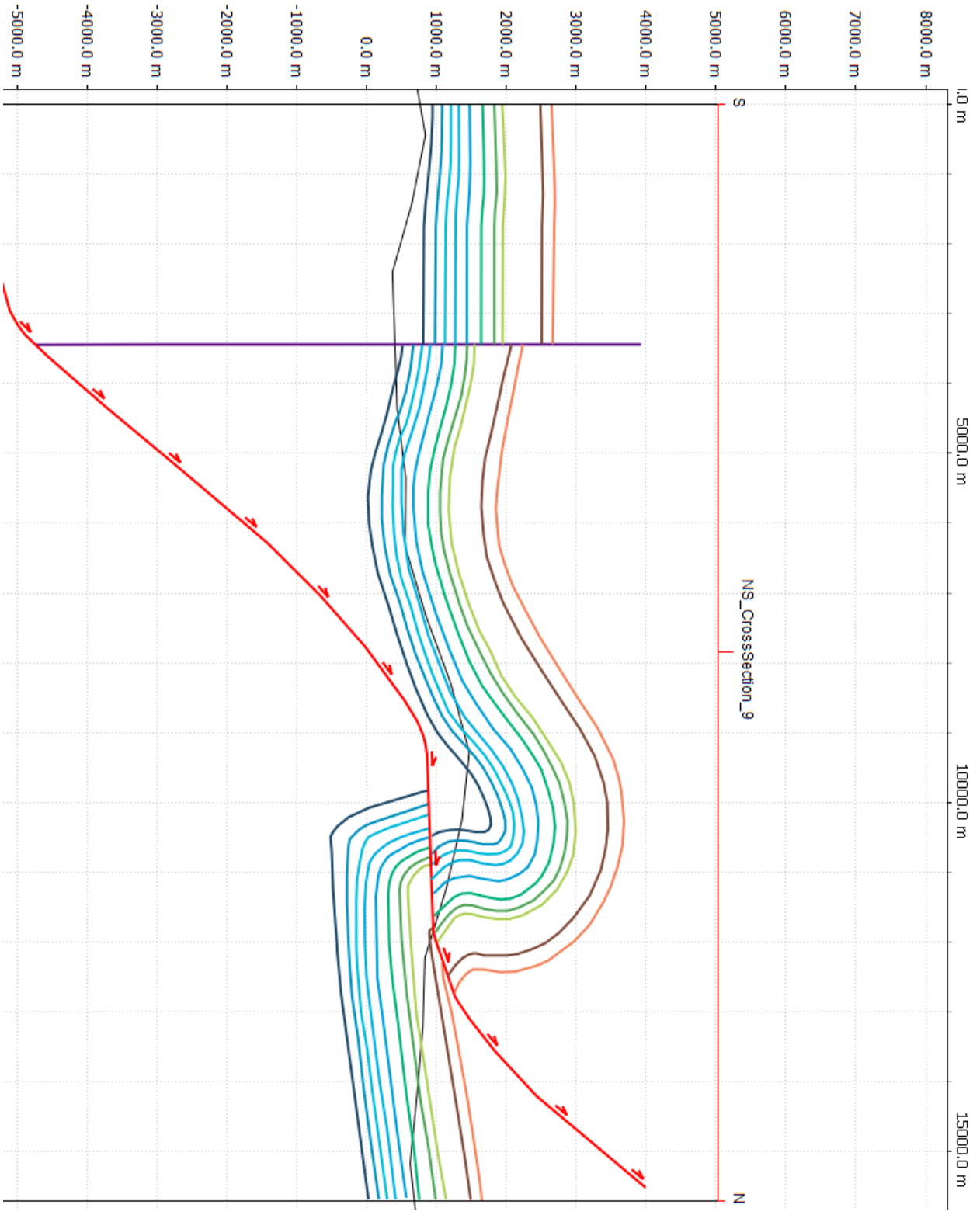

W-E cross-section_0

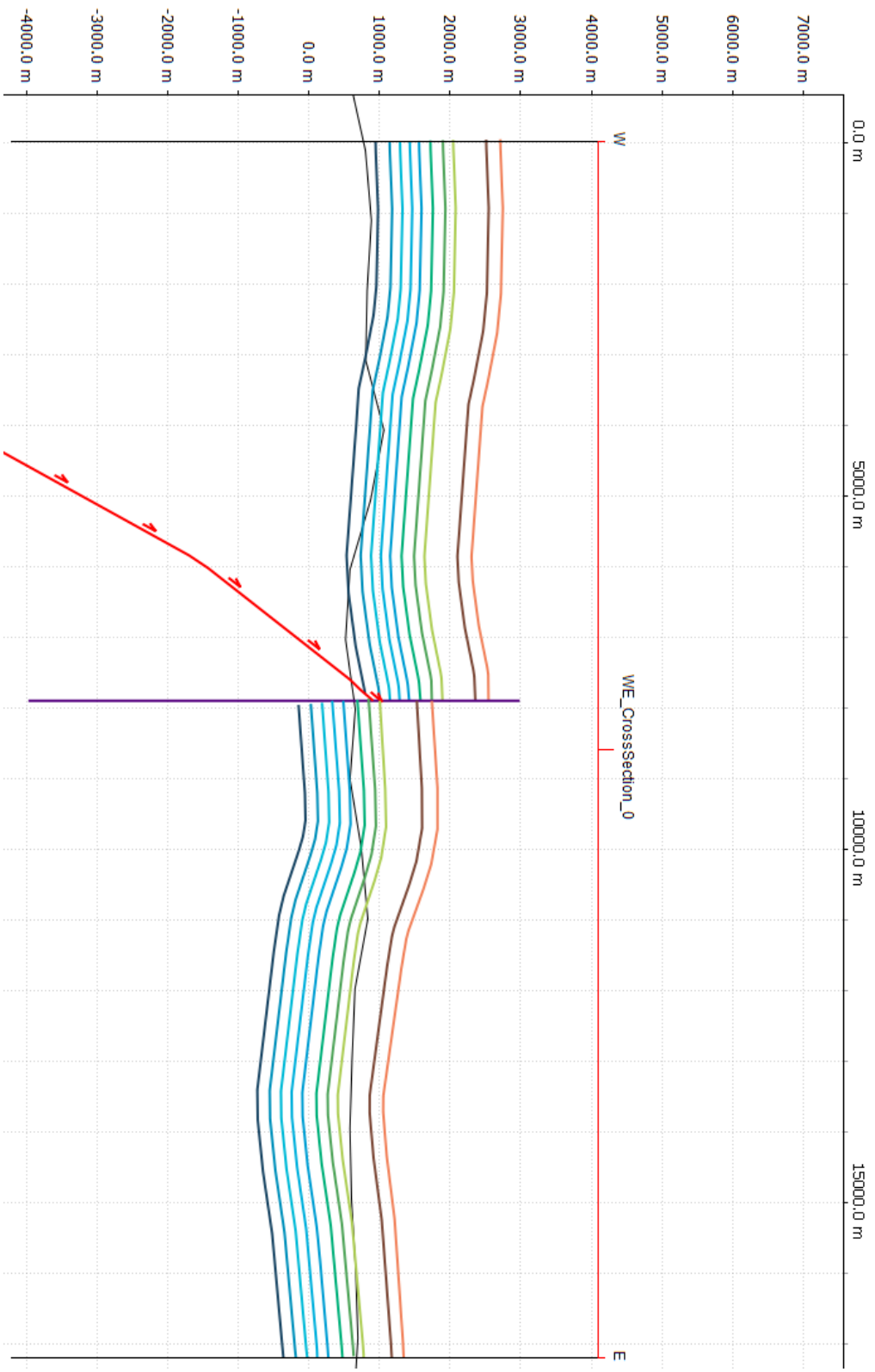

W-E cross-section 1

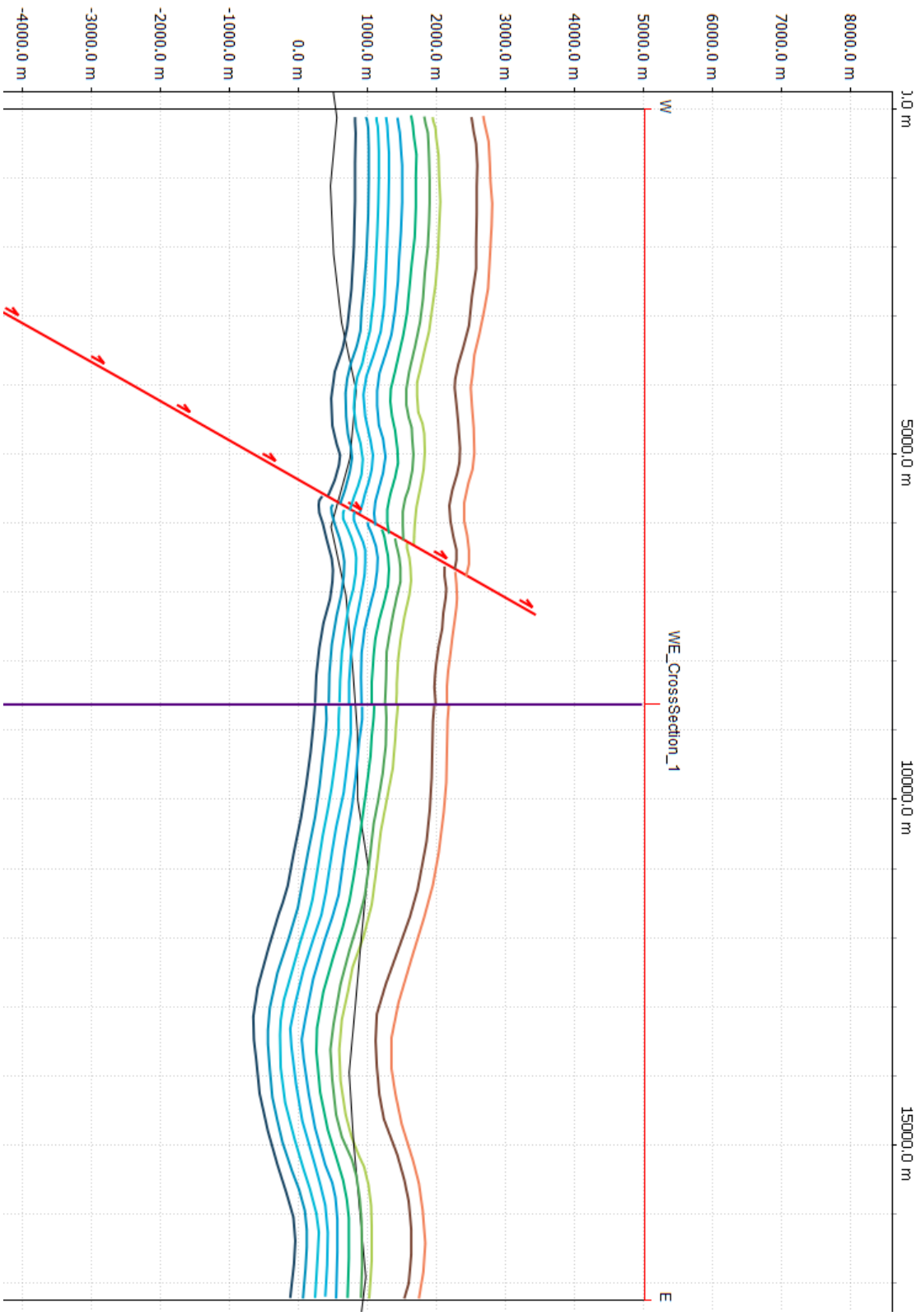

W-E cross-section_2

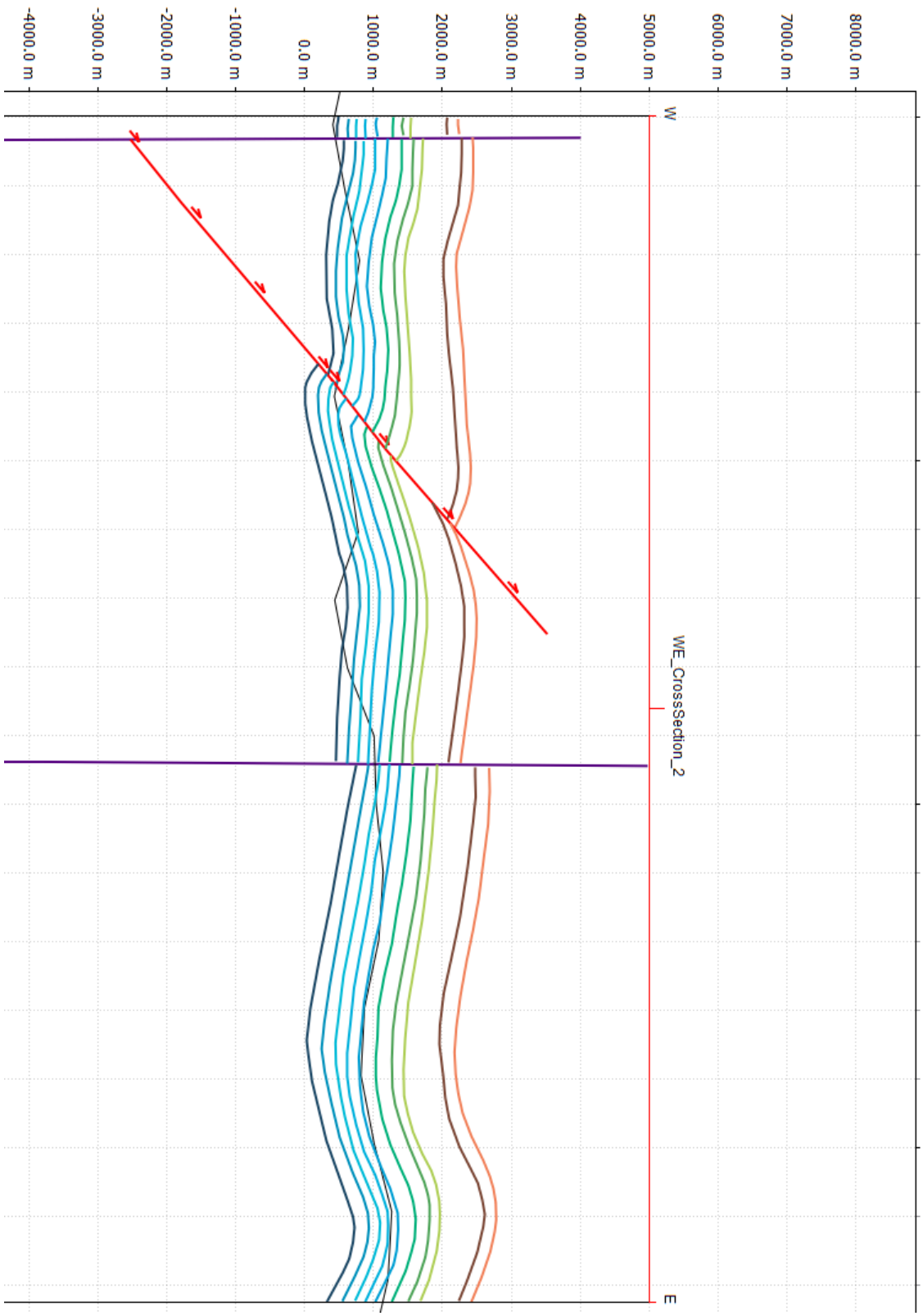

W-E cross-section 3

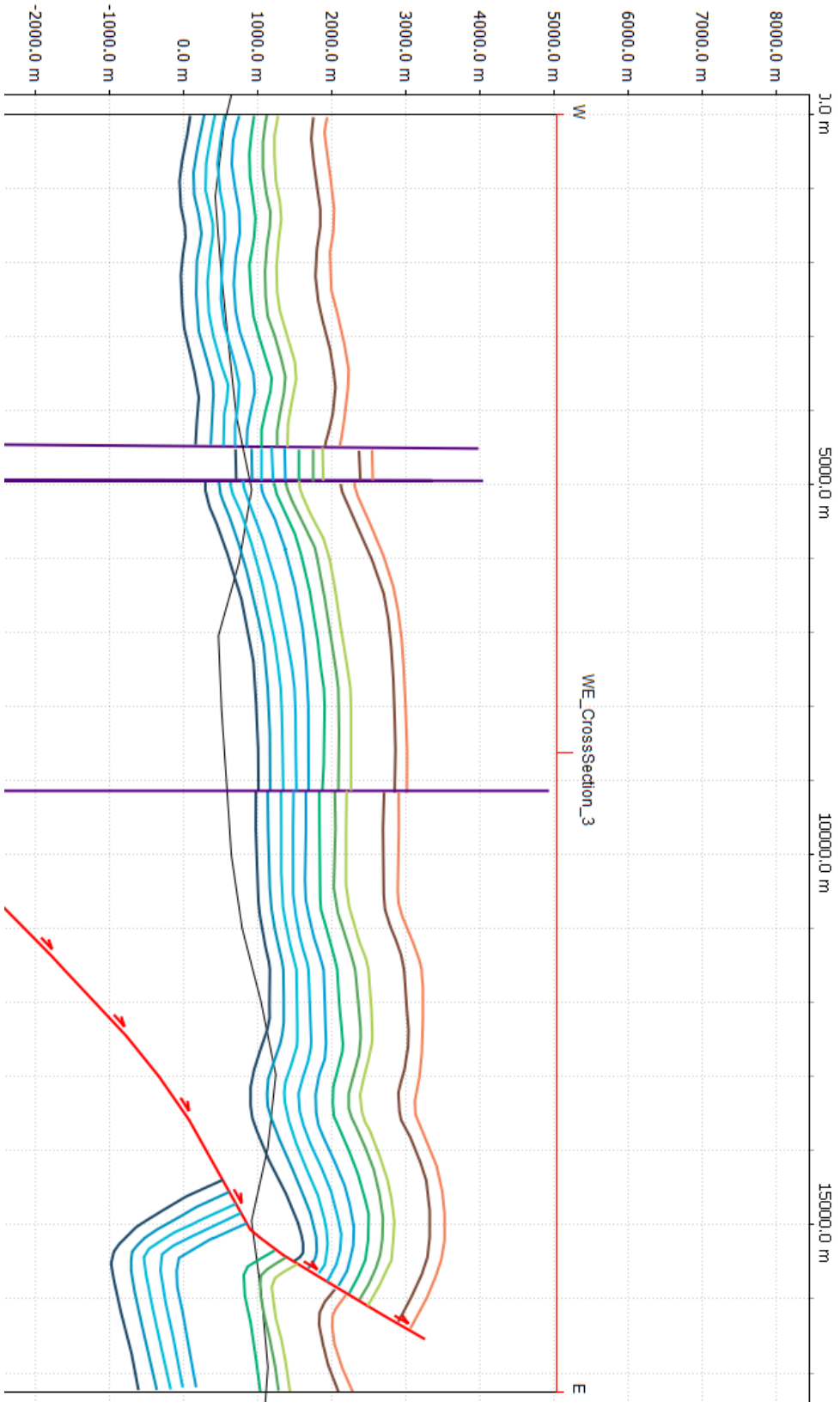

W-E cross-section 4

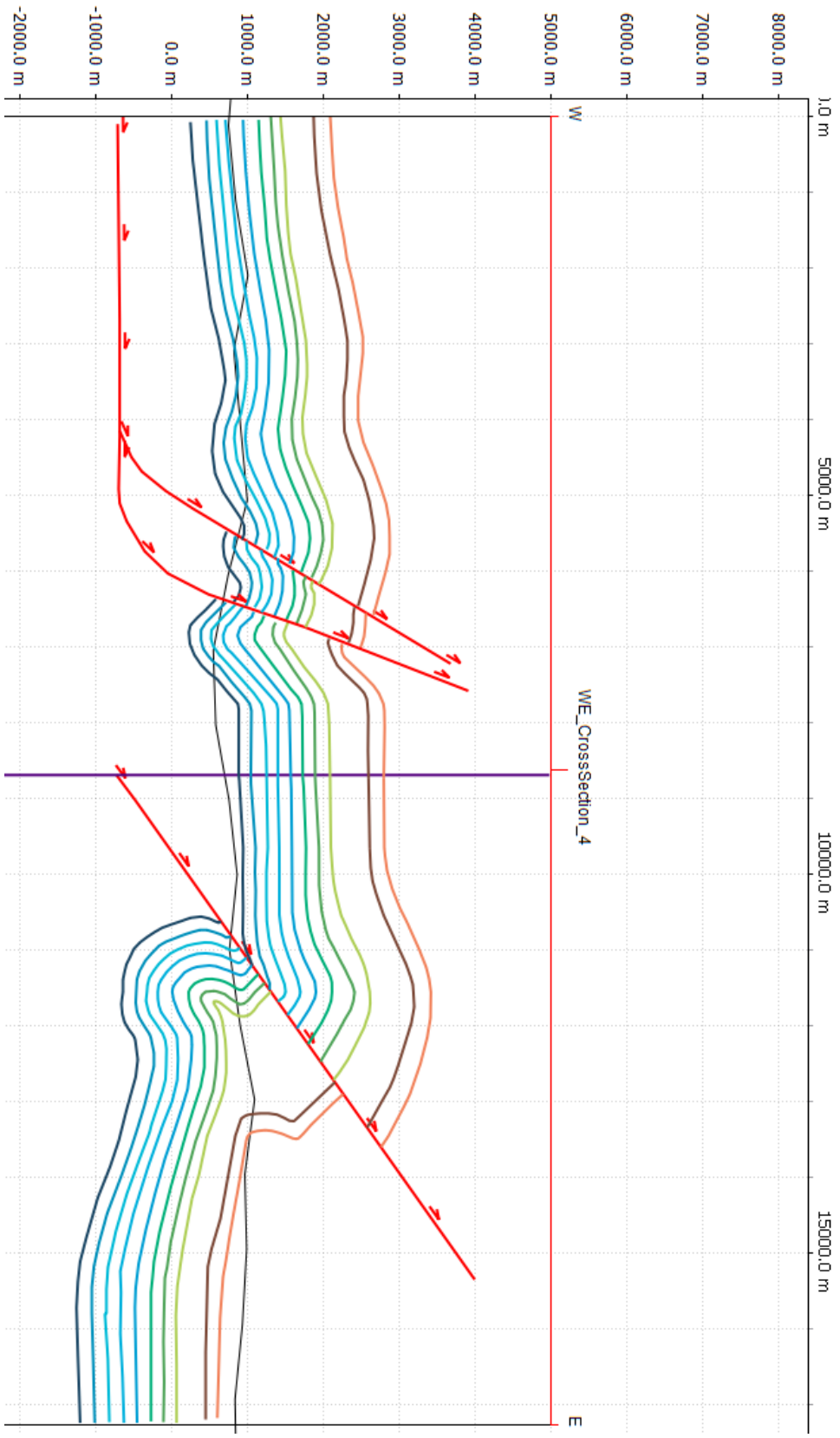

W-E cross-section_5

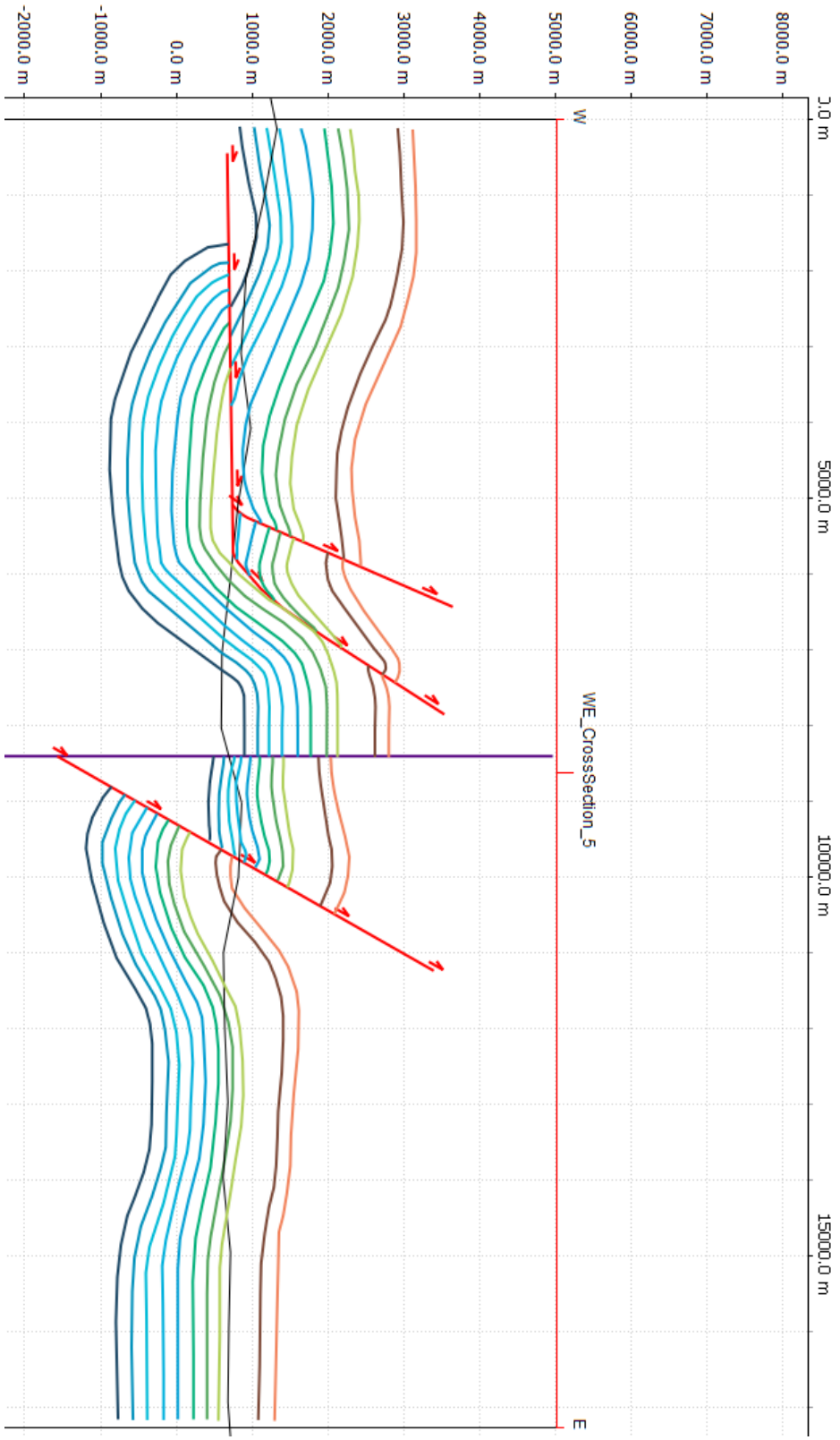

W-E cross-section 6

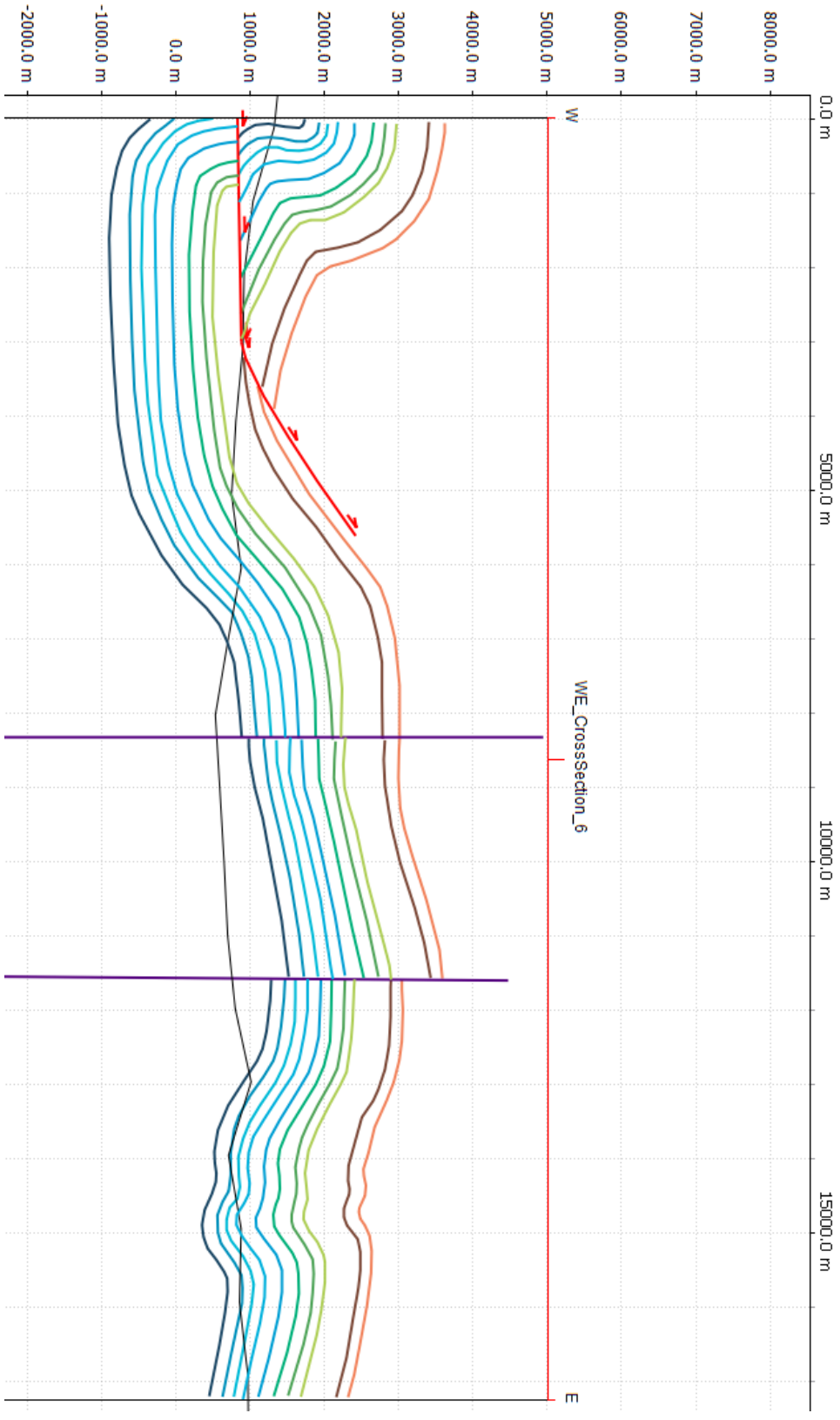

W-E cross-section 7

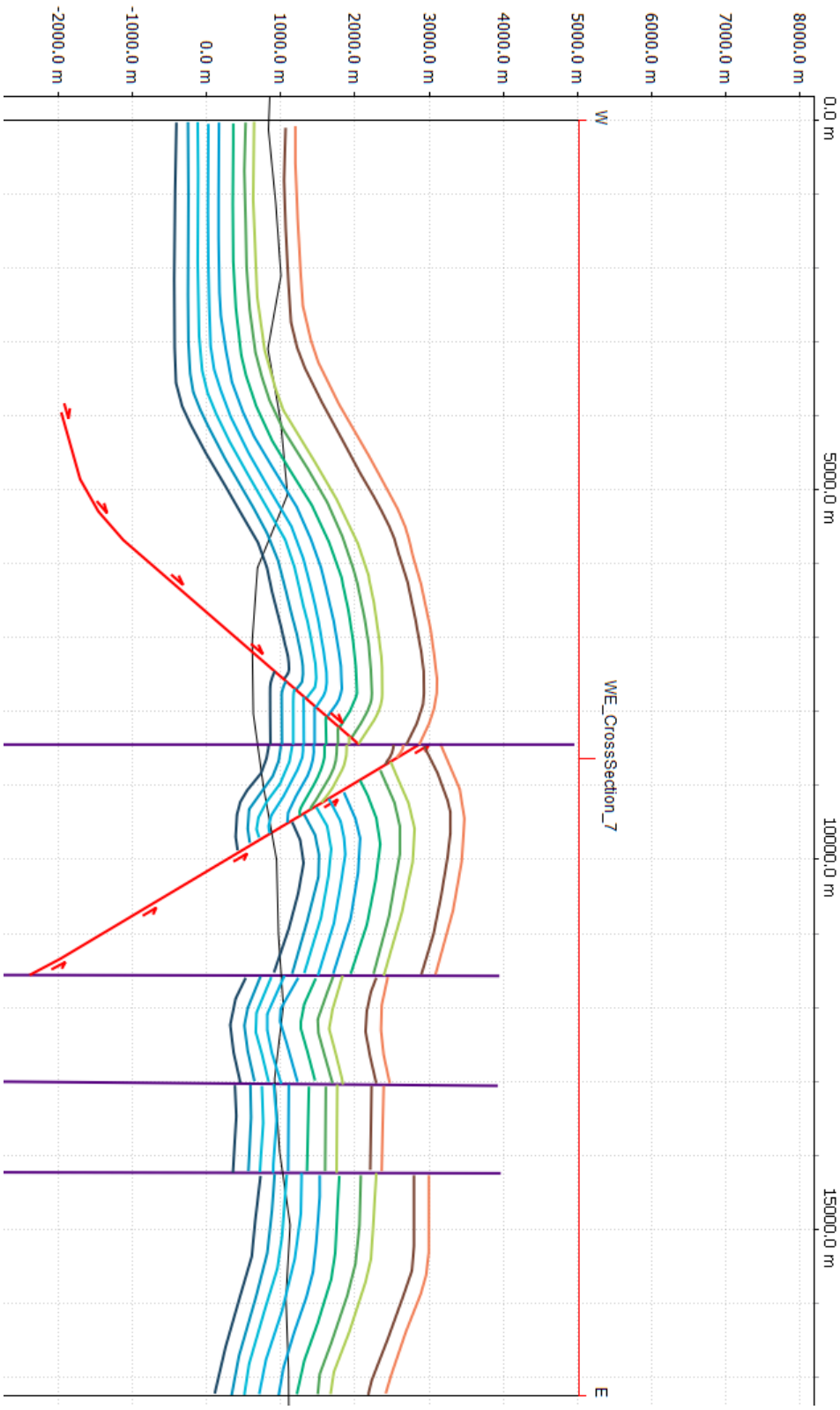

W-E cross-section 8

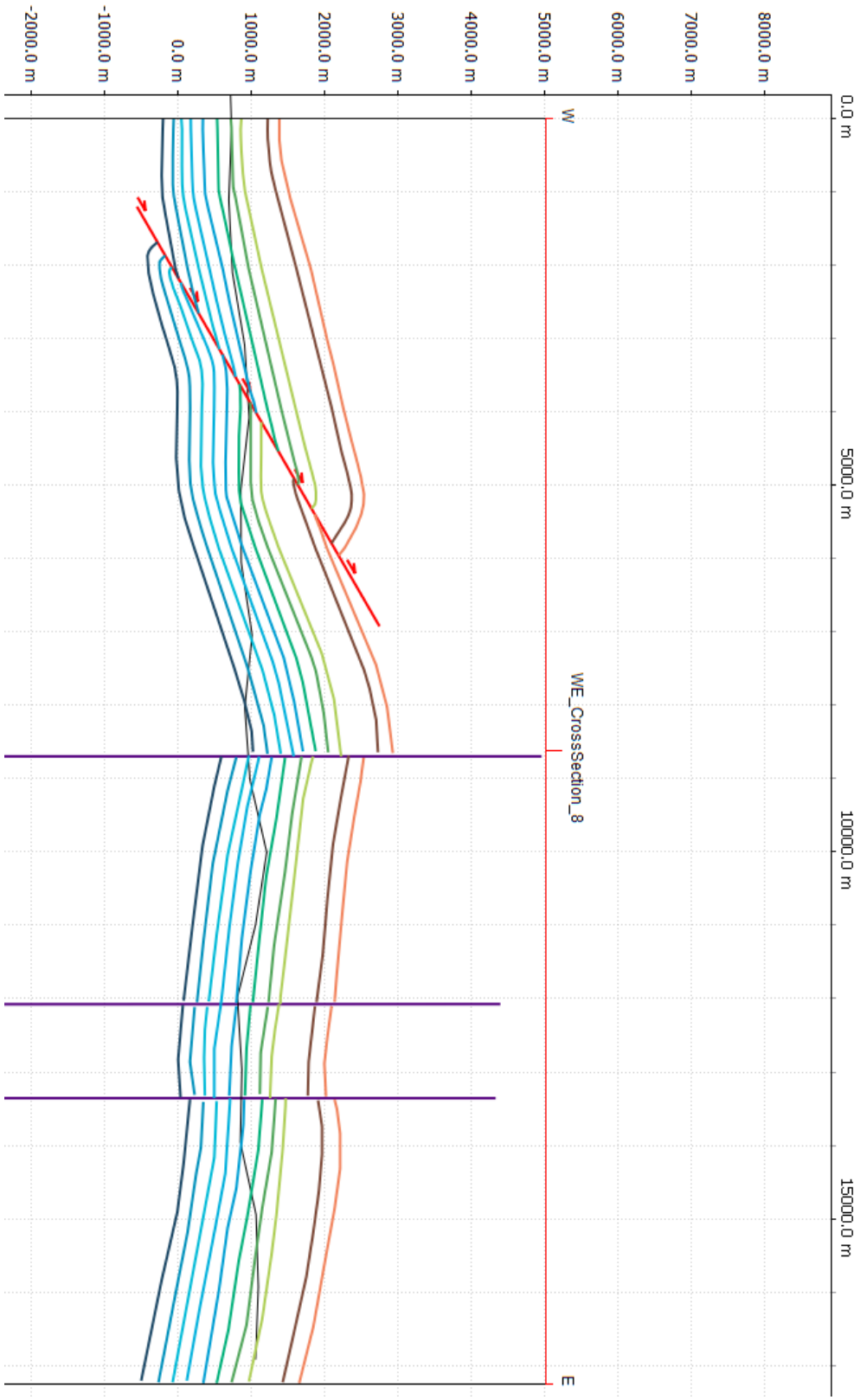

W-E cross-section 9

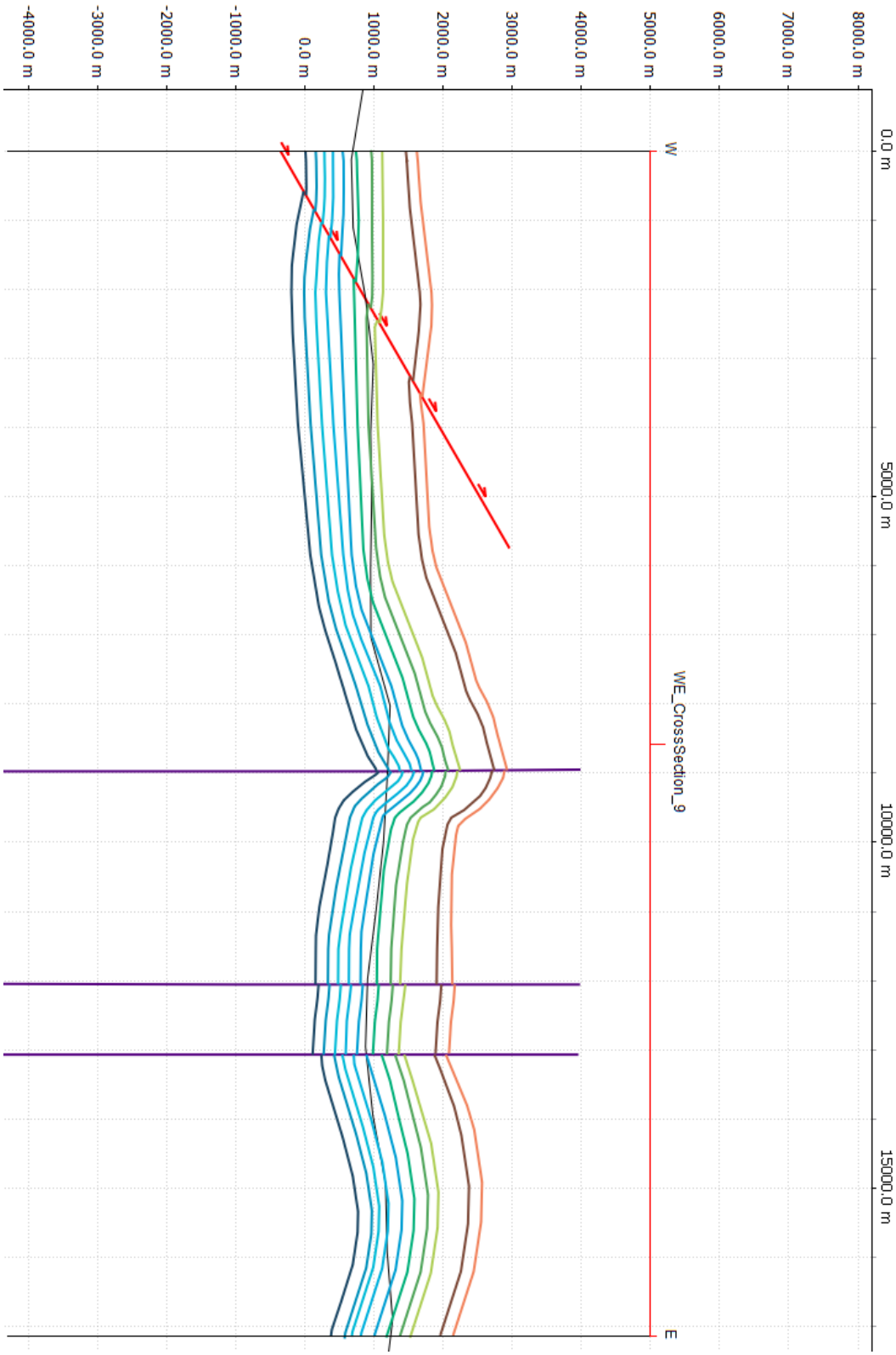

Appendix C: Python Script

Area Calculation

```
# Msc Thesis 2019 - Area Calculation 2D & 3D Model
#
# File: area_calculation.py
# Name: Cyrille Jones
# Date: 12/2/2019
#
# This program calculates the map area of the 2D & 3D model before and after
# deformation of the studied area in South of France.

import numpy as np

x = 1902.50; # [m]
y = 1752.30; # [m]
xL = 9*x;
yL = 9*y;

# Map Area [m2]
MapArea = xL * yL;

# Length (yL + y) of each NS cross-section after restoration
NS = [18962.4, 19905.1, 18314.7, 18695.5, 18645.7, 16173.2, 17710.5, 17294.9,
    17472.3, 18500.9]

# Length (yL + y) of each WE cross-section after restoration
WE = [17381.2, 17434.1, 17738.1, 19132.5, 20006.2, 21376.2, 20654.1, 18525.4,
```

```
    18938.2, 17795.3]

# Map area calculated after removing faults & folds
AreaNS = [];
AreaWE = [];

for i in range(0, len(NS)-1):
   x1 = 0;
   if NS[i] >= NS[i+1]:
      x1 = (NS[i+1]*x) + ((NS[i]*x) - (NS[i+1]*x))/2;
   else:
      x1 = (NS[i]*x) + ((NS[i+1]*x) - (NS[i]*x))/2;
   AreaNS.append(x1)

for i in range(0, len(WE)-1):
   x1 = 0;
   if WE[i] >= WE[i+1]:
      x1 = (WE[i+1]*y) + ((WE[i]*y) - (WE[i+1]*y))/2;
   else:
      x1 = (WE[i]*y) + ((WE[i+1]*y) - (WE[i]*y))/2;
   AreaWE.append(x1)

# Area of the top right corner of the map
a = NS[0] - (9*y);
b = WE[9] - (9*x);
CornerArea = (a*b)/2;

# Total Area after fault removal and unfolding
AreaNS[0] = (NS[0]*1707.71) + ((NS[1]*1707.71) - (NS[0]*1707.71))/2;
```

```
AreaT = sum(AreaNS)+sum(AreaWE)  - MapArea + CornerArea; # [m2]

# Amount of shortening of 2D model
Short2D = (AreaT - MapArea)/(10**6);  # [km2]

# Area of 3D model for East and West side
Area3DW = 158.68; # [km2]
Area3DE = 164; # [km2]
AreaT3D = Area3DW + Area3DE; # [km2]

# Amount of shortening of 3D model
Short3D = AreaT3D - (MapArea/(10**6));  # [km2]

# Percentage of shortening 2D model
frac2D = (Short2D/(AreaT/10**6))*100;  # [%]

# Percentage of shortening 3D model
frac3D = (Short3D/AreaT3D)*100;  # [%]

# Difference in area between 3D model & 2D model
Diff = Short2D - Short3D; # [km2]
DiffPer = frac2D - frac3D;
frac = frac3D/frac2D;
Marge = Diff/(MapArea/10**6);
```